Wetting of Pulsed Plasma Fluoropolymers

Eleanor Phoebe Milnes-Smith



A thesis submitted for the degree of

Doctor of Philosophy

Hilary Term 2019

Declaration

This thesis is submitted for the degree of Doctor of Philosophy in Physical and Theoretical Chemistry at the University of Oxford. I confirm that the work presented here is my own. Where information has been derived from other sources, I confirm that this has been indicated in the thesis.

Angle-resolved XPS measurements were performed by Dr Robert Palgrave at University College London. Contact angle measurements of chemical warfare agents were performed by Dr Corinne Stone at DSTL. Solid-state NMR measurements were performed by Dr Nicholas Rees at the University of Oxford. In all cases, the experiments were devised by the author, and all data analysis and interpretation is the author's own work.

Abstract

The work presented in this thesis is an investigation of the surface properties of fluoropolymers synthesized via pulsed plasma polymerization. The focus is on perfluoroalkyl acrylate (PFAC-*n*, where *n* is the number of carbons in the perfluoroalkyl chain) polymers which are used in the manufacture of military protective clothing. The aim of the study is to understand how PFAC-*n* polymer surfaces interact with liquids, particularly chemical warfare agents (CWA's). The properties of some other fluoropolymers are also briefly investigated; the acrylate group in PFAC-6 is exchanged for an alkene (PFO) and a perfluoroalkyl (PFH) group. Additionally, a co-polymer of PFAC-6 and 2-hydroxyethyl methacrylate (HEMA) was synthesized which shows good potential for use in oil/water separation.

The surfaces were characterized using ^{19}F solid-state nuclear magnetic resonance (NMR) spectroscopy, X-ray photoelectron spectroscopy (XPS), atomic force microscopy (AFM) and contact angle goniometry. It is shown that plasma conditions resulted in degradation of PFO and PFH, whilst PFAC-*n* polymerizes with retention of functionality. PFAC-4 and -6 exist in the liquid state at room temperatures, whilst PFAC-8 and -10 are disordered polycrystalline solids. All show increased side-chain ordering at the surface compared to the bulk, with preferential segregation of CF_3 at the surface. The two liquids have increased

ordering compared to the solids at room temperature and are therefore lower in surface energy.

The time- and temperature-dependence of contact angles of ethylene glycol (EG) and *n*-hexadecane (*n*-HD) is investigated, and these are shown to trigger surface reorganization of PFAC-*n* when the polymers are in the liquid state. The wetting behaviour of some CWA's and CWA simulants is also examined, and it was found that the CWA's display lower contact angles on PFAC-*n* than predicted by the wetting of conventional probe liquids, such as ethylene glycol and *n*-hexadecane, or by the wetting of CWA simulants.

Acknowledgements

First and foremost, I would like to thank my supervisor, Susan Perkin, for your support and guidance through what has been a fairly eventful DPhil. I am extraordinarily privileged to have worked with such a dedicated and insightful scientist for so many years.

I'd also like to thank Corinne Stone at DSTL, without whom I never would have had an opportunity to work on such a fantastic project. I've immensely enjoyed working with you.

I'm grateful to my disability mentor, Julia Hill, without whom I couldn't have made it through this DPhil. I have learned so much from working with you, and you have my complete admiration.

The various members of the Perkin Group, both past and present, have been excellent company, both in the lab and out.

My thanks to the various technical staff who have helped over the years: Robert Jacobs and Ashley Shepherd at the Surface Analysis Facility; Nichola Flanagan, Alison Crossley, and Phil Holdway at the Oxford Materials Characterisation Service (OMCS); Nicholas Rees in the Inorganic NMR Facility; and Robert Palgrave at HarwellXPS.

My love to The Fab House (later Shack) and everyone who has walked alongside me on this journey, however briefly. In particular Sally Le Page, who has kept me alarmed and entertained in equal measures for more than eight years and without whom I would know far less about pigeons, ladybirds, and friendship; Suzie Ford, whose kindness and creativity never ceases to amaze me; Laura Grima, who never fails to make me laugh and brightens up any room; and Mikayla Hunter, whose equal parts cynicism and enthusiasm has kept me going over the past few years.

Finally, my parents, Tom and Philippa, and my brother John*. I don't think that there is anything I could say that would adequately express my gratitude for the love and support you have given me over the years.

.

* Who is still shorter than me, no matter what he, or anyone else, might think

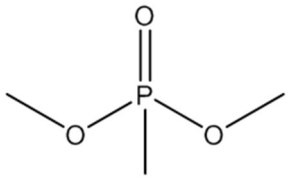
Chemical Structures and Acronyms

DD

$CH_3(CH_2)_8CH_3$

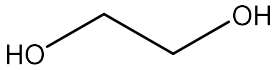
n-Dodecane

DMMP



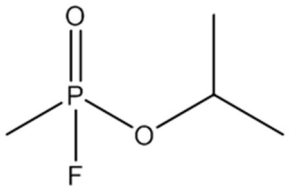
Dimethyl methylphosphonate

EG



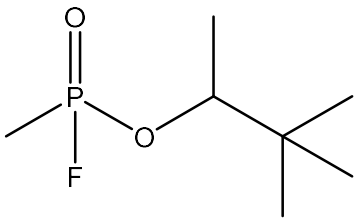
Ethylene glycol

GB



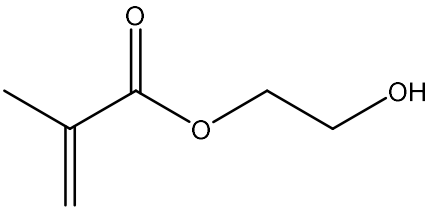
Sarin

GD



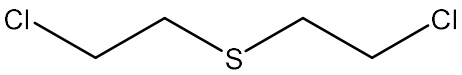
Soman

HEMA



2-Hydroxyethyl methacrylate

HD[†]



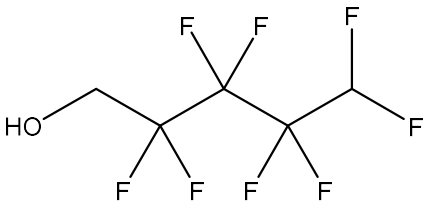
Sulfur mustard

n-HD[†]

$CH_3(CH_2)_{14}CH_3$

n-Hexadecane

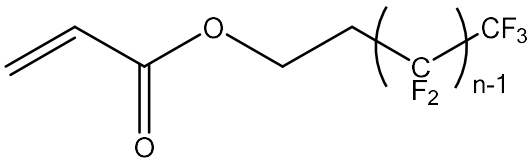
OFP



2,2,3,3,4,4,5,5-Octafluoro-1-pentanol

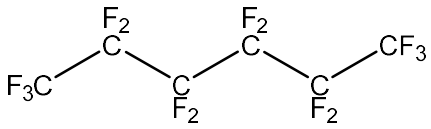
[†] 'HD' is the NATO weapon designation for sulfur mustard, as well as the commonly used acronym for *n*-hexadecane. To prevent confusion, *n*-hexadecane is abbreviated to '*n*-HD'

PFAC-*n*



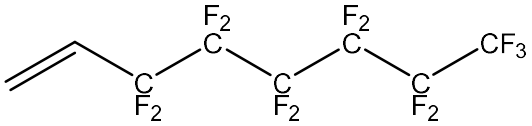
1H,1H,2H,2H-Perfluoro-n-yl acrylate

PFH



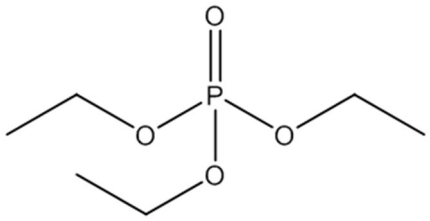
Perfluorohexane

PFO



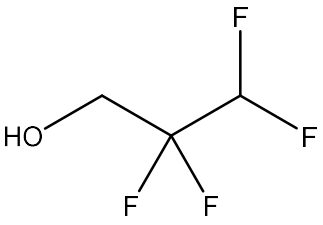
1H,1H,2H-Perfluoro-1-octene

TEP

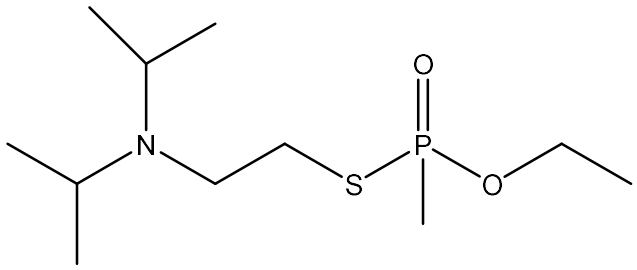


Triethyl phosphate

TFP



2,2,3,3-Tetrafluoro-1-propanol

VX 

VX

Table of Contents

Declaration ..... **i**

Abstract ..... **ii**

Acknowledgements ..... **iv**

Chemical Structures and Acronyms ..... **vi**

1. Introduction **1**

1.1. Designing a Low Energy Surface **1**

1.1.1. The low surface energy of fluorocarbons 3

1.1.2. The effect of surface roughness and topography on wetting 5

1.2. Plasmas and Plasma Polymerization **8**

1.2.1. Introduction to plasmas 8

1.2.2. Surface modification using plasmas 10

1.2.3. Continuous wave vs. pulsed conditions 11

1.2.4. Atmospheric vs. low pressure conditions 12

1.3. Aim of Study **13**

1.4. Summary of Thesis **17**

1.5. References **18**

2. Surface Characterization and Wetting Behaviours of Plasma Fluoropolymers: The Role of Polymerizable Group 23

2.1. Experimental 26

2.1.1. Monomers 26

2.1.2. Plasma chamber set-up and experimental conditions 26

2.1.3. X-ray photoelectron spectroscopy (XPS) 28

2.1.4. Solid-state nuclear magnetic resonance (NMR) spectroscopy 29

2.1.5. Atomic force microscopy (AFM) 29

2.1.6. Contact angle (CA) goniometry and surface energy measurement 30

2.2. Results and Discussion 31

2.2.1. Chemical composition (solid-state ^{19}F NMR) 31

2.2.2. Chemical composition (XPS) 33

2.2.3. Topography 43

2.2.4. Surface energy and wetting properties 44

2.2.5. Discussion 47

2.3. Conclusions 52

2.4. References 53

3. Surface Characterization and Wetting Behaviours of Plasma Polymerized Fluoroalkyl Acrylates 57

3.1. Experimental 60

3.1.1. Monomers 60

3.1.2. Plasma polymerization 60

3.1.3. Surface characterization 60

3.1.4. Differential scanning calorimetry (DSC) 61

3.2. Results and Discussion 61

3.2.1. Chemical composition (solid-state ^{19}F NMR) 61

3.2.2. Chemical composition (XPS) 65

3.2.3. Thermal analysis 75

3.2.4. Topography 78

3.2.5. Surface energy and wetting properties 80

3.2.6. Discussion 82

3.3. Conclusions 87

3.4. References 88

4. Thermal Behaviour and Adaptive Wetting of Fluoroalkyl Acrylate Polymers 91

4.1. Experimental 93

4.1.1. Variable temperature contact angle goniometry 93

4.2. Results and Discussion 94

4.2.1. Contact angle aging 94

4.2.2. Kinetics of drop spreading 102

4.2.3. Surface energy 107

4.2.4. Discussion 112

4.3. Conclusions 120

4.4. References 122

5. Wetting of Chemical Warfare Agents and Their Simulants on Fluoropolymer Surfaces 125

5.1. Experimental 127

5.1.1. Selection of probe liquids....127
5.1.2. Contact angle goniometry of chemical warfare agents and simulants .129
5.2. Results and Discussion 131
5.2.1. Predicting the contact angles of CWA's on PFAC-*n* using the OWRK method....131
5.2.2. Contact angles of CWA's and simulants....132
5.2.3. Discussion....134
5.3. Conclusions 137
5.4. References 138

6. Solid-State Nuclear Magnetic Resonance Spectroscopy Studies of Fluoroalkyl Acrylate Polymers....141
6.1. Background 143
6.1.1. Nuclear Magnetic Resonance [193,194] 143
6.1.2. Nuclear shielding and chemical shift [193,195]....144
6.1.3. Spin-spin coupling 146
6.1.4. Magic angle spinning (MAS) 147
6.1.5. NMR relaxation....149
6.2. Experimental 151
6.2.1. Sample preparation 151
6.2.2. Acquisition of one dimensional ^{19}F spectra at variable temperatures .151
6.2.3. Measurement of spin-lattice (T_1) relaxation times 151
6.3. Results and Discussion 153
6.3.1. Room temperature spectra....153
6.3.2. Variable temperature spectra 157

6.3.3. ^{19}F spin-lattice relaxation time 162

6.3.4. Discussion 167

6.4. Conclusions 172

6.5. References 173

7. Plasma Polymers for Oil/Water Separation 177

7.1. Experimental 179

7.1.1. Plasma polymerization 179

7.1.2. Surface characterization 180

7.2. Results and Discussion 181

7.2.1. Chemical composition 181

7.2.2. Topography 185

7.2.3. Surface energy and wetting properties 186

7.2.4. Discussion 188

7.3. Conclusions 191

7.4. References 192

8. Conclusions and Outlook 195

8.1. References 199

Appendix A: Complete Results for Drop Aging Experiments 201

1. Introduction

Liquid repellent surfaces are useful in a wide variety of contexts [1-6]: antifouling coatings for biomedical devices and membrane filters [7-9]; self-cleaning coatings for textiles, solar cells, and architecture [10,11]; anti-fogging and anti-icing surfaces [12,13]; microfluidics [14-16]; and many other applications. Liquids will wet a high energy surface more readily than a low energy surface, and so to obtain repellency across a wide range of liquids, the optimum surface is the one with the lowest surface energy.

1.1. Designing a Low Energy Surface

The overall wetting properties of a surface are a result of the combined effect of the intrinsic physiochemical properties of a surface, and the topography of the surface [3,17,18]. Before a discussion of these effects can take place, the matter of nomenclature must be addressed.

The *surface energy,* γ, of a material is the reversible work, dW, required to expand a surface area by amount, dA, such that

$$dW = \gamma dA. \tag{1.1}$$

In the liquid phase, the surface energy may be measured directly by expanding the surface. The same is not true for solids, where expanding the surface also

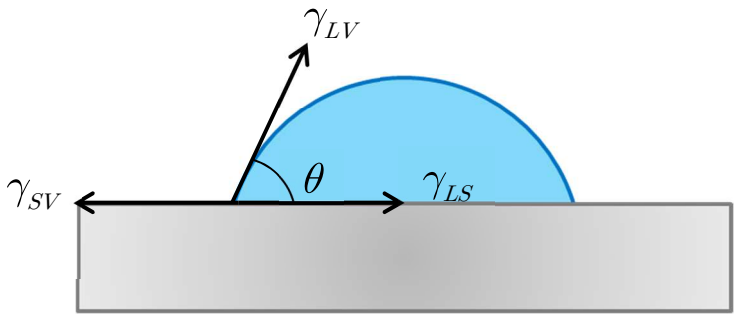


Figure 1.1 *A diagram of the profile of a liquid drop sitting on a solid surface. The Young equation, Eq. (1.2), which describes the relationship between γ_{SV}, γ_{LS}, and γ_{LV} assumes that the drop forms a spherical cap which is not affected by gravity [19]*

induces a surface stress. The overall effect of surface energy and surface stress is referred to as *surface tension*. Although surface tension and surface energy are interchangeable when referring to liquid, it is common to use surface *tension* when referring to liquids, and surface *energy* when referring to solids; this is the nomenclature used throughout this thesis. Methods for measuring solid surface energy are discussed in **2.1.6**.

The wetting behaviour of a surface is typically discussed in terms of the *contact angle* that is formed by the liquid on the solid (as shown in **Figure 1.1**). The contact angle, θ, is the result of the relationship between the liquid-solid surface energy, γ_{LS}, the liquid-vapour surface energy, γ_{LV}, and the solid-vapour surface energy, γ_{SV}, and is given by the Young equation;

$$\gamma_{SV} = \gamma_{LS} + \gamma_{LV} \cos\theta. \tag{1.2}$$

The method used for measuring contact angles are discussed in **Section 2.1.4**. The contact angle as defined by the Young equation is the equilibrium contact angle for ideal surfaces. When discussing real surfaces, it is necessary to define the static contact angle, θ_{stat}, which is the contact angle formed when a drop is

deposited onto a surface, and the dynamic contact angles , θ_{adv}, and , θ_{rec}, which are the angles formed when the triple phase line advances or recedes across the solid surface. For an ideal surface, these three angles are equivalent, but this does not hold for most real surfaces (see **Section 1.1.2**). The difference between θ_{adv} and θ_{rec} is known as the CA hysteresis, θ_{hys}.

Surfaces which have a water CA of less than 90° are described as *hydrophilic*, whilst those which have a water CA of greater than 90° are described has *hydrophobic*. A surface with a water CA of greater than 150° is described as *superhydrophobic*. The corresponding terms for the oil or hydrocarbon CAs are *oleophilic*, *oleophobic*, and *superoleophobic* [17]. Since hydrocarbons have lower surface tensions than water [20], a hydrophobic surface may not be sufficiently low energy to also be oleophobic. For many practical applications, it is desirable for a surface to possess both properties and for this, we turn our attention to fluorocarbons.

1.1.1. The low surface energy of fluorocarbons

Low energy surfaces are those that engage in weak intermolecular interactions, and, for this reason, materials which participate in purely dispersive interactions typically exhibit lower surface energies than polar or metallic materials [21]. This is demonstrated by the surface energy values shown in **Table 1.1**, where the non-polar materials, shown in *italics*, have lower surface energies than the polar/metallic materials.

Material	γ at 20 °C (mJ m^{-2})	Ref.
α-Alumina	889.6	[22]
Mercury	486.5	[20]
Water	72.9	[20]
Ethylene Glycol	48.4	[20]
Dodecane	*25.4*	[20]
PTFE (solid)	*20.5*	[23]

Table 1.1 *Surface energies of some common materials. Non-polar materials are shown in italics*

Alkanes fulfil the criteria of dispersive-only interactions and are nature's method of creating hydrophobic surfaces, as well as being used in synthesis [1,2]. Perfluoroalkanes also engage in purely dispersive interactions but are capable of achieving significantly lower surface energies than their alkyl equivalents [18]. The C—F bond is both more polar and more polarizable than the C—H bond [24] and one might therefore expect fluorocarbons to exhibit stronger intermolecular interactions than hydrocarbons; this, however, is not the case. Both experimental work and simulations have shown that the dominant factor in fluorocarbon hydrophobicity is the size of fluorine atom [25-27]. When considered in the context of the periodic table as a whole, fluorine is a rather small atom – small enough to replace hydrogen in the majority of organic compounds [28]. In comparison to hydrogen, however, it is large enough that the CF_3 moiety is more comparable in size to an isopropyl group than a methyl group [29]. The larger size of fluorine forces perfluoroalkyl chains to adopt a more rigid structure with the carbon backbone twisted into a helical shape, rather than the planar structure adopted by the backbone of an alkyl chain [30]. Perfluoroalkanes are therefore larger and pack less densely than their alkane counterparts. Fewer molecules per unit area

results in fewer cohesive interactions per unit area and this is what gives perfluoroalkanes their lower surface energy. **Table 1.2** shows the relationship between the volume of different alkyl or perfluoroalkyl groups and their surface energies. The mismatch in size between alkyl and perfluoroalkyl groups also results in weaker adhesive interactions between the two [31]; this is demonstrated by their low mutual solubility and, most importantly, the oleophobicity of perfluoroalkanes [32,33]. However, the maximum contact angle of water on a smooth surface is 120° [34] and this means that, whilst it is possible to achieve both hydro- and oleophobicity ($\theta > 90°$) on smooth, low energy surfaces, it is not possible to fulfil the criteria for *super* hydro- and oleophobicity ($\theta > 150°$). For this, we turn our attention to the surface topography.

Moiety	**Volume (Å^3) [29]**	**γ (mJ m^{-2}) [35,36]**
CH_2	27	36
CH_3	54	30
CF_2	38	18
CF_3	92	6

Table 1.2 *Volumes and surface energy of alkyl and perfluoroalkyl substituents*

1.1.2. The effect of surface roughness and topography on wetting

Discussion of surface energy and wetting has, up to this point, assumed that the surfaces in question are ideal, that is to say, they are both chemically homogeneous and smooth. Roughness affects both static and dynamic wetting (or dewetting) behaviour of liquids on solid surfaces, meaning that rough surfaces may exhibit non-equilibrium static contact angles, contact angle hysteresis, stick-

slip behaviour during spreading, and altered wicking behaviour [37-43]. Atomically smooth surfaces may be obtained by cleavage along the crystal plane of a material such as Muscovite mica [44]. Molecularly smooth surfaces may be obtained by solidifying a liquid film, as in glass manufacturing, or adsorbing a monolayer onto a smooth substrate, such a thiol on gold [42]. However, most real surfaces have some degree of roughness. The effect of roughness on wetting is highly complex; the geometry of the surface features, the lengthscale of the roughness (including multi-lengthscale hierarchical structures), and the ability of the liquid to penetrate into the surface structure all come into play.

There are two commonly used models which describe the wetting of macroscopically rough surfaces, the Cassie-Baxter model, and the Wenzel model [37,38]. Roughness on a lengthscale close to molecular dimensions differs considerably from these models and will not be considered in this thesis [43]. Both models extrapolate from the contact angle on a flat surface, θ_F, to the contact angle on a rough surface, θ_R. The Wenzel model introduces a roughness factor, r, which is defined as the ratio of the true area of the solid to the apparent, projected area such that

$$\cos\theta_R = r\cos\theta_F. \tag{1.3}$$

In the Wenzel wetting regime, the drop is in full contact with the surface, penetrating completely into any asperities. In the contrast, in the Cassie-Baxter wetting regime, the asperities penetrate into the drop either partially or not at all. The surface that the drop 'sees' could therefore be considered to be a chemically heterogeneous surface composed of proportional area f_S of solid, and

proportional area f_V of vapour. Assuming a liquid-vapour CA of 180°, the CA on a rough surface becomes

$$\cos\theta_R = f_S \cos\theta_F - f_V. \tag{1.4}$$

In the simplifying limit where the drop sits completely atop the asperities as depicted in **Figure 1.2**, **Eq. (1.4)** becomes

$$\cos\theta_R = f_S(\cos\theta_F - 1) + 1. \tag{1.5}$$

By replacing the vapour with liquid, the Cassie-Baxter model can also be extended to the opposite extreme where liquid penetrates into the asperities both under the drop and ahead of the macroscopic three-phase line – the impregnation regime. Given that the liquid-liquid CA will be 0°,

$$\cos\theta_R = f_S(\cos\theta_F + 1) - 1. \tag{1.6}$$

The transition from Cassie-Baxter to Wenzel occurs at

$$\cos\theta_F = (f_S - 1)/(r - f_S), \tag{1.7}$$

whilst the transition from Wenzel to the impregnation regime occurs at

$$\cos\theta_F = (1 - f_S)/(r - f_S). \tag{1.8}$$

Figure 1.2 shows the change in CA upon roughening a flat surface and depicts the difference in interfacial configuration for each of the three wetting regimes. It can be seen that roughening a low energy surface will achieve a higher contact angle. The cartoons depict drops sitting atop surfaces with regular pillar asperities. It is possible to design surfaces with highly regular geometries, using

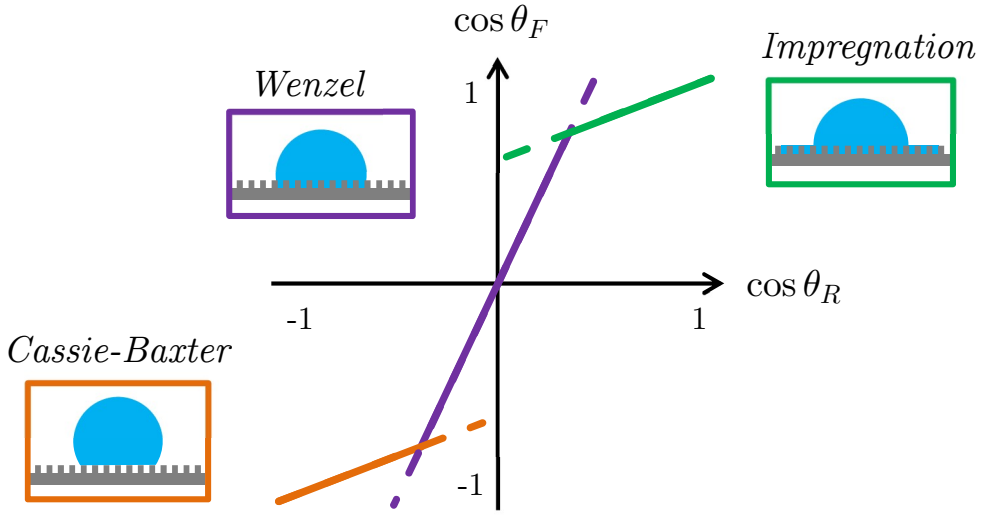


Figure 1.2 *Diagram showing the effect of macroscopic roughness on the contact angle of a drop, and the transitions between Cassie-Baxter, Wenzel, and impregnation regimes. The size of asperities and drop size are not to scale. Dashed lines represent metastable regimes. This diagram is adapted from Ref. [43].*

a variety of lithographical techniques [45,46]. However, many synthesis techniques will lead to surface with more irregular features (both in terms of size and distribution) and this is something which must be considered when examining the effect of roughness on wetting.

Having established that a rough, fluorinated surface is optimum in terms of achieving a highly liquid-repellent surface, the next section will now describe the synthesis of these surfaces using plasma polymerization.

1.2. Plasmas and Plasma Polymerization

1.2.1. Introduction to plasmas

Irving Langmuir coined the word *plasma* in his 1928 paper entitled '*Oscillations in Ionized Gases*' [47] and the term is used to describe the most abundent form of matter in the universe. A plasma is a gas containing a mixture of charged and

neutral particles and can be defined in terms of two fundamental properties – *collective behaviour* and *quasineutrality* [48].

In an ideal gas, the only interactions between particles are in the form of collisions, and particles cannot influence each other at large separations. In a plasma, the movement of charges creates electric fields which results in particles interacting with each other at larger separations. This gives rise to the notion of collective behaviour, and differentiates plasma from the gas phase.

Another property of plasma is that the Debye screening length is shorter than the dimensions of the plasma, meaning that the bulk plasma is shielded from local fields and is approximately neutral overall. This is the concept of quasineutrality, and is what differentiates a plasma from an ionized gas. The Debye length, λ_D, is the decay length of an electric field, ϕ, being screened by mobile charge carriers, such that

$$\phi = \phi_0 \exp\left(-\frac{|x|}{\lambda_D}\right), \tag{1.9}$$

where x is the distance from the origin of the electric field. The Debye length can be estimated as

$$\lambda_D \equiv \sqrt{\frac{\varepsilon_0 k_B T_e}{ne^2}}\,, \tag{1.10}$$

where ε_0 is the vacuum permittivity, k_B is the Boltzmann constant, T_e is the electron temperature, n is the plasma density, and e is the elementary charge [48]. It is primarily the electrons which are responsible for charge screening, since they

are more mobile than the ions. For this reason, it is the electron temperature which is used to estimate the Debye length.

Plasmas may be described as *isothermal*, where all the particles have the same temperature, or *non-isothermal*, where the lighter electrons are at a higher temperature than the ions and neutral species. The mismatch in mass between the electrons and the ions or neutrals means that energy cannot be efficiently transferred between them, and this maintains the non-isothermal state. For the glow discharges typically used in the low-pressure plasma processes described in this thesis, $T_e = 10^4 - 10^5$ K, and $T_{ions} \approx T_{gas} = 300 - 400$ K [49]. These 'cold' (i.e. non-isothermal) plasmas can therefore be used to treat a wide variety of substrates without the risk of damage.

1.2.2. Surface modification using plasmas

Plasmas can be used in a variety of surface modification techniques [44], including cleaning or etching [50-53], chemical reactions [54,55], and deposition of thin films [56,57]. These processes may occur concurrently and/or in competition and manipulation of parameters such as feed-gas pressure and composition, and of plasma power and frequency will dictate which of these processes dominate. This, in turn, will determine both the chemical composition and topography of the modified surface. The work in this thesis focusses on plasma polymerization, whereby organic monomers excited by the plasma are polymerized and grafted to a substrate.

There are a number of advantages associated with the used of plasmas to modify surfaces. The lack of solvent required makes plasma processing more

environmentally friendly than wet methods [58], and also allows multiple components with orthogonal solubilities to be used – such as fluorocarbons and hydrocarbons [59,60]. The quantities of precursor required are low, which adds to the green credentials of plasma processing [58]. Plasma can also be used to succesfully create polymers which would be inaccessible via traditional methods, using monomers such as maleic anhydride [61], or those without unsaturated groups, such as perfluorocyclohexane [62]. The use of vapour means that plasma methods are independent of substrate geometry and that etching or thin film deposition is uniform across the surface [63]. Furthermore, etching depth or film thickness is easily controlled by varying the plasma parameters, and it is possible to build multi-layer or gradated films [64-66].

1.2.3. Continuous wave vs. pulsed conditions

The primary disadvantage associated with plasma polymerization is the lack of selectivity in activating the monomer species, the fragmentation of the monomer species, and the ablation of the growing polymer chain. Plasma polymers are random, amorphous, cross-linked structures which bear little resemblance to the conventionally made polymer. Whilst these attributes may be useful in some circumstances, in many cases it represents loss of desirable functionality. A technique for combatting these issues by pulsing the plasma discharge was developed by Yasuda in the late 1970's [67] and has been further developed and popularized by researchers such as Timmons [68,69] and Badyal [62,70].

The pulsed plasma method relies on the differences in stability between the species produced by plasma excitation. The more energetic species have a lifetime of the order of μs-ms, whilst the π-radicals formed from the activation of an

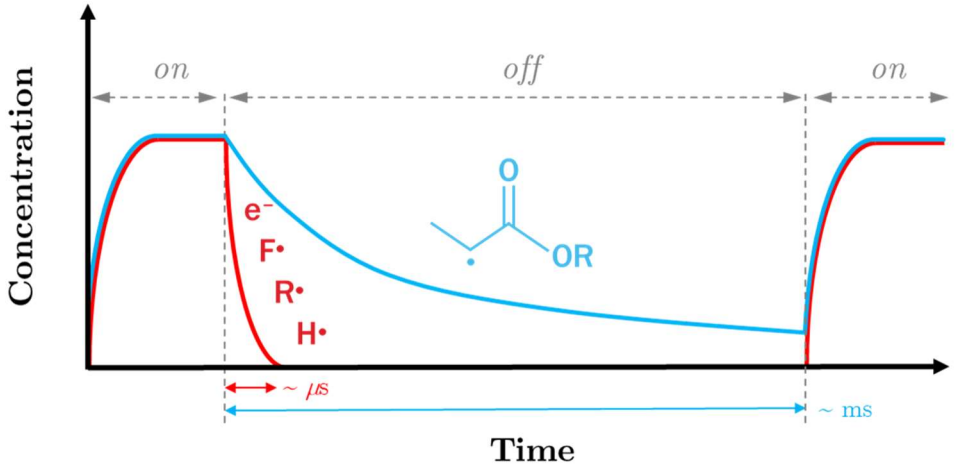


Figure 1.3 *Diagram depicting the concentration of different species during the on and off periods during pulsed plasma polymerization. The concentration of the more reactive species, which cause damage to the growing polymer film, is shown in red, whilst the concentration of the activated monomer species is in blue. The approximate lifetimes of the species are also shown*

unsaturated monomer have a lifetime of the order of ms-s [44]. During the 'on' period of the duty cycle, which typically lasts several μs, a mixture of species is produced. When the plasma discharge is switched off, typically for a period of several ms, the more energetic species quickly decay away, whilst the activated monomer species persists, and the polymer film continues to grow. **Figure 1.3** shows a diagram depicting the concentration of different species during a single duty cycle. The selectivity of the pulsed process can be enhanced by using a monomer which produces a more stable radical species. For example, an acrylate monomer radical is more stable than an alkene radical owing to the effect of conjugation from the ester group [71] and can therefore be polymerized efficiently using a shorter duty cycle.

1.2.4. Atmospheric vs. low pressure conditions

Although the work in this thesis focuses solely on plasmas produced at low ($<$ 1 mbar) pressures, recent years have seen focus shift towards plasma

processing at atmospheric pressure. The ability to perform continuous, rather than batch, processing, and the lower set-up costs make atmospheric conditions particularly attractive to industry [72]. Atmospheric pressure conditions are particularly well suited to processes using air or inert gas plasmas but are less well suited to systems with toxic or harmful by-products – such as fluorinated compounds.

1.3. Aim of Study

Although there are myriad uses for low energy surfaces, the work in this thesis is informed by their use in manufacturing protective clothing; more specifically, protection from chemical warfare agents (CWA's). The production, stockpiling, and use of CWA's is prohibited under the Chemical Weapons Convention [73]. However, in the event that an incident does occur (as in Salisbury in 2018 [74]), it is essential that first responders and other personnel are adequately protected. A respirator or self-contained breathing provides protection against inhalation of gaseous or volatile CWA's, whilst the gloves and boots are impermeable rubber and the fabric of the clothing is treated to be liquid-repellent, preventing dermal contact with CWA's [75]. Liquid CWA's have relatively low surface tensions, ranging from 25.0 mJ m^{-2} for Soman, a nerve agent, to 43.3 mJ m^{-2} for sulfur mustard [76], and the clothing should also offer additional protection from substances such as petrol or oil, which also have low surface tensions. Consequently, a low surface energy coating is required for the fabric.

Coulson *et al.* successfully developed a method for coating fabric, using the plasma phase to polymerize a fluorinated monomer, and graft it to the fabric in

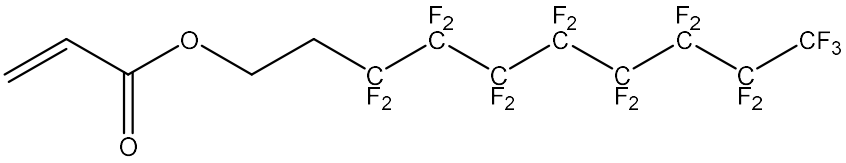


Figure 1.4 *1H,1H,2H,2H-perfluorodecyl acrylate monomer structure*

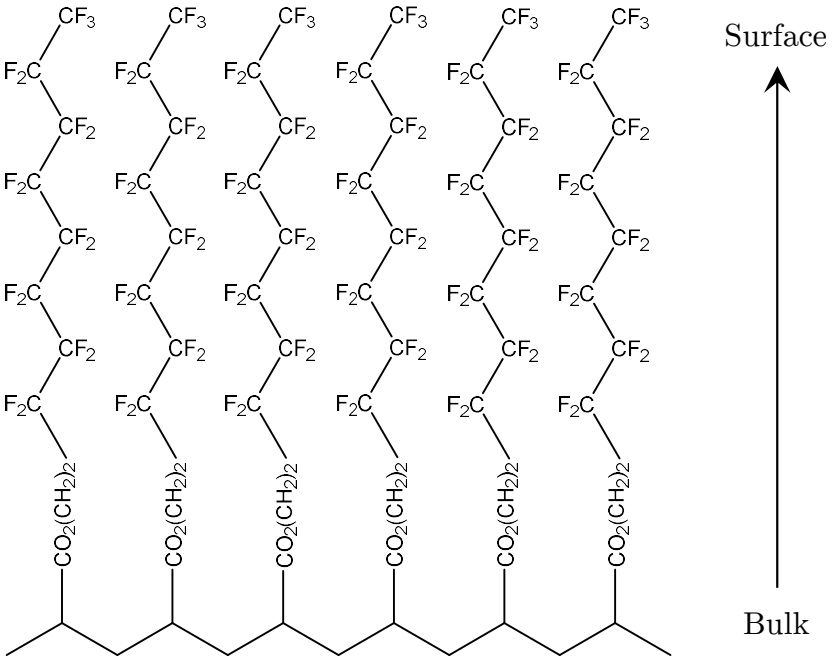


Figure 1.5 *Poly(1H,1H,2H,2H-perfluorodecyl acrylate) known as PFAC-8. The lowest surface energy arrangement is with the CF_3 groups oriented towards the surface and the polar acrylate groups buried in the bulk*

a single step [77,78]. The polymer in question, which is still used, is poly(1H,1H,2H,2H-perfluorodecyl acrylate), known as PFAC-8 (PerFluoro-8-yl ACrylate). **Figure 1.4** and **Figure 1.5** show the monomer and polymer structure respectively. The stability of the acrylate radical makes it ideal for pulsed plasma polymerization and the fluorinated side chains, which form a brush, provide the low energy surface. The polymer surface has a root mean square (rms) roughness of 7 nm, which, when applied to a textile [79], produces a surface with hierarchical roughness which is both superhydrophobic and superoleophobic. The treated

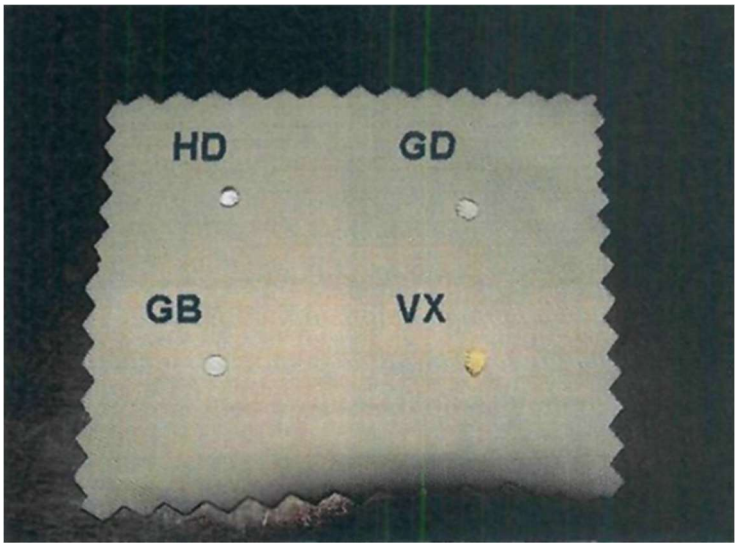


Figure 1.6 *Photograph of PFAC-8 coated fabric showing good repellency to the chemical warfare agents sulfur mustard (HD), Soman (GD), Sarin (GB) and VX. Reproduced with permission from Ref. [80]*

textile also shows good repellency towards CWA's including sulfur mustard (HD), Soman (GD), Sarin (GB), and VX – as shown in **Figure 1.6**.

Although initially developed with CWA protection in mind, and the process developed by Coulson *et al.* is now used in a wide range of applications where superhydrophobicity and superoleophobicity is required, including coatings for electronics and filtration devices [81]. Despite its efficacy, recent concerns about the bioaccumulation of compounds with eight or more fluorinated carbons mean that PFAC-8 must be phased out, and alternatives with fewer perfluorinated carbons must sought [82,83]. Unfortunately, the matter is not necessarily resolved by exchanging PFAC-8 for a shorter chain analogue. The use of PFAC-8 as a low surface energy coating rests on the fact that the polymer forms such that the fluorinated side chains are oriented out towards the surface, and the acrylate groups are oriented towards the bulk (as shown in **Figure 1.5**). Previous work by Honda *et al.* shows that PFAC-n polymers with shorter ($n < 8$) fluorinated

side chains are prone to surface reconstruction when exposed to water [84,85]. For surface reconstruction to occur, two criteria must be fulfilled. Firstly, the new conformation must be lower in energy; in the case of PFAC-n polymers, the driving force is the energetically favourable hydrogen bonding between the acrylate and the water. Secondly, the molecules must be sufficiently mobile that surface reconstruction is able to take place; in the case of PFAC-n, this depends on the length of the perfluorinated chain. These investigations were focussed on PFAC-n polymers synthesized in the solution phase, and it is unclear as to whether this behaviour extends to plasma polymers, which may have a significantly different morphology and molecular mobility to their solution-phase counterparts. There is also the question as to whether surface reorganization would occur in the presence of non-polar liquids, or where the acrylate group is replaced with a non-polar substituent, and what the implications might be for CWA repellency. In the cases where surface reconstruction does occur, questions also arise as to the kinetics of the processes involved.

This thesis is an investigation into the properties of plasma-polymerized fluoropolymer surfaces with a particular emphasis on their molecular mobility, and wetting properties – both in terms of the wetting of chemical warfare agents, and more broadly. The work in this thesis also aims to the explore the effect of polymerizable end group and fluorinated chain length on these properties independently of one another.

1.4. Summary of Thesis

Chapter 1 is an investigation of the surface composition, topography, and wetting properties of plasma fluoropolymers at room temperature. Specifically, it examines the effect of exchanging the polymerizable group in C6 perfluorinated monomers.

Chapter 3 is an investigation of the surface composition, topography, and wetting properties of plasma polymerized perfluoroalkyl acrylate (PFAC-n) polymers at room temperature.

Chapter 4 is an investigation of the adaptive wetting properties of PFAC-n polymers, and the temperature-, time-, and liquid-dependence of their wetting behaviour.

Chapter 5 describes the wetting of chemical warfare agents on PFAC-n polymer surfaces.

Chapter 6 is an investigation of the molecular motion in PFAC-n polymers using variable temperature ^{19}F solid-state NMR relaxometry.

Chapter 7 describes efforts to co-polymerize PFAC-6 with a hydrophilic monomer, and the surface properties of the resultant surface.

Chapter 8 summarizes the major conclusions of the thesis, along with ideas for future work.

1.5. References

[1] P. S. Brown and B. Bhushan, APL Materials **4**, 015703 (2016).

[2] S. Wang, K. Liu, X. Yao, and L. Jiang, Chemical Reviews **115**, 8230 (2015).

[3] H. Bellanger, T. Darmanin, E. Taffin de Givenchy, and F. Guittard, Chemical Reviews **114**, 2694 (2014).

[4] M. Nosonovsky and B. Bhushan, Current Opinion in Colloid & Interface Science **14**, 270 (2009).

[5] X. Zhang, F. Shi, J. Niu, Y. Jiang, and Z. Wang, Journal of Materials Chemistry **18**, 621 (2008).

[6] B. Wang, W. Liang, Z. Guo, and W. Liu, Chemical Society Reviews **44**, 336 (2015).

[7] G. D. Kang and Y. M. Cao, Journal of Membrane Science **463**, 145 (2014).

[8] V. Kumar, J. Pulpytel, H. Rauscher, I. Mannelli, F. Rossi, and F. Arefi-Khonsari, Plasma Processes and Polymers **7**, 926 (2010).

[9] J. Tsibouklis, M. Stone, A. A. Thorpe, P. Graham, V. Peters, R. Heerlien, J. R. Smith, K. L. Green, and T. G. Nevell, Biomaterials **20**, 1229 (1999).

[10] B. Leng, Z. Shao, G. de With, and W. Ming, Langmuir **25**, 2456 (2009).

[11] W.-L. Min, B. Jiang, and P. Jiang, Advanced Materials **20**, 3914 (2008).

[12] P. S. Brown, O. D. L. A. Atkinson, and J. P. S. Badyal, ACS Applied Materials & Interfaces **6**, 7504 (2014).

[13] C. Li, X. Li, C. Tao, L. Ren, Y. Zhao, S. Bai, and X. Yuan, ACS Applied Materials & Interfaces **9**, 22959 (2017).

[14] P. Aussillous and D. Quéré, Nature **411**, 924 (2001).

[15] J. Zhou, A. V. Ellis, and N. H. Voelcker, Electrophoresis **31**, 2 (2010).

[16] K. Ren, W. Dai, J. Zhou, J. Su, and H. Wu, Proceedings of the National Academy of Sciences **108**, 8162 (2011).

[17] A. Tuteja, W. Choi, M. Ma, J. M. Mabry, S. A. Mazzella, G. C. Rutledge, G. H. McKinley, and R. E. Cohen, Science **318**, 1618 (2007).

[18] J. Tsibouklis and T. G. Nevell, Advanced Materials **15**, 647 (2003).

[19] J. N. Israelachvili, *Intermolecular and Surface Forces, 3rd Edition* (Elsevier Academic Press Inc, San Diego, 2011).

[20] J. J. Jasper, Journal of Physical and Chemical Reference Data **1**, 841 (1972).

[21] W. Zisman, in *Contact Angle, Wettability, and Adhesion* (American Chemical Society, 1964), pp. 1.

[22] S. Rhee, Journal of the American Ceramic Society **55**, 300 (1972).

[23] H. W. Fox and W. A. Zisman, Journal of Colloid Science **5**, 514 (1950).

[24] D. R. Lide, *CRC Handbook of Chemistry and Physics* (CRC press, 2003), 84th edn.

[25] V. H. Dalvi and P. J. Rossky, Proceedings of the National Academy of Sciences **107**, 13603 (2010).

[26] J. Mecinovic, P. W. Snyder, K. A. Mirica, S. Bai, E. T. Mack, R. L. Kwant, D. T. Moustakas, A. Heroux, and G. M. Whitesides, Journal of the American Chemical Society **133**, 14017 (2011).

[27] C. Adam, L. Yang, and S. L. Cockroft, Angewandte Chemie International Edition **54**, 1164 (2015).

[28] D. M. Lemal, The Journal of Organic Chemistry **69**, 1 (2004).

[29] M. P. Krafft and J. G. Riess, Chemical Reviews **109**, 1714 (2009).

[30] C. W. Bunn and E. R. Howells, Nature **174**, 549 (1954).

[31] E. M. D. Siebert and C. M. Knobler, The Journal of Physical Chemistry **75**, 3863 (1971).

[32] P. Long and J. Hao, Advances in Colloid and Interface Science **171**–**172**, 66 (2012).

[33] N. M. Kovalchuk, A. Trybala, V. Starov, O. Matar, and N. Ivanova, Advances in Colloid and Interface Science **210**, 65 (2014).

[34] T. Nishino, M. Meguro, K. Nakamae, M. Matsushita, and Y. Ueda, Langmuir **15**, 4321 (1999).

[35] E. G. Shafrin and W. A. Zisman, The Journal of Physical Chemistry **64**, 519 (1960).

[36] R. H. Dettre and R. E. Johnson, Journal of Colloid and Interface Science **21**, 367 (1966).

[37] R. N. Wenzel, Industrial & Engineering Chemistry **28**, 988 (1936).

[38] A. B. D. Cassie and S. Baxter, Transactions of the Faraday Society **40**, 546 (1944).

[39] A. Lafuma and D. Quere, Nature Materials **2**, 457 (2003).

[40] A. Marmur, Langmuir **19**, 8343 (2003).

[41] T. S. Meiron, A. Marmur, and I. S. Saguy, Journal of Colloid and Interface Science **274**, 637 (2004).

[42] D. Quere, Annual Review of Materials Research **38**, 71 (2008).

[43] V. Kumar and J. R. Errington, Langmuir **29**, 11815 (2013).

[44] H. J. Butt, K. Graf, and M. Kappl, *Physics and Chemistry of Interfaces* (John Wiley & Sons, 2013), Third, Revised and Enlarged edn., Physics and Chemistry of Interfaces.

[45] J. Y. Shiu, C. W. Kuo, P. Chen, and C. Y. Mou, Chemistry of Materials **16**, 561 (2004).

[46] X. Gao, X. Yan, X. Yao, L. Xu, K. Zhang, J. Zhang, B. Yang, and L. Jiang, Advanced Materials **19**, 2213 (2007).

[47] I. Langmuir, Proceedings of the National Academy of Sciences **14**, 627 (1928).

[48] F. F. Chen, *Introduction to Plasma Physics and Controlled Fusion, Volume 1: Plasma Physics* 1975), Vol. 2, Plenum Press.

[49] J. F. Friedrich, *Plasma Chemistry of Polymer Surfaces: Advanced Techniques of Surface Design* (Wiley-VCH, Weinheim, 2012), Ebook central.

[50] J. W. Coburn and H. F. Winters, Journal of Applied Physics **50**, 3189 (1979).

[51] C. Mogab, A. Adams, and D. L. Flamm, Journal of Applied Physics **49**, 3796 (1978).
[52] J. Jeong, S. Babayan, V. Tu, J. Park, I. Henins, R. Hicks, and G. Selwyn, Plasma Sources Science and Technology **7**, 282 (1998).
[53] D. O'Kane and K. Mittal, Journal of Vacuum Science and Technology **11**, 567 (1974).
[54] E. Liston, L. Martinu, and M. Wertheimer, Journal of Adhesion Science and Technology **7**, 1091 (1993).
[55] J. Wolff, H. Steinhauser, and G. Ellinghorst, Journal of Membrane Science **36**, 207 (1988).
[56] J. Goodman, Journal of Polymer Science **44**, 551 (1960).
[57] H. Yasuda, Macromolecular Reviews Part D-Journal of Polymer Science **16**, 199 (1981).
[58] H. Yasuda and Y. Matsuzawa, Plasma Processes and Polymers **2**, 507 (2005).
[59] T. Fouquet, G. Mertz, M. Delmée, C. Becker, J. Bardon, and H. Sato, Plasma Processes and Polymers **13**, 862 (2016).
[60] C. S. Gudipati, J. A. Finlay, J. A. Callow, M. E. Callow, and K. L. Wooley, Langmuir **21**, 3044 (2005).
[61] M. E. Ryan, A. M. Hynes, and J. P. S. Badyal, Chemistry of Materials **8**, 37 (1996).
[62] A. Hynes, M. Shenton, and J. Badyal, Macromolecules **29**, 4220 (1996).
[63] C. M. Chan, T. M. Ko, and H. Hiraoka, Surface Science Reports **24**, 1 (1996).
[64] K. L. Parry, A. G. Shard, R. D. Short, R. G. White, J. D. Whittle, and A. Wright, Surface and Interface Analysis **38**, 1497 (2006).
[65] D. Hegemann, H. Brunner, and C. Oehr, Nuclear Instruments and Methods in Physics Research Section B **208**, 281 (2003).
[66] A. Liu, E. Goktekin, and K. K. Gleason, Langmuir (2014).
[67] H. Yasuda and T. Hsu, Journal of Polymer Science: Polymer Chemistry Edition **15**, 81 (1977).
[68] C. R. Savage, R. B. Timmons, and J. W. Lin, Chemistry of Materials **3**, 575 (1991).
[69] R. B. Timmons and A. J. Griggs, *Pulsed Plasma Polymerizations* (Imperial College Press, 2004), Plasma Polymer Films.
[70] W. C. E. Schofield and J. P. S. Badyal, Plasma Chemistry and Plasma Processing **26**, 361 (2006).
[71] G. Clayden, W. Warren, N. Greeves, and P. Wothers, *Organic Chemistry* (Oxford University Press, 2001).
[72] R. A. Wolf, *Atmospheric Pressure Plasma for Surface Modification* (John Wiley & Sons, Hoboken, N.J., 2013), Ebook central.
[73] United Nations Convention on the Prohibition of the Development, Production, Stockpiling and Use of Chemical Weapons and on their Destruction, Opened for signature 13th January 1993 entered into force 29th April 1997.

[74] Novichok Nerve Agent use in Salisbury: UK Government Response, https://www.gov.uk/government/news/novichok-nerve-agent-use-in-salisbury-uk-government-response (Accessed 2nd May 2018).
[75] A. Richardt, *CBRN Protection: Managing the Threat of Chemical, Biological, Radioactive and Nuclear weapons* (Wiley-VCH, Weinheim, 2013).
[76] C. A. Stone, T. G. D'Onofrio, and S. J. Pritchard, Determination of the Surface Energy Components of a Variety of CW agents and the Effects of Impurities on Measured Parameters, 2017.
[77] S. R. Coulson, I. S. Woodward, J. P. S. Badyal, S. A. Brewer, and C. Willis, Chemistry of Materials **12**, 2031 (2000).
[78] S. R. Coulson, (P2i Ltd., UK . 2013), p. 19pp.
[79] G. R. J. Artus, S. Jung, J. Zimmermann, H. P. Gautschi, K. Marquardt, and S. Seeger, Advanced Materials **18**, 2758 (2006).
[80] S. J. Pritchard, C. A. Stone, and C. Willis, Repellency Characteristics of Plasma-Polymerised 1H, 1H, 2H, 2H-Perfluorodecyl Acrylate (PFAC8) Towards Liquid Chemical Warfare Agents, 2009.
[81] S. Coulson, (P2i Ltd., UK . 2011), p. 29pp.
[82] M. P. Krafft and J. G. Riess, Current Opinion in Colloid & Interface Science **20**, 192 (2015).
[83] S. Merenyi, *REACH: Regulation (EC) No 1907/2006: Consolidated Version (June 2012) with an Introduction and Future Prospects Regarding the Area of Chemicals Legislation* (GRIN Verlag, 2012), Vol. 2.
[84] K. Honda, M. Morita, H. Otsuka, and A. Takahara, Macromolecules **38**, 5699 (2005).
[85] K. Honda, M. Morita, O. Sakata, S. Sasaki, and A. Takahara, Macromolecules **43**, 454 (2009).

2. Surface Characterization and Wetting Behaviours of Plasma Fluoropolymers: The Role of Polymerizable Group

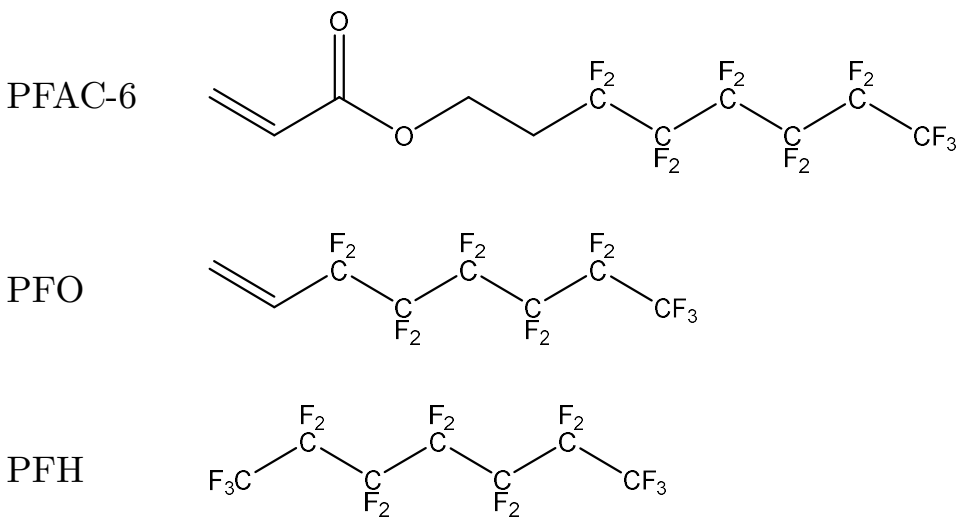


Figure 2.1 *The chemical structures of the three monomers used in this chapter*

The work in this chapter focusses on the role of the polymerizable group in determining the properties of plasma fluoropolymers. In this investigation, the acrylate group in PFAC-6 was exchanged for an alkene group (1H,1H,1H-perfluoro-1-octene, PFO), and a saturated perfluoroalkyl group (perfluorohexane, PFH). The structures of these three monomers are shown in **Figure 2.1**. The decision to use monomers with six membered perfluorinated chains was based on

the fact that it is the longest PFAC-n side chain for which there is evidence of surface reorganization [84], and which does not bioaccumulate [82].

Throughout this chapter, references will be made to "structurally intact" monomer and polymer species. In the case of the monomer species, this is simply the monomer as is, where no ablation, fragmentation, or other loss of functionality has taken place. In the case of the polymer species, this refers to the conventional polymer as formed through polymerization of the C=C group, with no other loss of functionality. Previous studies with both fluoroalkyl acrylates [77,86,87] and fluoroalkyl alkenes [88,89] indicate that PFAC-n and PFO monomer should polymerize via this route. The structures of the structurally intact PFAC-6 and PFO monomer and polymers are shown in **Figure 2.2** and **Figure 2.3** respectively. Since PFH is not a monomer in the conventional sense, lacking in unsaturated groups, any 'polymerization' will necessarily proceed via fragmentation of the fluorocarbon chain [62,89]. Therefore, the products of plasma polymerization of PFH are never structurally intact as here defined.

Although the overarching aim of the thesis is to investigate surface reconstruction and molecular mobility, it is first necessary to characterize the fundamental properties of these surfaces in air. The properties of plasma polymers are highly dependent on the deposition conditions; pressure, power, duty cycle, plasma generation method, and even chamber geometry [57,72,90,91]. It is therefore necessary to perform a complete characterization of each polymer, regardless of whether it has been subject to previous studies. For comparison purposes, the same plasma polymerization conditions were used. The chemical composition of

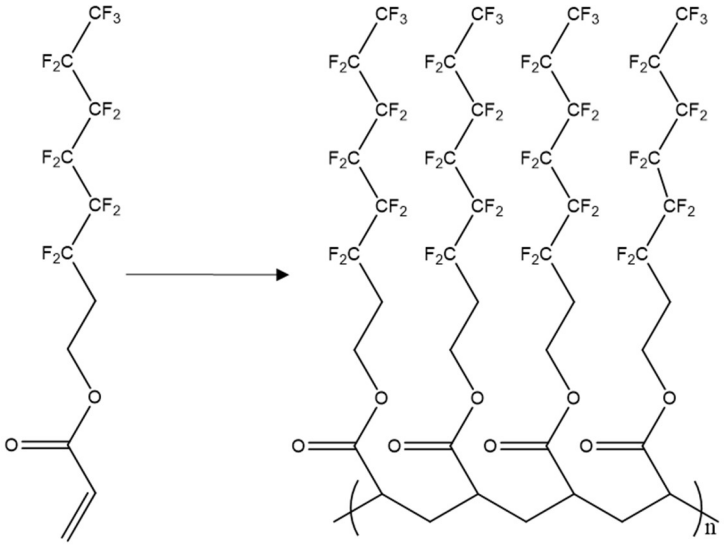


Figure 2.2 *Structure of PFAC-6 monomer (left) and conventional "structurally intact" polymer (right)*

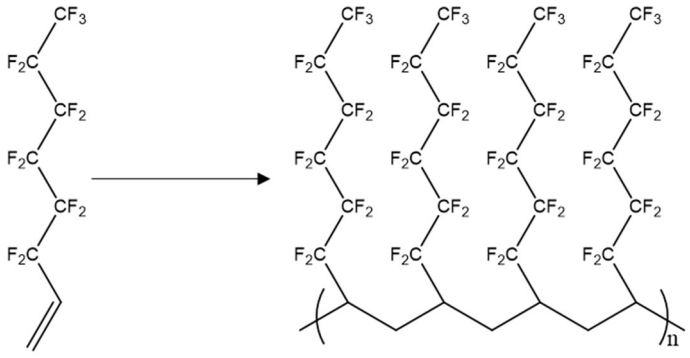


Figure 2.3 *Structure of PFO monomer (left) and conventional "structurally intact" polymer (right)*

the surfaces was investigated using XPS, with angle-resolved XPS being used to determine the orientation of the side chains at the surface. AFM was used to characterise the topography of the surface and contact angle goniometry was used to determine the surface energy and wetting properties of the polymer films.

2.1. Experimental

2.1.1. Monomers

The monomers used in the plasma polymer experiments were 1H,1H,2H,2H-perfluorooctyl acrylate (PFAC-6, Sigma-Aldrich, 97%), perfluorohexane (PFH, Sigma-Aldrich, 99%), and 1H,1H,1H-perfluoro-1-octene (PFO, Fluorochem, 98%). All monomers were purified by multiple freeze-thaw cycles. This involves placing the monomer into a Schlenk tube, sealing it off, attaching the tube to a vacuum system (as shown in the experimental setup), and allowing the system to pump down without opening the stopcock. When the system reaches base pressure, liquid nitrogen is used to freeze the monomer in the tube and then the stopcock is opened. The atmosphere in the monomer tube is pumped off until the system reaches base pressure once more. The liquid nitrogen is then removed and, when the monomer starts to thaw, the stopcock is sealed once more. This process is repeated until there is no rise in pressure when the stopcock to the frozen monomer tube is opened.

2.1.2. Plasma chamber set-up and experimental conditions

For the plasma polymerization and deposition process, an inductively coupled plasma chamber was used, which was set up as per the schematic in **Figure 2.4**. It is based on the setup used by Coulsen *et al.* and by the Defence Science and Technology Laboratory (DSTL) [77,92]. The substrates to be coated were glass slides for XPS, AFM, and CA measurements, or ground glass for NMR measurements. The substrates were placed in the chamber within the copper coils. The whole system was then evacuated to base pressure (5×10^{-3} mbar) before

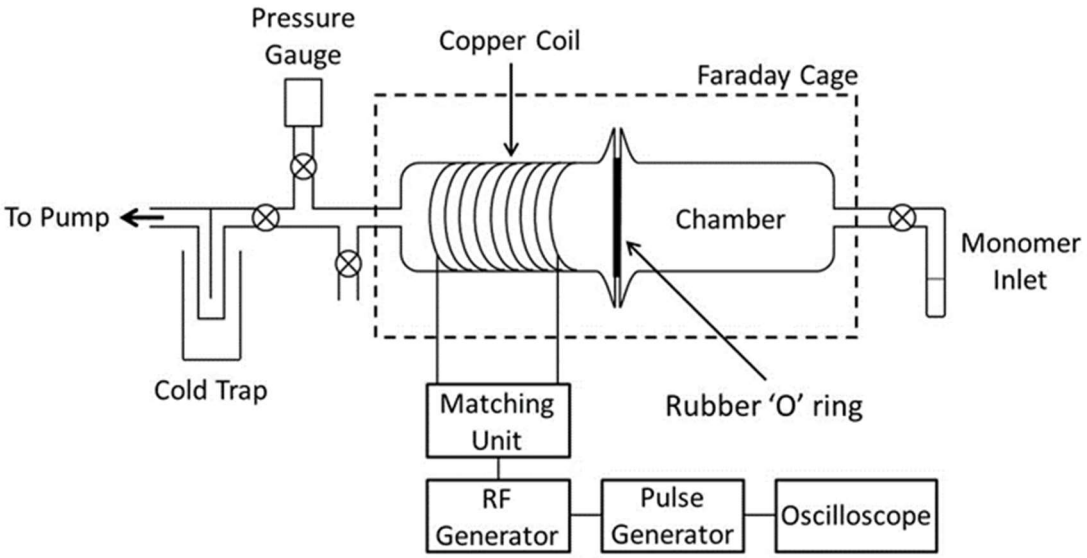


Figure 2.4 *Schematic of the plasma chamber used in the plasma polymerization experiments in this thesis. The dashed line around the main chamber represents the location of a Faraday cage, and the crossed circles represent Youngs taps. The radiofrequency (RF) generator produced a frequency of 13.56 MHz*

monomer vapour was introduced at a pressure of 2 x 10^{-1} mbar. After 5 minutes, the pressure gauge was sealed off, and the radiofrequency (RF) generator was switched on to ignite a continuous wave plasma (13.56 MHz, 40 W). After 30 seconds of the continuous wave deposition, the mode was switched to pulsed mode (t_{on}= 40 μs, t_{off}= 20 ms). The pulsed deposition was run for 10 minutes (20 minutes for PFH) for the glass slides, and 2 hours for the ground glass. When the deposition was complete, the RF generator was switched off and the pressure gauge opened up. When the pressure reached 2 x 10^{-1} mbar, the monomer vapour was allowed to flow for a further 5 minutes before being sealed off and the whole system was evacuated back to base pressure. After use, the chamber was cleaned prior to use by running an air plasma (2 x 10^{-1} mbar, 50 W) for two hours.

2.1.3. X-ray photoelectron spectroscopy (XPS)

XPS studies were carried out using a Thermo Scientific K-Alpha spectrometer, which utilises a monochromated Al K_α source. The Al K_α source is commonly used since it is sufficiently high in energy (1486.3 eV) to excite a broad range of core electrons, and also has a relatively narrow line width of 0.85 eV, so that resolution is not compromised [93]. In all cases, survey spectra were acquired by performing 5 scans at a range of binding energies from 0-1200 eV in steps of 0.4 eV. Regions of interest, typically spanning approximately 30 eV, were identified from the survey spectrum, and eight scans in steps of 0.1 eV were performed for each of these regions. The take-off angle was normal to the surface.

Angle-resolved XPS experiments were performed using a Thermo Scientific Theta Probe. Spectra were obtained in parallel at angles from 27.5°to 77.5° to the normal in 5° steps. To prevent damage to the surfaces, the X-rays were rastered across the surface in a 16x16 grid with 500 μm between points. At each point, the C(1s) spectrum was measured for 60 s, giving a total acquisition time of 256 min. The spectra at all points were summed to give a single, angle-resolved spectrum.

Data processing was carried out using CasaXPS software. Core-level spectra were fitted using peaks with Gaussian-Lorentzian (GL(30)) line-shape and equal full-width-half-maximum (FWHM), using the hydrocarbon C 1s peak at 285.0 eV for charge correction [94]. Elemental concentrations were calculated using standard sensitivity factors [95].

The average XPS analysis depth, d, is the depth from which 63% of the signal originates and is estimated as

$$d \sim \lambda \sin \theta, \tag{2.1}$$

where θ is the take-off angle measured relative to the surface, and λ is the electron inelastic mean free path. For fluoropolymers, where the photoelectrons are excited from the C 1s level by Al K_α, $\lambda \sim 3$nm [96].

2.1.4. Solid-state nuclear magnetic resonance (NMR) spectroscopy

Solid-state fluorine NMR was used to examine the bulk chemical composition of the surfaces at room temperature. A more detailed examination of the surfaces using solid-state NMR is carried out in **Chapter6**, along with a description of the experimental techniques used.

2.1.5. Atomic force microscopy (AFM)

Atomic force microscopy (AFM) was used to characterize the topography and roughness of the plasma polymer surfaces. Measurements were carried out using a Digital Instruments Multimode NanoScope IIIb in tapping mode. Tapping mode involves rastering an oscillating cantilever across the surface; the oscillations are then damped by interactions with the surface. The cantilevers used had a force constant of 40 N m^{-1} and a resonant frequency of 325 kHz. Data analysis was carried out in the NanoScope analysis program. Images were subject to a 2^{nd} order flatten to remove bow, which is an artefact created by the scanner motion, prior to roughness or section measurements.

2.1.6. Contact angle (CA) goniometry and surface energy measurement

A Krüss Drop Shape Analyser (DSA) 25 was used to measure advancing, receding and static contact angles on surfaces, and to estimate the surface energy of the surfaces. To measure static contact angles, a 5 μl drop was dispensed onto the surface using a motorised syringe fitted with a PTFE needle. The needle was then withdrawn from the drop, and the profile of the drop fitted computationally to obtain the static contact angle. To measure advancing contact angles, the syringe needle was brought close to the surface, and a 5 μl drop was dispensed onto the surface at a rate of 0.5 μl s^{-1}. To measure the receding contact angle, the liquid was then withdrawn from the drop at a rate of 0.5 μl s^{-1}. The advancing contact angle was defined as the *largest* angle made as the interfacial line advanced over the solid surface, and the receding contact angle was defined as the *smallest* angle made as the interfacial line receded across the solid interface. The test liquids used were water (polar) and dodecane (non-polar).

The surface energy of the solid surfaces was estimated using the Owens-Wendt-Rabel-Kaelble (OWRK) method [97,98] which assumes that surface energy, γ, can be separated into polar, γ^p, and dispersive, γ^d, components such that

$$\gamma = \gamma^p + \gamma^d. \tag{2.2}$$

The polar component also includes any contributions from hydrogen bonding. It is further assumed that the solid-liquid surface energy is the geometric mean of the polar and dispersive components, such that

$$\gamma_{SL} = \sqrt{\gamma_{SV}{}^{p}\gamma_{LV}{}^{p}} + \sqrt{\gamma_{SV}{}^{d}\gamma_{LV}{}^{d}}. \quad (2.3)$$

2.2. Results and Discussion

2.2.1. Chemical composition (solid-state ^{19}F NMR)

Figure 2.5 shows the solid-state ^{19}F NMR spectra of PFAC-6 and PFO polymers deposited on ground glass. Unfortunately, the deposition rate of PFH was sufficiently low that even running a deposition for approximately 5 hours did not yield enough material to be able to obtain a spectrum. Both PFAC-6 and PFO were deposited over a period of 2 hours and it can be inferred from the higher signal-to-noise ratio of the spectrum that PFAC-6 deposited at a greater rate than PFO. The PFAC-6 spectrum shows contributions from four different fluorine environments; a resonance at -85.6 ppm assigned to C$\underline{F}_3$—CF_2, a resonance at -117.6 ppm assigned to C$\underline{F}_2$—CH_2, a broad resonance centred at approximately -127 ppm assigned to C$\underline{F}_2$—CF_2, and a resonance at -130.4 assigned to C$\underline{F}_2$—CF_3. Deconvolution of the spectrum reveals that the peak at -124 ppm can be resolved into three peaks, which is consistent with PFAC-6 having a six membered perfluorinated chain. A more detailed investigation of the solid-state NMR of PFAC-n polymers is carried out in **Chapter 6**. Overall, the spectrum is consistent with PFAC-6 having polymerized with full retention of its fluorocarbon functionality and is similar to ^{19}F NMR spectra of the PFAC-6 monomer [99]. This result is also in keeping with other work on pulsed-polymerized fluorocarbons where similar levels of structural retention have been achieved [100,101].

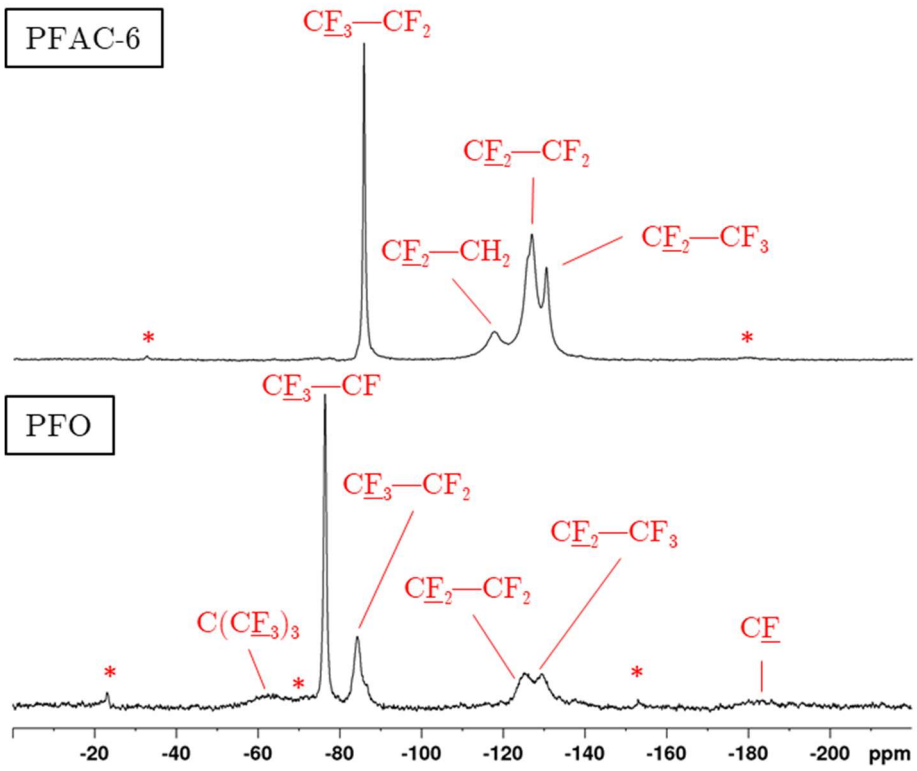


Figure 2.5 *Solid-state ^{19}F NMR spectra of PFAC-6 and PFO polymers deposited onto ground glass. The asterisks indicate sidebands, which occur at integer multiples of the magic angle spinning frequency (20 kHz) away from the primary peaks. Sidebands which overlap with primary peaks have not been marked. Peak assignments are with respect to $CFCl_3$ and are based on Refs [102,103]*

Since the PFO monomer has the same number and type of fluorine environments as PFAC-6, the two spectra are expected to be nearly identical – this is clearly not the case. There are three peaks associated with three different CF_3 environments; a broad resonance at approximately -62.5 assigned to $C(C\underline{F}_3)_3$, a resonance at -76.4 assigned to $CF—CF_3$, and a resonance at -84.4 ppm assigned to $C\underline{F}_3—CF_2$. There are a further two peaks associated with CF_2 groups; a resonance at -126.4 assigned to $C\underline{F}_2—CF_2$, and a resonance at -129.4 assigned to $C\underline{F}_2—CF_3$. There is no obvious peak associated with the $C\underline{F}_2—CH_2$ moiety, which would be expected to appear at approximately -115 ppm. Finally, there is a broad peak centred at -185 ppm which is assigned to $C\underline{F}$. Overall, the results are consistent with the PFO polymer being cross-linked. The results are extremely

similar to poly(1H,1H,2H-perfluorododecene) films produced by Kinmond *et al.* under continuous wave plasma conditions, although the experiments with the same monomer under pulsed conditions were able to generate polymers with complete structural retention [88,89].

2.2.2. Chemical composition (XPS)

Figure 2.6 shows the XPS survey spectra for the PFH and PFO polymers obtained at a take-off angle normal to the surface. The presence of silicon peaks in the PFH survey spectrum indicates that either there is incomplete coverage of the underlying glass substrate, or that the polymer film is thinner than the sampling depth of the instrument – approximately 3 nm [96]. The lack of silicon peaks in the PFO spectrum indicates that the glass substrate was completely covered by the polymer film and, although not shown here, silicon peaks were also absent in the PFAC-6 survey spectrum. This is consistent with the deposition rate of PFH being considerably lower than either PFAC-6 or PFO.

The presence of a small oxygen peak in the PFO spectrum, which accounts for 1 % of the elemental composition, indicates that some oxidation of the polymer film occurs. This is due to the presence of trace amounts of air during polymerization. In the PFH spectrum, it was not possible to resolve the O 1s peak into contributions from the oxygen present in the underlying glass substrate and contributions from oxygen present in the polymer film. Likewise, a small increase in oxygen content due to oxidation of the PFAC-6 film would be obscured by the oxygen content due to the acrylate group. However, it seems reasonable to assume that all three polymer films suffered similar levels of oxidation.

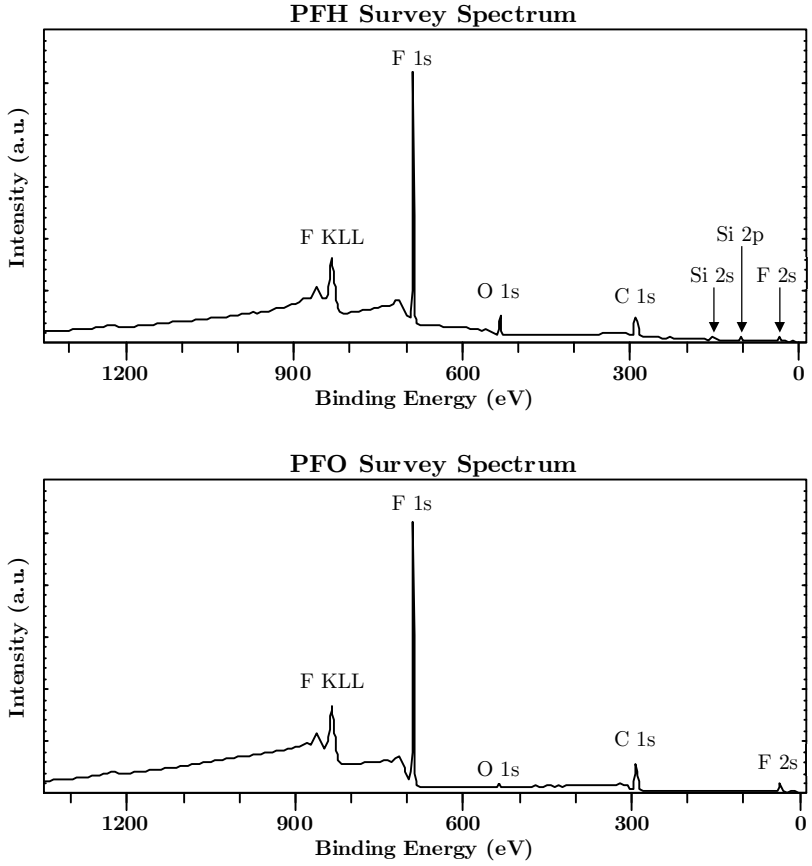


Figure 2.6 *Survey spectra for PFH and PFO polymers. The F KLL peak is an Auger peak. Peak assignments based on Ref [94]*

Figure 2.7 shows the amounts of carbon, fluorine, and oxygen present in the PFAC-6, PFO, and PFH polymer films compared to the amounts predicted using the monomer structure and assuming a structurally intact polymer. The sampling depth of the instrument is approximately 3 nm, which is greater than the length of the monomer units; it is therefore expected that all moieties present in the polymer should contribute to the spectra, although those closer to the surface will contribute more. The measured values for PFAC-6 match the predicted values, which is consistent with the NMR data showing that the PFAC-6 monomer retains its functionality during polymerization. Conversely, both the PFO and PFH polymers have an overabundance of carbon, and an underabundance of fluorine, indicating that monomer has fragmented during the

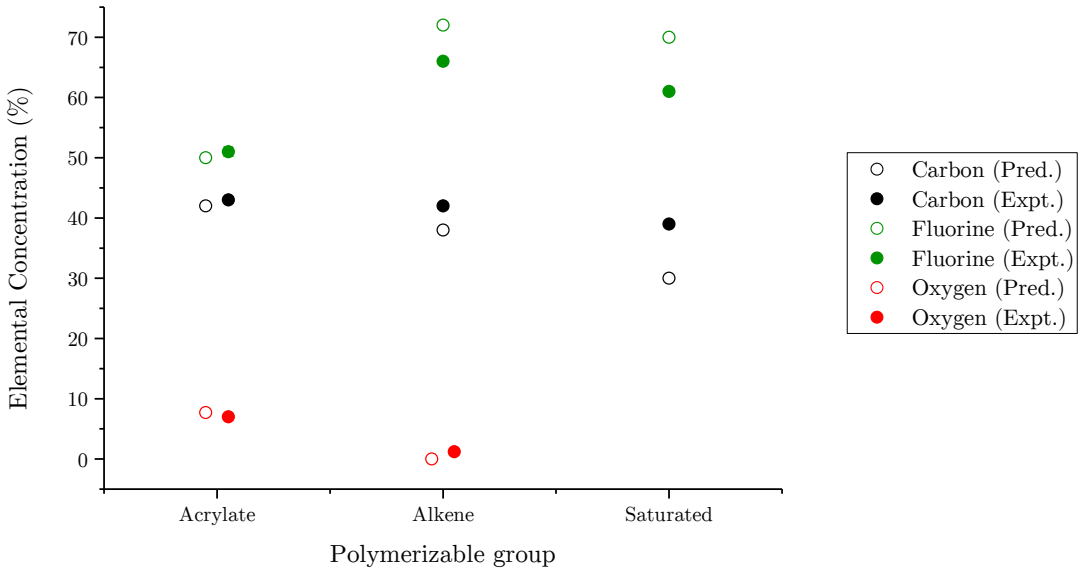


Figure 2.7 *The concentrations of carbon, fluorine, and oxygen present in PFAC-6, PFO, and PFH plasma polymers. The predicted values (open circles) are calculated assuming complete structural retention of the monomer species during polymerization, and random orientation of the polymer. The measured values (solid circles) are calculated from the areas of the 1s peaks in the XPS survey scans. Hydrogen, which is not detectable via XPS, has been excluded from both calculations. In all cases the error bars are smaller than the symbol size*

plasma process, with overall loss of fluorine. This is consistent with the NMR data, which shows that the PFO polymer is highly cross-linked, and suggests that the PFH polymer is similarly cross-linked. Previous studies with perfluorohexane and similarly saturated fluorocarbon monomer species also show a similar loss of fluorine functionality [62,104].

Examination of the C(1s) region allows a more detailed analysis of the different species present in the plasma polymer films. **Figure 2.8** shows the deconvoluted C(1s) spectra obtained at a take-off angle normal to the surface. The PFAC-6 spectrum could be resolved into contributions from six different environments; $\underline{C}$—CH_n/$\underline{C}$—C=O(O) at 285.0 eV, $\underline{C}$—CF_n at 285.8 eV, $\underline{C}$—O at 286.7 eV, $\underline{C}$=O at 288.8 eV, $\underline{C}F_2$ at 291.1 eV, and CF_3 at 293.4 eV.

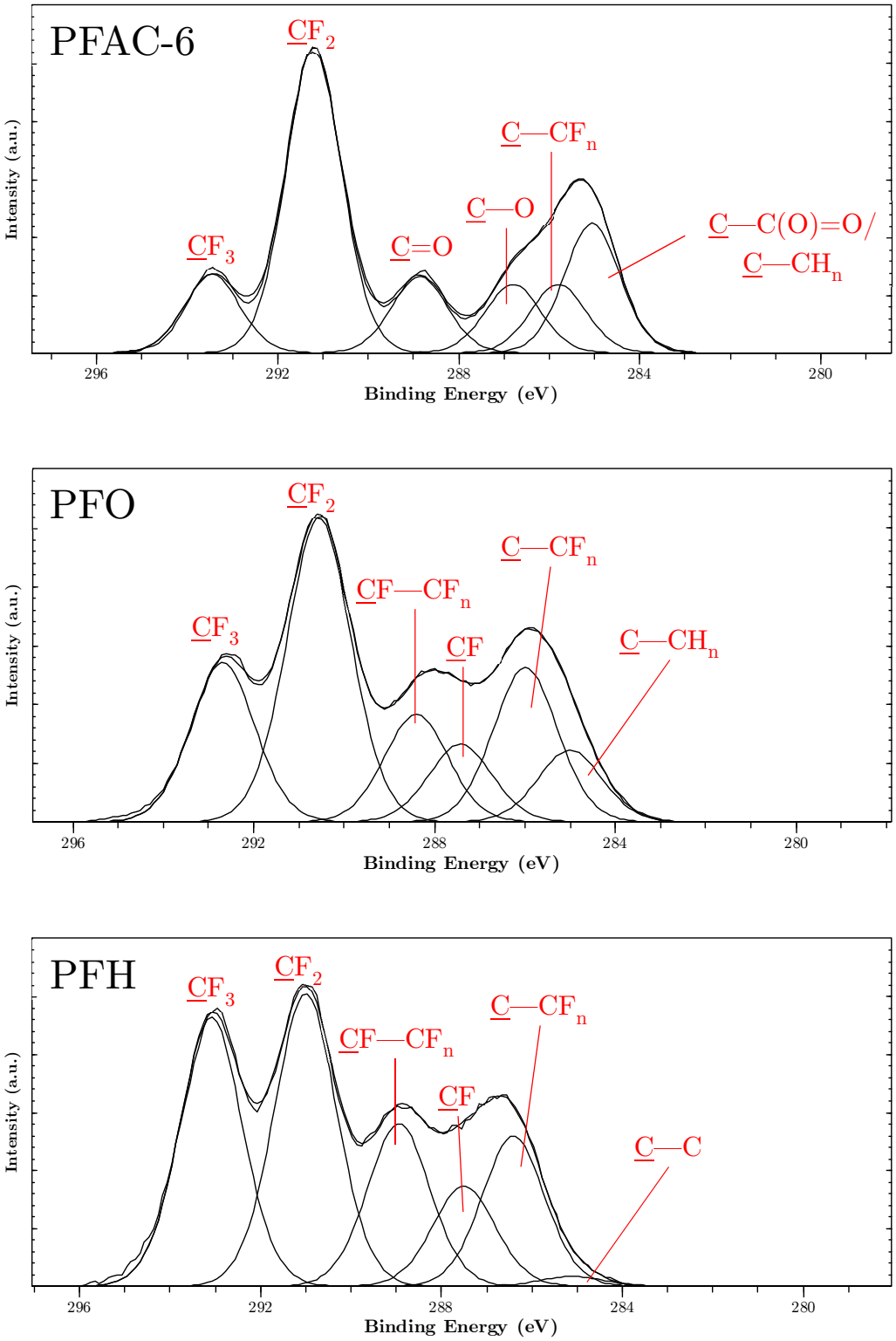


Figure 2.8 *Carbon 1s XPS spectra of PFAC-6 (top, FWHM = 1.44 eV), PFO (middle, FWHM = 1.66 eV), and PFH (bottom, FWHM = 1.63 eV). Peak assignments are based on Refs [104,105]*

To assist in resolving the three overlapping peaks at lower binding energy, the peaks at 285.8 eV and 286.7 eV were constrained to have equal areas as per stoichiometry. The spectrum for PFO could be resolved into contributions from six different carbon environments; $\underline{C}$—CH_n at 285.0 eV, $\underline{C}$—CF_n at 286.0 eV, $\underline{C}F$ at 287.4 eV, $\underline{C}F$—CF_n at 288.4 eV, $\underline{C}F_2$ at 290.6 eV, and $\underline{C}F_3$ at 292.7 eV. The spectrum for PFH could likewise be resolved into six contributions; a minor peak at 285.0 eV for $\underline{C}$—C, $\underline{C}$—CF_n at 286.3 eV, $\underline{C}F$ at 287.4 eV, $\underline{C}F$—CF_n at 288.8 eV, $\underline{C}F_2$ at 290.9 eV, and $\underline{C}F_3$ at 292.9 eV. In both cases, the presence of the $\underline{C}F$ and $\underline{C}F$—CF_n confirms that fragmentation of the monomer has taken place.

Figure 2.9 shows the composition of the three polymer films as determined by the area under the peaks in the deconvoluted C(1s) spectra shown **Figure 2.8**. The measured values for PFAC-6 broadly match the predicted values. The differences between the measured and predicted values for PFO and PFH are starker. In both cases, the formation of cross-linked groups CF, $\underline{C}F$—CF_n, and $\underline{C}$—CF_n (PFH only) is primarily at the expense of the CF_2 groups which decreases to 55% of its predicted concentration for PFO and 44% of its predicted concentration for PFH. Whilst PFH also sees a loss of CF_3 functionality (~80 % of predicted value), albeit a less dramatic one, PFO actually gains CF_3 groups (~150 % of predicted value). This is likely due to the presence of atomic fluorine in the plasma, which fluorinates the surface and increases the amount of CF_3 present [106]. PFO also sees an increase in the $\underline{C}$—CH_n functionality and a loss of $\underline{C}$—CF_n functionality. The presence of a minor $\underline{C}$—C peak in the PFH spectrum, which accounts for 1% of the total composition, can either be attributed to a small amount of hydrocarbon contamination or the presence of

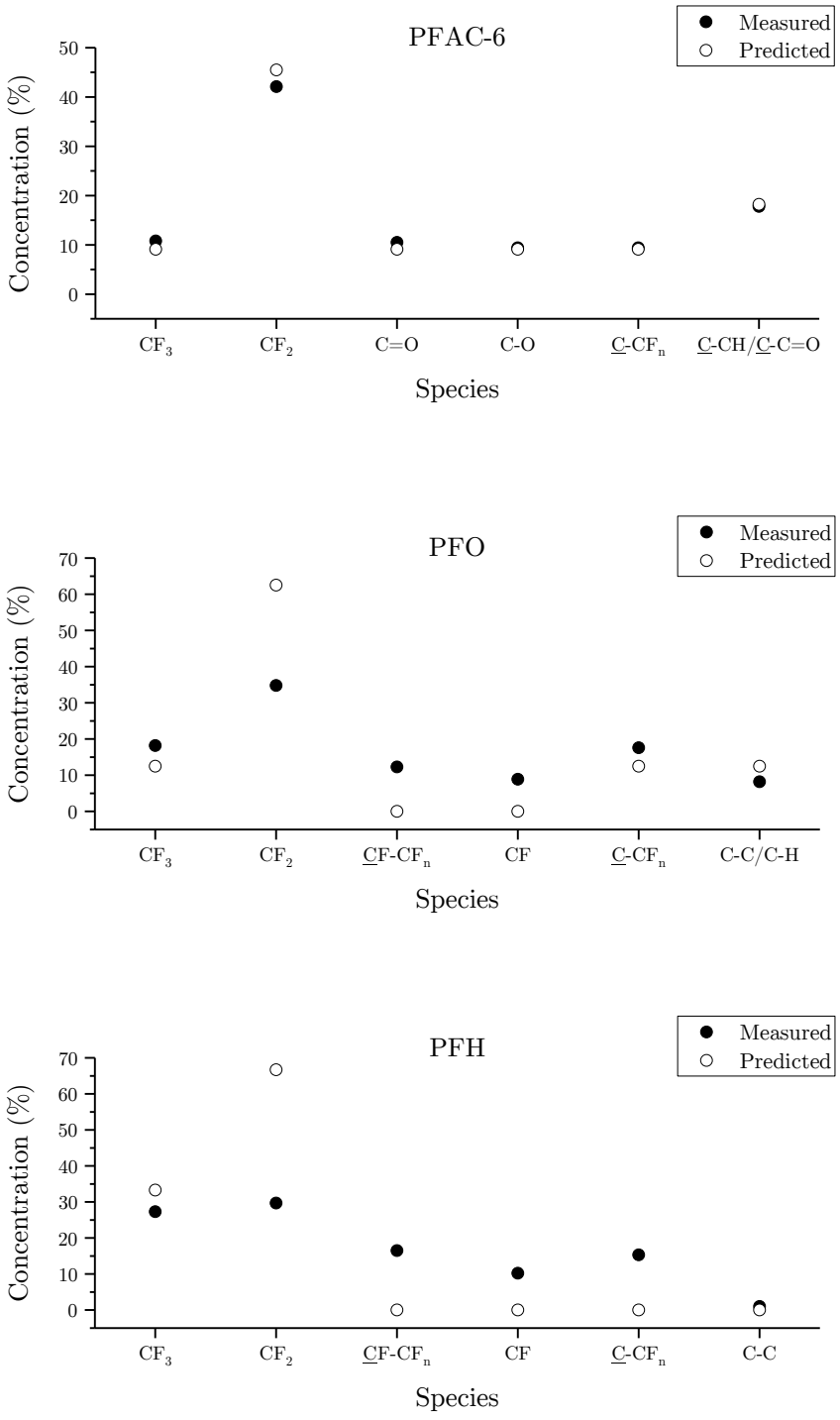


Figure 2.9 *Compositions of PFAC-6 (top), PFO (middle), and PFH (bottom) plasma polymer films as determined from peak area of deconvoluted C(1s) XPS spectra. The predicted values are based on a randomly oriented polymer formed from intact monomer species*

quaternary carbon functionality but it is clear that the fragmentation and recombination mechanisms do not favour formation of ^{t}Bu groups.

Figure 2.10 shows the angle resolved C(1s) spectra of PFAC-6, PFO, and PFH. Spectra were obtained in parallel at angles from 22.5° (blue) to 77.5° (red) to the surface normal in steps of 5°. In order to allow for the fact that the sensitivity of the technique decreases with increasing angle to the normal, the area under the peaks for each of the spectra was normalised. The shape of the PFAC-6 spectrum changes significantly with sampling depth. As the angle to the normal increases and the technique becomes increasingly surface sensitive, the height of the CF_3 shoulder (~293 eV) increases in intensity, and the height of the CF_2 peak (~291 eV) decreases. The intensity at lower binding energy, which is associated with hydrocarbon functionality, also decreases. The PFO spectrum also changes shape as the acquisition angle changes; the height of the CF_3 peak (~293 eV) increases with increasing surface sensitivity, as does the height of the CF_2 peak (~291 eV). There is a corresponding decrease in the heights of the central CF peak (~289 eV) and of the hydrocarbon peak at (~284 eV). The PFH spectrum is shifted towards a slightly higher binding energy, indicating a preferential arrangement of CF_3 and CF_2 at the surface, but does not otherwise change shape significantly.

The lower signal intensity of the angle resolved spectra results in broader peaks. To perform peak fitting for the angle resolved spectra, the normalised spectra were summed to form a single spectrum and peak fitting was carried out as before. The peak positions were fixed and exported to each of the angle-resolved spectra and peak intensity and FWHM were optimised as before. PFO could be resolved into six peaks as before, whilst PFAC-6 could only be resolved into five peaks. The PFH spectra could not be adequately fitted; the overlapping peaks at lower binding energy could not be resolved, and the slight shift in the apparent position

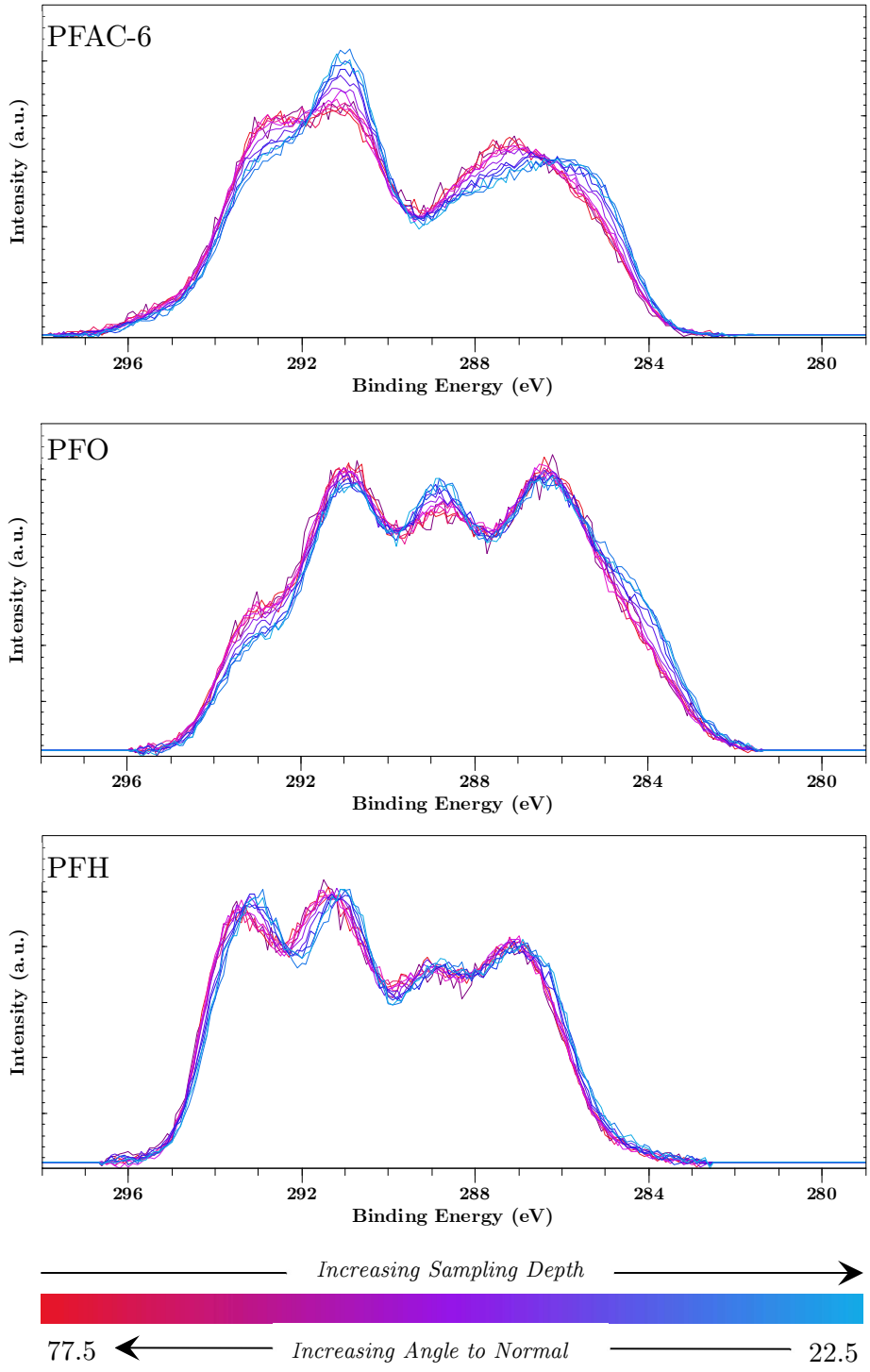


Figure 2.10 *Angle resolved carbon 1s XPS spectra of PFAC-6, PFO, and PFH. Measurements were obtained in parallel at angles from 22.5° from the normal (blue, least surface sensitive) to 77.5° to the normal (red, most surface sensitive) in 5° intervals. Since the signal intensity decreases as the technique becomes more surface sensitive, the area of under the peaks was normalised*

of the CF_3 and CF_2 peaks made it difficult to pinpoint the true peak position.

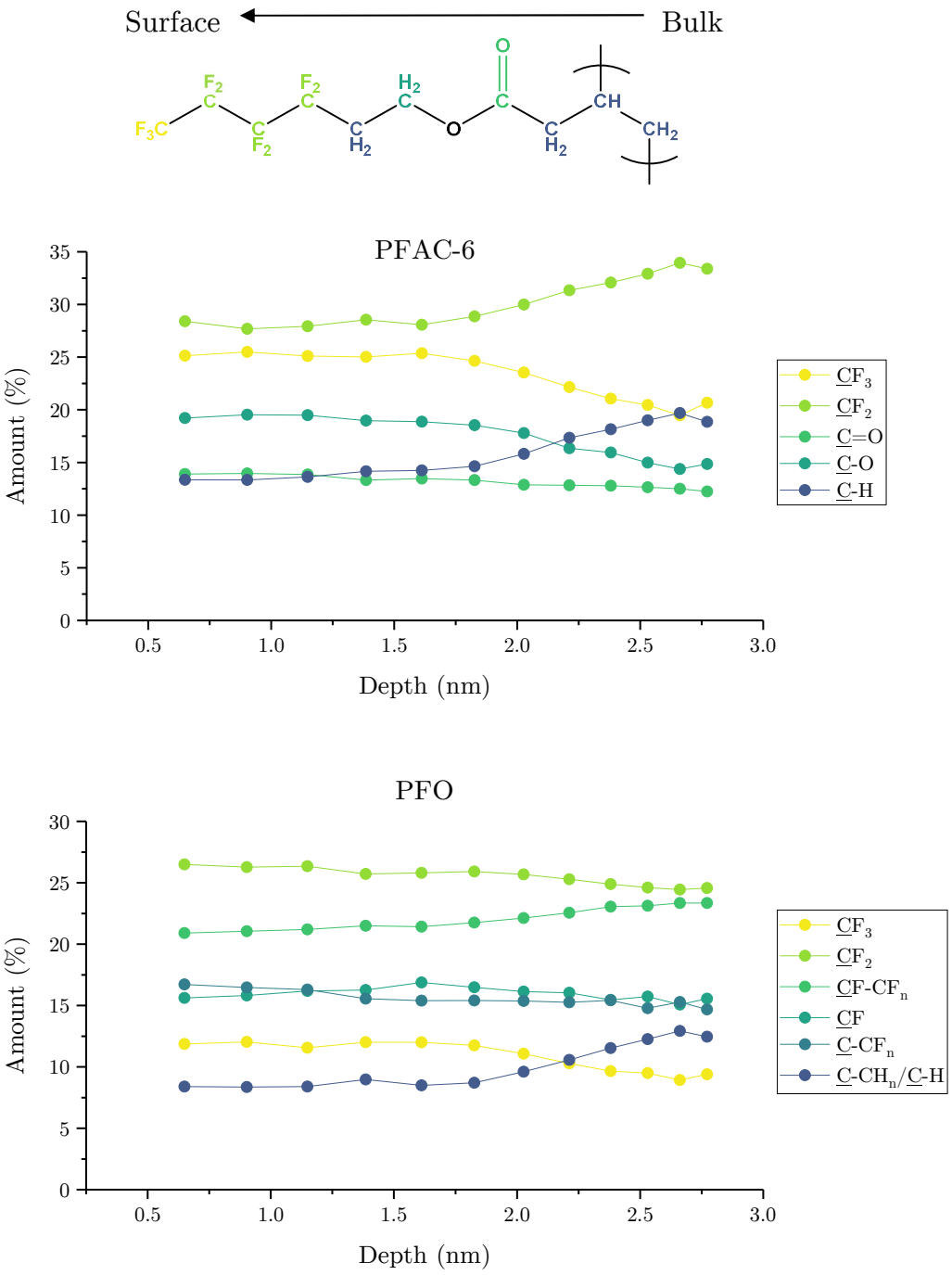


Figure 2.11 *(**Top**) Relative orientation of the PFAC-6 side chain to the surface and variation with depth of the concentration of different carbon species in a PFAC-6 surface. (**Bottom**) variation with depth of the concentration of different carbon species in a PFAC-6 surface*

Figure 2.11 shows the how the concentration of different carbon species varies with XPS analysis depth in PFAC-6 and PFO surfaces. For PFAC-6, the concentrations of CF_2 and C—H are proportional and are depleted at the surface.

Meanwhile, the concentrations of CF_3 and C=O are proportional to one another, and anti-correlated to CF_2 and C—H. The concentration of C—O remains unchanged. For PFO, the concentrations of CF_3 and C—H are also anti-correlated, with an excess of CF_3 at the surface. However, there is also an excess of CF_2 at the surface, which is anti-correlated to the concentration of the $\underline{C}F—CF_n$ at the surface. The concentrations of CF and $\underline{C}—CF_n$ remain constant.

Figure 2.12 shows that the concentrations of CF_3 and hydrocarbon groups, which are at opposite ends of the side chain, are anti-correlated for both PFAC-6 and PFO. This suggests that the side chains are standing approximately upright with the CF_3 oriented towards the surface, and the other end buried in the bulk. Both graphs show a change in concentration gradient at a depth of ~1.75 nm which suggests that there is a distinct surface layer, although not necessarily a well-ordered one.

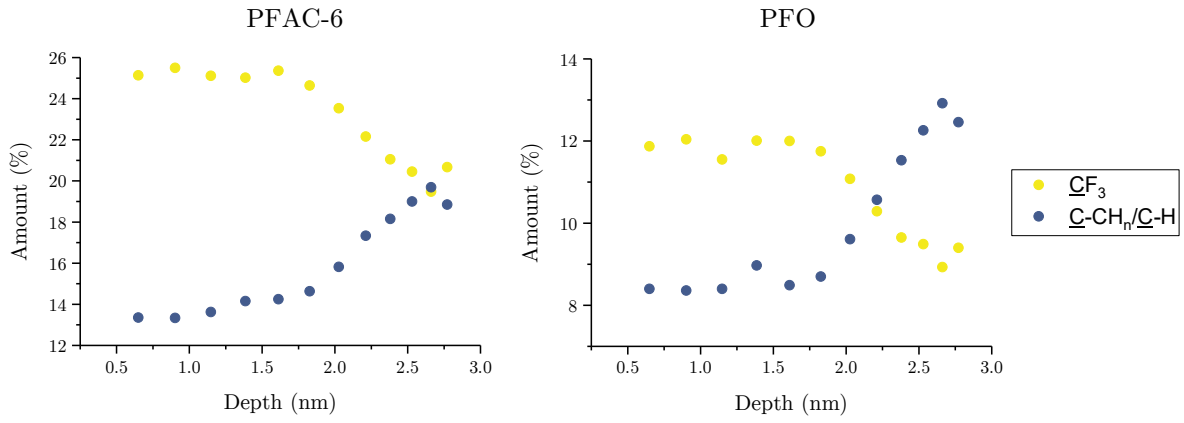


Figure 2.12 *Concentrations of CF_3 (yellow) and hydrocarbon (blue) groups with varying depth in PFAC-6 and PFO surfaces*

2.2.3. Topography

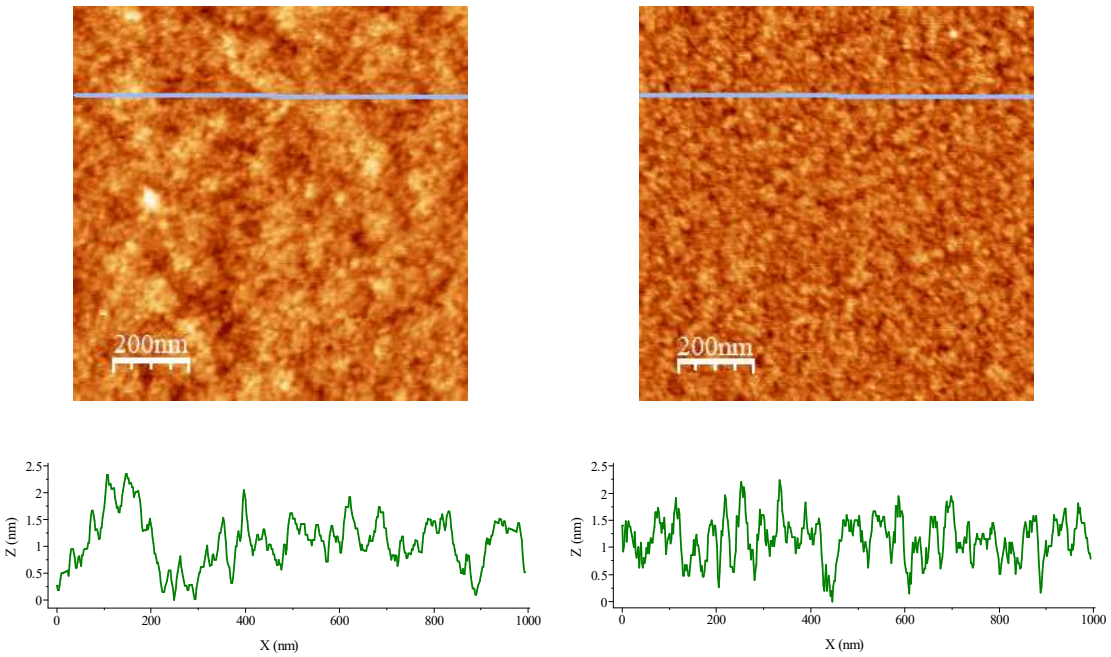


Figure 2.13 *A 1x1 μm^2 AFM micrograph and section profile of PFH. The z scale of the micrograph is 4 nm*

Figure 2.14 *A 1x1 μm^2 AFM micrograph and section profile of PFO. The z scale of the micrograph is 4 nm*

Figure 2.13 and **Figure 2.14** show AFM micrographs and cross sections of PFH and PFO respectively. The RMS roughness of both micrographs is 0.4 nm. Attempts to measure the topography of PFAC-6 using AFM were unsuccessful, and the results are therefore not shown. The micrographs obtained were flat and featureless to within the noise level of the instrument. Differential scanning calorimetry (DSC) measurements, which are discussed in detail in **Section 3.2.3**, indicate that PFAC-6 undergoes melting transitions at and/or below room temperature and so these surfaces were too soft to acquire meaningful measurements, even when using a cantilever with a low spring constant (3 Nm^{-1}).

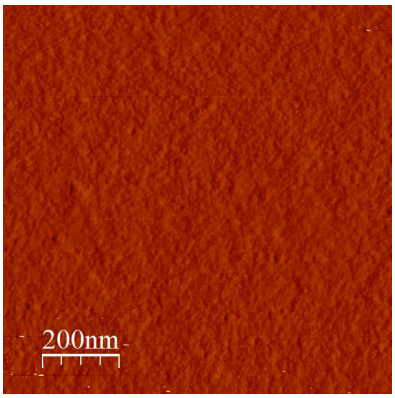


Figure 2.15 *The phase data associated with the micrograph of PFH in Figure 2.13 A 1x1 μm2 AFM micrograph and section profile of PFH. The z scale of the micrograph is 4 nmThe z scale is 10°*

Figure 2.15 shows the phase data obtained at the same time as the topographical data in the micrograph of PFH in **Figure 2.13**. The homogeneity of the phase data indicates that the composition of the surface is similarly homogenous, with full coverage of the underlying glass substrate.

2.2.4. Surface energy and wetting properties

Figure 2.16 and **Figure 2.17** show the advancing (θ_{adv}) and receding (θ_{rec}) contact angles of water and dodecane (DD) respectively on PFAC-6, PFO, and PFH surfaces. The error bars, which represent one standard deviation from the mean across fifteen measurements (five measurements on three surfaces) are dominated by the differences between individual surfaces, rather than the variation between the measurements on a single surface. In both cases, PFO and PFH have similar θ_{adv} and PFAC-6 displays higher θ_{adv} than either of these. This corresponds to values of ~120° for water PFO and PFH, and ~140° for water on PFAC-6. In the case of DD, this corresponds to ~70° for PFO and PFH, and ~140° for PFAC-6. In terms of contact angle hysteresis, PFAC-6 > PFO > PFH.

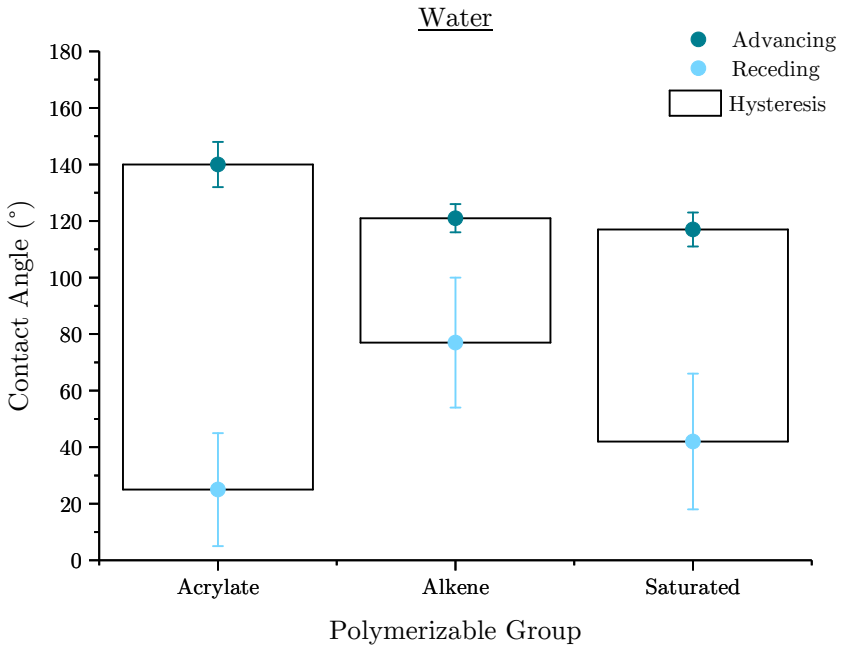


Figure 2.16 *Advancing (dark) and receding (light) contact angles of water on PFAC-6, PFO, and PFH. The contact angle hysteresis, which is the difference between the advancing and receding contact angles is shown as a floating bar. The error bars correspond to one standard deviation from the mean*

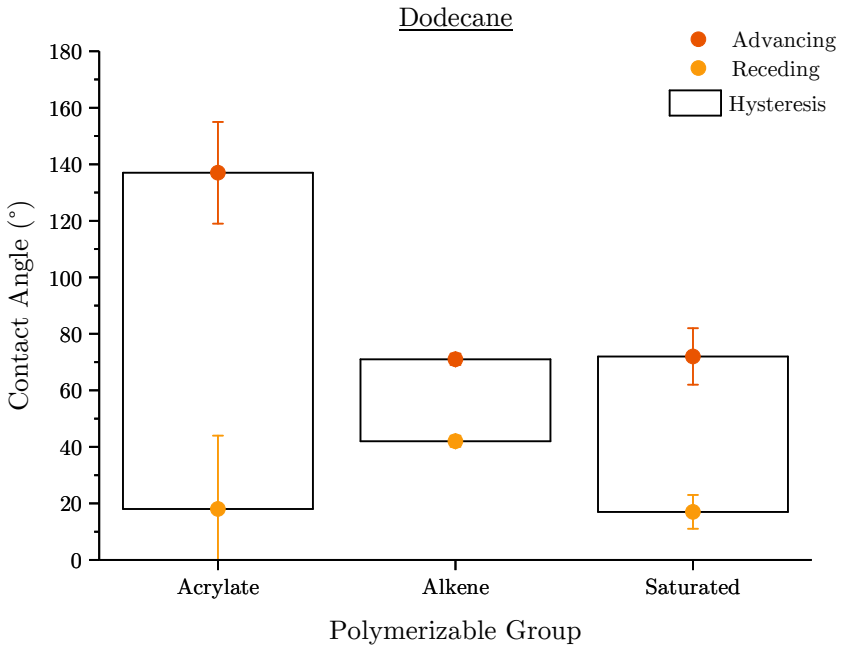


Figure 2.17 *Advancing (dark) and receding (light) contact angles of dodecane on PFAC-6, PFO, and PFH. The contact angle hysteresis, which is the difference between the advancing and receding contact angles is shown as a floating bar. The error bars correspond to one standard deviation from the mean*

The larger contact angles on PFAC-6 are in keeping with the larger proportion of CF_3 groups at the PFAC-6 surface than the other two surfaces. The similarity in θ_{adv} for both DD and water on PFAC-6 despite their large difference in surface tension (γ^W= 72.9 mJ m^{-2} and γ^{DD} = 25.4 mJ m^{-2}) indicates that a maximum has been reached, and the value is approximately consistent with the maximum contact angle in the Wenzel wetting regime of ~150° [37,43]. The large contact angle hysteresis could be the effect of pinning on topographical features (which were too soft to measure using AFM), or chemical heterogeneity of the surface [107,108]. In the case of chemical heterogeneity of the surface, this could be a feature present in air, or only when the surface is exposed to a liquid. **Section 1.1.2** discusses the effect of roughness on wetting and introduces the concept of maximum contact angles. In the case of PFO and PFH, the similarities in θ_{adv} are consistent with their similar chemical compositions. Despite the fact that PFO and PFH have the same, rather low, RMS roughness of 0.4 nm, both of these surfaces display contact angle hysteresis. The contact angle hysteresis is larger for PFO than PFH, which could be due to the different shape of the asperities on the surface.

Table 2.1 shows the surface energies of the three polymers as determined using the OWRK method. At this point, it must be emphasised that these numbers do not reflect the equilibrium surface energy as defined in **Section 1.1**. Rather, it is an *effective* surface energy; that is, the combined effect of the intrinsic surface energy of the substance and the effect of roughness or heterogeneity [41,109] [37,38]. Although not the true value of the surface energy, these values are nonetheless useful in predicting how a liquid will behave in contact with a solid

surface. The total surface energy, γ_{SV}, for PFAC-6 is only slightly higher than the value for a smooth surface consisting of close-packed CF_3 groups (6 mJ m^{-2}), whilst the values for PFO and PFH fall between the value for a smooth CF_3 surface and the value for smooth PTFE (21 mJ m^{-2}) [34,35]. All three materials engage primarily in dispersive, rather than polar, interactions with $\gamma_{SV}{}^{p}$ being negligible. This is consistent with the surfaces being composed solely of fluorocarbon groups, with the acrylate group in PFAC-6 being buried. PFH has a slightly larger polar component than the other two, but this is likely an artefact due to roughness effects.

Surface	$\boldsymbol{\gamma_{SV}}$ (mJ m^{-2})	$\boldsymbol{\gamma_{SV}{}^{d}}$ (mJ m^{-2})	$\boldsymbol{\gamma_{SV}{}^{p}}$ (mJ m^{-2})
PFAC-6	8	7.5	0.5
PFO	16.5	15.5	0.5
PFH	15	13.5	1.5

Table 2.1 *The total surface energy, γ_{SV}, and dispersive and polar components of the surface energy of the polymer films*

2.2.5. Discussion

The composition of the polymers is determined by the ratios of different species present in the plasma during the polymerization process. During the 'on' period of the duty cycle, the monomer species fragment. Although there is some preference for scission at weaker bond sites ($\pi > \sigma$ and C—C > C—H > C—F in terms of preference), the fragmentation process is largely random [88] and previous work has shown that there is little difference in deposition rates between saturated and unsaturated monomer species during continuous wave deposition [57]. The recombination process is equally random, and the resulting polymer is therefore randomly branched and cross-linked – as shown in **Figure 2.18**.

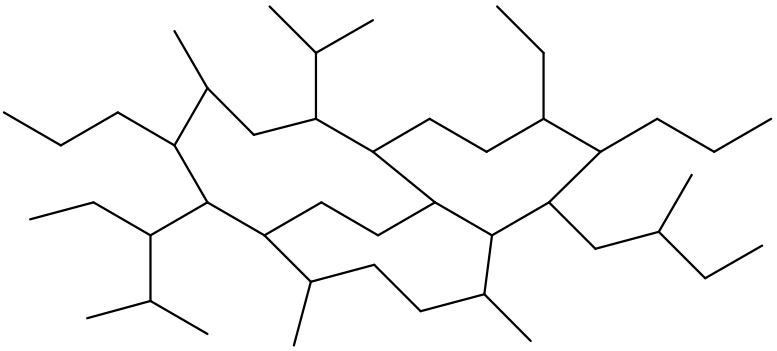


Figure 2.18 *Highly branched and cross-linked polymer produced by a continuous wave discharge or during the 'on' period of the duty cycle during pulsed deposition*

The growing polymer film is also subject to fragmentation and ablation during the on period [67]. Overall, the three monomers polymerize via the same mechanism during the on period, irrespective of end group. The more energetic species responsible for the fragments have a lifetime of the order of μs-ms, whilst the π-radicals formed from the activation of an unsaturated monomer have a lifetime of the order of ms-s [44]. Since the shorter-lived species are the only means by which PFH can polymerize, PFH polymer can only form during the on period; this is why the deposition rate of PFH is so low. During the off period, any remaining alkene (PFO) or acrylate (PFAC-6) radicals initiate radical chain reactions which are responsible for the growth of the structurally intact polymers. The longer off time in relation to on time is to ensure that this process dominates. Therefore, all three polymers contain some amount of cross-linked species, and PFAC-6 and PFO also contain structurally intact species – as depicted in **Figure 2.19**.

The increased stability of the acrylate radical over the alkene radical [71] means that the activated monomer species is present in far greater quantities in the off period of PFAC-6 polymerization than during PFO polymerization. This means

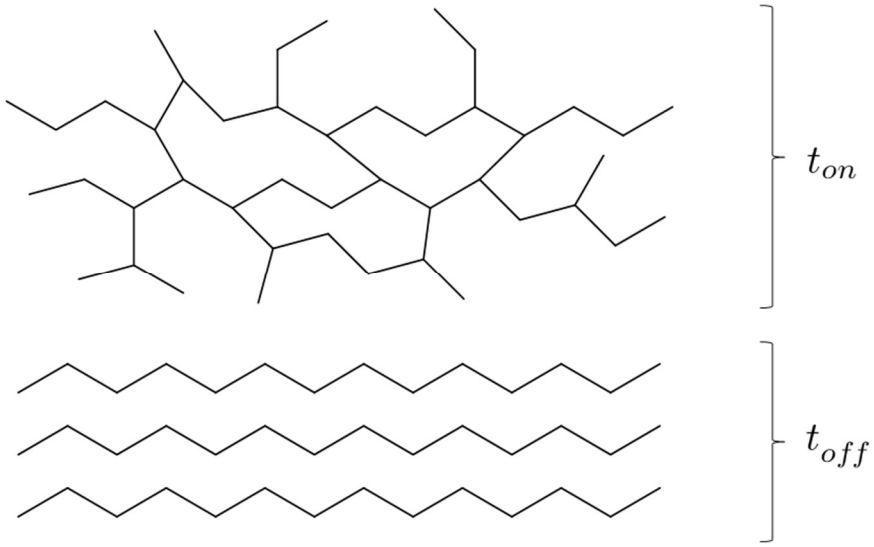


Figure 2.19 *Different polymer morphologies produced in the on and off periods of a pulsed plasma deposition. A highly branched and cross-linked structure is formed during the on period, whilst a more conventional polymer forms during the off period. Note that this diagram is not meant to imply that a layered structure forms, as the on period is too short for a complete surface layer to form. Adapted from Ref [110]*

that a far greater proportion of the PFAC-6 polymer is produced during the off period, and that a greater quantity of the PFAC-6 polymer forms in total – hence the higher deposition rate of PFAC-6 compared to PFO. The disparity in the amounts of PFAC-6 formed during the different parts of the duty cycle is sufficiently large to completely mask the presence of any cross-linked product via NMR or XPS. The amounts of the two different polymer species are more evenly distributed in the PFO polymer. This result for PFO is somewhat at odds with the literature, where perfluoroalkyl alkenes have been successfully polymerized under pulsed plasma conditions with better structural retention [88]. **Figure 2.20** shows schematically the concentrations of the active monomer species during the on and off periods of the duty cycle. **Figure 2.21** shows the proposed structure of the PFO polymer.

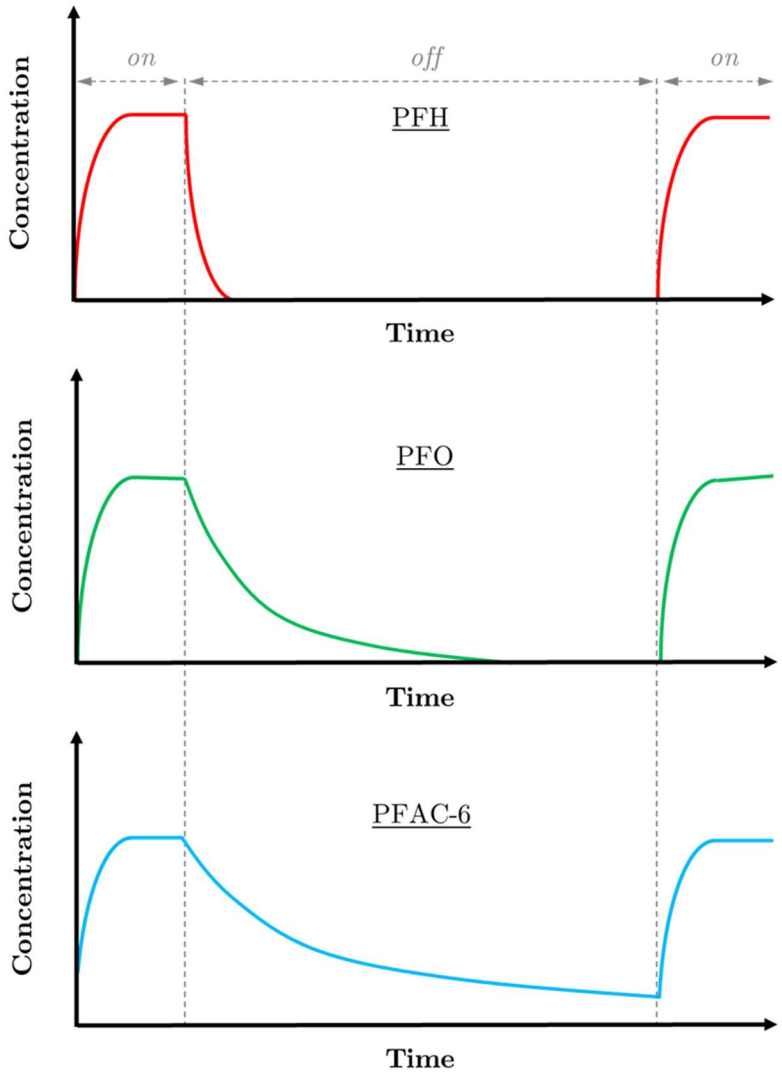


Figure 2.20 *Schematic indication of the concentrations of active monomer species during the on and off periods of the duty cycles. The cross-linked species is deposited during the on period and the structurally intact polymer species forms during the longer off period.*

Angle resolved XPS indicated little change in composition for the PFH polymer with sampling depth. Previous studies with plasma fluoropolymers using near edge X-ray absorption fine structure (NEXAFS) spectroscopy have indicated that highly cross-linked polymers produced in the continuous wave do not form with any particular orientation [111]. In the case of PFAC-6, the surface excess of CF_3 and the proportional depletion of hydrocarbon functionality suggests that the side chains are oriented approximately upright with the CF_3 at the surface. This

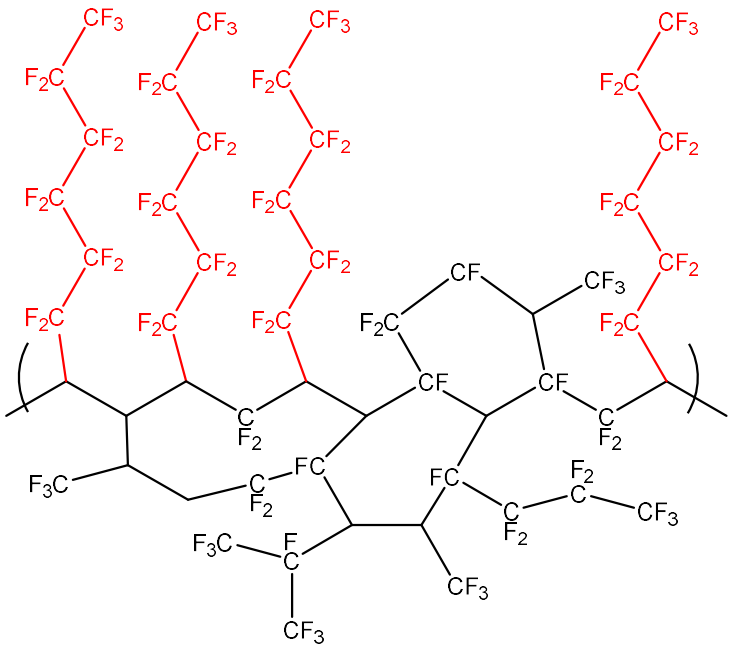


Figure 2.21 *Proposed composite structure of the PFO polymer. The cross-linked regions are shown in black, whilst the structurally intact regions are shown in red*

finding is in keeping with angle-resolved XPS studies of a number of polymers with fluorinated side chains produced both via the solution phase[112,113] and under pulsed plasma conditions [111]. A more detailed discussion of side-chain orientation in PFAC-6 is provided in the next chapter. PFO also had an excess of CF_3 and proportional depletion of hydrocarbon which suggests that the structurally intact regions behaved in the same way as PFAC-6. However, whilst the CF_2 functionality was depleted at the PFAC-6 surface, the opposite was true in the PFO surface. This, coupled with the fact that the amounts of CF and $\underline{C}F—CF_n$ stayed constant with depth, lends itself to the conclusion that the cross-linked regions of the polymer behave in much the same way as PFH.

2.3. Conclusions

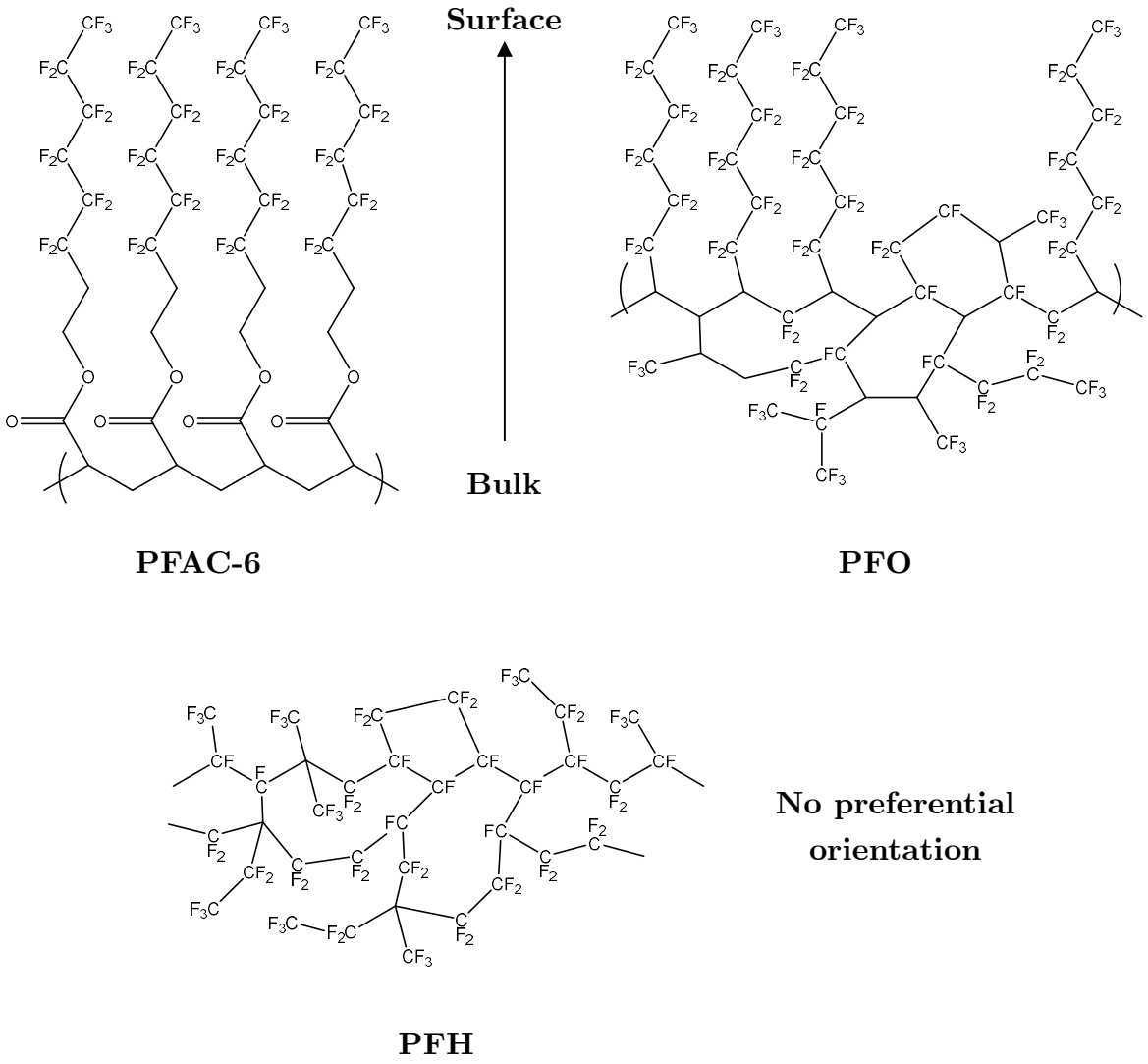


Figure 2.22 *Structure and orientation relative to the surface of PFO, PFAC-6, and PFH*

Figure 2.22 shows the structures of the three polymers, as well as the relative orientation of their functional groups to the surface. PFAC-6 was successfully polymerized under pulsed conditions to form a structurally intact, low surface energy polymer. PFH polymerized to form a highly fragmented and cross-linked polymer as predicted. PFO appears to have formed a polymer with a composite

morphology, consisting of both fragmented and structurally intact regions. The moieties in the cross-linked polymers are randomly oriented, whilst the structurally intact polymers have preferential segregation of the CF_3 groups at the surface. Cross-linking inhibits molecular mobility and prevents surface reconstruction. Whilst this makes PFH a useful baseline material, the composite structure of the PFO polymer renders it useless as a comparator in molecular mobility studies. Furthermore, the low deposition rates of PFO and PFH preclude their use in NMR relaxometry studies, which are discussed later in this thesis. With some work and adjustment of the plasma parameters, it is likely that a structurally intact PFO polymer would be attainable, but this is beyond the scope of this thesis. For the rest of the work in this thesis, the work will focus on PFAC-n polymers.

2.4. References

[34] T. Nishino, M. Meguro, K. Nakamae, M. Matsushita, and Y. Ueda, Langmuir **15**, 4321 (1999).

[35] E. G. Shafrin and W. A. Zisman, The Journal of Physical Chemistry **64**, 519 (1960).

[37] R. N. Wenzel, Industrial & Engineering Chemistry **28**, 988 (1936).

[38] A. B. D. Cassie and S. Baxter, Transactions of the Faraday Society **40**, 546 (1944).

[41] T. S. Meiron, A. Marmur, and I. S. Saguy, Journal of Colloid and Interface Science **274**, 637 (2004).

[43] V. Kumar and J. R. Errington, Langmuir **29**, 11815 (2013).

[44] H. J. Butt, K. Graf, and M. Kappl, *Physics and Chemistry of Interfaces* (John Wiley & Sons, 2013), Third, Revised and Enlarged edn., Physics and Chemistry of Interfaces.

[57] H. Yasuda, Macromolecular Reviews Part D-Journal of Polymer Science **16**, 199 (1981).

[62] A. Hynes, M. Shenton, and J. Badyal, Macromolecules **29**, 4220 (1996).

[67] H. Yasuda and T. Hsu, Journal of Polymer Science: Polymer Chemistry Edition **15**, 81 (1977).

[71] G. Clayden, W. Warren, N. Greeves, and P. Wothers, *Organic Chemistry* (Oxford University Press, 2001).
[72] R. A. Wolf, *Atmospheric Pressure Plasma for Surface Modification* (John Wiley & Sons, Hoboken, N.J., 2013), Ebook central.
[77] S. R. Coulson, I. S. Woodward, J. P. S. Badyal, S. A. Brewer, and C. Willis, Chemistry of Materials **12**, 2031 (2000).
[82] M. P. Krafft and J. G. Riess, Current Opinion in Colloid & Interface Science **20**, 192 (2015).
[84] K. Honda, M. Morita, H. Otsuka, and A. Takahara, Macromolecules **38**, 5699 (2005).
[86] V. Kumar, J. Pulpytel, and F. Arefi-Khonsari, Plasma Processes and Polymers **7**, 939 (2010).
[87] A. M. Coclite, Y. Shi, and K. K. Gleason, Advanced Functional Materials **22**, 2167 (2012).
[88] E. J. Kinmond, S. R. Coulson, J. P. S. Badyal, S. A. Brewer, and C. Willis, Polymer **46**, 6829 (2005).
[89] S. R. Coulson, I. S. Woodward, J. P. S. Badyal, S. A. Brewer, and C. Willis, Langmuir **16**, 6287 (2000).
[90] H. Biederman, *Plasma Polymer Films* (World Scientific, 2004).
[91] R. Förch, Z. Zhang, and W. Knoll, Plasma Processes and Polymers **2**, 351 (2005).
[92] C. Stone, Personal Communication, 2013.
[93] F. Reniers and C. Tewell, Journal of Electron Spectroscopy and Related Phenomena **142**, 1 (2005).
[94] B. V. Crist, *XPS Handbook: Elements & Native Oxides* (XPS International, 2007).
[95] C. D. Wagner, L. E. Davis, M. V. Zeller, J. A. Taylor, R. H. Raymond, and L. H. Gale, Surface and Interface Analysis **3**, 211 (1981).
[96] P. J. Cumpson, Surface and Interface Analysis **31**, 23 (2001).
[97] D. K. Owens and R. C. Wendt, Journal of Applied Polymer Science **13**, 1741 (1969).
[98] D. H. Kaelble, Journal of Adhesion **2**, 66 (1970).
[99] L. Wang, S. Wen, and Z. Li, Canadian Journal of Chemistry **95**, 605 (2017).
[100] K. K. Lau and K. K. Gleason, Journal of The Electrochemical Society **146**, 2652 (1999).
[101] K. K. S. Lau and K. K. Gleason, Journal of Fluorine Chemistry **104**, 119 (2000).
[102] E. Katoh, H. Sugimoto, Y. Kita, and I. Ando, Journal of Molecular Structure **355**, 21 (1995).
[103] J. Emsley and L. Phillips, Progress in Nuclear Magnetic Resonance Spectroscopy **7**, 1 (1971).
[104] D. Clark and D. Shuttleworth, Journal of Polymer Science: Polymer Chemistry Edition **18**, 27 (1980).
[105] D. Briggs and M. P. Seah, *Practical Surface Analysis by Auger and X-ray Photoelectron Spectroscopy* (John Wiley & Sons, 1983), 2 edn.

[106] S. R. Cain, F. D. Egitto, and F. Emmi, Journal of Vacuum Science & Technology A **5**, 1578 (1987).
[107] N. Belman, K. Jin, Y. Golan, J. N. Israelachvili, and N. S. Pesika, Langmuir **28**, 14609 (2012).
[108] H. Tavana, D. Jehnichen, K. Grundke, M. L. Hair, and A. W. Neumann, Advances in Colloid and Interface Science **134**–**135**, 236 (2007).
[109] A. J. B. Milne and A. Amirfazli, Advances in Colloid and Interface Science **170**, 48 (2012).
[110] J. Friedrich, Plasma Processes and Polymers **8**, 783 (2011).
[111] C. I. Butoi, N. M. Mackie, L. J. Gamble, D. G. Castner, J. Barnd, A. M. Miller, and E. R. Fisher, Chemistry of Materials **12**, 2014 (2000).
[112] R. Bongiovanni, G. Beamson, A. Mamo, A. Priola, A. Recca, and C. Tonelli, Polymer **41**, 409 (2000).
[113] G. Beamson and M. Alexander, Surface and Interface Analysis **36**, 323 (2004).

3. Surface Characterization and Wetting Behaviours of Plasma Polymerized Fluoroalkyl Acrylates

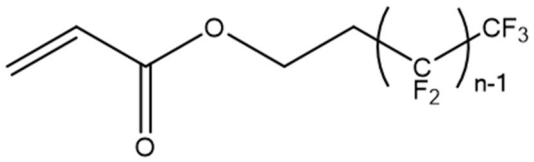


Figure 3.1 *Chemical structure of the PFAC-n monomer*

Until recently, much of the work on manufacturing low surface energy polymers relied on the use of monomers containing perfluoroalkyl chains of more than eight carbons. However, as outlined in the **Aim of Study**, there are significant concerns around the bioaccumulation of these compounds, and attention is turning to analogues with shorter perfluoroalkyl chains [82,83]. Perfluoroalkyl chains are able to crystallize at a length of eight carbons and the increased mobility of the shorter chain analogues can have a significant impact on the surface composition, topography, morphology and, consequently, the wettability of fluorinated surfaces [84,114]. The work in this chapter focusses on the role that the length of the perfluoroalkyl chain plays in determining the characteristics of plasma polymerized perfluoroalkyl acrylates (PFAC-*n*). The generic structure of the PFAC-*n* monomer is shown in **Figure 3.1**.

Perfluoroalkyl acrylates are a well-studied group of polymers; In particular, Takahara *et al.* have performed extensive characterization of fluoroalkyl acrylate (and methacrylate) polymers, exploring the role of chain length [84,85], alpha substituent [115], and molecular weight [116] on the molecular mobility of the fluorinated side chains using techniques such as XPS and wide-angle X-ray diffraction (WAXD). These studies were performed on polymers which were synthesized in the solution phase (and are therefore structurally intact), and which were typically annealed post-synthesis. Annealing in particular allows the fluoroalkyl chains to orient themselves in their lowest surface energy configuration and, for longer chains, to crystallise in that configuration – thus inhibiting surface reorganization. The differences in production method and lack of annealing mean that the plasma polymers are likely to exhibit differences in composition and morphology to the solution-phase polymers which have already been studied.

As outlined in the **Aim of Study**, PFAC-8 is particularly well suited to manufacturing hydrophobic coatings via pulsed plasma polymerization and the literature yields a number of detailed studies on the surface properties of PFAC-8 polymers produced in this way [8,77,86,87,117]. Although there were some commonalities, such as the preferential segregation of CF_3 at the surface, the resulting polymers varied significantly in terms of degree of crystallinity and crystallographic orientation, molecular weight, topography, and overall wetting properties. This highlights the fact that the properties of polymers produced in this manner are dependent on the plasma processing parameters and reinforces the need to conduct a complete characterization of the PFAC-n surfaces produced for this thesis.

A number of factors were taken into consideration when selecting which PFAC-n monomers to use in this investigation. From a practical perspective, monomers for which $n > 10$ are not volatile enough to be suitable candidates for plasma polymerization. For $n > 2$, there is preferential segregation of the fluoroalkyl groups at the surface, whilst the polar acrylate group is buried in the bulk. This arrangement is a requirement for a low energy surface and therefore excludes $n \leq 2$ from the investigation, leaving $n = 4$, 6, 8, and 10 as suitable candidates.[‡] Exposure of PFAC-n surfaces to polar liquids such as water can trigger reconstruction at the surface, where the acrylate group migrates from the bulk to the surface. Crystallization of the fluoroalkyl side chain inhibits the mobility of the acrylate group, preventing surface reconstruction. Previous studies on solution phase PFAC-n has shown crystallisation occurs only where $n \geq 8$ [84] and it is therfore anticipated that a range of surface reconstruction behaviours will be observed across the selected polymers.

This chapter presents XPS, solid-state NMR, AFM, and DSC characterization of the PFAC-n plasma polymer surfaces. These methods are largely described in the preceding chapter with the exception of DSC, which is used to characterize the thermal and phase behaviour of the polymers.

[‡] PFAC-n with odd values of n are not easily available for $n > 1$

3.1. Experimental

3.1.1. Monomers

The monomers used in the plasma polymer experiments were 1H,1H,2H,2H-perfluorododecyl acrylate (PFAC-10, Fluorochem, 97%), 1H,1H,2H,2H-perfluorodecyl acrylate (PFAC-8, Sigma-Aldrich, 97%), 1H,1H,2H,2H-perfluorooctyl acrylate (PFAC-6, Sigma-Aldrich, 97%) and 1H,1H,2H,2H-perfluorohexyl acrylate (PFAC-4, Fluorochem, 97%). These were purified using repeated freeze-thaw cycles.

3.1.2. Plasma polymerization

Plasma polymerization experiments were performed as described in **Section 2.1.2**. The only difference was in the polymerization of PFAC-8 and PFAC-10, which are less volatile than the other monomers used. To achieve a pressure of 2×10^{-1} mbar, the entire rig was heated to 30 ºC for PFAC-8 and to 50 ºC for PFAC-10. All other depositions were carried out at room temperature.

3.1.3. Surface characterization

XPS studies (including angle-resolved studies) were carried out as described in **Section 2.1.3.** AFM was carried out as described in **Section 2.1.5** and contact angle goniometry and surface energy calculations were carried out as described in **Section 2.1.6.** Solid-state NMR is described in **Section 6.2.**

3.1.4. Differential scanning calorimetry (DSC)

PFAC-8 and -10 samples were prepared by running an hour-long plasma deposition; the polymer was then scraped off the chamber walls and approximately 5 mg of sample was used for DSC characterization. PFAC-4 and -6 samples were deposited onto ground glass in two repetitions of an hour-long plasma deposition. Approximately 15 mg of sample (ground glass + polymer) was used for DSC characterization.

A Perkin Elmer PYRIS Diamond DSC was used in the thermal analysis of PFAC samples. The samples were loaded at -50 ℃, and equilibrated for 2 min. The samples were then heated from -50 to 150 ℃ at a rate of 10 ℃ min^{-1}, held at 150 ℃ for 5 min, and then cooled to -50 ℃ at a rate of 10 ℃ min^{-1}. The samples were held at -50 ℃ for 5 min and the heating and cooling cycle was then repeated once more. Data was analysed using the PYRIS software.

3.2. Results and Discussion

3.2.1. Chemical composition (solid-state ^{19}F NMR)

The solid-state ^{19}F NMR spectra of the PFAC-*n* polymers are shown in **Figure 3.2 to Figure 3.5.** Each spectrum shows contributions from four different fluorine environments; C$\underline{F}_3$—CF_2, C$\underline{F}_2$—CH_2, C$\underline{F}_2$—CF_2, and C$\underline{F}_2$—CF_3. **Table 3.1** shows the position of each of these peaks for the different polymers. None of the spectra show contributions from C$\underline{F}$, CF(C$\underline{F}_3$)$_2$, or C(C$\underline{F}_3$)$_3$, which indicates that no cross-linking or branching has occurred, and so the PFAC-*n* polymers are all structurally intact.

PFAC-*n*	**Assigned Peak Position** (ppm)			
	$C\underline{F_3}—CF_2$	$C\underline{F_2}—CH_2$	$C\underline{F_2}—CF_2$	$C\underline{F_2}—CF_3$
4	-85.4	-117.5	-128.4	129.8
6	-85.6	-117.6	-127 (broad)	130.4
8	-86.1	-117.5	-124 (broad)	130.4
10	-86.0	-117.0	-125 (broad)	130.4

Table 3.1 *Peak positions in the ^{19}F spectra of PFAC-n polymers (excluding sidebands). For $n > 4$, there are multiple contributions to the CF_2—CF_2 peak, which broadens the signal and shifts the peaks slightly downfield. Peak assignments are with respect to $CFCl_3$ and are based on Refs [102,103].*

A significant difference between the PFAC-4 and -6 spectra and the PFAC-8 and -10 spectra is the appearance of sidebands in the latter spectra, which are marked with an asterisk. Sidebands appear at integer multiples of the MAS frequency (20 kHz) away from the primary peaks and their appearance is related to the chemical shift anisotropy (CSA). This is a quantity which is averaged out by molecular motion; in liquids, the tumbling of the molecules is rapid compared to the NMR timescale and so the CSA is averaged to a single isotropic value. In solids, the comparative lack of molecular motion leads to broad peaks. To overcome the broadening effect of CSA, magic angle spinning (MAS) was used. When the spinning frequency is much larger than the CSA, the spectra appear similar to their solution-phase counterparts – as per the PFAC-4 and -6 spectra. When this condition is not fulfilled, sidebands appear – as per PFAC-8 and -10. From this, we can infer that the fluorinated side chains in PFAC-4 and -6 are more mobile than in PFAC-8 and -10. **Chapter 6** contains much more detailed analyses of the PFAC-*n* spectra, as well as introducing the concepts of chemical shift anisotropy and magic angle spinning.

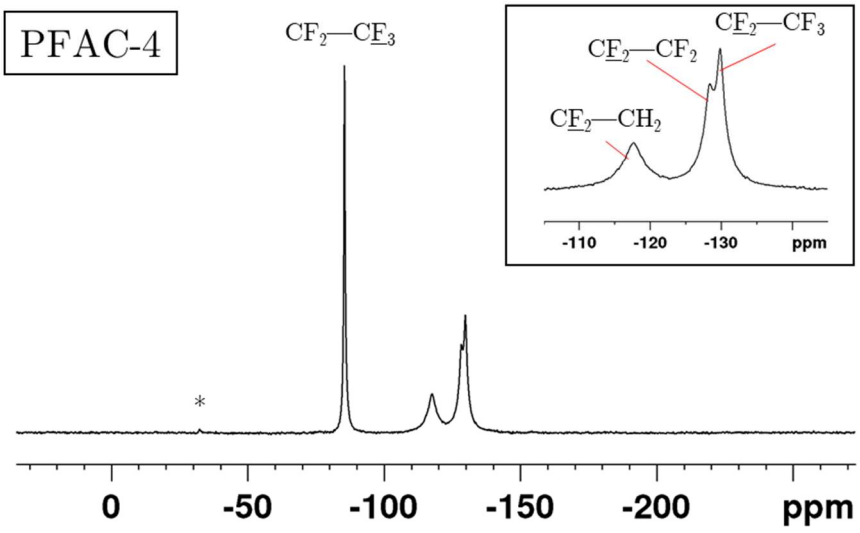


Figure 3.2 *Solid-state ^{19}F NMR spectra of PFAC-4 polymer deposited onto ground glass. The asterisks indicate sidebands, which occur at integer multiples of the magic angle spinning frequency (20 kHz) away from the primary peaks.*

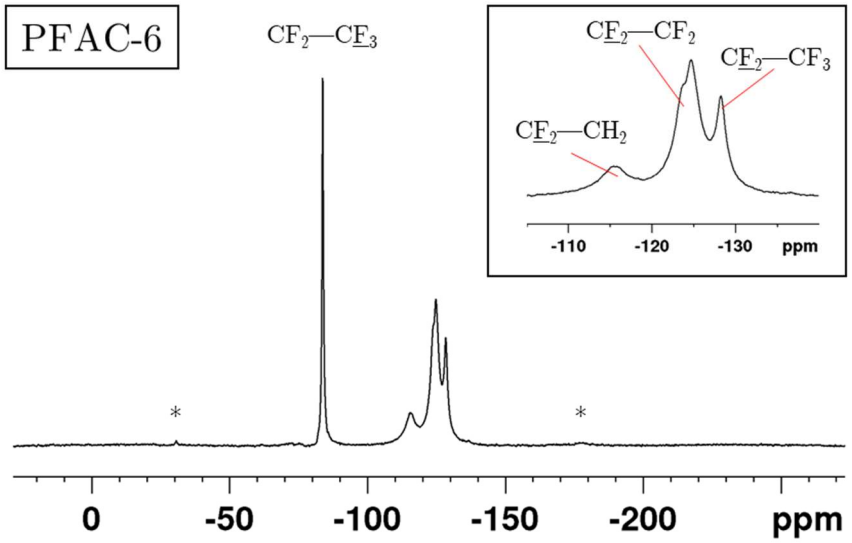


Figure 3.3 *Solid-state ^{19}F NMR spectra of PFAC-6 polymer deposited onto ground glass*

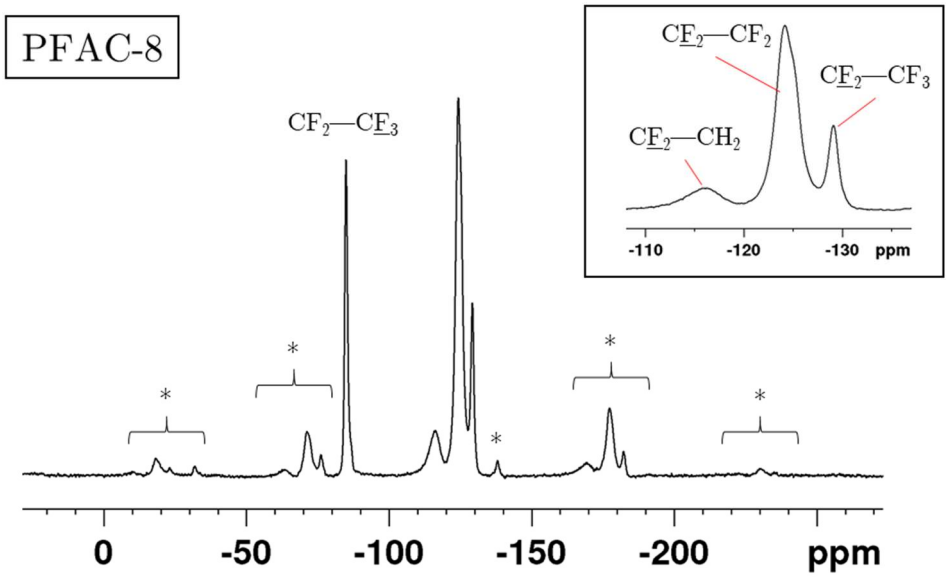


Figure 3.4 *Solid-state ^{19}F NMR spectra of PFAC-8 polymer deposited onto ground glass*

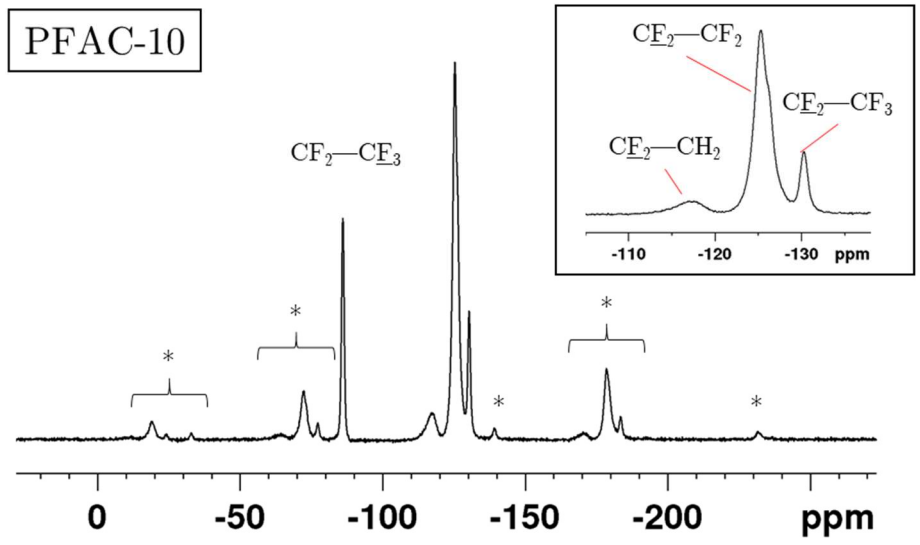


Figure 3.5 *Solid-state ^{19}F NMR spectra of PFAC-10 polymer deposited onto ground glass*

3.2.2. Chemical composition (XPS)

Figure 3.6 shows the concentrations of carbon, oxygen, and fluorine in PFAC-n polymers, as calculated from the survey spectra acquired at a take-off angle normal to the surface. The measured values are all similar to the predicted values, and in most cases are within the margin of error. This indicates that all polymers are structurally intact. PFAC-4, -6, and -8 all show a slight underabundance of oxygen, which is likely due to the orientation of the side chains. **Figure 3.7** shows the deconvoluted C(1s) spectra of the PFAC-n surfaces. Each surface contains six carbon environments; $\underline{C}F_3$, $\underline{C}F_2$, $\underline{C}$=O, $\underline{C}$—O, $\underline{C}$—CF_n, and $\underline{C}$—CH_n, the positions of which are shown in **Table 3.2**. Again, this is consistent with the PFAC-n polymers being structurally intact.

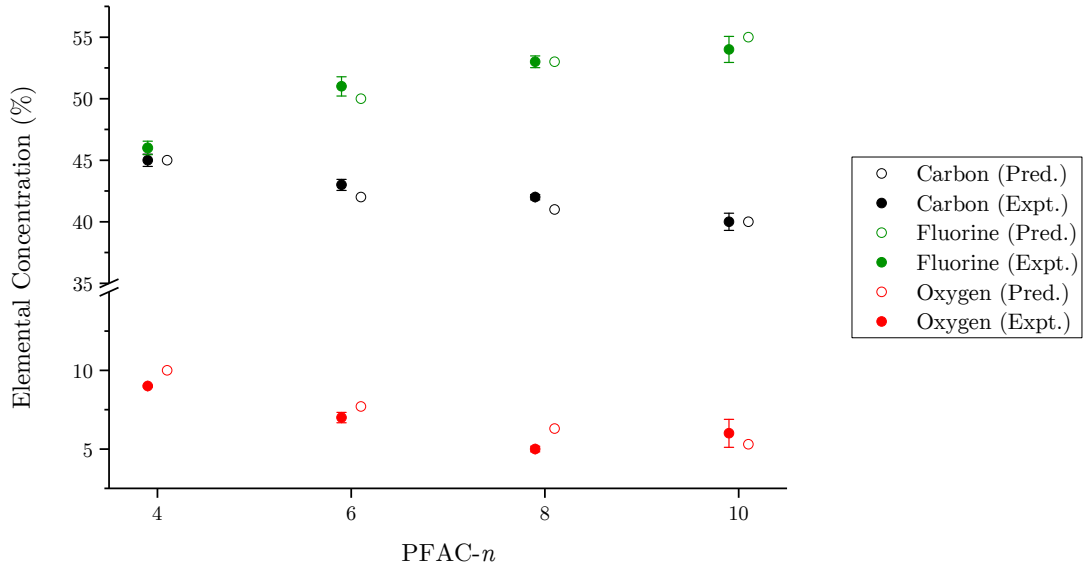


Figure 3.6 *The concentrations of carbon, fluorine, and oxygen present in PFAC-6, PFO, and PFH plasma polymers. The predicted values (open circles) are calculated assuming complete structural retention of the monomer species during polymerization, and random orientation of the polymer. The measured values (solid circles) are calculated from the areas of the 1s peaks in the XPS survey scans. Hydrogen, which is not detectable via XPS, has been excluded from both calculations. The error bars represent two standard deviations from the mean. Note that the predicted values for carbon and fluorine are identical for PFAC-4*

PFAC-*n*	Peak Position (eV)					
	CF_3 *(a)*	CF_2 *(b)*	C=O *(c)*	C—O *(d)*	$\underline{C}$—CF_n *(e)*	$\underline{C}$—CH_n *(f)*
4	293.3	291.0	288.7	286.8	285.9	285.0
6	293.4	291.2	288.9	286.8	285.8	285.0
8	293.3	291.1	288.7	286.7	285.8	285.0
10	293.2	291.1	288.7	286.8	285.8	285.0

Table 3.2 *Peak positions and assignments from the deconvoluted C(1s) XPS spectra. The hydrocarbon peak position is calibrated to be 285.0 eV. The FWHM are PFAC-4 (1.35 eV), PFAC-6 (1.44 eV), PFAC-8 (1.64 eV), and PFAC-10 (1.86 eV). The letters in superscript correspond to the marked peaks in* **Figure 3.7**

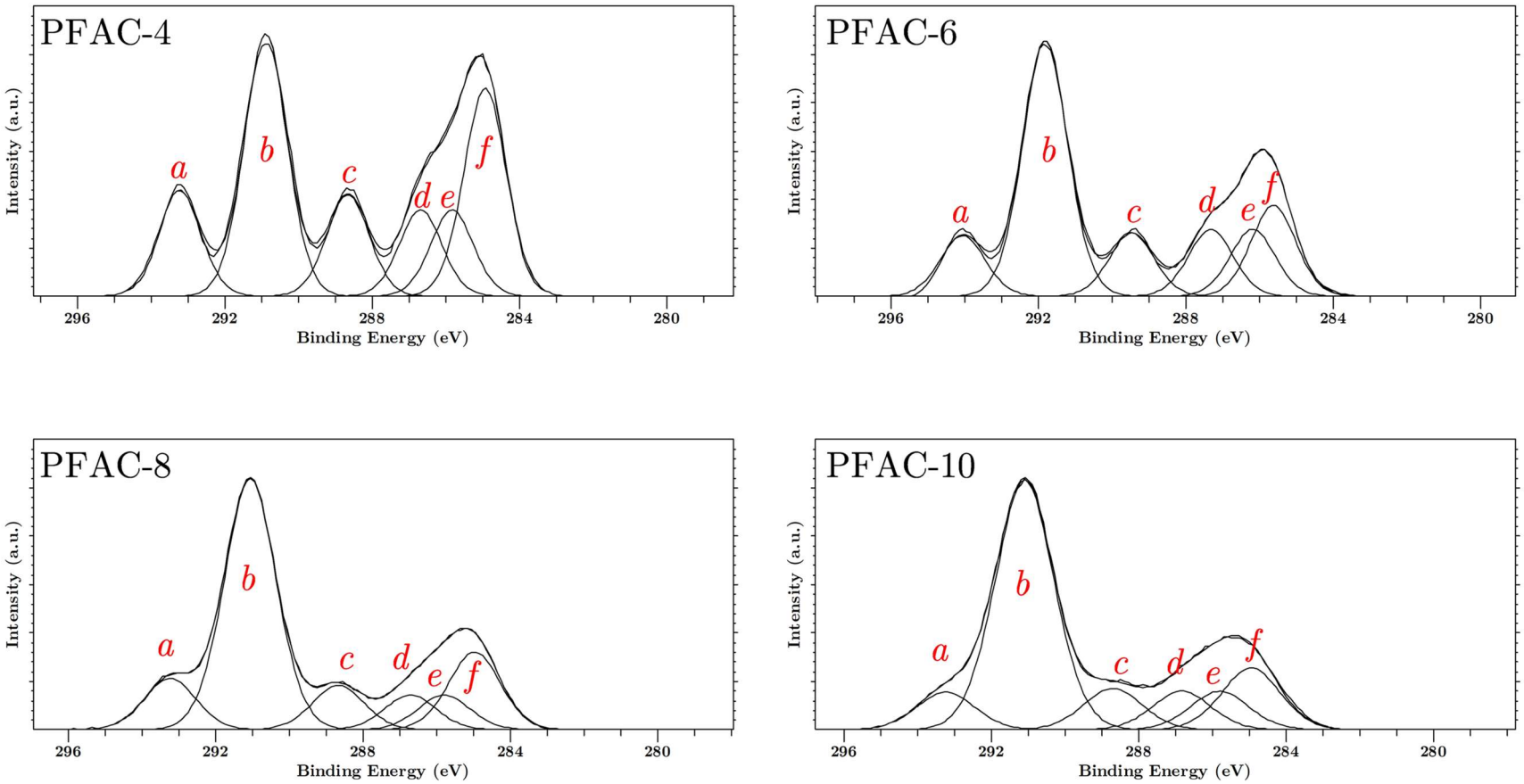


Figure 3.7 *Carbon XPS spectra of PFAC-n polymers acquired at a take-off angle of 90. The letters correspond to the peak assignments in* **Table 3.2**

Figure 3.8 and **Figure 3.9** show the angle-resolved C(1s) spectra of the PFAC-*n* surfaces, acquired in parallel at take-off angles ranging from 22.5° to 77.5° from the normal. In the PFAC-4 spectra, the appearance of a satellite peak at approximately 296 eV is immediately evident – this is a π-π* shake-up. The PFAC-4 spectral components are sharper, with a lower FWHM than the other PFAC-*n* surfaces and this peak appears as a shoulder at the upper end of the other spectra. The area under this peak is not included in any subsequent analysis.

The PFAC-6 and -10 spectra show a marked change in shape as the take-off angle is varied, with an increase in the CF_3 (~294 eV) component at shallower angles and a corresponding decrease in the CF_2 (~292 eV) and hydrocarbon (~285 eV) components. The changes in the PFAC-4 and -8 spectra are less apparent by eye. PFAC-4 shows a decrease in the hydrocarbon shoulder at the surface, as well as an increase in the height of the CF_2 (~291 eV) peak and the combined C—O/C—CF_n peak (~286 eV). By eye, PFAC-8 spectrum sees a shift toward higher binding energies, which indicates an increase in the amount of fluorinated carbon and a decrease in the hydrocarbon components.

The narrower peaks in the PFAC-4 spectra allowed for deconvolution into six different components, whilst the broader peaks in the other PFAC-*n* spectra only allowed for deconvolution into five components. In the latter case, the overlap between the $\underline{C}$—CH_n and $\underline{C}$—CF_n meant that their contributions could not be separated. **Figure 3.10** to **Figure 3.13** compare the concentrations of different carbon species with varying XPS analysis depth within each of the PFAC-*n* surfaces. **Figure 3.14** compares the concentration of individual carbon species

across all PFAC-n surfaces. As in the previous chapter, the XPS analysis depth was calculated using Eq. (2.1), assuming an inelastic mean free path of 3 nm for all of the polymers [96].

PFAC-6, -8, and -10 display very similar behaviour in terms of their variation in composition with depth. In all three cases, the concentration of CF_2 and C—H are roughly proportional to one another and both are depleted at the surface compared to the bulk. The concentration of CF_3 is approximately anti-correlated to that of CF_2 and C—H and is found in excess at the surface. Examining **Figure 3.14**, the curves for PFAC-8 and -10 for the concentration of CF_3 map onto each other almost exactly, albeit with a displacement in the y direction. Whilst the concentration of CF_3 in PFAC-8 and -10 initially decreases in an approximately linear fashion with depth, the concentration of CF_3 at the surface of PFAC-6 plateaus before starting to decrease at a sampling depth of ~1.75 nm, whereupon it follows the same curve shape as PFAC-8 and -10. In the case of the CF_2 functionality, the PFAC-6 and -8 curves map onto each other exactly, whilst the PFAC-10 curve deviates slightly for the first nm in depth, before following the same trend as PFAC-6 and -8.

PFAC-4 displays markedly different behaviour in comparison to the other three surfaces in that the variation in composition with depth is relatively modest. This is particularly apparent in the cases of CF_3 and CF_2. As in the other three cases, there is a slight excess of CF_3 at the surface although, unlike the other surfaces, there is also a slight excess of CF_2. In the case of the C—H curve, all four surfaces show similar behaviour.

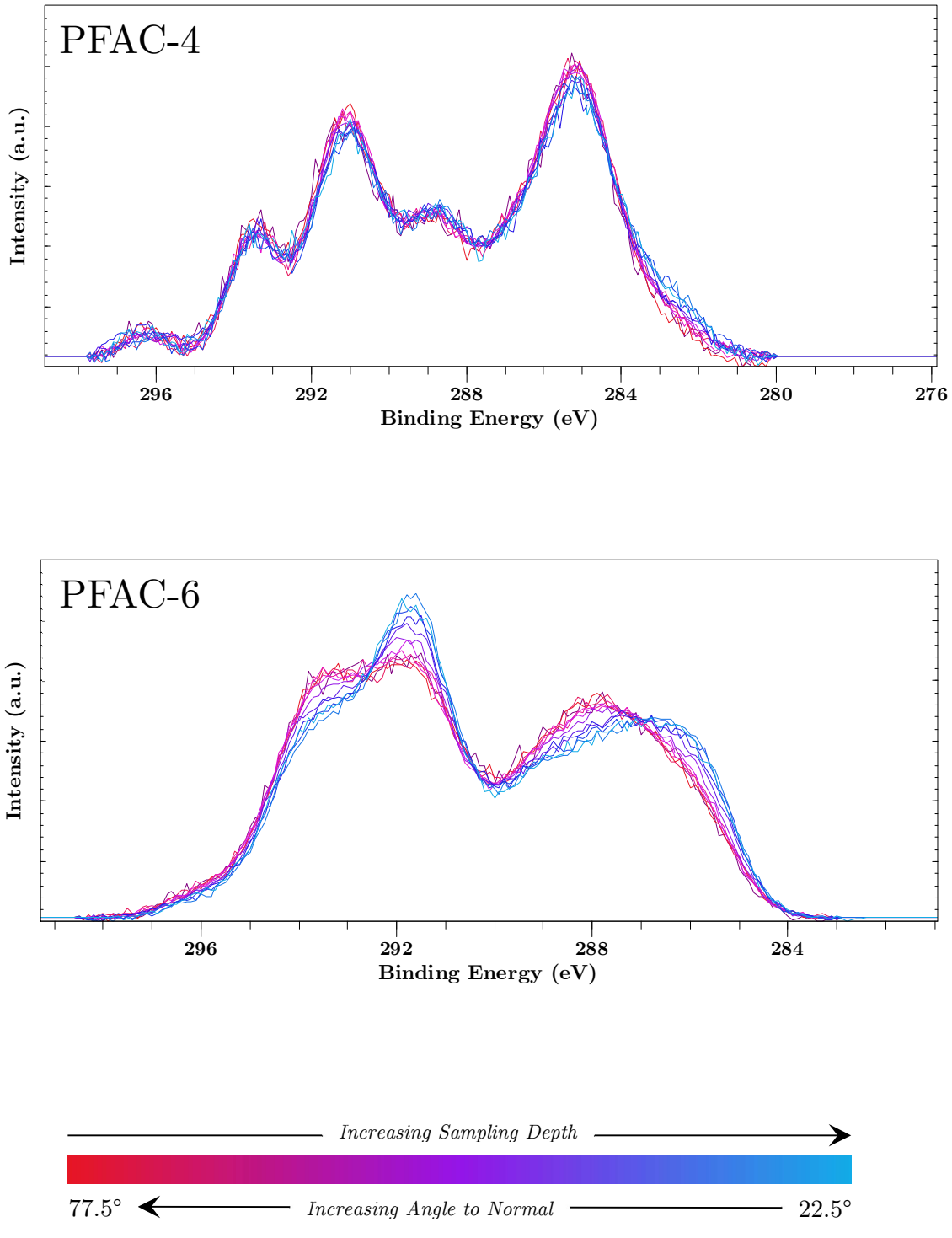


Figure 3.8 *Angle resolved carbon 1s XPS spectra of PFAC-4 and PFAC-6. Measurements were obtained in parallel at angles from 22.5° from the normal (blue, least surface sensitive) to 77.5° to the normal (red, most surface sensitive) in 5° intervals. Since the signal intensity decreases as the technique becomes more surface sensitive, the area of under the peaks was normalised.*

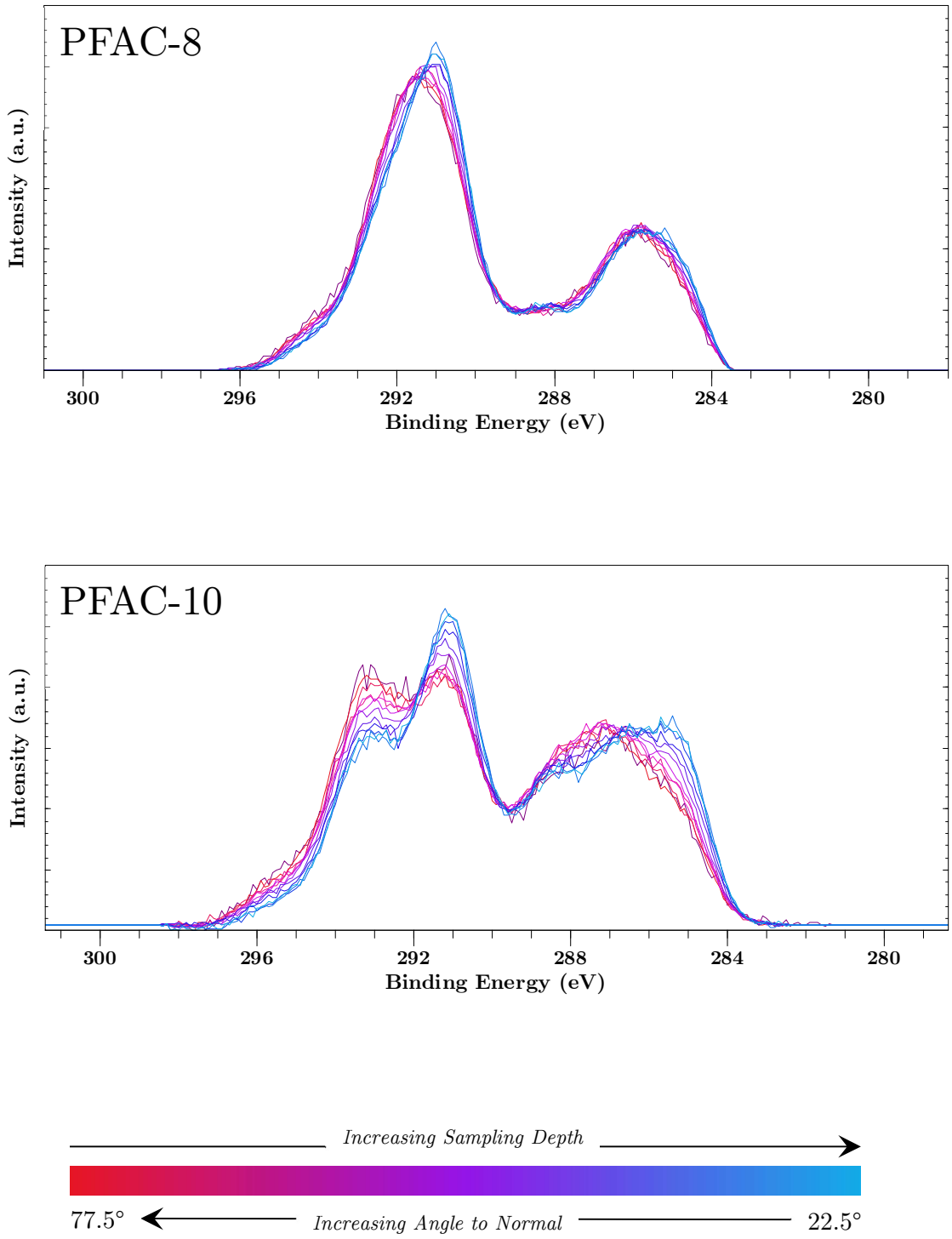


Figure 3.9 *Angle resolved carbon 1s XPS spectra of PFAC-8 and PFAC-10. Measurements were obtained in parallel at angles from 22.5° from the normal (blue, least surface sensitive) to 77.5° to the normal (red, most surface sensitive) in 5° intervals. Since the signal intensity decreases as the technique becomes more surface sensitive, the area of under the peaks was normalised.*

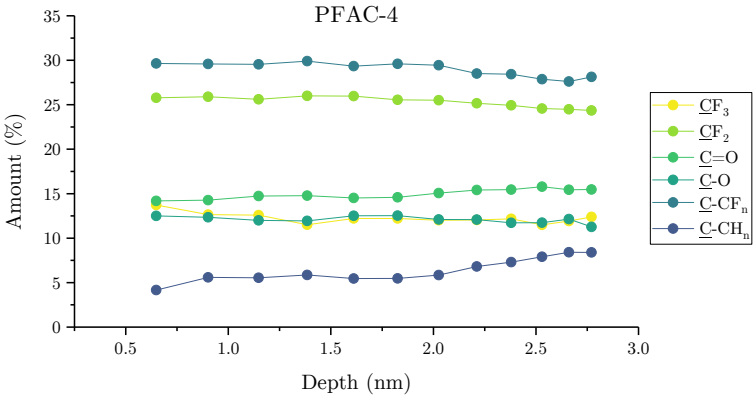


Figure 3.10 *Variation with depth of the concentration of different carbon species in a PFAC-4 surface*

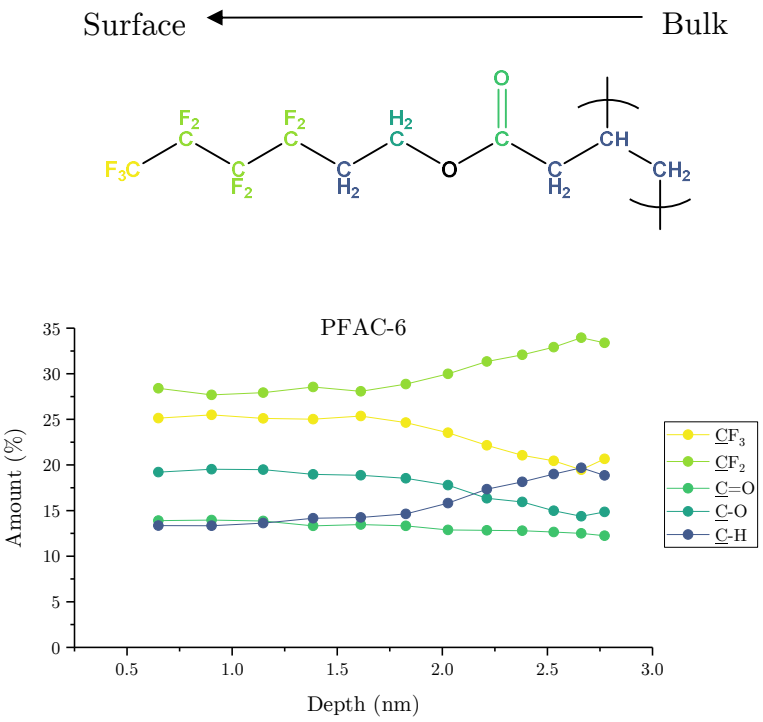


Figure 3.11 *(Top) Orientation of the PFAC-6 side chain relative to the surface (Bottom) Variation with depth of the concentration of different carbon species in a PFAC-6 surface. The colours correspond to those in the structure above*

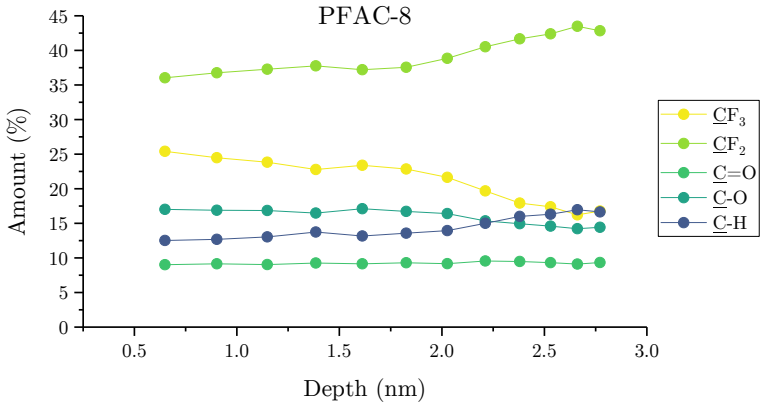


Figure 3.12 *Variation with depth of the concentration of different carbon species in a PFAC-8 surface. Note that the y axis is different in this graph spans a larger range than the others*

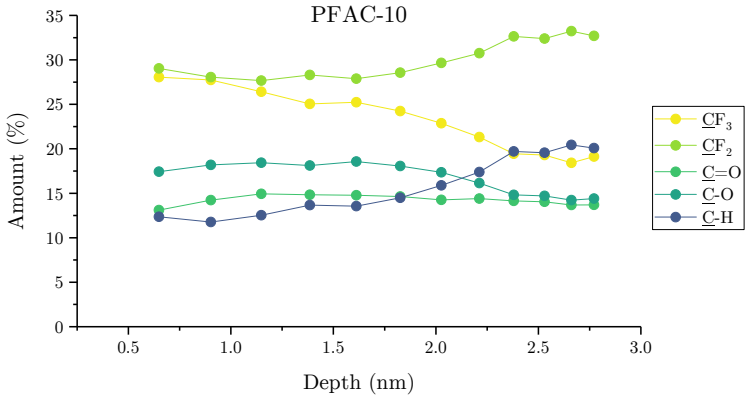


Figure 3.13 *Variation with depth of the concentration of different carbon species in a PFAC-10 surface*

The behaviour of the C=O and C—O groups is less well-defined and shows variation between the surfaces. The concentration of C=O changes little with depth across the surfaces, and the same is largely true of the behaviour of C—O. In the latter case, the concentration of C—O in the PFAC-10 surface changes more significantly across the sampling depth. **Figure 3.15** shows the relationship between the CF_3 and hydrocarbon moieties, which are located at opposite ends of the side chain. In all cases, the two curves are anti-correlated, which suggests

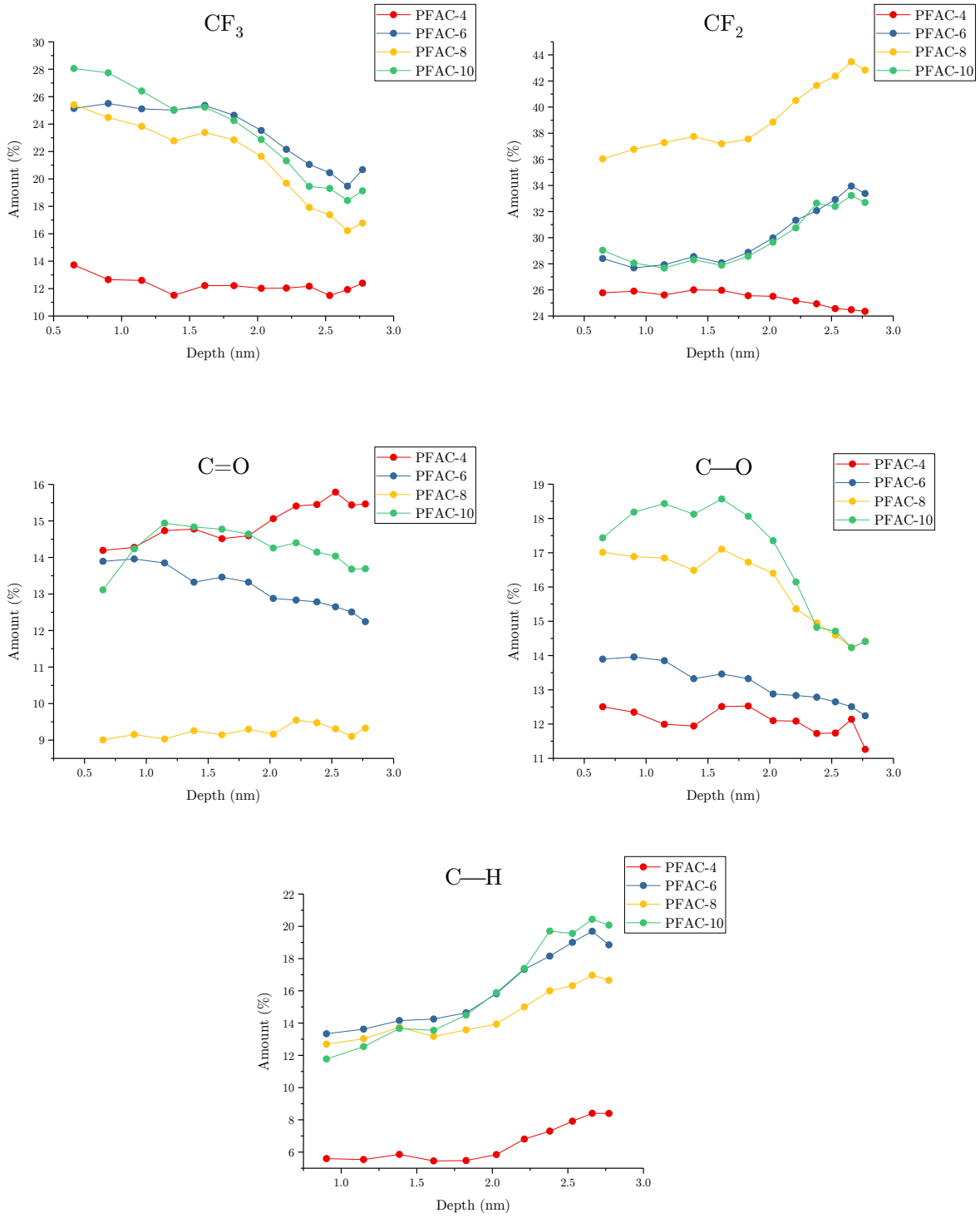


Figure 3.14 *Comparison between different polymers as to how the concentration of individual carbons species vary with depth. Note that y axes for CF_3 and CF_2 are different to the other three, although all have the same range. Lines have been added to guide the eye*

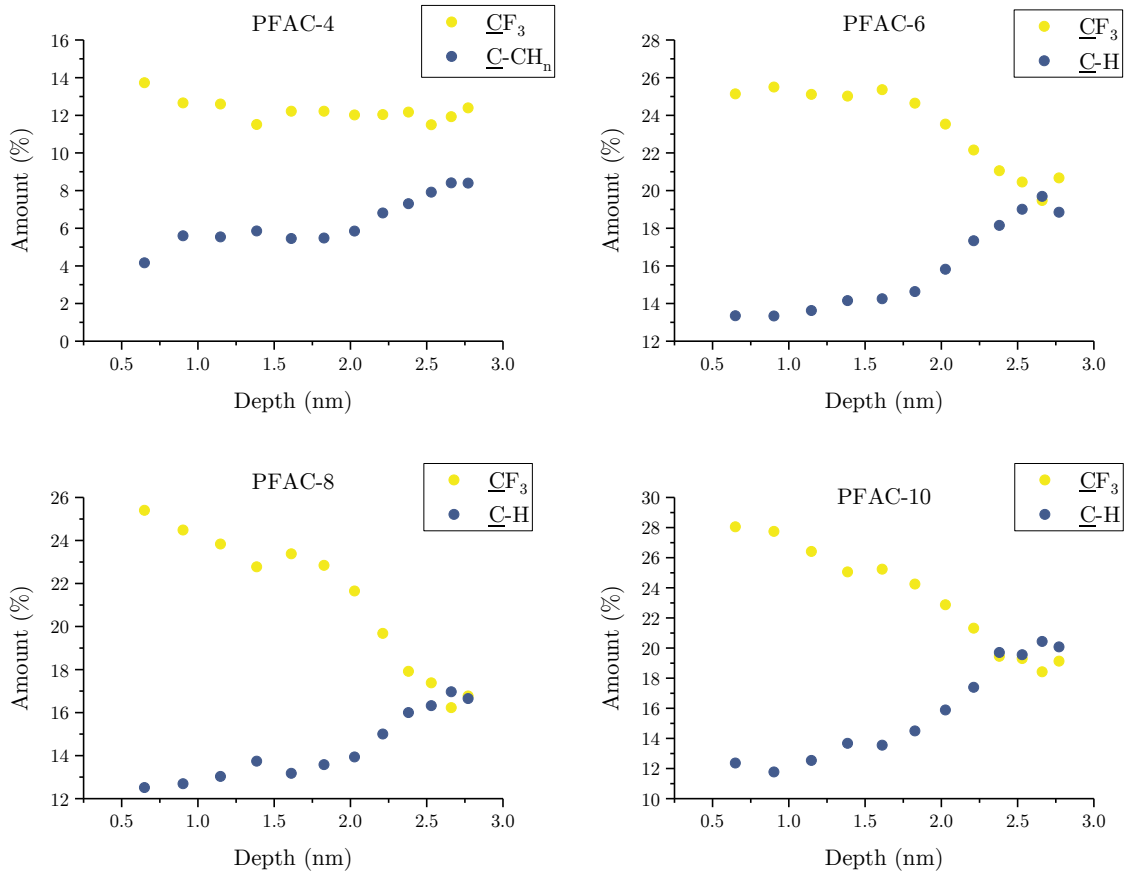


Figure 3.15 *Concentrations of CF_3 and hydrocarbon moieties with depth*

that the sidechains have a general orientation with the CF_3 groups towards the surface, and the other end of the side chain towards the bulk. However, the more complex behaviour of the oxygenated groups and the discontinuities in the concentration curves also suggest that the side chains are not aligned perfectly perpendicular to the surface. Rather, they likely possess some degree of tilt and flexibility, and variation in orientation.

3.2.3. Thermal analysis

Differential scanning calorimetry of PFAC-8 and -10 shows both irreversible and reversible phase transitions. The former appear solely in the first heating cycle, whilst the latter emerge in the second heating cycle. The trace for the first heating

cycle of PFAC-10 shows one large, continuous endothermic peak with a secondary peak at ~125 °C. The broad peak is indicative of a broad range of crystallites with variable melting temperatures. The second heating trace shows a sharper double peak between 120 and 130 °C. This is characteristic of a side-chain liquid crystal melting via a mesophase [118]. The PFAC-8 DSC trace has a low intensity peak from roughly 50 to 70 °C, followed by a sharp peak at 70 °C which also appears in the second heating trace. This indicates that the PFAC-8 has less polydispersity of crystallites than PFAC-10, and more closely resembles the annealed structure. Not visible by eye in either of the traces are minor melting transitions at -25 and 20 °C present in both polymers. PFAC-4 and -6 displayed only reversible melting transitions; both had melts at -25 and 20 °C and PFAC-4 had an additional melt at 23 °C. The smaller quantities of PFAC-4 and -6 used meant that the transitions were not visible by eye in the traces and instead the background subtracted traces are shown in **Figure 3.17** and **3.18**. The reversible phase transitions are summarised in **Figure 3.19**.

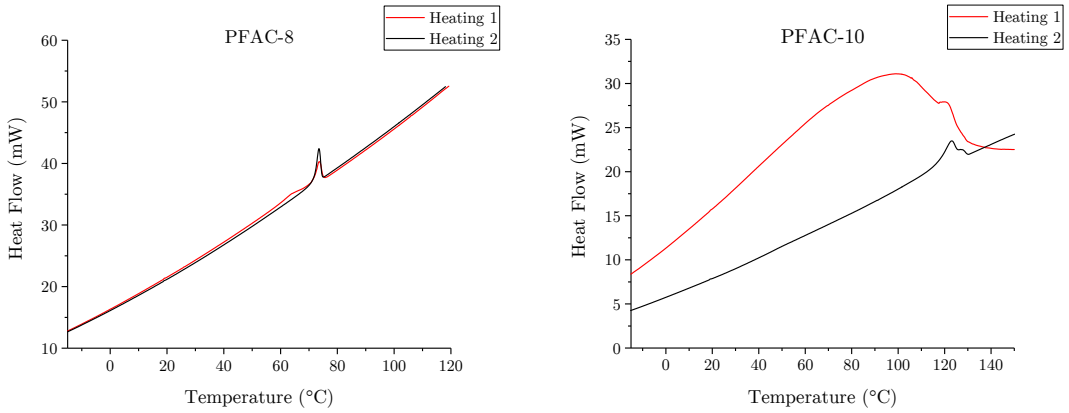


Figure 3.16 *DSC traces of PFAC-8 and -10 showing heat flow with temperature for the first (red) and second (black) heating cycles. These traces are shown endothermic up*

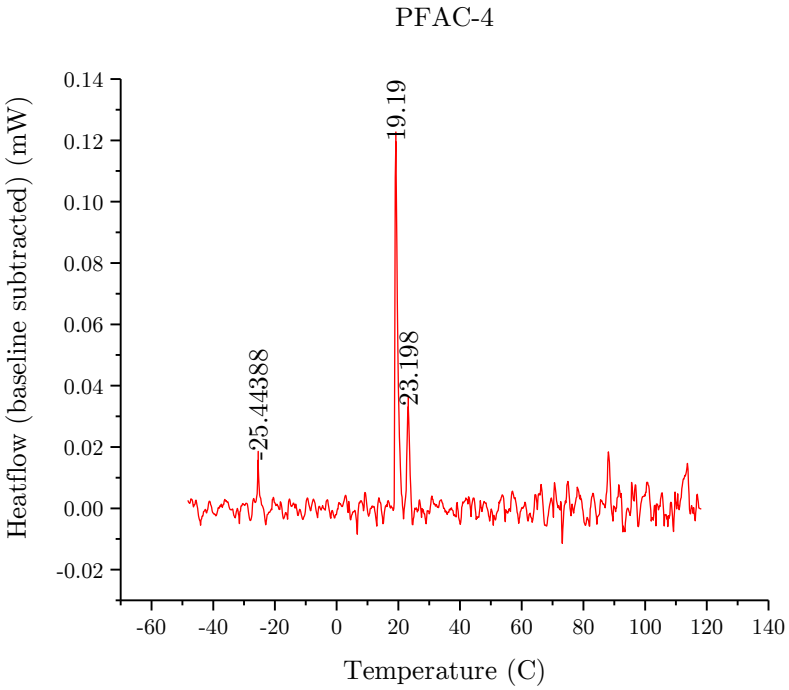


Figure 3.17 *Background subtracted DSC trace of PFAC-4*

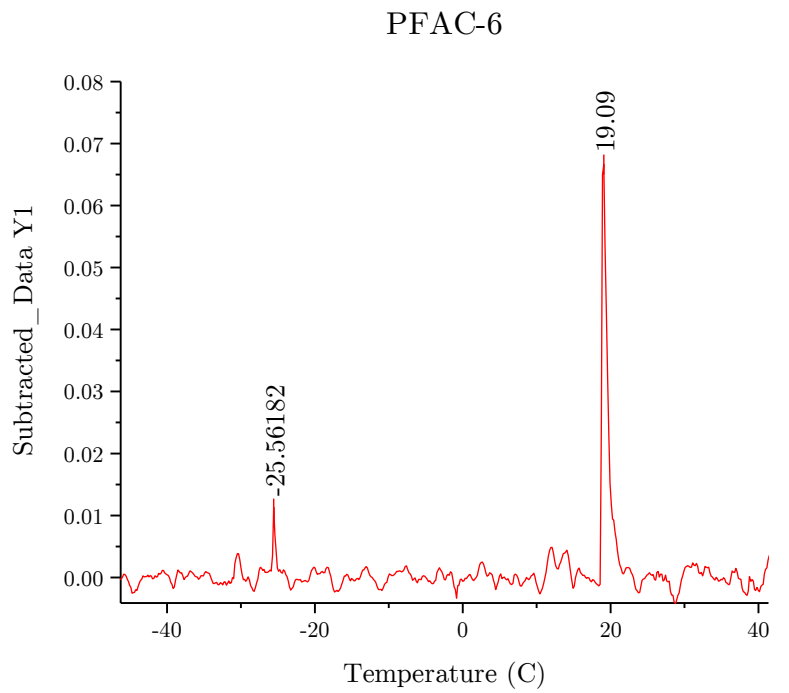


Figure 3.18 *Background subtracted DSC trace of PFAC-6*

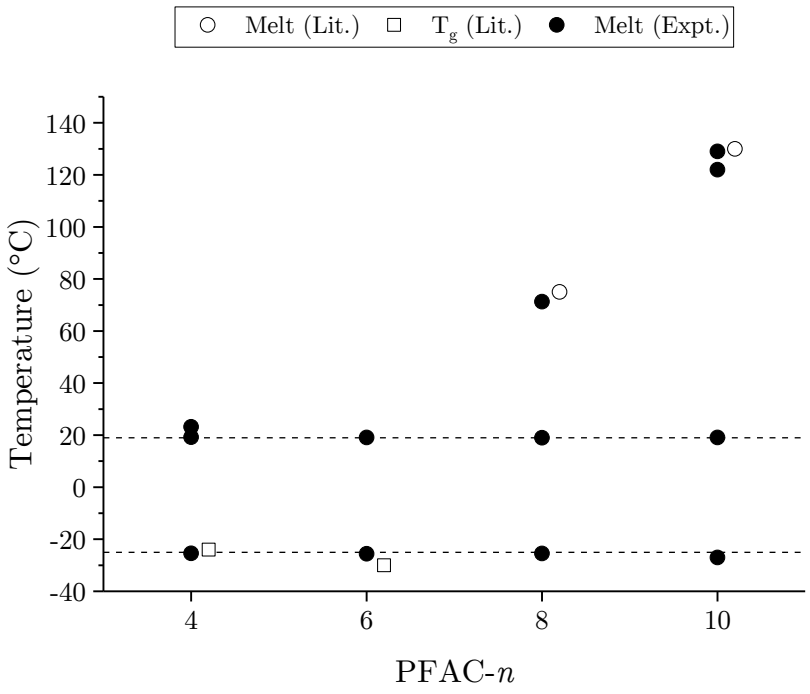


Figure 3.19 *Temperatures of the reversible melts in each of the PFAC-n polymers. The literature values are from Ref [84]*

3.2.4. Topography

Figure 3.20 and **Figure 3.21** show AFM micrographs and cross sections of PFAC-8 and –10 respectively. The root mean square (RMS) roughness of these micrographs are 38 nm (PFAC-8) and 34 nm (PFAC-10). The features on both surfaces are globular but differ in both in terms of size and distribution; the features on the PFAC-10 surface have a larger polydispersity in terms of both lateral and vertical dimensions and are less evenly distributed than on the PFAC-8 surface.

Figure 3.22 shows the phase data obtained at the same time as the topographical data in **Figure 3.20**. The homogeneity of the phase data indicates that the composition of the surface is similarly homogenous, with full coverage of the underlying glass substrate. Although not shown here, the phase data acquired

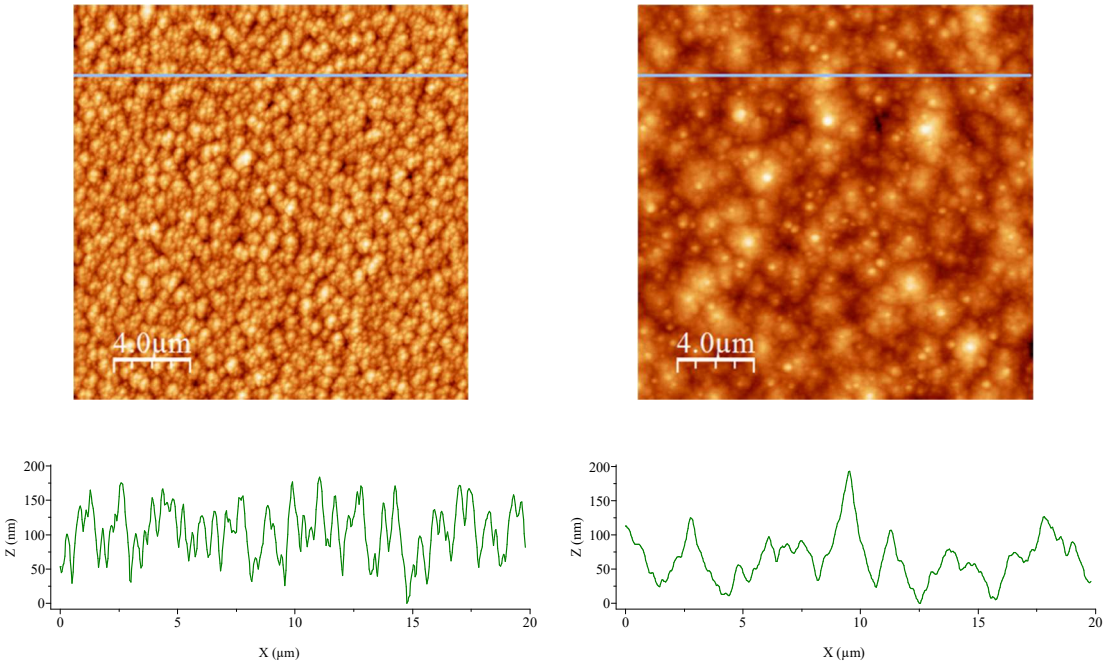


Figure 3.20 *A 20x20 µm² AFM micrograph and section profile of PFAC-8. The z scale of the micrograph is 300 nm*

Figure 3.21 *A 20x20 µm² AFM micrograph and section profile of PFAC-10. The z scale of the micrograph is 300 nm*

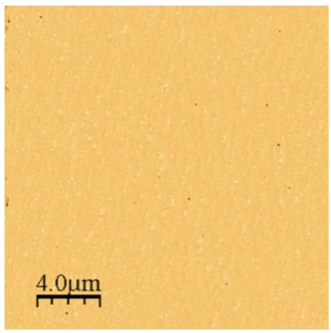


Figure 3.22 *The phase data associated with the AFM micrograph in Figure 2.2. The z scale is 180°*

for the PFAC-10 surfaces was similarly lacking in contrast and the same conclusions regarding composition and coverage may be drawn.

Attempts to measure the topography of PFAC-4 and PFAC-6 using AFM were unsuccessful, and the results are therefore not shown. The micrographs obtained were flat and featureless to within the noise level of the instrument. Differential

scanning calorimetry (DSC) measurements, which are discussed in detail in Chapter 3, indicate that both PFAC-4 and -6 undergo melting transitions at and/or below room temperature and so these surfaces were too soft to acquire meaningful measurements, even when using a cantilever with a low spring constant (3 Nm^{-1}).

3.2.5. Surface energy and wetting properties

Figure 3.23 and **Figure 3.24**. show the advancing (θ_{adv}) and receding (θ_{rec}) contact angles of water and DD respectively on PFAC-n surfaces. The error bars, which represent one standard deviation from the mean across fifteen measurements (five measurements on three surfaces) are dominated by the differences between individual surfaces, rather than the variation between the measurements on a single surface. For water, θ_{adv} is similar for PFAC-4, 6, and 8, and fall at ~140° whilst PFAC-10 displays a lower θ_{adv} of ~120°. For DD, θ_{adv} increases on going from $n = 4$ to $n = 6$, and then decreases as n increases. The difference in behaviour between water and DD is similar to that in the previous chapter (**Section 2.2.4**) where the higher surface tension water had achieved its maximum contact angle, but the DD had not. Again, this suggests that the wetting is in the Wenzel regime. The contact angle hysteresis on PFAC-4 and PFAC-6 is considerably larger than on the other two surfaces.

Table 3.3 shows the surface energy of the polymers calculated using the OWRK method. As per the previous chapter, it is emphasised that this is an *effective* surface energy, rather than the true, equilibrium value. The total surface energies decrease in the order $n = 10 \approx 4 > 8 > 6$. The dispersive components dominate

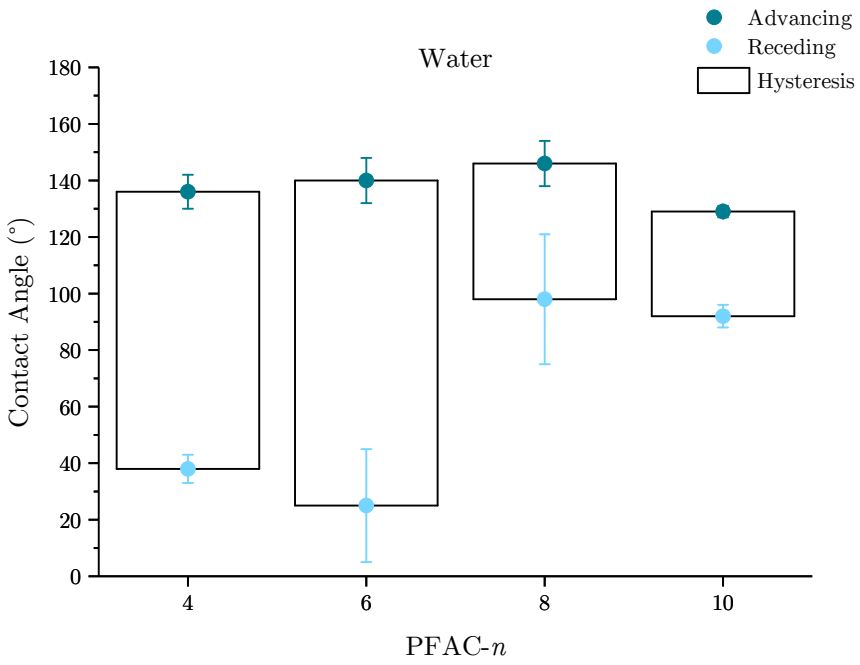


Figure 3.23 *Advancing (dark) and receding (light) contact angles of water on PFAC-n. The contact angle hysteresis, which is the difference between the advancing and receding contact angles is shown as a floating bar. The error bars correspond to one standard deviation from the mean*

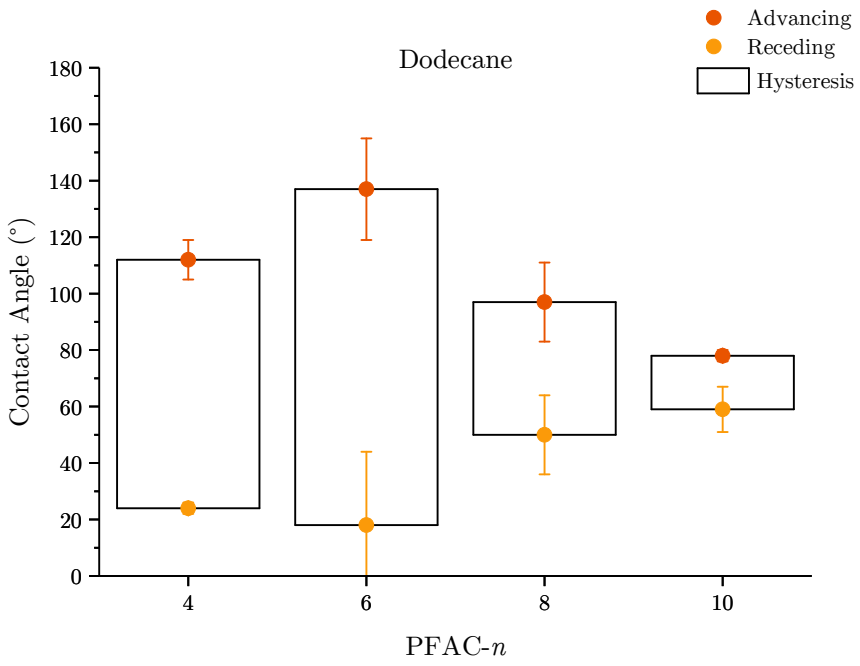


Figure 3.24 *Advancing (dark) and receding (light) contact angles of water on PFAC-n. The contact angle hysteresis, which is the difference between the advancing and receding contact angles is shown as a floating bar. The error bars correspond to one standard deviation from the mean*

in all cases, although PFAC-4 has a larger polar component (2 mJ m^{-2}) than the other surfaces.

Material	γ_{SV} (mJ m^{-2})	γ_{SV}^{p} (mJ m^{-2})	γ_{SV}^{d} (mJ m^{-2})
PFAC-4	12	10	2
PFAC-6	8	7.5	0.5
PFAC-8	10	9.5	0.5
PFAC-10	12.5	11.5	1

Table 3.3 *Surface energies of PFAC-n polymers as calculated using the OWRK method*

3.2.6. Discussion

The optimum configuration for the fluoroalkyl chains in PFAC-*n* polymers in terms of lowering surface energy is one where the side chains are crystallised perpendicular to the surface, creating a layer of hexagonally close packed CF_3 moieties at the surface [34,119]. This is the smectic B structure and is shown in **Figure 3.25**. The DSC data indicates rather complex phase behaviour and does not lend itself to the conclusion that any of the side-chains crystallise into this structure (although the side chains in PFAC-8 and -10 crystallise after the first heating cycle). All four polymers undergo minor melting transitions at -25 and +20 °C, which are assigned as being a property of the backbone rather than the side chain and thus occur at the same temperature for all values of *n*. PFAC-4 undergoes a reversible melting transition at 23 °C, whilst there is no evidence of any other phase transitions in the PFAC-6 polymer. The side chains for PFAC-4 and -6 therefore appear to be liquid at or near room temperature. PFAC-10 contains a broad range of crystallites, which melt at a broad range of temperatures from below 0 °C to 120 °C. The behaviour of PFAC-10 may

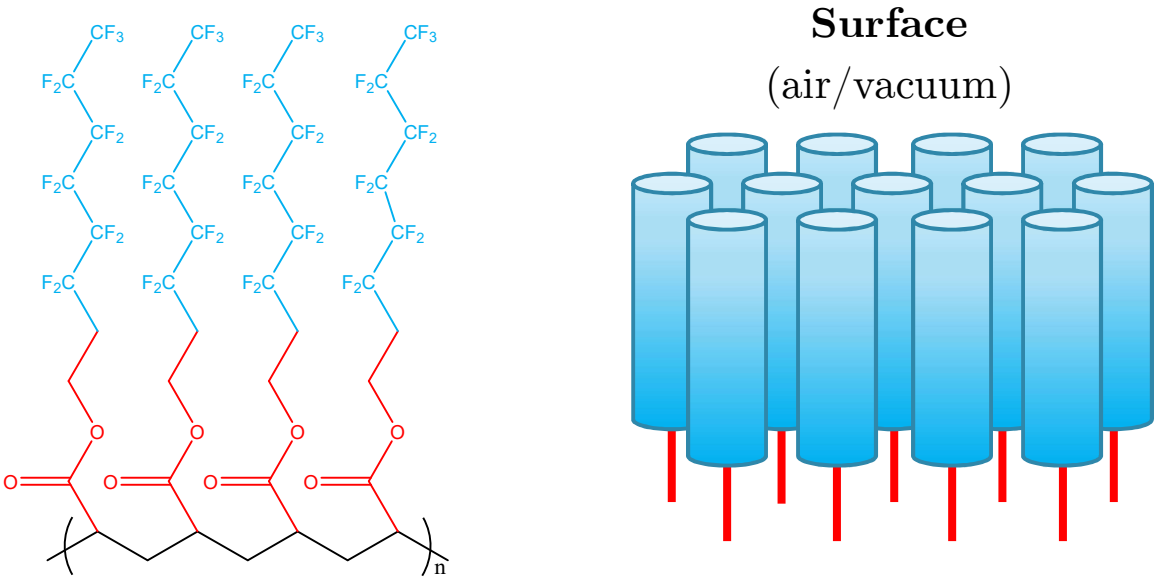


Figure 3.25 *(L) Structure of PFAC-6; the perfluoroalkyl groups is shown in blue, the acrylate group in red, and the polymeric backbone in black (R) Crystalline smectic B structure of PFAC-n; the fluorocarbon is represented as a rigid cylinder and the acrylate spacer group is shown in red. The polymeric backbone is not shown*

be because it is deposited considerably below the reversible melting temperature of the polymer, and so it cannot adopt its equilibrium morphology. The phase behaviour of PFAC-8 more closely resembles that of the solution-synthesized polymer, although there are still low intensity broad peaks which indicate crystalline impurities. Given that all four polymers undergo one or more melting transitions near or below room temperature, the possibility of surface reconstruction cannot be ruled out and this will be subject to investigation in the following chapters.

The angle-resolved XPS data is rather complex and not entirely straightforward to interpret. The CF_3 and C—H peaks appear at upper and lower extremes of binding energy in the C(1s) spectra and their peak positions are easy to ascertain. The changes in intensity of these peaks are also visible by eye in the raw spectra shown in **Figure 3.8** and **Figure 3.9**. The CF_2 peak is the most intense peak in

all cases, which allows the peak position to be determined and, again, changes in intensity are visible by eye in the raw data. However, there is only 0.7 eV difference in binding energy between the $\underline{C}H_n$—CH_n and $\underline{C}H_n$—CF_n peaks, which prevented them being resolved separately in the analysis of PFAC-6, -8, and -10, and a 1 eV difference between the $\underline{C}H_n$—CF_n peak and C—O peak. The lower signal intensity of the angle-resolved spectra compared to conventional XPS, particularly at grazing angles, results in peaks with a larger FWHM; ~2 eV in the case of the PFAC-*n* surfaces. There is therefore more scope for error in determining the concentration of the oxygenated carbons. It should also be noted that the high angular resolution in this study is at the expense of signal intensity.

There have been a number of studies using angle-resolved XPS to examine the orientation of fluorinated side chains [87,112,113,120,121], as well as using techniques such as near-edge X-ray absorption fine structure (NEXAFS) [122-124] and wide-angle X-ray diffraction (WAXD) [84,85,116,119,125]. These studies have shown segregation of CF_3 at the surface for a wide range of fluorocarbon surfaces, including polymers and self-assembled monolayers with a variety of chain lengths, spacer groups, and polymerizable groups. Previous studies on PFAC-4 suggest that the lower cohesion between the shorter chains leads to a lower propensity for the fluoroalkyl chains to orient themselves preferentially at the surface; this was found to be the case [115,121]. The PFAC-6, -8, and -10 surfaces all displayed significant preferential arrangement of the CF_3 groups at the surface. The relationship between the CF_3, CF_2, and C—H moieties suggests that the fluoroalkyl chains are ordered with the CF_3 at the surface, and the hydrocarbon near the backbone buried in the bulk. This is in line with the

findings in the aforementioned studies. However, the concentrations of the C—O and the C=O functionalities, which are adjacent to the hydrocarbon groups, should follow the same trend as the concentration of C—H; this is not the case, and somewhat confuses the picture. Unfortunately, most other studies have focussed on the CF_3 and CF_2 functionalities. One study by Beamson *et al.* on polymers with fluoroalkyl side chains containing ester linkages to the backbone found that the C=O content followed the same trend as C—H [113]. Most angle-resolved XPS studies have performed measurements at only two or three different take-off angles, and so the detailed depth profiling of the different functionalities in this study is presented here for the first time. It is particularly interesting that the profiles for the same functional groups in the PFAC-6, -8 and -10 surfaces should match each other so exactly; this aspect merits further investigation.

In terms of wetting behaviour and surface energy, studies on smooth PFAC-*n* surfaces produced in the solution phase have shown that these have surfaces energies starting at 12 mJ m^{-2} for PFAC-4 and decreasing with increasing chain length to 6-8 mJ m^{-2} for PFAC-10 [84,115]. The latter value is for fluoroalkyl chains arranged in a smectic B phase as shown in **Figure 3.25** [34]. The higher value for PFAC-4 reflects the inability of the shorter side chains to crystallise [119] and the greater proximity of the ester group to the surface [121]. The behaviour reported in this investigation is different, with the surface energy decreasing upon transitioning from $n = 4$ (12 mJ m^{-2}, which matches literature values) to $n = 6$ (8 mJ m^{-2}), and then increasing upon transitioning from to $n = 8$ (10 mJ m^{-2}) and then to $n = 10$ (12 mJ m^{-2}). The higher value for PFAC-4 is justified by the relatively modest degree of surface segregation of CF_3 groups

compared to the other three. To rationalise the other three (n = 6, 8, 10), a justification is need for the surface energy minimum at $n = 6$, and the larger than expected value at $n = 10$. First, it must be borne in mind that these are not ideal surfaces; PFAC-8 and -10 are not smooth (as seen in the AFM images), and the differences in *apparent* surface energy may be the effect of the topography on the contact angle. PFAC-8 has a slightly larger RMS roughness and sharper asperities than PFAC-10. PFAC-6 was smooth as measured by AFM, although this does not entirely rule out the presence of extremely soft features on the surface. Furthermore, pinning of the triple phase line can occur on both physical asperities, and regions of chemical heterogeneity [38,43,109], and so regions of exposed polar groups under the drop may result in higher contact angles and larger contact angle hysteresis. Secondly, from a chemical perspective, examination of the concentration of CF_3 in the near surface region of PFAC-6, PFAC-8, and PFAC-10 revealed a thicker layer of CF_3 groups in the PFAC-6 surface than the other two (**Figure 3.14**); thus the lower apparent surface energy of PFAC-6 may be a real (i.e chemical, rather than topographical) effect. PFAC-10 also displayed an excess of C—O at the surface, which could increase its surface energy. Unfortunately, it is not possible to separate out all of these contributions to the measured surface energy and they may also act concurrently.

Where the pinning of the triple phase line occurs due to chemical heterogeneity, the question arises as to whether this heterogeneity is present in air (or vacuum), or whether it is triggered by the presence of the liquid. Previous work on smooth, annealed PFAC-n surfaces found that these surfaces underwent reconstruction when exposed to water such that the acrylate groups migrated to the surface [84].

The PFAC-n surface directly under the liquid and at the triple phase line therefore had high adhesion to the liquid whilst the area ahead of the drop had lower adhesion, resulting in pinning and a large contact angle hysteresis. Similar behaviour has been observed on other fluoropolymer surfaces [108,126], and surface reconstruction could explain the large contact angle hystereses displayed by the PFAC-4 and -6 surfaces in comparison to PFAC-8 and -10. The concept of surface reconstruction of PFAC-n will be explored in more detail in the next chapter.

3.3. Conclusions

PFAC-n polymers ($n = 4, 6, 8, 10$) were successfully synthesized via pulsed plasma polymerization. The polymers were shown to be structurally intact with good retention of chemical functionality. Angle-resolved XPS demonstrated preferential segregation of CF_3 at the polymer surfaces and was used to perform depth-profiling of the different carbon environments. DSC measurements showed that PFAC-4 and -6 are liquid at room temperature, whilst PFAC-8 and -10 are solid. The phase behaviour of PFAC-4 and -6 meant it was not possible to acquire AFM images of these surfaces, whilst PFAC-8 and -10 were found to have an RMS roughness of 35-40 nm. The surface energy of the polymers was measured and was found to exhibit the trend PFAC-4 $\approx$ PFAC-10 $>$ PFAC-8 $>$ PFAC-6; this is contrary to previous work on solution-synthesized PFAC-n which has demonstrated a decrease in surface energy with increasing side chain length. PFAC-4 and -6 were found to have larger contact angle hystereses, and it is hypothesised that this is a consequence of surface reconstruction, a phenomenon which will be investigated in the next chapter.

3.4. References

[8] V. Kumar, J. Pulpytel, H. Rauscher, I. Mannelli, F. Rossi, and F. Arefi-Khonsari, Plasma Processes and Polymers **7**, 926 (2010).

[34] T. Nishino, M. Meguro, K. Nakamae, M. Matsushita, and Y. Ueda, Langmuir **15**, 4321 (1999).

[38] A. B. D. Cassie and S. Baxter, Transactions of the Faraday Society **40**, 546 (1944).

[43] V. Kumar and J. R. Errington, Langmuir **29**, 11815 (2013).

[77] S. R. Coulson, I. S. Woodward, J. P. S. Badyal, S. A. Brewer, and C. Willis, Chemistry of Materials **12**, 2031 (2000).

[82] M. P. Krafft and J. G. Riess, Current Opinion in Colloid & Interface Science **20**, 192 (2015).

[83] S. Merenyi, *REACH: Regulation (EC) No 1907/2006: Consolidated Version (June 2012) with an Introduction and Future Prospects Regarding the Area of Chemicals Legislation* (GRIN Verlag, 2012), Vol. 2.

[84] K. Honda, M. Morita, H. Otsuka, and A. Takahara, Macromolecules **38**, 5699 (2005).

[85] K. Honda, M. Morita, O. Sakata, S. Sasaki, and A. Takahara, Macromolecules **43**, 454 (2009).

[86] V. Kumar, J. Pulpytel, and F. Arefi-Khonsari, Plasma Processes and Polymers **7**, 939 (2010).

[87] A. M. Coclite, Y. Shi, and K. K. Gleason, Advanced Functional Materials **22**, 2167 (2012).

[96] P. J. Cumpson, Surface and Interface Analysis **31**, 23 (2001).

[102] E. Katoh, H. Sugimoto, Y. Kita, and I. Ando, Journal of Molecular Structure **355**, 21 (1995).

[103] J. Emsley and L. Phillips, Progress in Nuclear Magnetic Resonance Spectroscopy **7**, 1 (1971).

[108] H. Tavana, D. Jehnichen, K. Grundke, M. L. Hair, and A. W. Neumann, Advances in Colloid and Interface Science **134**–**135**, 236 (2007).

[109] A. J. B. Milne and A. Amirfazli, Advances in Colloid and Interface Science **170**, 48 (2012).

[112] R. Bongiovanni, G. Beamson, A. Mamo, A. Priola, A. Recca, and C. Tonelli, Polymer **41**, 409 (2000).

[113] G. Beamson and M. Alexander, Surface and Interface Analysis **36**, 323 (2004).

[114] Q. Wang, Q. Zhang, X. Zhan, and F. Chen, Journal of Polymer Science Part A: Polymer Chemistry **48**, 2584 (2010).

[115] K. Honda, I. Yamamoto, M. Morita, H. Yamaguchi, H. Arita, R. Ishige, Y. Higaki, and A. Takahara, Polymer **55**, 6303 (2014).

[116] H. Yamaguchi, M. Kikuchi, M. Kobayashi, H. Ogawa, H. Masunaga, O. Sakata, and A. Takahara, Macromolecules **45**, 1509 (2012).

[117] M. Gupta and K. K. Gleason, Langmuir **22**, 10047 (2006).

[118] C. B. McArdle, *Side Chain Liquid Crystal Polymers* (Springer Science & Business Media, 1990).
[119] J. Wang, G. Mao, C. K. Ober, and E. J. Kramer, Macromolecules **30**, 1906 (1997).
[120] S. Nojima, T. Shinohara, Y. Higaki, R. Ishige, T. Ohishi, D. Kobayashi, H. Setoyama, and A. Takahara, Polymer Journal **46**, 637 (2014).
[121] M. Stone, T. G. Nevell, and J. Tsibouklis, Materials Letters **37**, 102 (1998).
[122] J. Genzer and K. Efimenko, Science **290**, 2130 (2000).
[123] J. Genzer, E. Sivaniah, E. J. Kramer, J. Wang, M. Xiang, K. Char, C. K. Ober, R. A. Bubeck, D. A. Fischer, M. Graupe, R. Colorado, O. E. Shmakova, and T. R. Lee, Macromolecules **33**, 6068 (2000).
[124] J. Genzer, E. Sivaniah, E. J. Kramer, J. Wang, H. Körner, K. Char, C. K. Ober, B. M. DeKoven, R. A. Bubeck, D. A. Fischer, and S. Sambasivan, Langmuir **16**, 1993 (2000).
[125] V. V. Volkov, N. A. Platé, A. Takahara, T. Kajiyama, N. Amaya, and Y. Murata, Polymer **33**, 1316 (1992).
[126] R. David and A. W. Neumann, Advances in Colloid and Interface Science **206**, 46 (2014).

4. Thermal Behaviour and Adaptive Wetting of Fluoroalkyl Acrylate Polymers

The concept of surface reconstruction was first introduced in the **Aim of Study** in the context of replacing C8 perfluorinated polymers with shorter chain analogues. Work by Honda *et al.* has shown that PFAC-n polymers with $n < 8$ synthesized in the solution phase undergo surface reconstruction when exposed to water, resulting in the migration of the acrylate groups to the surface and an overall increase in surface energy [84,85]. Questions arise as to whether the plasma polymers will behave in the same way as those synthesized in solution, and also as to what stimuli might trigger surface reconstruction. Whilst the work by Honda *et al.* focussed on the role of polar liquids at room temperature, this investigation will also investigate non-polar liquids and the effect of temperature.

Up until this point, surface reconstruction has been described in terms of loss of desirable functionality – in this investigation, of hydrophobicity. However, there are many cases where surface reconstruction in response to a particular stimulus – temperature, electric potential, humidity, or certain liquids – is a useful attribute [127-132]. These so-called 'smart surfaces' are useful in a wide variety of contexts, including drug delivery [133,134], oil-in-water separation [6,135,136], anti-biofouling [137,138], and numerous other applications.

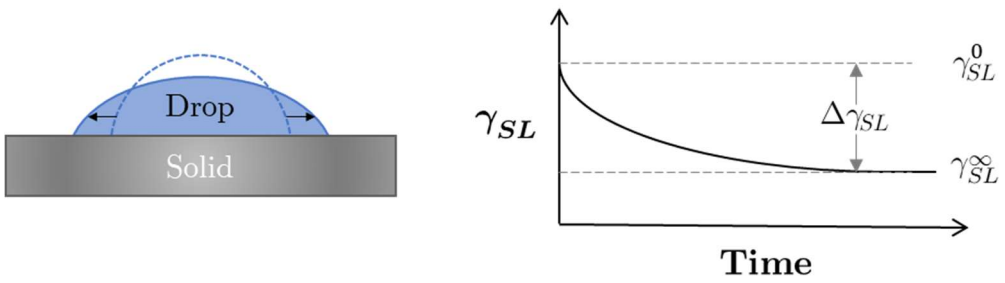


Figure 4.1 Left: *Sessile drop spreading spontaneously on an adaptive surface. The dashed line represents the profile at $t = 0$ and the solid line represents the profile at $t = \infty$* **Right***: The change in interfacial energy with time associated with the spreading of the drop. Adapted from Ref. [139]*

Butt *et al.* recently proposed a model for adaptive surfaces which spontaneously change in the presence of liquids or vapours [139]. Change in this context may be surface reconstruction, but may also refer to swelling of the polymer [140-143], adsorption of vapour/liquid on the surface (or replacement of adsorbed species) [107,144,145], surfactants binding at both the solid-liquid and liquid-vapour interfaces [146,147], and ordering of the liquid molecules at the solid-liquid/liquid-vapour interfaces [148,149]. These effects may be concurrent, and it may not be possible to separate out these effects. The timescale of adaptive processes is characteristic of the system, and measurements of surface properties such as wetting will necessarily mirror this timescale. Since the change induced by the liquid is spontaneous, the interfacial tension of the solid-liquid interface is lowered[§] and the contact angle decreases. **Figure 4.1** shows a sessile drop spreading on adaptive surface and the associated change in surface energy, $\Delta\gamma_{SL}$. The surface energy decreases from its initial value, γ_{SL}^{0}, associated with its initial configuration, to its equilibrium value, γ_{SL}^{∞}, associated with the surface after

[§] Except in the rare cases of autophobicity [150] G. Reiter and R. Khanna, Langmuir **16**, 6351 (2000).

reconstruction to its final state. For simplicity, the model assumes that the relaxation of the surface energy occurs with first order kinetics, such that

$$\gamma_{SL}(t) = \gamma_{SL}^{\infty} + \Delta\gamma_{SL}e^{-t/\tau_{SL}} \tag{4.1}$$

where $\gamma_{SL}(t)$ is the solid-liquid surface energy at time t, and τ_{SL} is the relaxation time. Butt *et al.* also model the case for dynamic (advancing and receding) contact angles, although this scenario is rather more complex.

The work in this chapter investigates the time and temperature dependent wetting properties of PFAC-n polymer surfaces produced via plasma polymerization. The validity of the first-order kinetic model proposed by Butt *et al.* will be investigated by examining the spreading of sessile drops of ethylene glycol and n-hexadecane on PFAC-4, -6, -8 and -10 at temperatures ranging from 20 °C to 100 °C.

4.1. Experimental

4.1.1. Variable temperature contact angle goniometry

Variable temperature contact angle measurements were carried out using a Krüss DSA100 goniometer fitted with a TC40 temperature-controlled chamber. Measurements were performed on PFAC-4, -6, -8, and -10 polymers deposited onto clean glass slides; the procedure for manufacturing these samples is described in **Section 2.1.2**. The work in the previous chapter found that the experimental scatter in measurements made on different PFAC-n samples was greater than in measurements on the same sample. Here, we report measurements made at different locations on a single, representative, sample surface. Measurements were

carried out at temperatures ranging from 20-100 °C at intervals of 10 °C. Prior to measuring at each temperature point, the samples were allowed to reach thermal equilibrium over a period of 10 mins.

To reduce the possible impact of drop evaporation on the contact angle, the probe liquids from the previous chapter (water and DD) were exchanged for the less volatile ethylene glycol (EG) and *n*-hexadecane (*n*-HD)[**]. As it was not possible to heat the probe liquids, the drop volume was decreased from 5μl to 2μl to ensure that the liquid reached thermal equilibrium with the surface more rapidly after deposition. As ethylene glycol is hygroscopic, measurements were also performed under a flow of dry air. The drop deposition and image recording procedures were fully automated to ensure consistency; the liquid was dispensed, the needle withdrawn from the drop, and a video of the drop was recorded from 1s after deposition to 10s after deposition at a frame rate of 2.5 fps. The initial delay of 1s was to ensure that any vibrations in the drop caused by the needle withdrawing did not affect the measurements. Each measurement was repeated three times. Image analysis was performed using the Krüss Advance software.

4.2. Results and Discussion

4.2.1. Contact angle aging

Figure 4.2 and **Figure 4.3** show how the static contact angles, θ_{stat}, of ethylene glycol (EG) and *n*-hexadecane (*n*-HD) evolve after deposition on PFAC-*n* surfaces at a variety of temperatures (T). The contact angles of EG are shown in blue,

[**] More commonly abbreviated to simply 'HD'. However, the NATO weapons designation for sulfur mustard, which is used in the next chapter, is also 'HD'

and the contact angles of *n*-HD are shown in orange; darker colours indicate lower temperature, whilst lighter colours indicate higher temperatures. **Figure 4.4** shows θ_{stat} measured at 1 s (dark) and 10 s (light) after deposition on each of the PFAC-*n* surfaces. **Figure 4.5** shows how the evolution of θ_{stat} differs between different PFAC-*n* surfaces at 20 °C and 100 °C, which were the lowest and highest temperature intervals respectively. Although each measurement was repeated three times, these results show the result for only one drop of each liquid for clarity; what matters is how each individual drop ages and showing the average contact angle for all three drops with time will obscure the magnitude of any changes that take place. For completeness and an indication of the reproducibility of the contact angles, the average contact angles at 1 s and 10 s and the average change in contact angle are shown in **Figure 4.6**.

Figure 4.2 a) and **b)** show that θ_{stat} on PFAC-10 has little time or temperature dependence for either liquid. At 100 °C, there is slight divergence between θ_{stat} of EG at time $t = 1$ s and $t = 10$ s; this can be seen in the line in **Figure 4.2 a)**, which has a small downward slope. Looking next at PFAC-8 (**Figure 4.2 c)** and **d)**), θ_{stat} for both liquids show no time dependence up until 70 °C, whilst above this temperature, θ_{stat} decreases with increasing t. This coincides with the melting transition at 72 °C, and above this temperature, $\Delta\theta_{\text{stat}}(t)$ increases with increasing T. As well as the beginning of a time-dependency effect, the θ_{stat} at $t = 1$ s also sees a sharp increase for both liquids. For EG, θ_{stat} at 1s remains approximately constant in the range $T < 70$ °C, and approximately constant at $T > 70$ °C, albeit at different values. For *n*-HD, there is a decrease in θ_{stat} at $t = 1$s with temperature in both regimes.

Examining PFAC-6 (**Figure 4.3 a)** and **b)**), the θ_{stat} at lower temperatures initially shows no time dependence, before starting to diverge at approximately 40 °C. This divergence increases with increasing T. The value of θ_{stat} for EG at $t = 1$s remains roughly constant up until 50 °C, where it starts to decrease. The value for *n*-HD also remains constant before starting to increase, but the transition occurs at the higher temperature of approximately 70 °C. PFAC-4 (**Figure 4.3 c)** and **d)**) displays the opposite behaviour to PFAC-6 in that there is a decrease in θ_{stat} with t at lower temperatures, but that the values for $t = 1$s and $t = 10$ s converge at higher temperatures. For both liquids, θ_{stat} initially decreases with increasing T, before starting to plateau as the time dependent values converge at higher values of T.

Figure 4.5 shows the time dependence of the contact angles of both liquids on all four surfaces at 20 °C and 100 °C. At 20 °C, the only surface to display any time dependence for the contact angles is PFAC-4. For the other three surfaces, it can be inferred that either drop spreading does not occur, or that it takes place on a timescale much longer than the experimental time-frame of 10 s. At the other extreme of temperature, neither PFAC-4 nor PFAC-10 displays any time dependence, whilst θ_{stat} decreases with time for both PFAC-6 and -8; the decay occurs more quickly for PFAC-6 than -8. At this temperature, it can be inferred that the drop spreading for PFAC-4 occurs in less than 1s, whilst the spreading for PFAC-6 and -8 occur within the experimental timeframe and spreading on PFAC-10 either does not occur, or occurs over a longer time-frame. Hence, the relaxation time decreases with decreasing chain length such that PFAC-10 > PFAC-8 > PFAC-6 > PFAC-4.

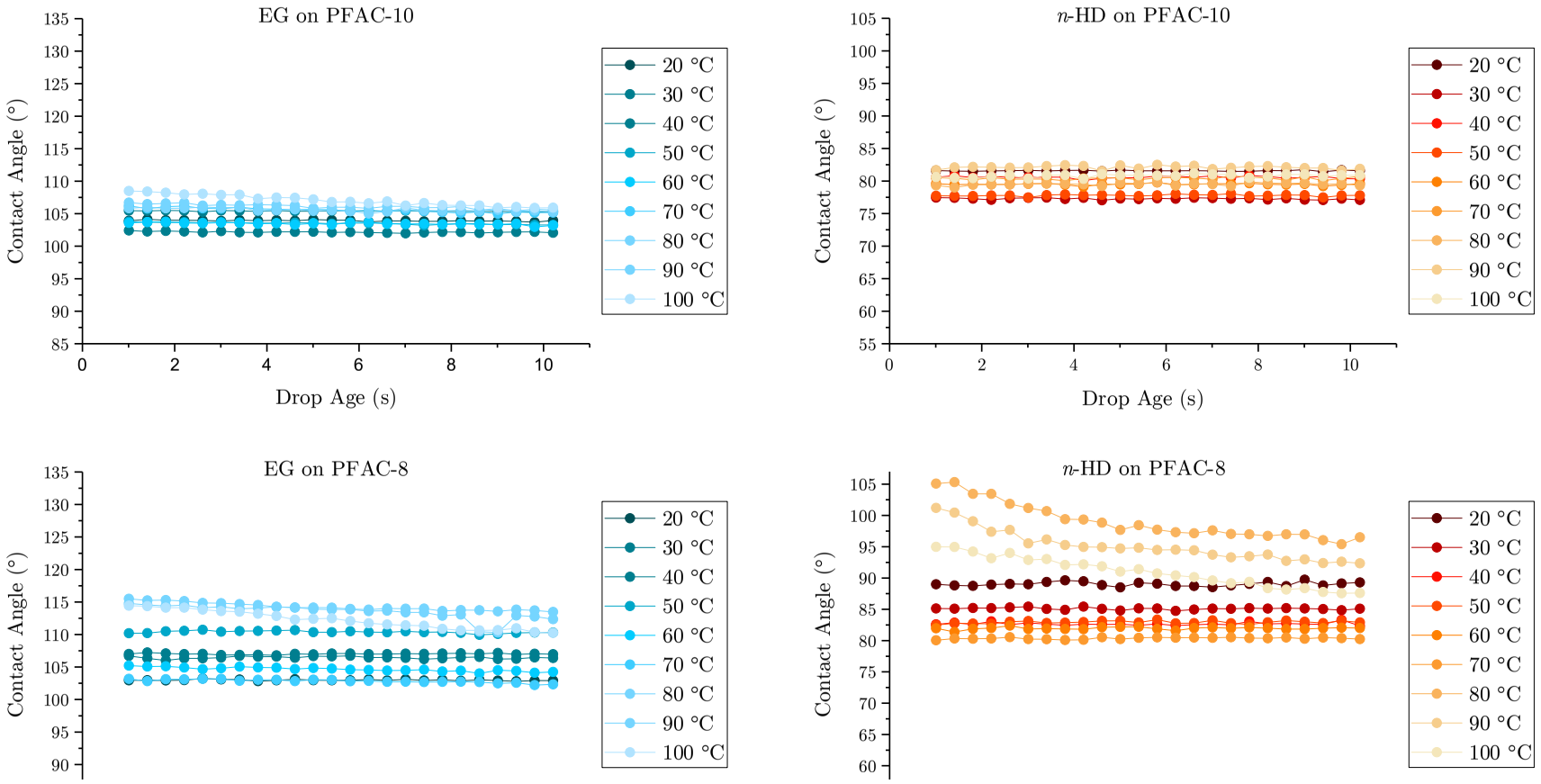


Figure 4.2 *Evolution of static contact angles with time on PFAC-10 and -8 surfaces at temperatures from 20 °C (dark) to 100 °C (light). The probe liquids were ethylene glycol (EG, blue), which is polar, and n-hexadecane (n-HD, orange), which is non-polar*

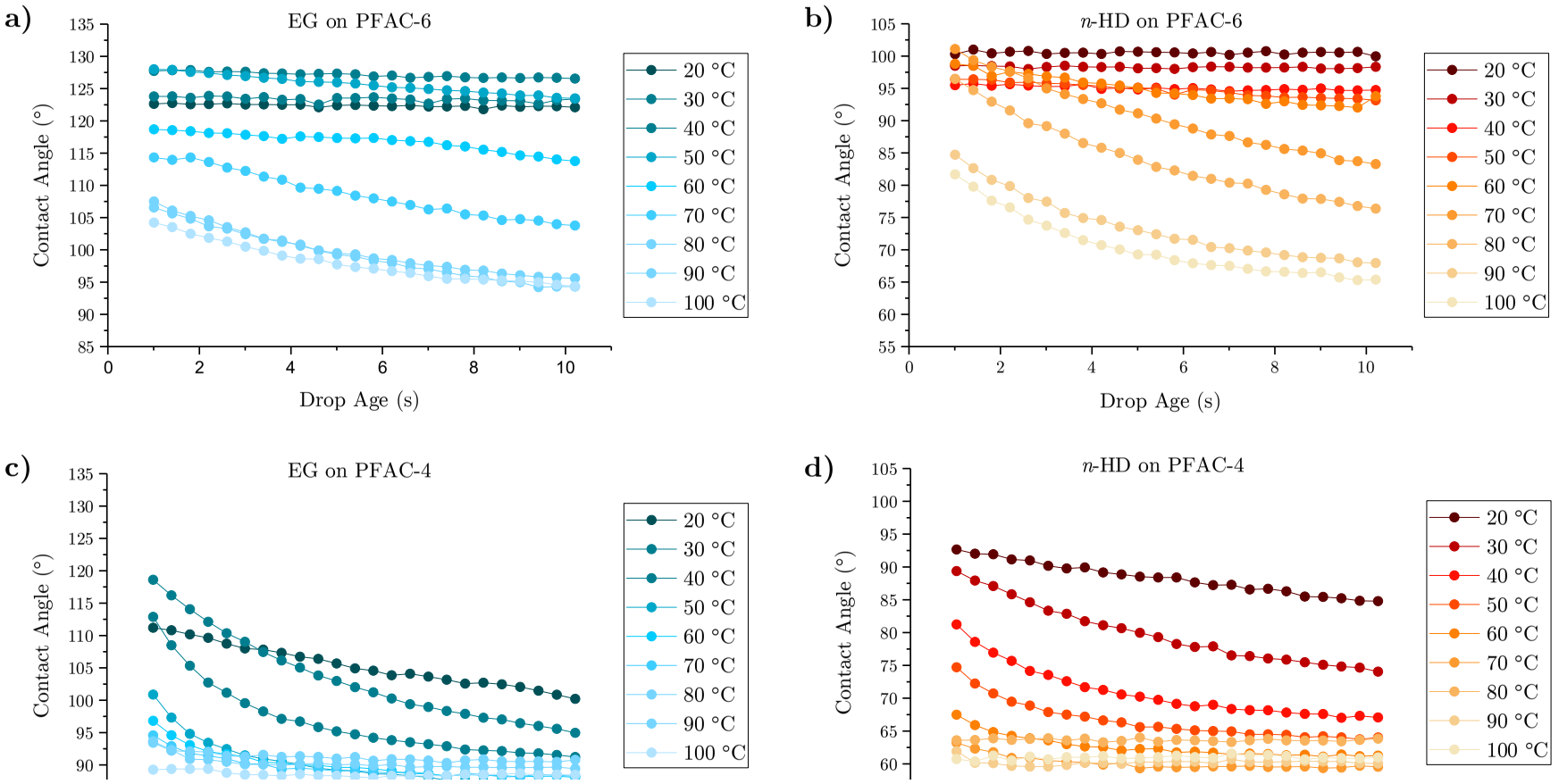


Figure 4.3 *Evolution of static contact angles with time on PFAC-6 and -4 surfaces at temperatures from 20 °C (dark) to 100 °C (light). The probe liquids were ethylene glycol (EG, blue), which is polar, and n-hexadecane (n-HD, orange), which is non-polar*

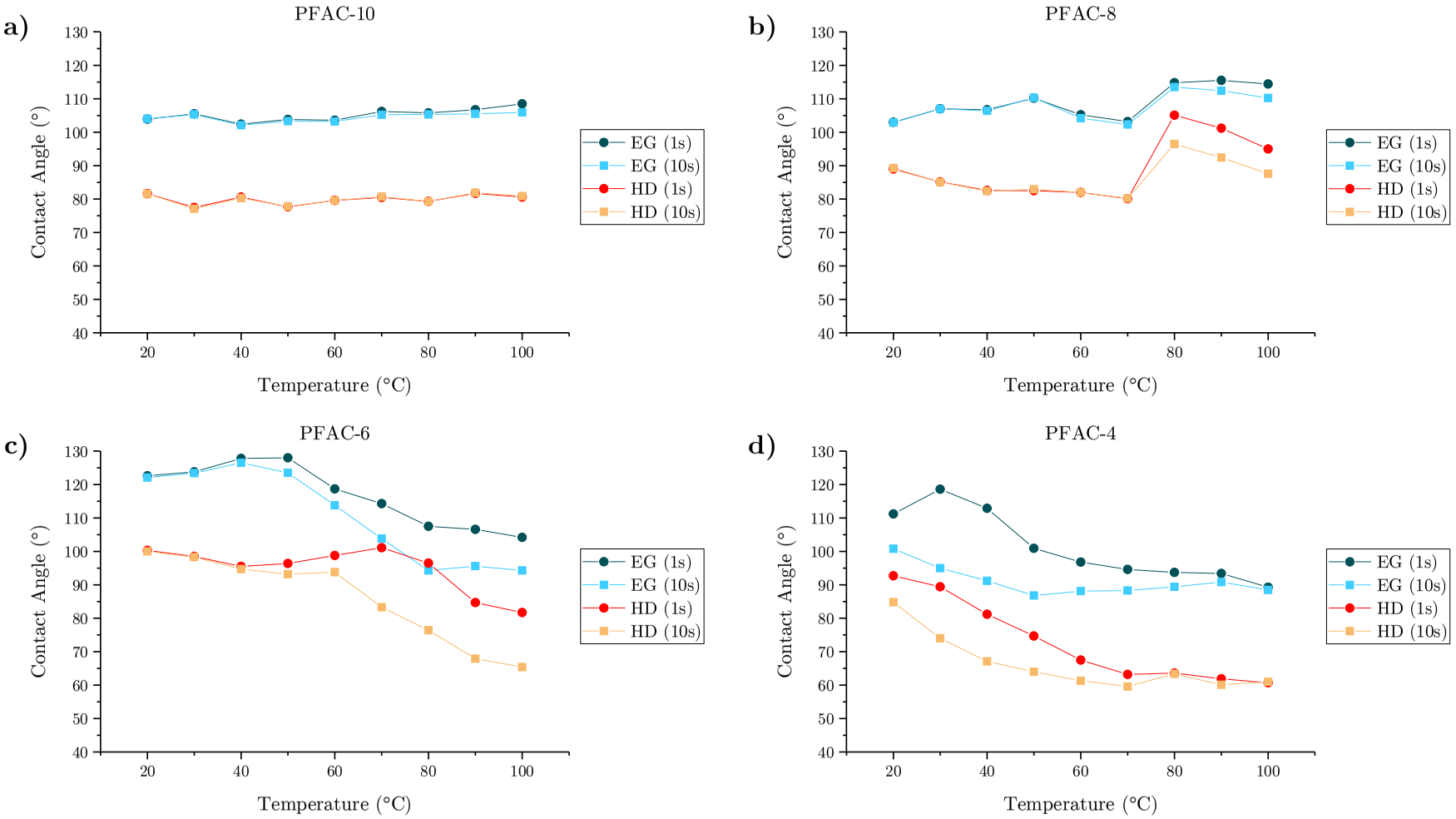


Figure 4.4 *Contact angles of EG (blue) and n-HD (orange) measured at 1 s (dark) after deposition and 10 s (light) after deposition*

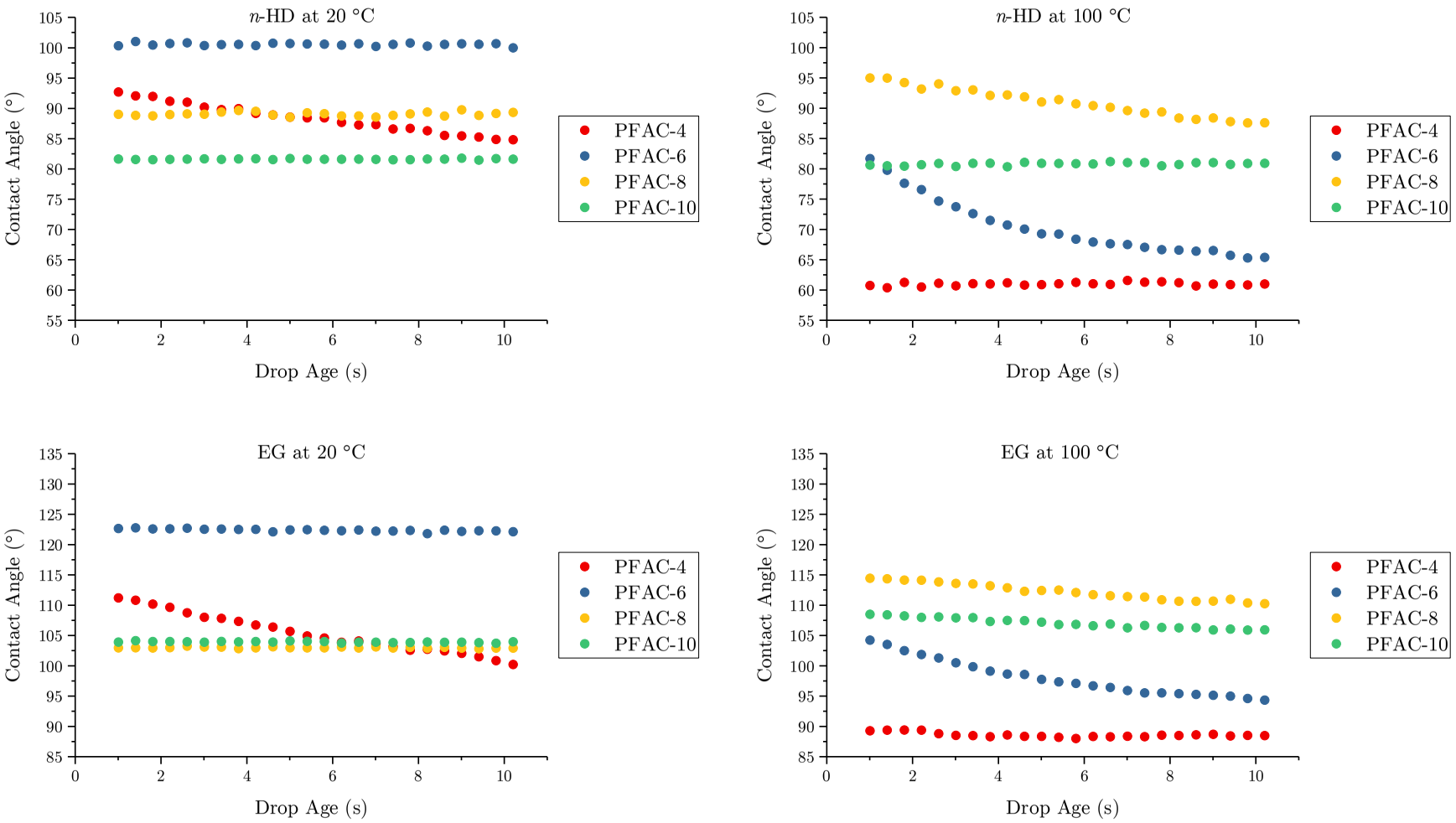


Figure 4.5 *Comparison of contact angle aging on different PFAC-n surfaces at 20 °C and 100 °C*

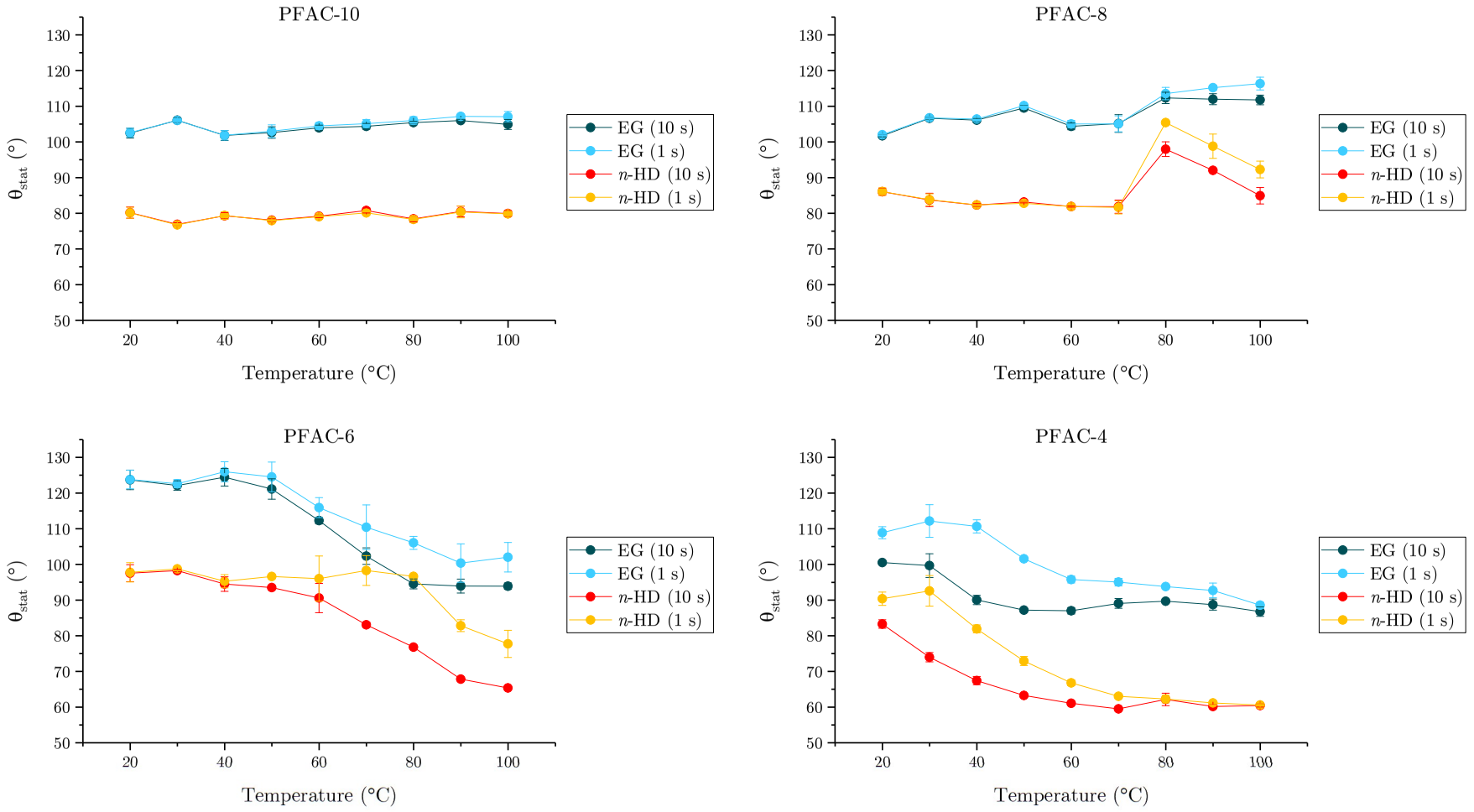


Figure 4.6 *Average contact angles of EG and n-HD on PFAC-n surfaces. The error bars represent one standard deviation from the mean*

4.2.2. Kinetics of drop spreading

To investigate the kinetics of drop spreading, $\cos\theta_{\text{stat}}$ was plotted against t for each liquid on each surface at each temperature. The data was then fitted to the following expression, which arises directly from comparison of **Eq. (4.1)** with the Young equation, **Eq. (1.1)**:

$$\cos\theta_{\text{stat}}(t) = \cos\theta_{\text{stat}}^{\infty} + \Delta\cos\theta_{\text{stat}}\, e^{-t/\tau}, \tag{4.2}$$

where $\theta_{\text{stat}}^{\infty}$ is the contact angle at $t = \infty$, $\Delta\cos\theta_{\text{stat}}$ is the difference between $\theta_{\text{stat}}^{\infty}$ and θ_{stat}^{0}, t is time, and τ is the relaxation time. To achieve a good fit for the data, the relaxation time, τ, needs to fall within the timeframe of the experiment such that $1 \lesssim \tau \lesssim 10$. **Figure 4.7** demonstrates the cases where τ falls inside (40°C) and outside (20 °C and 100 °C) the experimental time for EG on PFAC-4. For PFAC-4, the data could be fitted for $40 \leq T \leq 80$ for EG, and $30 \leq T \leq 70$ for *n*-HD. For PFAC-6, the data could be fitted for $80 \leq T$ for EG, and $70 \leq T$ for *n*-HD. None of the data for PFAC-8 or -10 could be fitted using an experiment time of 10 s. In all cases, the successful fits had an adjusted $R^2 > 0.96$ (mostly > 0.98), and a $\chi^2 \leq 6 \times 10^{-5}$. The complete set of fitted data can be found in **Appendix A**: Complete Results for Drop Aging Experiments, along with the individual values of adjusted R^2 and of χ^2.

Figure 4.8 and **Figure 4.9** show the relaxation times of EG and *n*-HD respectively on PFAC-4 and -6. The results for all three measurements carried out at each temperature are plotted separately, with the error bars representing the goodness of fit. In some cases (EG on PFAC-6 at 90 °C, *n*-HD on PFAC-6 at 90 °C, *n*-HD on PFAC-4 at 70 °C), one of the measured values is significantly

different to the other two; where this occurs, the point is plotted as a filled circle. The appearance of these outliers suggests that the surfaces have some degree of inhomogeneity, which could be chemical and/or topographical.

As expected, there is a decrease in relaxation time with increasing temperature across both liquids on both surfaces as molecular mobility increases. The curves for both liquids on PFAC-6 are shifted to higher temperatures than PFAC-4 and only overlap at two points; 80 °C for EG and 70 °C for *n*-HD. At both of these points, τ for PFAC-4 is substantially shorter than for PFAC-6; the shift in the curve position suggests that this is the case across the temperature range studied. τ for *n*-HD are shorter than EG at the same temperature on both surfaces. There is also a lower onset temperature for curve fitting, which also suggests that τ is shorter for *n*-HD than EG.

Figure 4.10 and **Figure 4.11** show θ_{stat} calculated by fitting measurements in the range $1 \leq t \leq 10$ to **Eq. (4.2)** for $t = 0$ and $t = \infty$ for EG (blue) and *n*-HD (orange) on PFAC-6 and PFAC-4 respectively (note the different temperature ranges). Examining the graph for PFAC-4, the contact angles decrease with increasing temperature before reaching a plateau. The decrease is more marked for θ^0 than θ^∞ and these values start to converge at higher temperatures. These behaviours are also seen in the graph for PFAC-6, although the decrease in θ^0 is less marked than for PFAC-4. In all cases, the error bars for θ^∞ are smaller than for θ^0. The small error shows that, despite there being some scatter in the initial contact angle as deposited on the surface, and some variation in τ at 90 °C (PFAC-6) and 70 °C (PFAC-4), the surfaces are all converging on the same final state.

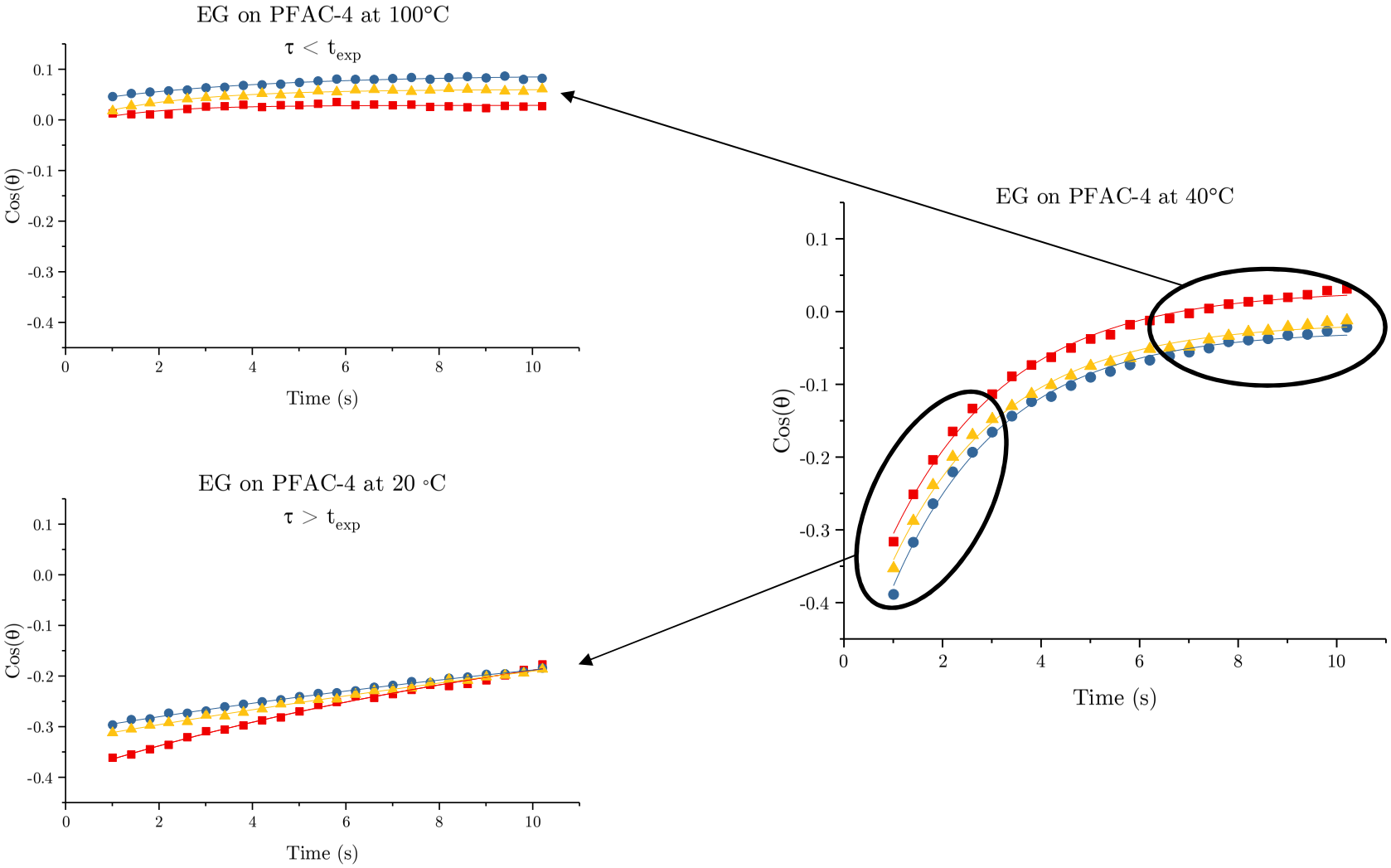


Figure 4.7 $\cos\theta_{stat}$ *plotted against time for different values of the relaxation time,* τ*. The different colours represent the three drops used for each measurement. If the relaxation time is longer than or approaching 10s (top left) or shorter than or near 1 s (bottom left) the change in contact angle will be too small to fit the data accurately*

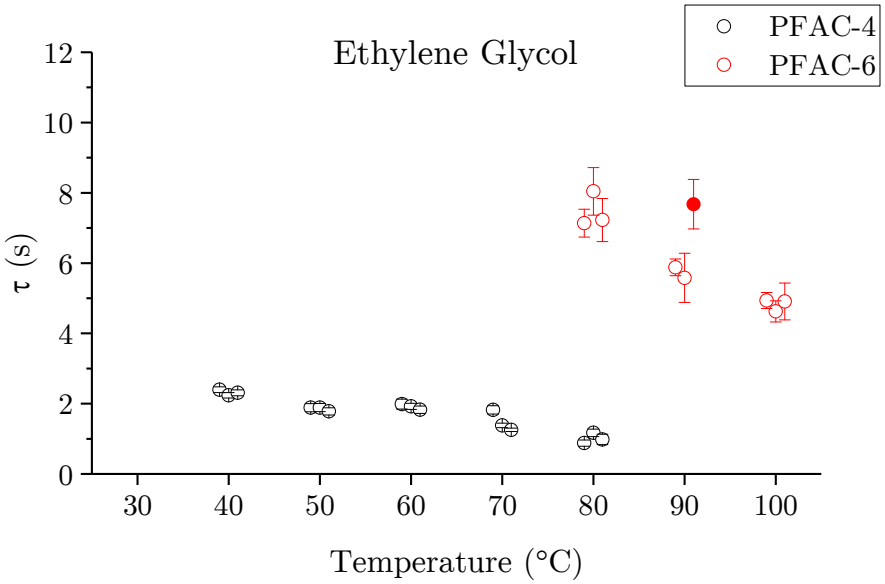


Figure 4.8 *Relaxation times of EG on PFAC-4 (black) and PFAC-6 (red). The results for all three drops of liquid are plotted at each temperature, with a slight offset in the x direction to allow the different data points to be viewed more clearly. The error bar representing the goodness of fit of Eq. 4.2. Where one of the values is clearly different to the other two values at that temperature, the data point is plotted as a filled circle*

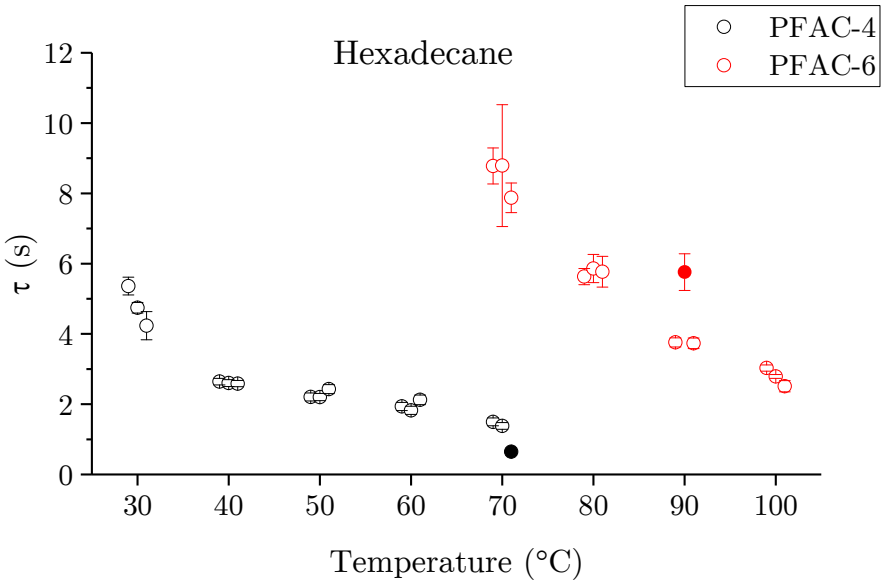


Figure 4.9 *Relaxation times of n-HD on PFAC-4 (black) and PFAC-6 (red). The results for all three drops of liquid are plotted at each temperature, with a slight offset in the x direction to allow the different data points to be viewed more clearly. The error bar representing the goodness of fit of Eq. 4.2. Where one of the values is clearly different to the other two values at that temperature, the data point is plotted as a filled circle*

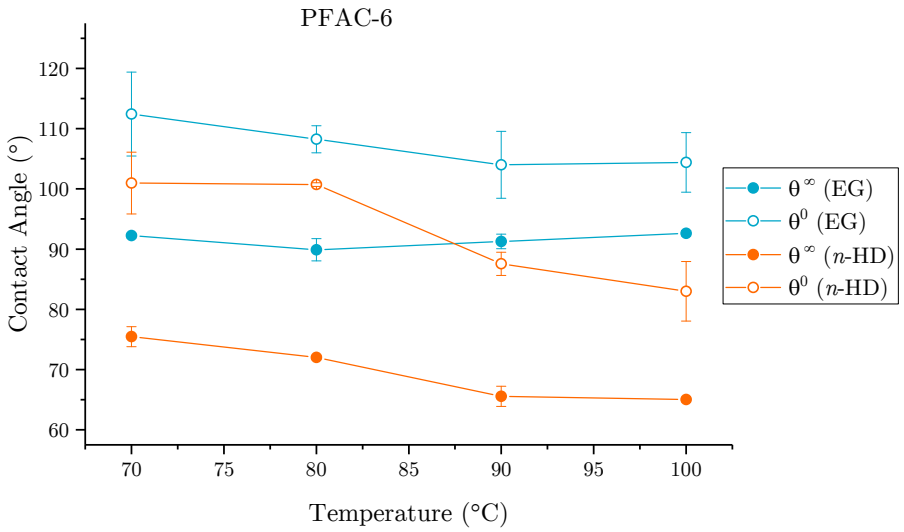


Figure 4.10 θ_{sta} *of ethylene glycol (blue) and hexadecane (orange) on PFAC-6 calculated for* $t = 0$ (θ^0) *and* $t = \infty$ (θ^∞)*. The lines are to guide the eye*

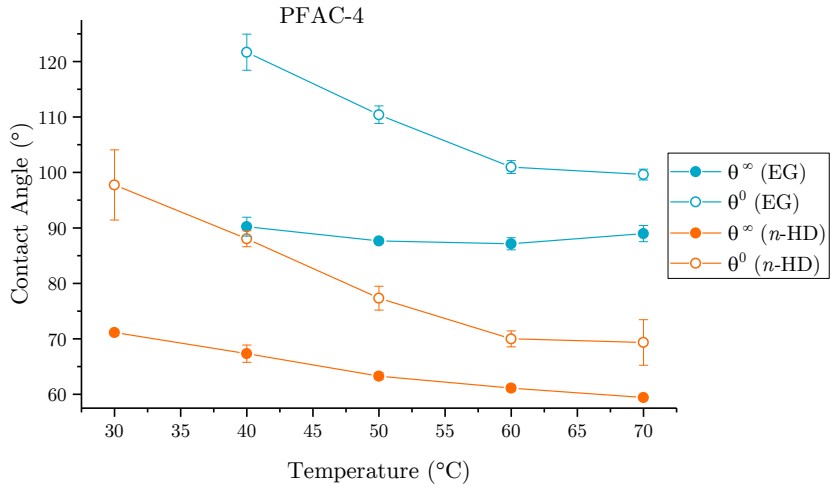


Figure 4.11 θ_{stat} *of ethylene glycol (blue) and hexadecane (orange) on PFAC-4 calculated for* $t = 0$ (θ^0) *and* $t = \infty$ (θ^∞)*. The lines are to guide the eye*

4.2.3. Surface energy

The surface energy of the PFAC-*n* surfaces was calculated from the contact angles of EG and *n*-HD at 1 s and 10 s after deposition. As in the previous chapters, the OWRK method was used, although this time the probe liquids were ethylene glycol and *n*-hexadecane, rather than water and DD.

One of the limitations of the OWRK model [97,98] and, indeed, all other models which use contact angles to estimate solid surface energy [151-154], is the assumption that the solid composition at the solid-liquid and solid-vapour interfaces is the same. Where surface reconstruction in the presence of a liquid occurs, this is clearly not the case. **Figure 4.12** demonstrates the difference between (a) the real, physical scenario, where only the regions of solid under the drop or near the triple-phase line undergo reconstruction, and (b) the scenario as formally described by the OWRK model, which assumes that the entire solid surface is uniform. Therefore, whilst the following section reports values for the solid-vapour surface energy (which is the property calculated using this model), it is intended as an indication of the behaviour of the solid-liquid interface.

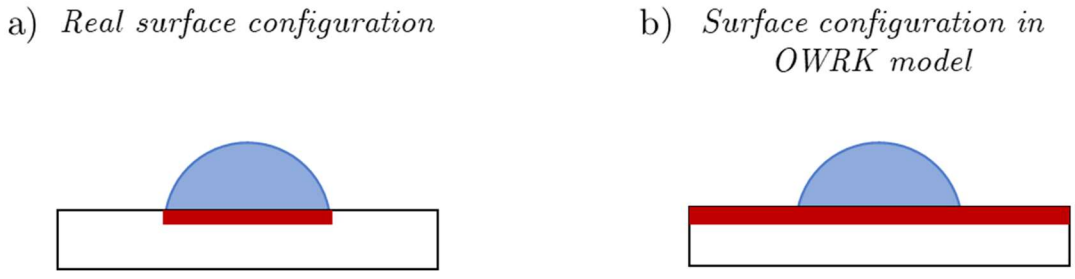


Figure 4.12 *a) surface configuration where liquid-induced surface reconstruction has taken place; only the liquid-solid interface is affected b) surface configuration as extrapolated by the OWRK method; the solid-vapour interface is assumed to be the same as the solid-liquid interface*

The OWRK model assumes that the total surface energy for a substance is the sum of polar and dispersive components such that

$$\gamma = \gamma^p + \gamma^d. \tag{4.3}$$

The values for γ_{LV}^p and γ_{LV}^d of EG and *n*-HD are well-defined at room temperature [155] but have not been measured at temperatures above this. The total surface energy, γ, for both materials is well known across the temperature ranges studied here [20]. The surface energy calculations were carried out assuming that the liquids came into thermal equilibrium with the surfaces immediately after deposition and used the values for γ_{LV} at the appropriate temperatures. It was further assumed that the ratio $\gamma_{LV}^p/\gamma_{LV}^d$ for both liquids remains constant across the temperature range.

Figure 4.13 shows γ_{SV} and γ_{SV}^p for PFAC-10 at variable temperature calculated using the room temperature values for γ_{LV}, γ_{LV}^p, and γ_{LV}^d, whilst **Figure 4.14** shows the values calculated using the correction for liquid temperature. The latter shows a decrease in surface energy with temperature, which is in line with expectation. The dispersive component of the surface energy, γ_{SV}^d, which is not plotted, is the difference between the total and polar surface energies.

Figure 4.15 shows γ_{SV} and γ_{SV}^p for the PFAC-*n* surfaces at 1s and 10 s after deposition. At 20 °C, which is the temperature which the measurements in the previous chapter were made, the total surface energies for PFAC-6, -8, and -10 match the previously reported values to within error. For PFAC-4, the values reported in the last chapter are closer to the value measured at 10 s, rather than

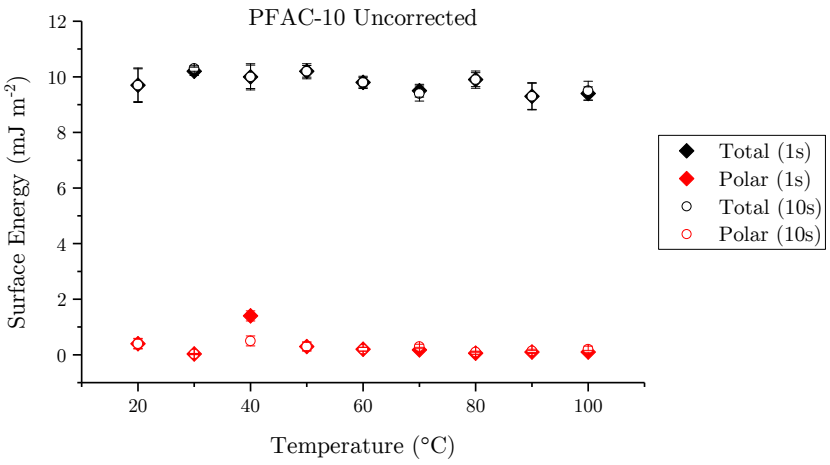


Figure 4.13 *Surface energy of PFAC-10 using the surface tension of EG and n-HD at 20 °C. The dispersive component of the surface energy is the difference between the total and polar components*

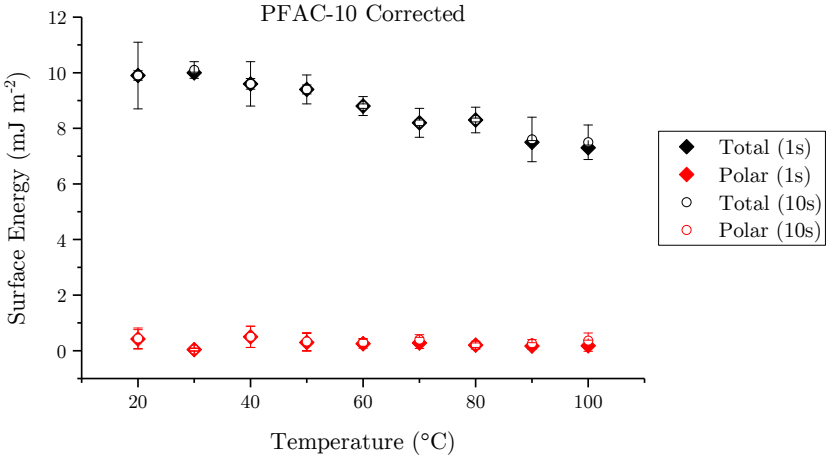


Figure 4.14 *Surface energy of PFAC-10 calculated using surface tension of EG and n-HD at the same temperature of the solid, assuming the ratio $\gamma_{LV}^{p}/\gamma_{LV}^{d}$ remains constant with temperature. The dispersive component of the surface energy is the difference between the total and polar components*

1 s, which is consistent with the way the measurements were performed. The polar component is also slightly lower than previously measured. Overall, there appears to be little liquid dependence of the surface energy measurements.

The surface energy for PFAC-10, which did not display drop aging behaviour, decreases with temperature, but shows no other significant effect related to either

time or temperature. PFAC-8 displays the same behaviour for γ_{SV} with respect to T up until its melting transition, when γ_{SV} drops sharply, before starting to increase again. γ_{SV}^{p} for PFAC-8 decreases between 20 to 30 °C and then remains constant within error. Any possible time-dependency of γ_{SV} for PFAC-8 remains within the margin of error. Looking next at PFAC-6, γ_{SV} and γ_{SV}^{p} initially remain constant with temperature, before starting to increase. As with PFAC-8, the increase in γ_{SV} appears to derive mainly from the dispersive component, γ_{SV}^{d}. The increase in total surface energy occurs between 50-60 °C for the surface energy measured at 10 s, and at 70-80 °C for the surface energy measured at 1 s. The divergence between the time-dependent values increases with temperature, being within the margin of error for $T < 80$ °C. For PFAC-4, the total surface energy increases with temperature before reaching a plateau at higher temperatures. As with PFAC-6 and -8, the dominant effect seems to be from the contribution from the dispersive, rather than polar, component. The time dependent values are divergent at lower temperature, with the surface energy measured at 10 s being higher than at 1s; these values converge as the surface energy starts to plateau.

Figure 4.16 and **Figure 4.17** show the surface energies of PFAC-6 and -4 calculated using the values of $\theta_{\text{stat}}^{\infty}$ shown in **Figure 4.10** and **Figure 4.11**. This represents the surface energy of the final, equilibrium configuration of the surface under the liquid drop. In both cases, the γ_{SV} increases with temperature, rather than decreasing as expected whilst γ_{SV}^{p} decreases with temperature. At 70 °C, which is the only value of T where the graphs overlap, γ_{SV}(PFAC-6) $>$ γ_{SV}(PFAC-4) whilst γ_{SV}^{p}(PFAC-4) $>$ γ_{SV}^{p}(PFAC-6).

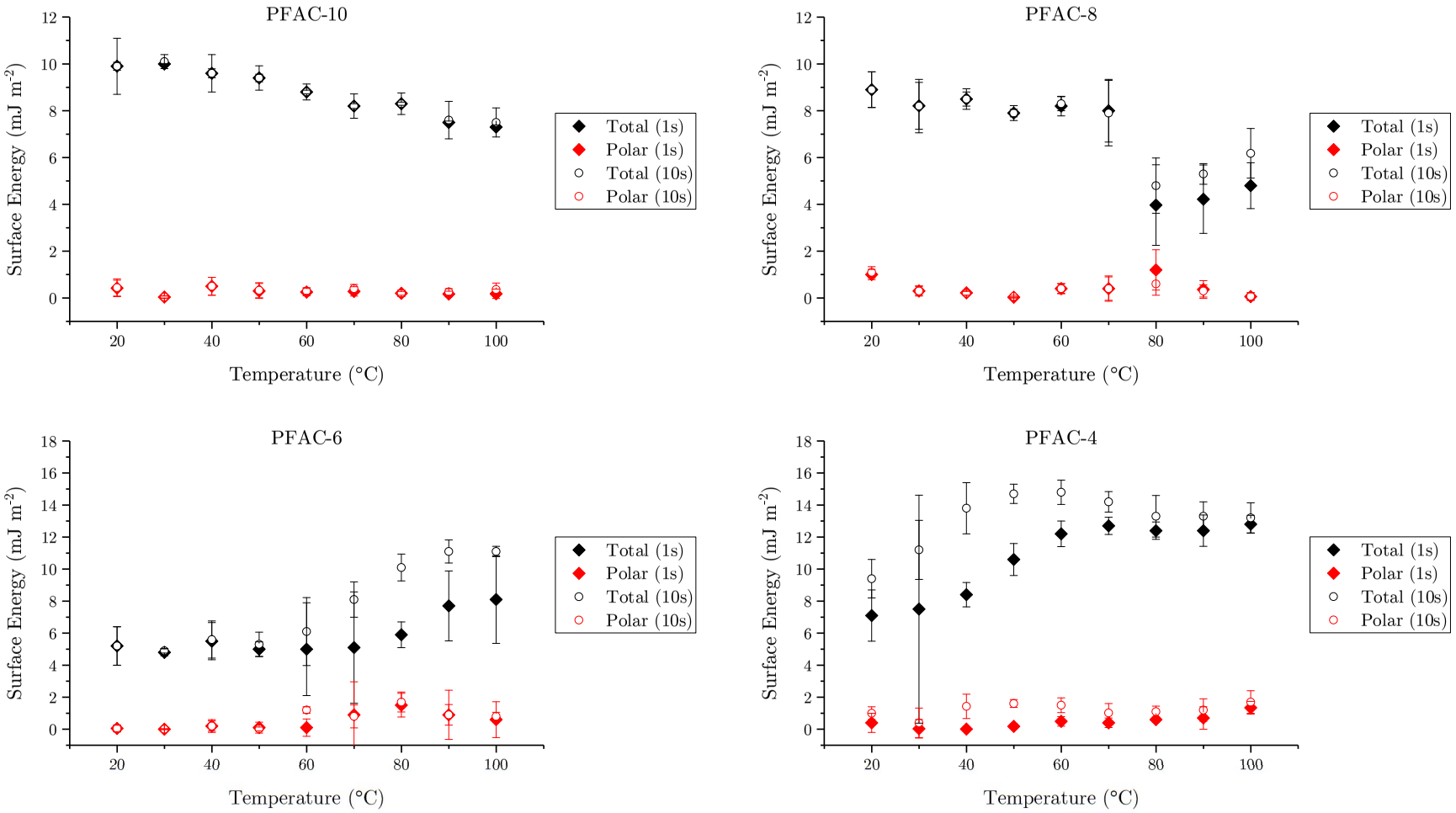


Figure 4.15 *Variation of surface energy with temperature of PFAC-n surfaces . Note that the y axes for PFAC-8 and -10 are different to those for PFAC-6 and-4*

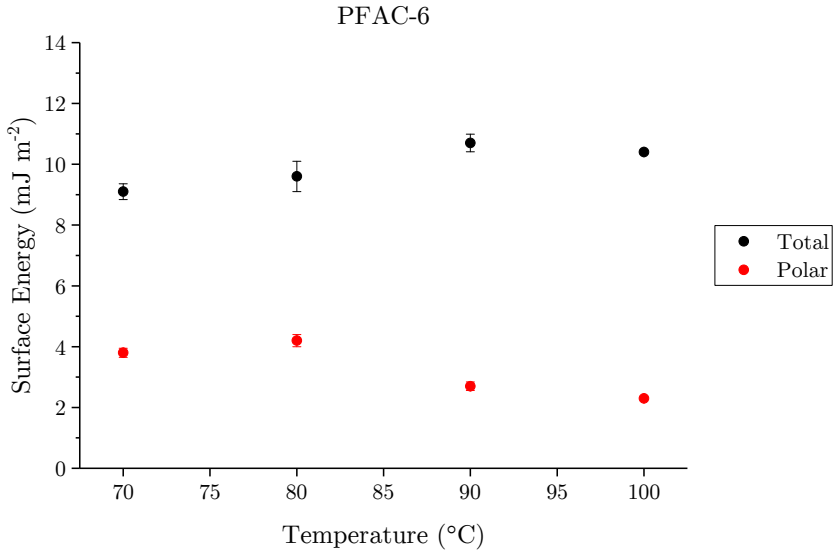


Figure 4.16 *Surface energy of PFAC-6 calculated using θ^{∞}*

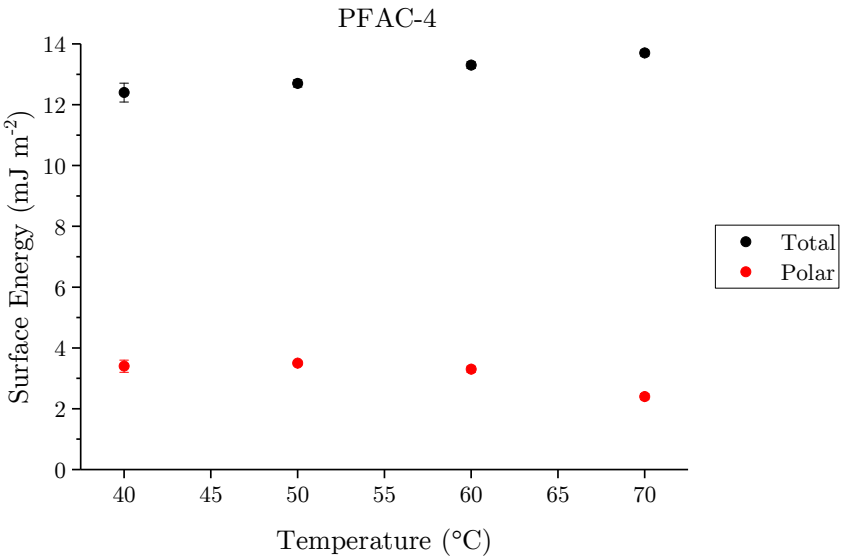


Figure 4.17 *Surface energy of PFAC-4 calculated using θ^{∞}*

4.2.4. Discussion

Before examining the effect of liquid on the PFAC-*n* surfaces, it is first helpful to discuss the effect of temperature and side-chain length on the surfaces in air. In

the instance where there are no orientational effects, or the surface is otherwise homogeneous, surface energy decreases with increasing temperature. The picture is then complicated when the effects of side chain orientation are considered. As previously discussed, the lowest surface energy configuration is with the CF_3 groups at the surface and this is the configuration that dominates at low temperature. This is also the enthalpically favoured configuration in terms of cohesion between the side chains. This cohesive interaction increases with increasing n for PFAC-n, and for $n \geq 8$ is sufficient for the side chains to crystallise. As T increases and the entropic effects start to dominate, the side chain orientations tend towards isotropy. The surface energy of the isotropic state is determined by the stoichiometry of the different functional groups. Fluorination increases with increasing n and so PFAC-10 is expected to have the lowest surface energy in the isotropic state whilst PFAC-4 is expected to have the highest. The transition to isotropy is expected to occur gradually for non-crystalline side chains (PFAC-4 and -6), and more sharply after the melting transition in polymers with crystalline side chains (PFAC-8 and -10). **Figure 4.18** shows the configurations of the side chains in the low and high temperature regimes and the transition between them for both $n < 8$ and $n \geq 8$.

Examining the results first for PFAC-4 and -6 at 1 s after deposition; the measured surface energies for PFAC-4 matches the mid-to-high temperature region of the predicted curve, and the results for PFAC-6 match the low-to-mid temperature region of the predicted curve. The temperature offset for PFAC-4 compared to -6 is consistent with the lower cohesion of the shorter side chains.

The measured surface energies for PFAC-8 and PFAC-10 bear less resemblance to the prediction in **Figure 4.18**. Both PFAC-8 and -10 show a gradual decrease in surface energy with temperature; this persists up to 70 °C for PFAC-8 and across the whole range for PFAC-10. Although this is similar to the predicted low temperature behaviour, the measured values of surface energy (γ_{SV} = 10 mJ m^{-2} at 20 °C) are higher than would be expected for a crystalline CF_3 surface (γ_{SV} = 6 mJ m^{-2} at 20 °C), and higher than for PFAC-6. This behaviour can be rationalised by the difference between the deposition temperature and the melting temperatures of the polymers. Both PFAC-8 and -10 are deposited below their melting temperatures and, whilst the angle-resolved XPS spectra presented in the previous chapter indicate preferential segregation of CF_3 at the surface, their DSC demonstrates that neither of them is crystalline as shown in the figure. PFAC-10 in particular has a very broad range of crystallites which will have a variety of orientations. The effect of this is that both PFAC-8 and -10 are kinetically trapped in a higher surface energy state up until their melting points; this state is shown in **Figure 4.19 a**).

It should be noted that the temperature at which the surface achieves isotropy is typically higher than the isotropic melting point of the bulk, owing to the energetic favourability of surface segregation of CF_3 [156]. Genzer *et al.* found that for a polymer with an isoprene backbone and C8 perfluorinated side chain, the surface had not achieved isotropy even when 30 °C above its bulk isotropic melting point (70 °C) [124]. The reason why the surface energy of PFAC-8 initially drops as the temperature rises above the melting point is that the molecules are sufficiently mobile to reorient to the lowest surface energy

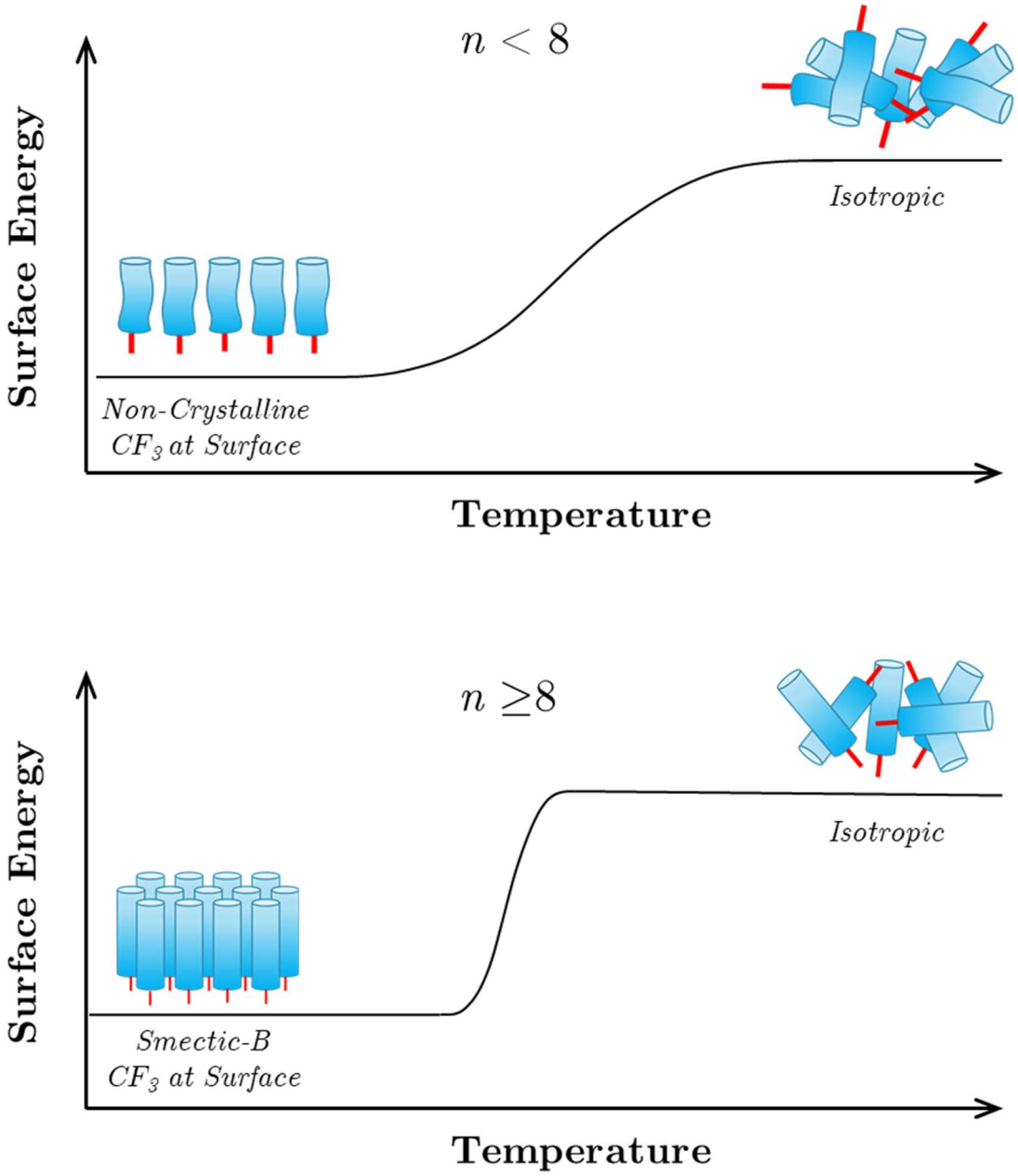


Figure 4.18 *Schematic showing temperature dependence of side chain configuration and the effect on surface energy. The blue cylinders represent the fluorinated functionality, with the CF_3 at the lighter-coloured end; for smaller values of n, the cylinders are distorted to reflect the increased flexibility of the fluorocarbon chain and the polar groups are shown in red. For clarity, the polymeric backbone is not shown.*

state (**Figure 4.19 b)**). As the temperature increases further, the surface tends towards the isotropic state and the surface energy increases (**Figure 4.19 c)**).

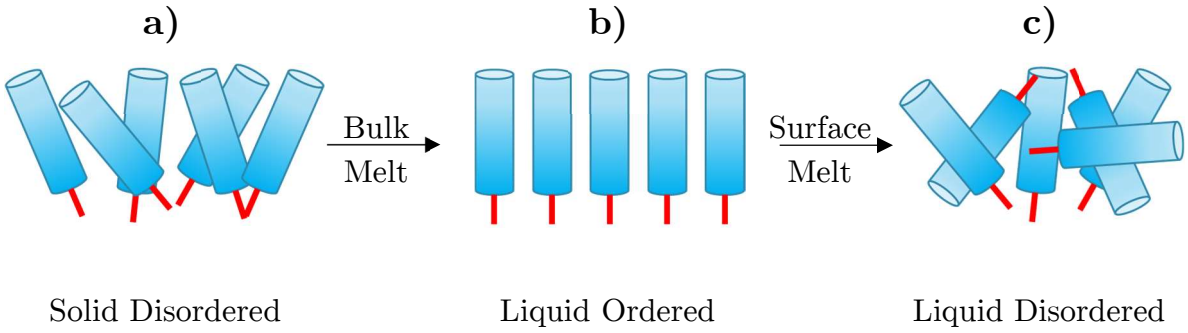


Figure 4.19 *The surface structures of PFAC-8 and -10* **a)** *below their melting temperature* **b)** *immediately above their isotropic bulk melting temperature, and* **c)** *at high temperatures, where entropic effects dominate*

Moving on to the case where the surface is exposed to liquid; in this chapter, it has been shown that the static contact angles of ethylene glycol and *n*-hexadecane on PFAC-*n* surfaces display time and temperature dependence, as well as a dependence on the value of *n*. On a smooth, chemically homogenous surface without the capability to rearrange, $\theta_{\text{stat}} \equiv \theta_{\text{eqm}}$, where θ_{eqm} is the equilibrium contact angle as defined by the Young equation (**Eq. (1.1)**). On a non-ideal substrate, two additional effects become relevant. Firstly, surface reorganization, swelling, or adsorption of liquid/vapour onto the surface can lower the energy of the solid-liquid interface, resulting in a decrease in θ_{stat}. Secondly, the triple-phase line can become pinned on an asperity or other topographical feature, which will prevent the drop spreading. In order to separate the former from the latter, a number of results from the previous chapter must also be considered. Firstly, the DSC data shows that PFAC-4 and PFAC-6 are melts at room temperature and can therefore be assumed to be smooth; this is reinforced by the AFM results. Similarly, the onset of time-dependent behaviour for PFAC-8 is also above the melting temperature and so the PFAC-8 surface can therefore be assumed to be

smooth in this regime. Furthermore, the contact angle hystereses of PFAC-4 and PFAC-6 at room temperature are considerably larger than for either PFAC-8 or -10. If this hysteresis was due to pinning on physical features, then drop spreading on PFAC-4 and -6 should be inhibited in comparison to spreading on either PFAC-8 or -10. Instead, the opposite is true, and the onset temperature of time-dependency, T_n, increases such that $T_4 < T_6 < T_8 < T_{10}$. This is not to say that surface topography is completely irrelevant, indeed, it may still inhibit spreading on PFAC-8 and -10 to some degree – it is simply not the dominant effect.

Figure 4.20 shows the effect of depositing a liquid on a surface which can reconstruct. Here, the optimum configuration is where the acrylate groups migrate to the surface. At lower temperatures, the surface is kinetically trapped in its initial configuration and is unable to reconstruct. As the temperature increases, molecular mobility increases, and the surface is able to reconstruct. At low temperatures, the relaxation time is long, and so the surface undergoes only small changes during the experiment time. As temperature increases further, the relaxation time decreases, and the surface is eventually able to attain its equilibrium state within the experimental timeframe. As the temperature increases yet further, entropic effects begin to dominate, and the surface starts to tend towards isotropy. The predicted curve in this figure matches the results for the total surface energy of PFAC-4 (mid-high temperature region) and PFAC-6 (low-mid temperature region) shown in **Figure 4.14**. However, the increase in total surface energy as the surface reconstructs is expected to be driven by an increase in the polar component of the surface energy, which is not the case.

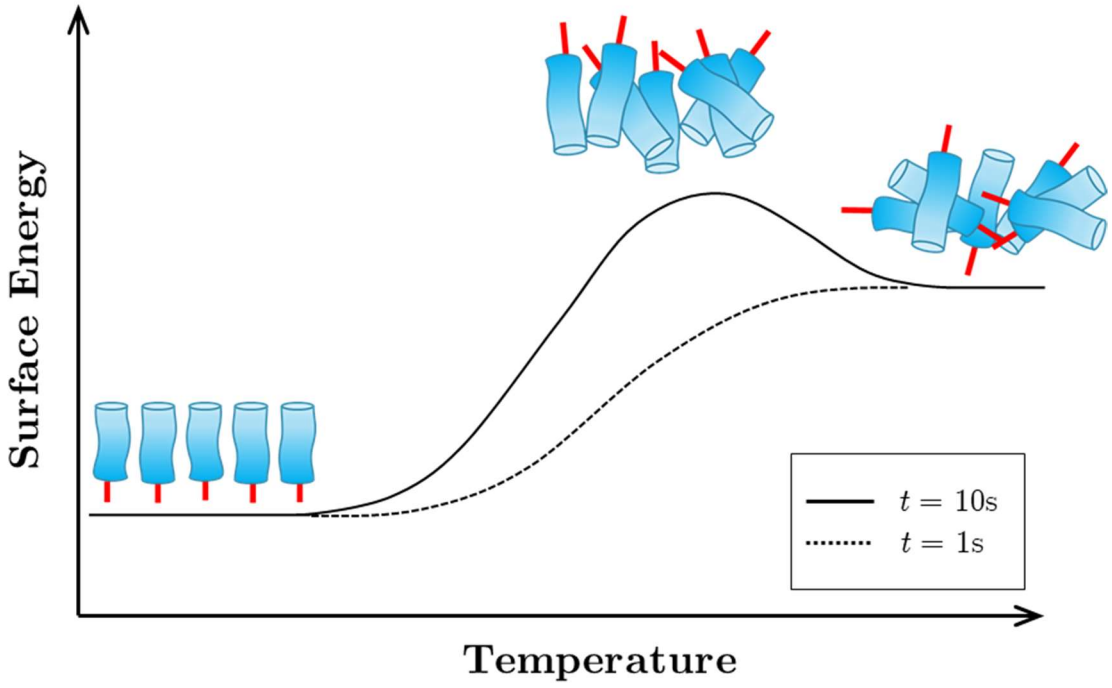


Figure 4.20 *Effect of depositing a liquid on a surface which is able to undergo reconstruction*

If surface reconstruction is driven by polar interactions, it is expected that contact angle aging should only occur using polar liquids such as EG. However, *n*-HD also displayed contact angle aging behaviour despite being non-polar. A concept which was briefly introduced in **Section 1.1.1** is the weak interactions between hydrocarbon and fluorocarbon moieties in comparison with either hydrocarbon-hydrocarbon or fluorocarbon-fluorocarbon systems [27,31,157]. Segregation of the two moieties occurs in both liquid and solid systems of semifluorinated alkanes [29,32,158] and in co-polymer systems containing both fluorocarbon and hydrocarbon side chains [159,160]. It is perhaps a similar effect that drives the spreading of *n*-HD on PFAC-*n* surfaces. There are consequences of the weak interactions between fluorocarbons and hydrocarbons in terms of the surface energy calculations. Firstly, the higher initial contact angles of hydrocarbon liquids on fluorocarbon surfaces result in a lower estimation of the total surface

energy at $t = 0$ [21,152,157,161]. Secondly, if both the polar and non-polar probe liquids trigger surface reconstruction which brings the acrylate group to the surface (albeit for different reasons) then it will result in an underestimate of the polar surface energy for $t > 0$. This could be mitigated by replacing the non-polar probe liquid with a fluorocarbon. However, liquid perfluoroalkanes have extremely low surface tensions and are highly likely to spread on the surfaces, rendering it impossible to measure the time-dependency of the surface energy.

The model proposed by Butt *et al.* [139] was used successfully to fit the data from the contact angle aging experiments on both PFAC-4 and -6, although not across the entire temperature range. As shown in **Figure 4.7**, the shapes of the curves outside the temperature ranges where fitting was possible were consistent with the predicted curves where $\tau < 1$ s and $\tau > 10$ s. Assuming that the same processes are responsible for contact angle aging, it seems reasonable to assume that the first-order behaviour persists across the temperature range. The data for PFAC-8 could not be fitted, although the shape of the curve is similar to PFAC-4 and -6 where $\tau > 10$ s. Being more mobile, PFAC-4 has a lower onset temperature of drop aging and shorter relaxation times than PFAC-6. As discussed in the introduction, the model does not differentiate between the processes which may be occurring at the surface – swelling of the polymer, surface reconstruction, and even liquid ordering. However, the characteristic timescales of these processes are very different; molecular liquid ordering occurs on a ns timescale, polymer swelling on a ms timescale, and polymer reconstruction can occur on anything between the s to day timescale [162-164]. Overall, it seems that the relaxation times measured in this investigation are associated with

reconstruction at the polymer surface. This process was not found to follow Arrhenius behaviour. The presence of outlying values of τ (**Figure 4.8** and **Figure 4.9**) is taken to indicate patches of polymer which start in a different configuration to the majority of the surface, and have a different characteristic relaxation time.

The model was used to extract both the values of $\theta_{\text{stat}}^{\infty}$ and γ_{SL}^{∞} for both PFAC-4 and -6 at a variety of temperatures. Of particular interest was the fact that the calculate values of $\theta_{\text{stat}}^{\infty}$ had a very small standard deviation in comparison with the measured values of $\theta_{\text{stat}}$and despite the appearance of more than one characteristic value of τ at several temperatures. This indicates that despite some initial inhomogeneity in air, the surfaces tend towards homogeneity in liquid. The maximum values of γ_{SL}^{∞} at any temperature were 14 mJ m^{-2} for PFAC-4 and 11 mJ m^{-2} for PFAC-6; these values are still lower than for PTFE, which would indicate that there is still a significant amount of fluorine present at the surface even after reconstruction. However, it also seems likely that this reflects an inadequacy of the OWRK method to accurately obtain solid surface energy values.

4.3. Conclusions

In this chapter, it was found the contact angles of ethylene glycol and hexadecane on PFAC-*n* polymers displayed time and temperature dependence, as well as a dependence on *n*.

The deposition conditions for PFAC-8 and -10 meant that these surfaces were kinetically trapped in a higher surface energy state than the enthalpic minimum

– crystallisation in the smectic B structure with CF_3 at the interface. This is in contrast with previous studies using annealed PFAC-*n* polymers. PFAC-8 was able to achieve the lowest surface energy state immediately after the bulk isotropic melting point, whilst PFAC-10 remained in this state across the whole temperature range. PFAC-4 and -6 were deposited above their melting points and so the surface could assume the lowest energy configuration at low temperatures. At high temperatures, the surfaces tended towards isotropy.

The time dependency of the contact angles on PFAC-4, -6, and -8 is considered to be a result of polymers reorienting themselves at the surface. The driving force for this reorganization is the polar interactions between ethylene glycol and the ester group in the polymer, and the stronger dispersive interactions between *n*-hexadecane and the hydrocarbon groups in the polymer. The rate of reorganization increases with increasing temperature and decreases as side chain length increases. At high temperatures, entropic effects start to dominate, and the side chain orientations tend towards isotropy.

The first order kinetic model proposed by Butt *et al.* is able to predict the contact angle aging on PFAC-4 and -6 provided that the relaxation time fall approximately within the experimental timeframe. Outside of this timeframe, it is assumed that the model continues to be valid but cannot conclusively be stated. Likewise, the relaxation times for PFAC-8 above its melting point of 70 °C are longer than the experimental timeframe and cannot be modelled. The relaxation times in the region where the model is valid are of the order of seconds, which is consistent with a reorientation process at the solid surface.

4.4. References

[6] B. Wang, W. Liang, Z. Guo, and W. Liu, Chemical Society Reviews **44**, 336 (2015).

[20] J. J. Jasper, Journal of Physical and Chemical Reference Data **1**, 841 (1972).

[21] W. Zisman, in *Contact Angle, Wettability, and Adhesion* (American Chemical Society, 1964), pp. 1.

[27] C. Adam, L. Yang, and S. L. Cockroft, Angewandte Chemie International Edition **54**, 1164 (2015).

[29] M. P. Krafft and J. G. Riess, Chemical Reviews **109**, 1714 (2009).

[31] E. M. D. Siebert and C. M. Knobler, The Journal of Physical Chemistry **75**, 3863 (1971).

[32] P. Long and J. Hao, Advances in Colloid and Interface Science **171–172**, 66 (2012).

[84] K. Honda, M. Morita, H. Otsuka, and A. Takahara, Macromolecules **38**, 5699 (2005).

[85] K. Honda, M. Morita, O. Sakata, S. Sasaki, and A. Takahara, Macromolecules **43**, 454 (2009).

[97] D. K. Owens and R. C. Wendt, Journal of Applied Polymer Science **13**, 1741 (1969).

[98] D. H. Kaelble, Journal of Adhesion **2**, 66 (1970).

[107] N. Belman, K. Jin, Y. Golan, J. N. Israelachvili, and N. S. Pesika, Langmuir **28**, 14609 (2012).

[124] J. Genzer, E. Sivaniah, E. J. Kramer, J. Wang, H. Körner, K. Char, C. K. Ober, B. M. DeKoven, R. A. Bubeck, D. A. Fischer, and S. Sambasivan, Langmuir **16**, 1993 (2000).

[127] J. Hu, H. Meng, G. Li, and S. I. Ibekwe, Smart Materials and Structures **21**, 053001 (2012).

[128] F. Xia, H. Ge, Y. Hou, T. Sun, L. Chen, G. Zhang, and L. Jiang, Advanced Materials **19**, 2520 (2007).

[129] I. Luzinov, S. Minko, and V. V. Tsukruk, Progress in Polymer Science **29**, 635 (2004).

[130] N. Nath and A. Chilkoti, Advanced materials **14**, 1243 (2002).

[131] S. Peng and B. Bhushan, RSC Advances **2**, 8557 (2012).

[132] T. P. Russell, Science **297**, 964 (2002).

[133] S. J. P. McInnes, E. J. Szili, S. A. Al-Bataineh, R. B. Vasani, J. Xu, M. E. Alf, K. K. Gleason, R. D. Short, and N. H. Voelcker, Langmuir **32**, 301 (2016).

[134] D. A. Lavan, T. McGuire, and R. Langer, Nature Biotechnology **21**, 1184 (2003).

[135] L. Zhang, Z. Zhang, and P. Wang, NPG Asia Materials **4**, e8 (2012).

[136] Z. Chu, Y. Feng, and S. Seeger, Angewandte Chemie International Edition **54**, 2328 (2015).

[137] J. Genzer and K. Efimenko, Biofouling **22**, 339 (2006).

[138] G. Cheng, H. Xue, Z. Zhang, S. Chen, and S. Jiang, Angewandte Chemie **120**, 8963 (2008).
[139] H.-J. Butt, R. Berger, W. Steffen, D. Vollmer, and S. A. L. Weber, Langmuir **34**, 11292 (2018).
[140] J. N. Lee, C. Park, and G. M. Whitesides, Analytical Chemistry **75**, 6544 (2003).
[141] Y. H. Bae, T. Okano, and S. W. Kim, Journal of Polymer Science Part B: Polymer Physics **28**, 923 (1990).
[142] P. Colombo, R. Bettini, P. Santi, A. De Ascentiis, and N. Peppas, Journal of Controlled Release **39**, 231 (1996).
[143] I. Tokarev and S. Minko, Soft Matter **5**, 511 (2009).
[144] J. N. Israelachvili, N. A. Alcantar, N. Maeda, T. E. Mates, and M. Ruths, Langmuir **20**, 3616 (2004).
[145] M. K. Bernett and W. Zisman, Journal of Colloid and Interface Science **28**, 243 (1968).
[146] R. Mohammadi, J. Wassink, and A. Amirfazli, Langmuir **20**, 9657 (2004).
[147] A. J. B. Milne and A. Amirfazli, Langmuir **26**, 4668 (2010).
[148] E. A. Gobrogge, B. L. Woods, and R. A. Walker, Faraday Discussions **167**, 309 (2014).
[149] R. S. Hansen and M. Miotto, Journal of the American Chemical Society **79**, 1765 (1957).
[150] G. Reiter and R. Khanna, Langmuir **16**, 6351 (2000).
[151] W. Zisman, *Contact Angle, Wettability, and Adhesion* (AMERICAN CHEMICAL SOCIETY, 1964), Vol. 43, Advances in Chemistry, 43.
[152] F. M. Fowkes, Industrial & Engineering Chemistry **56**, 40 (1964).
[153] A. Neumann, R. Good, C. Hope, and M. Sejpal, Journal of Colloid and Interface Science **49**, 291 (1974).
[154] S. Wu, Journal of Polymer Science Part C: Polymer Symposia **34**, 19 (1971).
[155] J. Dann, Journal of Colloid and Interface Science **32**, 302 (1970).
[156] J. Lüning, J. Stöhr, K. Y. Song, C. J. Hawker, P. Iodice, C. V. Nguyen, and D. Y. Yoon, Macromolecules **34**, 1128 (2001).
[157] M. K. Chaudhury and G. M. Whitesides, Science **255**, 1230 (1992).
[158] Y. J. Lee, C. G. Clark, R. Graf, M. Wagner, K. Müllen, and H. W. Spiess, The Journal of Physical Chemistry B **113**, 1360 (2009).
[159] P. L. Nostro, Advances in Colloid and Interface Science **56**, 245 (1995).
[160] L. Wilson and A. Griffin, Macromolecules **27**, 1928 (1994).
[161] M. K. Chaudhury, Materials Science and Engineering: R: Reports **16**, 97 (1996).
[162] T. Yasuda, T. Okuno, K. Yoshida, and H. Yasuda, Journal of Polymer Science Part B: Polymer Physics **26**, 1781 (1988).
[163] H. Yasuda, A. K. Sharma, and T. Yasuda, Journal of Polymer Science: Polymer Physics Edition **19**, 1285 (1981).
[164] J. A. Crowe and J. Genzer, Journal of the American Chemical Society **127**, 17610 (2005).

5. Wetting of Chemical Warfare Agents and Their Simulants on Fluoropolymer Surfaces

The use of toxic chemicals to kill or incapacitate during warfare has a long history, with the first recorded incident being in 1000 BC in ancient China [75]. After the rapid expansion of the chemicals industry in the latter half of the 19th and early 20th centuries, the First World War saw the first large scale usage of chemical warfare agents (CWA's) and the birth of modern chemical warfare [75]. In the modern era, the Chemical Weapons Convention has prohibited the production, stockpiling, and use of CWA's since 1997 [73]. Despite international efforts to the contrary, legislation has not proved to be a sufficiently effective deterrent. Most notably, the Syrian Civil War has seen repeated use of chemical weapons, starting with a Sarin attack on the Ghouta district of Damascus in 2013 [165]. A significant domestic event was the 2018 poisoning of Sergei and Yulia Skripal in Salisbury in 2018 [74]. The aftermath of a CWA attack requires emergency workers to be able to safely enter the contaminated area to treat the injured, assess damage, and begin the lengthy decontamination process. In order to perform their duties safely, emergency personnel require specially adapted clothing and respirator equipment to allow them to work safely. The protective clothing worn by military personnel consists of two layers; an outer layer of fabric

and an inner layer of an adsorbent material which prevents any toxic vapour or liquids from reaching the wearer. The outer layer is treated with a liquid repellent finish to act as a first line of defence and ensure that the adsorbent layer does not become saturated [75,166,167]. Plasma polymerized PFAC-8 was developed with the aim of creating such a coating for the outer layer of fabric. As discussed in the **Aim of Study**, environmental concerns mean that PFAC-8 and similar C8 perfluorinated compounds are being phased out. The work in this chapter focusses on forming an understanding of the wetting behaviours of CWA's on PFAC-*n* surfaces so that effective alternatives may be sought.

Working with CWA's is both difficult and potentially dangerous, and so preliminary testing takes place with CWA simulants. These are materials which mimic certain physical or chemical properties of a specific CWA (or groups of CWA's) but are less potently toxic than the CWA's themselves. [168,169]. In some cases, even the simulants may be dangerous in their own right. For example, the G-series nerve agents Sarin and Soman are both fluorophosphates, which contain the O=P—F functionality, and most compounds of this type are toxic to some degree [170]. This investigation will explore the wetting behaviour of both CWA's and their simulants.

The work in this chapter explores the wetting behaviour of Sarin, Soman, VX, and sulfur mustard on PFAC-*n* surfaces at room temperature. Several CWA simulants have been selected and their wetting behaviours on PFAC-*n* will also be explored. First, predictions of the contact angles of CWA's on PFAC-*n* will be made using the OWRK model; this will be performed using the surface energies of PFAC-*n* measured in previous chapters and by using literature values of the

surface energies of CWA's. Next, measurements of the contact angles of CWA's and simulants will be made. The measurements will be compared to the predicted values and discussed in context of the properties of the PFAC-n polymers explored in previous chapters – including polar and dispersive surface energies, and adaptive wetting properties.

5.1. Experimental

5.1.1. Selection of probe liquids

The CWA's used in this chapter were Sarin (GB[††]), Soman (GD[††]), VX[††], and sulfur mustard (HD[††]), the structures of which are shown in **Figure 5.1**. Dimethyl methylphosphonate (DMMP) and triethyl phosphate (TEP), the structures of which are shown in **Figure 5.2**, were also investigated as they are commonly used, readily available, and non-toxic simulants of the phosphorus-containing nerve agents (GB, GD, and VX). DMMP and TEP also have similar surface tensions to nerve agents (see **Table 5.1**) and similar sorption behaviour on a number of surfaces [171,172]. When it became apparent that the CWA's containing fluorine were exhibiting lower contact angles on the surfaces than expected, two additional fluorocarbon simulants were selected, these were 2,2,3,3-tetrafluoro-1-propanol (TFP) and 2,2,3,3,4,4,5,5-octafluoro-1-pentanol (OFP). These two fluorocarbons were selected because, like the phosphorus-based simulants, they have similar surface tensions to the three nerve agents, GB, GD, and VX. They are also some of the highest known surface tension fluorocarbon

[††] Acronyms are NATO weapon designations

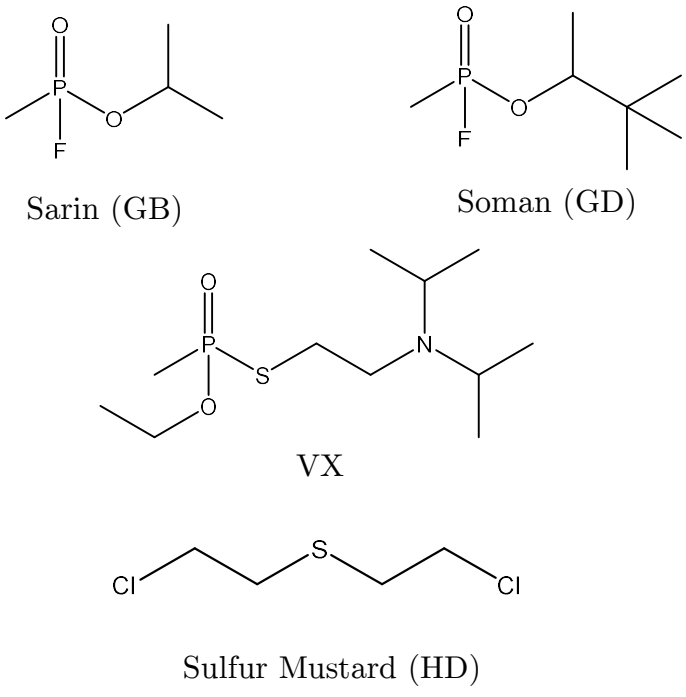


Figure 5.1 *Chemical structures of the CWA's used in this chapter*

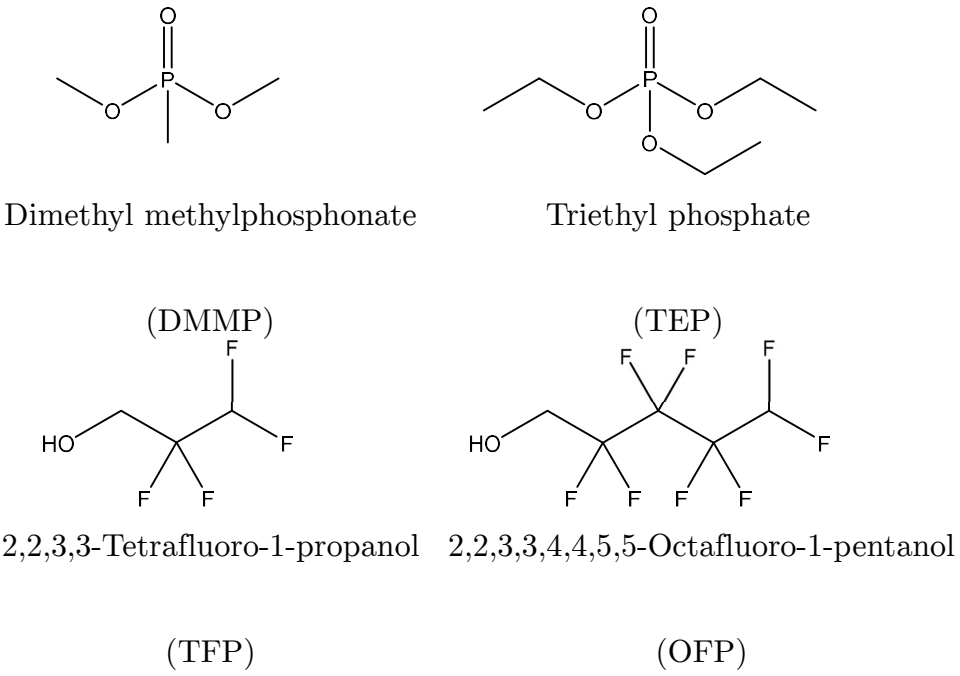


Figure 5.2 *Chemical structures of the simulants used in this chapter*

liquids which are readily available and OFP has been used previously in an investigation comparing the properties of PFAC-6 and -8 polymers produced under pulsed and continuous wave plasma conditions [173].

5.1.2. Contact angle goniometry of chemical warfare agents and simulants

Safety considerations concerning the extreme toxicity of CWA's impose a number of practical constraints when working with them. In the context of contact angle measurements, this meant that measurements were performed in a fume hood and 2 μl drops of liquid had to be manually deposited onto the surface, rather than being dispensed from a motorized syringe (as in previous chapters). This precluded the measurement of dynamic contact angles. A fume hood is not an optimal environment for contact angle measurements due to the high air flow and vibrations. In order to determine whether dispensation method and environment affected the contact angle, measurements using ethylene glycol and hexadecane were repeated using manual dispensation. Each measurement was repeated three times on each of the PFAC-n surfaces, and image capture and data analysis were performed as described in previous chapters.

The surface energy values calculated in the last chapter using the OWRK method and EG and n-HD as probe liquids were used to construct wetting envelopes of the PFAC-n surfaces [97,98]. A wetting envelope is a method of modelling the expected wetting behaviour for a solid with known $\gamma_{SV}{}^{p}$ and $\gamma_{SV}{}^{d}$. $\gamma_{LV}{}^{d}$ is plotted against $\gamma_{LV}{}^{p}$ using the equation

$$(1+\cos\theta)\gamma_{LV} = 2\sqrt{{\gamma_{SV}}^{p}{\gamma_{LV}}^{p}} + 2\sqrt{{\gamma_{SV}}^{d}{\gamma_{LV}}^{d}} \quad (5.1)$$

at a variety of values of θ. Liquids with known values of ${\gamma_{LV}}^{d}$ and ${\gamma_{LV}}^{p}$ are then added to the graph, which allows their contact angles to be predicted.

As well as the probe liquids from the previous chapter (ethylene glycol and hexadecane), the calculations were also performed using the surface tension values of the chemical warfare agents, as measured by Stone *et al.* [76] and set out in **Table 5.1**. The polar and dispersive components of the surface tensions of DMMP, TEP, TFP, and OFP have not been measured and are not available in the literature.

Material	$\boldsymbol{\gamma_{LV}}$ (mJ m^{-2})	$\boldsymbol{{\gamma_{LV}}^{d}}$	$\boldsymbol{{\gamma_{LV}}^{p}}$	**Ref.**
Dimethyl methylphosphonate (DMMP)	31.2	-	-	[173]
2,2,3,3,4,4,5,5-Octafluoro-1-pentanol (OFP)	24.5	-	-	[20]
Sarin (GB)	25.1	17.6	7.5	[76]
Soman (GD)	25.0	17.1	7.8	[76]
Sulfur mustard (HD)	43.3	39.0	4.3	[76]
2,2,3,3-Tetrafluoro-1-propanol (TFP)	27.6	-	-	[20]
Triethyl phosphate (TEP)	30.0	-	-	[20]
VX	29.4	28.9	0.5	[76]

Table 5.1 *Surface tensions of some liquid CWA's and their simulants used in this wetting study. The superscripts 'd' and 'p' refer to the polar and dispersive components of the liquids*

5.2. Results and Discussion

5.2.1. Predicting the contact angles of CWA's on PFAC-*n* using the OWRK method

Figure 5.3 shows the wetting envelopes for the PFAC-*n* polymers, which were constructed using the solid surface energy as measured in **Section 3.2.5** using the contact angles of EG and *n*-HD. The values of ${\gamma_{LV}}^d$ and ${\gamma_{LV}}^p$ for each of the CWA's has also been plotted using the surface energy values measured by Stone *et al.* [76] and the predicted contact angles for each of these liquids falls

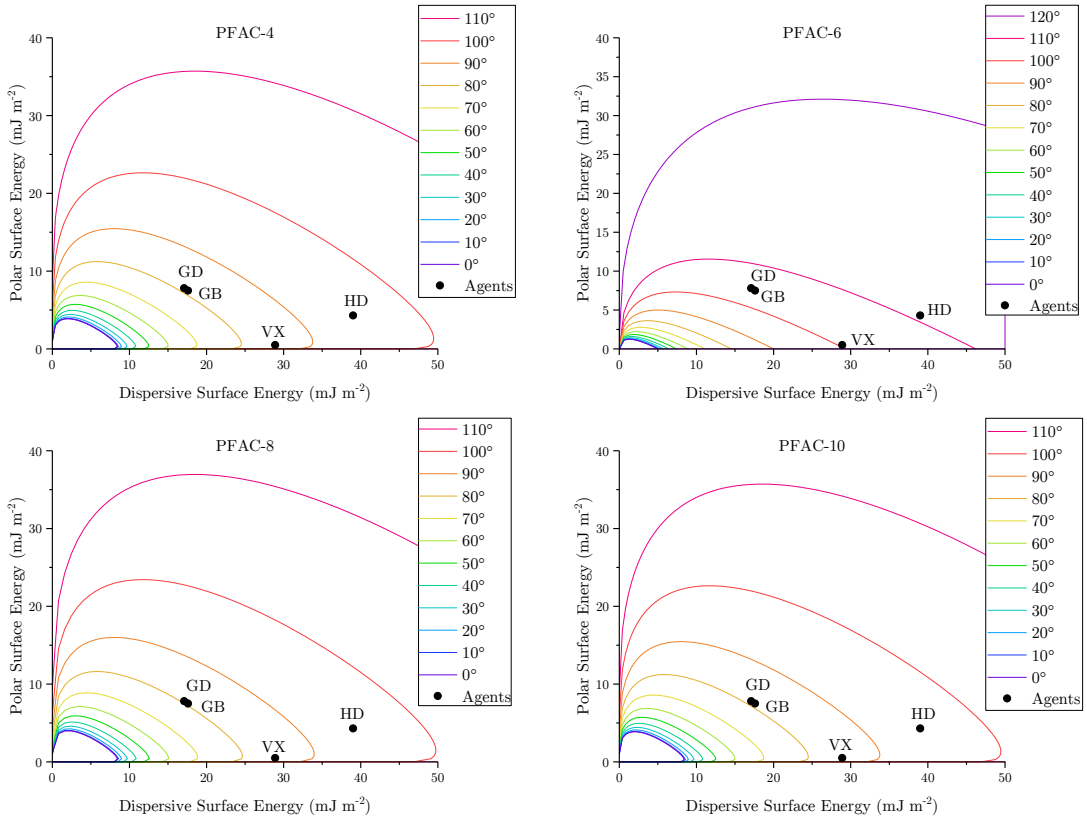


Figure 5.3 *Wetting envelopes for PFAC-n calculated using the contact angles of EG and n-HD and the OWRK method of calculating surface energy. The lines are* ${\gamma_{SV}}^p$ *and* ${\gamma_{SV}}^d$ *plotted for Eq. (5.1) using values of* θ_{stat} *at 10° intervals*

somewhere between the lines on either side. In the case of PFAC-4, -8, and -10, the predicted contact angles for GB, GD, and VX are in the range 80-90° (with GB and GD being at the lower end of this range) and the predicted contact angles for HD fall between 90-100°. For PFAC-6, the predicted contact angles for the CWA's are a little higher; 100-110° for GB, GD, and VX, and 110-120° for HD. In the case of PFAC-6, it is predicted that VX will have a lower contact angle than GB and GD.

5.2.2. Contact angles of CWA's and simulants

Repetitions of contact angle measurements using ethylene glycol and hexadecane using the manual dispense method did not significantly affect the results in comparison with the measurements made in the previous chapter.

Figure 5.4 shows the contact angles measured for the chemical warfare agents and simulants on the PFAC-n surfaces. **Figure 5.5** compares the measured CA's for the CWA's with those predicted from the wetting envelopes in previous sections. The results differ significantly from the predicted values; the contact angles of HD on PFAC-8 and -10 (89° and 91° respectively) match the predicted values, albeit at the lowest end of the range, but otherwise the contact angles are lower than predicted. The contact angle dependence on n also differs significantly from the trends reported in previous chapters for both CWA's and their simulants. Here, the contact angles generally increase with increasing n, whereas in previous chapters, the surface energy increased such that PFAC-6 $<$ 8 $<$ 10 $\approx$ 4, and the contact angles trended accordingly. As the surface with the shortest

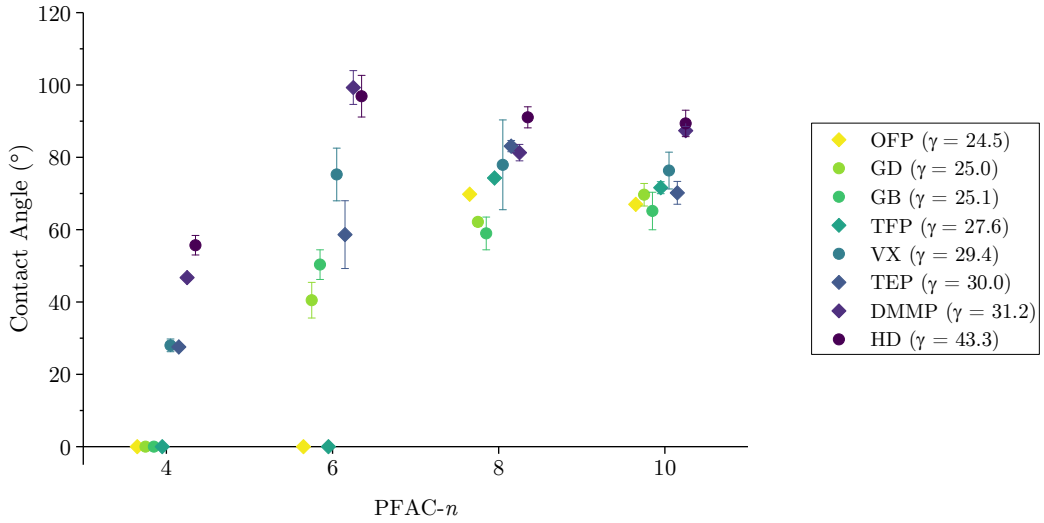


Figure 5.4 *Contact angles of chemical warfare agents (circles) and simulants (diamonds) on PFAC-n surfaces; the points have been offset in the x direction to allow overlapping points to be distinguished. The error bars show one standard deviation from the mean. The surface tension of each of the liquids is shown in the legend*

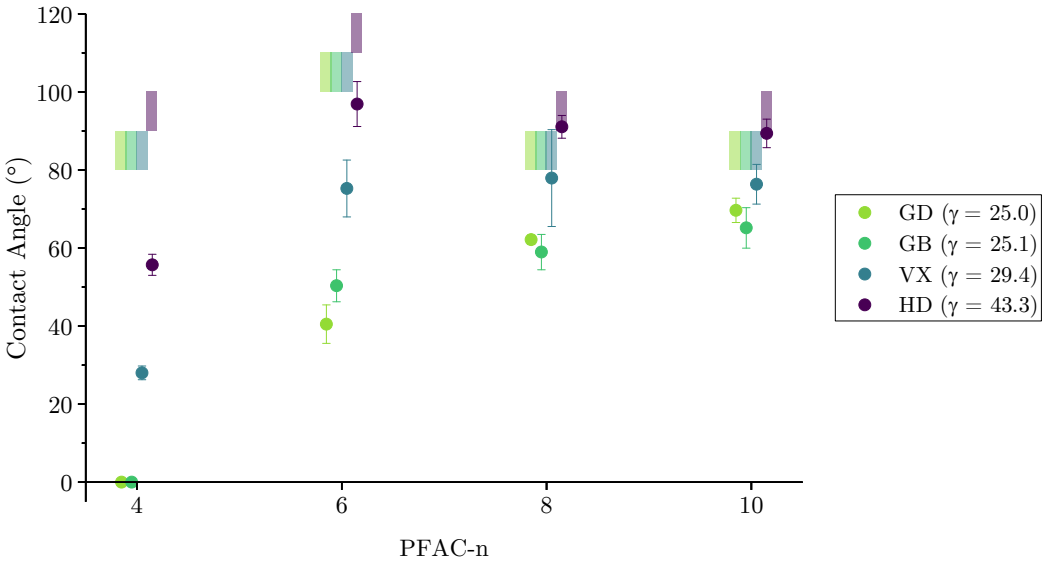


Figure 5.5 *Comparison between the measured contact angles (circles) of CWA's and the contact angles predicted using the wetting envelopes (range shown as a bar)*

side chains (smallest n), the contact angles on PFAC-4 are particularly low and GB, GD, OFP, and TFP spread completely on this surface. The fluorinated simulants, OFP and TFP also spread on PFAC-6. Examining the effect of n more

closely, the contact angles increase and start to plateau as n increases. The probe liquids with higher surface tensions level off at lower value of n and so the distribution of the contact angles narrows.

5.2.3. Discussion

This investigation has shown that surface energy estimates using the OWRK method with conventional probe liquids such as ethylene glycol and alkanes do not correctly predict the wetting behaviour of chemical warfare agents. This could reflect a failure of common probe liquids to accurately determine the surface energy of the PFAC-n surfaces, or it could represent a failure to accurately determine the surface energy components of the CWA's, or some combination of the two. Similarly, the investigation has shown that DMMP and TEP, despite their widespread use as simulants for GB and GD, do not predict the wetting behaviour of these CWA's on shorter-chain PFAC-n surfaces. Meanwhile, the two fluorinated simulants, OFP and TFP, mimic the spreading of GB and GD on PFAC-4, but then also spread on PFAC-6, in contrast with the CWA's.

Sections 1.1.1 and **4.2.4** discussed the weak nature of fluorocarbon-hydrocarbon interactions, and it has been shown that use of hydrocarbon probe liquids will underestimate the surface energy of fluorocarbons [26,157]. The fact that the two fluorinated simulants spread completely on PFAC-4 and -6 would indicate that this is the case. Previous work using the contact angles of fluorocarbons on PFAC-8 to calculate surface energy via the Zisman method estimated a surface energy of 20 mJ m^{-2} [173]. Although the difference in model does not make the results directly comparable with the results in this investigation, it is still significantly higher than the 10 mJ m^{-2} estimated in this

study. However, Stone *et al.* used paraffin wax as a means of determining the surface energy of components of the CWA's [76] which, as the CWA's are also hydrocarbon-based, should predict *lower* contact angles of the CWA's on fluorocarbons than is observed [21,152].

The various models used to determine solid surface energy via contact angle measurements also assume that the solid surfaces are inert, that is, they do not undergo any adaptive processes, and it may be that a process such as liquid sorption or polymer reorientation is responsible for the low contact angles observed. The dependence of the contact angle on n for PFAC-n surfaces suggests that surface reorientation effects may play a role in determining wetting behaviour of the CWA's and simulants. However, it seems unlikely that this is the dominant effect. As shown in **Table 5.2**, GB and GD are less polar than EG – both in an absolute sense, and as a proportion of the total intermolecular interactions. The acrylate group in the PFAC-n polymers is a hydrogen (H) bond acceptor, whilst EG is a H-bond donor and the phosphate group is an H-bond acceptor. Overall, the polar interaction between EG and the acrylate group is expected to be stronger than the polymer-surface interaction with any of the CWA's. As with EG, the presence of the hydroxyl group in OFP and TFP may help drive the spreading of these two liquids on PFAC-4 and -6. In the case where surface reorientation is triggered by the favourability of hydrocarbon-hydrocarbon interactions over hydrocarbon-fluorocarbon interactions, it would be expected that the alkyl phosphates (TEP and DMMP) would interact more strongly with the hydrocarbon moieties in the polymer than either GB or GD would. In all cases, it is not expected that GB and GD should trigger a higher degree of surface

reorganization (and therefore greater degree of spreading) than several of the other probe liquids.

Material	γ_{LV} (mJ m^{-2})	$\gamma_{LV}{}^{d}$	$\gamma_{LV}{}^{p}$	$\gamma_{LV}{}^{p}/\gamma_{LV}{}^{d}$
Ethylene Glycol (EG)	48.4	26.8	21.6	0.81
n-Hexadecane (*n*-HD)	27.5	27.5	0	0.00
Sarin (GB)	25.1	17.6	7.5	0.43
Soman (GD)	25.0	17.1	7.8	0.46
Sulfur mustard (HD)	43.3	39.0	4.3	0.11
VX	29.4	28.9	0.5	0.02

Table 5.2 *The surface energies of EG and n-HD and the CWA's, including the ratio of the polar and dispersive components*

Continuing on the theme of adaptive wetting; the sorption properties of CWA's and simulants to PFAC-*n* surfaces has not been investigated here but could provide an explanation for the observed wetting behaviours. In particular, the increased molecular mobility in the PFAC-4 and -6 surfaces may allow the CWA and simulant molecules to diffuse into the polymers more easily than the longer chain PFAC-8 and -10 polymers [174]. This effect is likely to be more pronounced for the two fluorinated simulants, which will interact more strongly with the fluoroalkyl side chains in PFAC-*n*. Jing *et al.* conducted molecular dynamics (MD) simulations of the interactions between organophosphates and fluoroalkylsilane self-assembled monolayers (SAM's) on silica [175]. This study showed that the phosphates exhibited stronger interactions with the C6 perfluorinated SAM's than the C8 perfluorinated SAM's. This was due to the P=O moiety being able to penetrate more deeply into the more mobile C6 brush and thus interacting more strongly with the underlying silica substrate. However,

the surface coatings used in this thesis are several orders of magnitude thicker than a SAM [166] and it is therefore not expected that the interaction between liquids and PFAC-n would be driven by underlying substrate. Comparing the sorption of different organophosphates showed that smaller molecules were able to diffuse more easily into the polymer structure. In the context of the work in this thesis, it would therefore be expected for DMMP to exhibit greater sorption into the polymers in comparison to the other CWA's and phosphorus-based simulants.

To attempt an explanation of these observations, it is noted that that both GB and GD, which exhibit the lowest contact angles on PFAC-n, contain fluorine. It is hypothesised that the fluorine-fluorine self-interaction enhances the liquid-surface interaction compared to non-fluorinated probe liquids. This would result in both enhanced adhesion and enhanced sorption of GB and GD on PFAC-n surfaces, particularly PFAC-4 and -6, which are both more fluorinated at the surface, and are more mobile.

5.3. Conclusions

Spreading of chemical warfare agents on low-energy surfaces has not been reported in the literature, and these initial measurements are reported here. Indeed, other studies on fluorinated surfaces have reported good repellency of CWA's [176,177]. On a similar vein, MD work by Jing *et al.* reports results where the interaction between organophosphates and a fluorinated SAM is primarily driven by the underlying polar substrate, which is unlikely to apply to a coating which is hundreds of nm thick. Overall, a complex picture emerges, where the

wetting behaviour of CWA's cannot be rationalised using simple OWRK theory, or by using conventional probe liquids such as water, ethylene glycol, and alkanes. Although the disparity between measured and predicted wetting behaviour was greatest for GB and GD, the results for VX and HD also fell short of predicted values. It is not clear whether this disparity is specific to the PFAC-n system, or whether it represents a more general failing of the model. As outlined in the introduction, both TEP and DMMP are commonly used simulants for GB and GD and are largely regarded as good indicators of the behaviour of CWA's on solid surfaces [168,178]. The work in this chapter has shown that the efficacy of these simulants requires further exploration.

The mechanism which drives the low contact angles of CWA's, and of GB and GD in particular, is not clear. It has been hypothesised that the lower than predicted contact angles of GB and GD may be a result of the interaction of the fluorinated moiety in these liquids with the fluorinated surfaces. Although the use of fluorinated CWA simulants has been avoided in this study due to safety considerations, further investigation with these liquids could shed further light on this matter.

5.4. References

[20] J. J. Jasper, Journal of Physical and Chemical Reference Data **1**, 841 (1972).

[21] W. Zisman, in *Contact Angle, Wettability, and Adhesion* (American Chemical Society, 1964), pp. 1.

[26] J. Mecinovic, P. W. Snyder, K. A. Mirica, S. Bai, E. T. Mack, R. L. Kwant, D. T. Moustakas, A. Heroux, and G. M. Whitesides, Journal of the American Chemical Society **133**, 14017 (2011).

[73] United Nations Convention on the Prohibition of the Development, Production, Stockpiling and Use of Chemical Weapons and on their Destruction, Opened for signature 13th January 1993 entered into force 29th April 1997.

[74] Novichok Nerve Agent use in Salisbury: UK Government Response, https://www.gov.uk/government/news/novichok-nerve-agent-use-in-salisbury-uk-government-response (Accessed 2nd May 2018).
[75] A. Richardt, *CBRN Protection: Managing the Threat of Chemical, Biological, Radioactive and Nuclear weapons* (Wiley-VCH, Weinheim, 2013).
[76] C. A. Stone, T. G. D'Onofrio, and S. J. Pritchard, Determination of the Surface Energy Components of a Variety of CW agents and the Effects of Impurities on Measured Parameters, 2017.
[97] D. K. Owens and R. C. Wendt, Journal of Applied Polymer Science **13**, 1741 (1969).
[98] D. H. Kaelble, Journal of Adhesion **2**, 66 (1970).
[152] F. M. Fowkes, Industrial & Engineering Chemistry **56**, 40 (1964).
[157] M. K. Chaudhury and G. M. Whitesides, Science **255**, 1230 (1992).
[165] J. P. Zanders, European Union Institute for Security Studies, SSUE Brief **33** (2013).
[166] S. A. Brewer, C. A. Stone, M. J. Summers, and C. R. Willis, in *International Symposium on New Frontiers in Fiber Materials Science* Charleston, South Carolina, USA, 2011).
[167] P. Malshe, PhD Thesis, North Carolina State University, 2011.
[168] S. L. Bartelt-Hunt, D. R. U. Knappe, and M. A. Barlaz, Critical Reviews in Environmental Science and Technology **38**, 112 (2008).
[169] S. R. Bennett, *Environmental hazards of chemical agent simulants* 1984).
[170] B. C. Saunders and A. R. Todd, *Some Aspects of the Chemistry and Toxic Action of Organic Compounds Containing Phosphorus and Fluorine* (University Press Cambridge:, 1957).
[171] E. D. Davis, W. O. Gordon, A. R. Wilmsmeyer, D. Troya, and J. R. Morris, The Journal of Physical Chemistry Letters, 1393 (2014).
[172] A. A. Gorzkowska-Sobas, Chemical Warfare Agents and their Interactions with Solid Surfaces, 2013.
[173] E. P. Milnes-Smith, Thesis for Master of Chemistry, University of Oxford, 2014.
[174] D. Paul, Berichte der Bunsengesellschaft für Physikalische Chemie **83**, 294 (1979).
[175] C. Jing, PhD Thesis, North Carolina State University, 2015.
[176] W. O. Gordon, G. W. Peterson, and E. M. Durke, ACS Applied Materials & Interfaces **7**, 6402 (2015).
[177] P. Malshe, M. Mazloumpour, A. El-Shafei, and P. Hauser, Surface and Coatings Technology **217**, 112 (2013).
[178] J. Lavoie, S. Srinivasan, and R. Nagarajan, Journal of Hazardous Materials **194**, 85 (2011).

6. Solid-State Nuclear Magnetic Resonance Spectroscopy Studies of Fluoroalkyl Acrylate Polymers

The work so far in this thesis has focussed on the surface properties of PFAC-n polymers and the majority of characterization techniques up to this point (CA goniometry, XPS, and AFM) are sensitive only to the top few nanometres of surface material. Although the PFAC-n polymeric side chains at the surface exhibit different behaviour in terms of ordering and mobility to those in the bulk, their behaviour is still governed overall by bulk behaviour [124,156]. For example, surface rearrangement of PFAC-8 is only able to occur above the bulk melting point. NMR is a bulk sensitive technique, which is used extensively to characterize the composition, conformation, and mobility of polymer systems [179-184]. The work in this chapter uses solid-state ^{19}F NMR to characterize some of the bulk properties of the PFAC-n polymers, including their morphology and molecular mobility characteristics.

The ^{19}F nucleus is particularly well suited to NMR studies; it has an abundance of 100 %, it has high sensitivity (83 % compared to ^{1}H) due to its large magnetogyric ratio, and it has a spin of 1/2. The chemical shift range is approximately 300 ppm, which results in well-defined and well-separated peaks

and allows subtle changes in environment to be observed [185]. This is particularly useful in the context of solid-state NMR, where the peaks are broader owing to the chemical shift anisotropy (CSA) (see **Section 6.1.2**). Magic angle spinning (MAS) can be used as a means of averaging out CSA to produce narrower peaks, enhancing the resolution of the technique further. This high level of sensitivity means that ^{19}F MAS NMR is able to probe not just the immediate, intramolecular environment of the fluorine nucleus, but also the local, intermolecular environment. The technique has been used to examine the aggregation structure of semifluorinated alkanes [158], perfluoroalkanoic SAM's [186], fluorinated micelles [187,188], and fluoropolymers [189,190]. Unlike techniques such as WAXD, it does not rely on the presence of long-range order; this is particularly useful for investigating the properties of the PFAC-n polymers with shorter side chains.

As with the DSC results presented earlier on in this investigation, solid-state NMR can be used as a means of examining phase transitions in polymers. In particular, NMR relaxometry can also be used to investigate the more subtle range of molecular motions which may occur above and below the phase transitions [189,191,192]. The work in this investigation uses the spin-lattice relaxation time (T_1) to investigate the molecular motion in the PFAC-n side chains. This relaxation corresponds to the segmental motions within the polymer which occurs on the timescale of hundreds of milliseconds to seconds. This is the approximate timescale of the drop aging experiments in **Chapter 4.**

In this chapter, the ^{19}F MAS NMR spectra have been acquired at temperatures ranging from 0-100 °C in 10 °C intervals. These spectra will be examined in terms

of changes in chemical shift, peak width, and sidebands. The spin-lattice relaxation time will also be examined across the same temperature range, and discussed in terms of molecular mobility.

6.1. Background

6.1.1. Nuclear Magnetic Resonance [193,194]

All nuclei have an intrinsic angular momentum, known as *spin*, which is characterized in terms of a *spin quantum number, I,* which can take the values 0, $^1/_2$, 1, $^3/_2$, 2... etc. Nuclei with an even number of protons *and* an even number of neutrons have $I = 0$. Nuclei with an odd number of protons and/or neutrons will have $I > 0$, and have non-zero angular momentum, and a non-zero magnetic moment. The nuclear magnetic moment is quantized into $2I + 1$ directions, described by the magnetic quantum number, m, such that

$$m = I, I - 1, I - 2, \ldots -I. \tag{6.1}$$

A nucleus with $I = {}^1/_2$ will therefore have two energy levels, corresponding to $m = + {}^1/_2$ and $m = - {}^1/_2$, which will be degenerate in the absence of an applied magnetic field. As soon as a magnetic field is applied, the spins align either parallel (low energy), or anti-parallel (high energy) to the field, with the populations of the energy levels being determined by Boltzmann statistics. The energy of a given level, E, is given by

$$E = -m\hbar\gamma B, \tag{6.2}$$

where B is the strength of the applied magnetic field, and γ is the magnetogyric

ratio of the nucleus. The selection rule $\Delta m = \pm 1$ applies to transitions between energy levels, giving the resonance condition

$$\Delta E = \hbar \gamma B, \tag{6.3}$$

and the resonance frequency,

$$\nu_{\mathrm{NMR}} = \frac{|\gamma| B}{2\pi} \ . \tag{6.4}$$

The resonance frequency is characteristic of an individual nuclide. However, building up from an isolated nucleus, to atoms, molecules, and bulk structures requires consideration of the role of electrons, and how nuclei interact with one another.

This thesis will only deal with ^{19}F nuclei, where $I = {}^1/_2$. Although not considered here, nuclei with $I > {}^1/_2$ are referred to as quadrupolar and possess an electric quadrupole in addition to their magnetic dipole – something which impacts the interactions discussed in the following sections.

6.1.2. Nuclear shielding and chemical shift [193,195]

The magnetic field actually experienced by the nucleus in an atom differs from that experienced by a bare nucleus. The application of a magnetic field causes the electrons to precess in opposition to the applied field, partially shielding the nucleus from the external field. The resonance frequency associated with an atom is known as the Larmor frequency,

$$\nu_0 = -\frac{\gamma B}{2\pi}(1 - \sigma) \ , \tag{6.5}$$

where σ is the shielding constant. The sign of ν_0 describes the direction of precession around the magnetic field vector.

In a molecule, adjacent substituent will affect the electron density around the nucleus and may also set up currents of electrons – both of which will affect the shielding of the nucleus. NMR therefore allows the chemical environment of a nucleus to be determined. Rather than attempting to measure the shielding constant in absolute terms, it is more practical to define the chemical shift, δ, as a dimensionless parameter in terms of a reference nucleus such that

$$\delta = 10^6 \frac{(\nu_0 - \nu_{0,\,\mathrm{ref}})}{\nu_{0,\,\mathrm{ref}}}. \tag{6.6}$$

The distribution of electrons around a nucleus is not typically spherical – it is anisotropic. The chemical shift therefore depends on the orientation of the molecule with respect to the magnetic field.

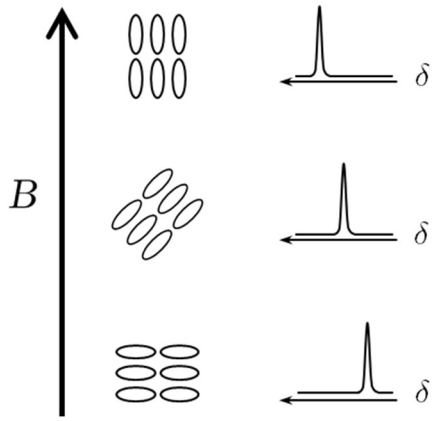


Figure 6.1 *Chemical shift dependence on the orientation of a particle, relative to the magnetic field,* $\boldsymbol{B}$

Figure 6.1 depicts the change in peak position in NMR spectra of a single crystal at different orientations relative to the magnetic field; a spectrum of a powdered sample would be a weighted superposition of the single crystal spectra. In the liquid state, the molecules tumble rapidly in comparison to the NMR timescale, and so the observed signal is a sharp peak at the average chemical shift.

6.1.3. Spin-spin coupling

Much like two classically interacting magnetic dipoles, spins are able to interact with one another through space – a phenomenon which is known as dipolar coupling. This type of coupling is dependent on the separation and relative orientation of the spins. For a single crystal containing a pair of heteronuclear spins (AX), both with $I = {}^1/_2$, the peak from A will be split into a doublet, as it interacts with the two possible spin states of X (see **Figure 6.2**). As in the case for chemical shift anisotropy, the spectrum of a powder will be a superposition of single crystal spectra from the range of possible dipole orientations. As before, the rapid and isotropic tumbling of particles in a liquid means that dipolar coupling is averaged on the NMR timescale.

As well as direct-, through-space, coupling of the spins, coupling can also be mediated by the valence electrons separating the nuclei – it can be said to occur through bonds. This form of coupling is commonly referred to as *J*-coupling. Unlike dipolar coupling, *J*-coupling interactions are not averaged out in liquids and are consequently used extensively for structural elucidation in solution state NMR. However, *J*-coupling is a weaker interaction than dipolar coupling, with coupling constants typically falling in the range 1-100 Hz, whilst dipolar coupling

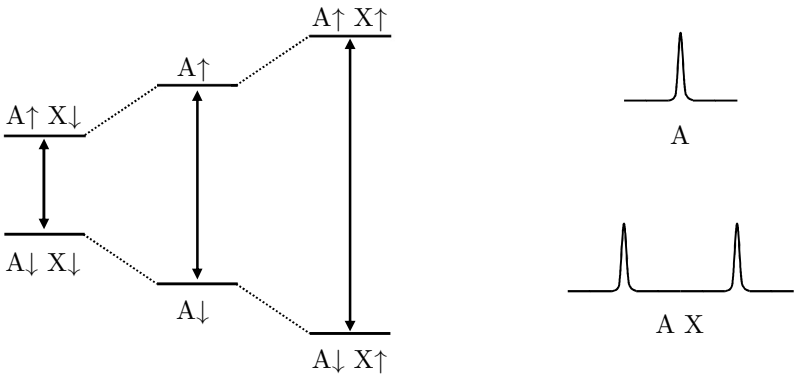


Figure 6.2 *Spin-spin coupling between nuclei A and X, both with $I = {}^1/_2$, leads to the splitting of energy levels, and the formation of a doublet in the spectrum of A*

constants fall in the range 1-100 kHz. For this reason, splitting due to *J*-coupling is not always visible in solid-state NMR spectra, as it can be masked by more prominent effects from dipolar coupling, and from chemical shift anisotropy.

6.1.4. Magic angle spinning (MAS)

As discussed in the preceding sections, anisotropic interactions between nuclei lead to broader, more complex peaks in solid-state NMR (unless the sample is a single crystal, which is not typically the case). However, the use of a technique known as *magic-angle spinning* (MAS) allows these anisotropic interactions to be averaged out to some extent, resulting in a spectrum with sharper, more resolved peaks.

Figure 6.3 a) depicts a dipole placed at the origin of an (x, y, z) co-ordinate system, and pointing along the positive z axis. The dipole produces a magnetic field which, at the polar co-ordinates (r, θ), has a component in the z direction of

$$B_z = \left(\frac{\mu_0 \mu}{4\pi r^3}\right)(3\,cos^2\,\theta - 1)\ , \tag{6.7}$$

where μ_0 is the vacuum permeability, and μ is the magnitude of the dipole. The anisotropic contributions to shielding, and to coupling therefore have an angular dependence proportional to $(3\,cos^2\,\theta - 1)$. At $\theta = 54.7°$, the term $(3\,cos^2\,\theta - 1) = 0$, and so the anisotropic terms average out; dipolar coupling to zero, and chemical shift anisotropy to a non-zero value. Magic angle spinning (MAS), involves rotating the sample about an axis tilted 54.7° (the "magic angle") to the magnetic field vector, $\boldsymbol{B}$, as depicted in **Figure 6.3 b)**.

In order to achieve sharply resolved peaks, the frequency of rotation should be larger than the width of the peak in the static spectrum. Dipolar coupling constants are typically larger than CSA's, with magnitudes in the range of 1-100

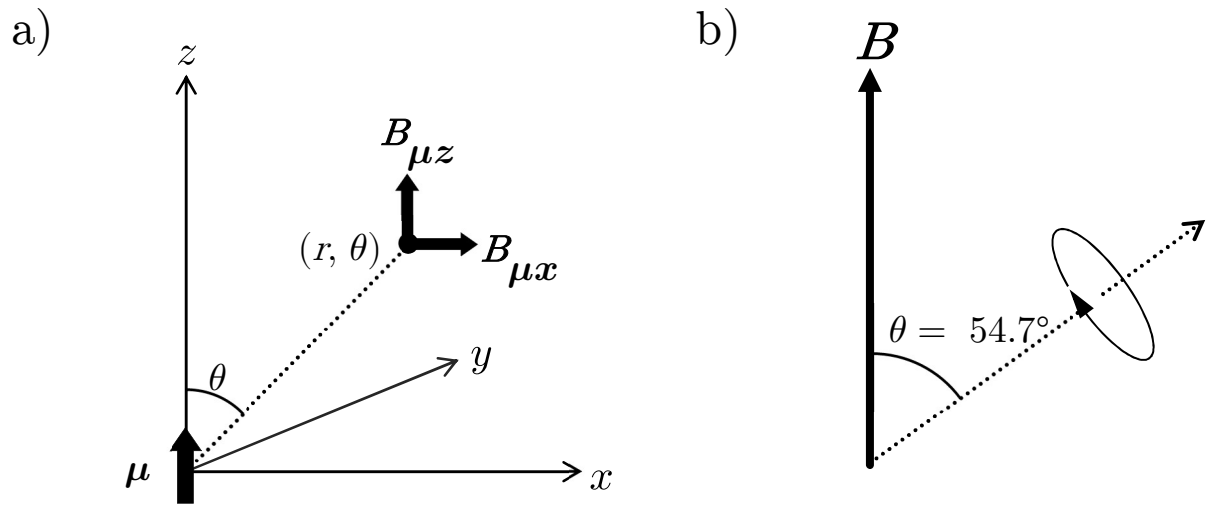


Figure 6.3 a) *A magnetic dipole, μ, placed at the origin, and pointing in the z-direction, produces a magnetic field, B_μ. The magnitude of the field in the z-direction at position (r, θ) is described in* **b)** *Rotation of the sample about an axis at an angle of 54.7° to the magnetic field vector, $\boldsymbol{B}$, is known as 'magic angle spinning' (MAS). Adapted from Ref. [193]*

kHz, whilst MAS typically falls in the range of tens of kHz; MAS may therefore not completely average out all anisotropic interactions, depending on the identity of the sample, and the equipment available. An additional complication of MAS is that fact that **Eq. (6.7)** is periodic; this leads to the appearance of satellite peaks, or *sidebands*, at intervals of $\pm\frac{n\nu_0}{2\pi}$ from the central peak. Whilst the position of the central peak does not depend on the frequency of MAS, sidebands can be distinguished by their frequency dependence. Thus, it is usually necessary to repeat the MAS experiment at two different frequencies. Furthermore, although not discussed here, it should be noted that quadrupolar coupling constants are larger still, falling in the range of 200 kHz [196].

6.1.5. NMR relaxation

Having been excited to a higher energy state, spins will eventually relax back to their equilibrium state. Neglecting quadrupolar interactions, which involve electric field effects, relaxation occurs because of inhomogeneities in the local magnetic field. Relaxation mechanisms involve radiationless energy transfer and are broadly split into two categories – *spin-lattice relaxation* (T_1), which describes equilibration in the direction parallel to the magnetic field vector, and *spin-spin relaxation* (T_2), which describes equilibration perpendicular to the magnetic field vector.

Spin-lattice relaxation occurs due to the transfer of energy from the excited spin system to the molecular motions of the surrounding molecules (the lattice), where it is dissipated as heat. As relaxation occurs, fewer spins are oriented along the magnetic field vector, and the intensity of the NMR signal decays. Spin-spin

relaxation when energy is transferred between spins, resulting in a loss of coherence in the xy plane. The loss of phase results in a broader NMR signal. The time constants associated with spin-lattice relaxation, and spin-spin relaxation are called T_1 and T_2 respectively, whereby

$$\frac{dM_z(t)}{dt} = \frac{M_z^0 - M_z(t)}{T_1} \ , \tag{6.8}$$

and

$$\frac{dM_{xy}(t)}{dt} = -\frac{M_{xy}(t)}{T_2} \ , \tag{6.9}$$

where M_z and M_{xy} are the magnetization vectors of the spins in the z direction and xy plane respectively, M^0 denotes the equilibrium magnetization vector, and t is time.

In spin $^1/_2$ nuclei, the primary mechanism of relaxation is via instantaneous coupling of dipoles during molecular motion. For this process to be efficient, the molecular motion must create a fluctuation in the local magnetic field with a component which corresponds to ν_0. Tumbling of molecules and rotations within a molecule operate on the NMR timescale, and so it is these motions which contribute to relaxation processes. Conversely, relaxation times can also be used to extract information on molecular mobility. For spin-lattice relaxation, paramagnetic, scalar, chemical shift anisotropy, and spin-rotation mechanisms also apply; for spin-spin relaxation, inhomgeneities in the applied magnetic field may contribute.

6.2. Experimental

6.2.1. Sample preparation

PFAC-4, -6, -8 and -10 were all deposited onto ground glass, in the same way as the PFAC-4 and -6 samples were prepared for DSC experiments described in **Section 3.1.4**. The PFAC-8 and -10 samples were also annealed for 3 hours at 150 °C prior to use.

6.2.2. Acquisition of one dimensional ^{19}F spectra at variable temperatures

Experiments were carried out using a Bruker Avance III spectrometer, operating at ~376 MHz for ^{19}F detection, and using a 3.2 mm HFX probe. $CFCl_3$ was used as an external reference. Spectra were acquired with 16 scans, having a 90° pulse width of 2.5 μs, and a delay time of less than 10 s. All spectra were acquired using magic angle spinning (MAS) at a rate of 20 kHz. Variable temperature experiments were carried out at temperatures of 0-100 °C, at increments of 10 °C. To take into account the heating of the sample due to friction at high spinning speeds, the temperature was calibrated using ^{207}Pb spectra of lead (II) nitrate [197]. Data analysis was carried out using Topspin 3.2 software.

6.2.3. Measurement of spin-lattice (T_1) relaxation times

Spin-lattice relaxation times (T_1) were measured at a variety of temperatures using the inversion-recovery method. The intensities of spectral peaks, I_τ, were plotted against the delay times, τ, and T_1 was determined by assuming the relationship

$$I_\tau = I_\infty + A \exp\left(\frac{-\tau}{T_1}\right) \ , \tag{6.10}$$

where A is an arbitrary constant, and I_∞ is taken by convention to be the peak intensity at $\tau \gg 5T_1$, where the magnetization vector has effectively returned to equilibrium after the initial application of the 180° pulse.

The pulse sequence for the inversion-recovery experiment is depicted in **Figure 6.4**. The experiment begins with the application of an 180° pulse to invert the magnetization vector so that it points down the -z axis. The system then undergoes spin-lattice relaxation and starts to return to equilibrium. Before equilibration can occur, and after a delay time, τ, a 90° pulse is applied to the system. The magnetization vector flips to the xy plane and rotates around the z axis, giving a measurable free induction decay (FID). The process is then repeated at multiple different delay times.

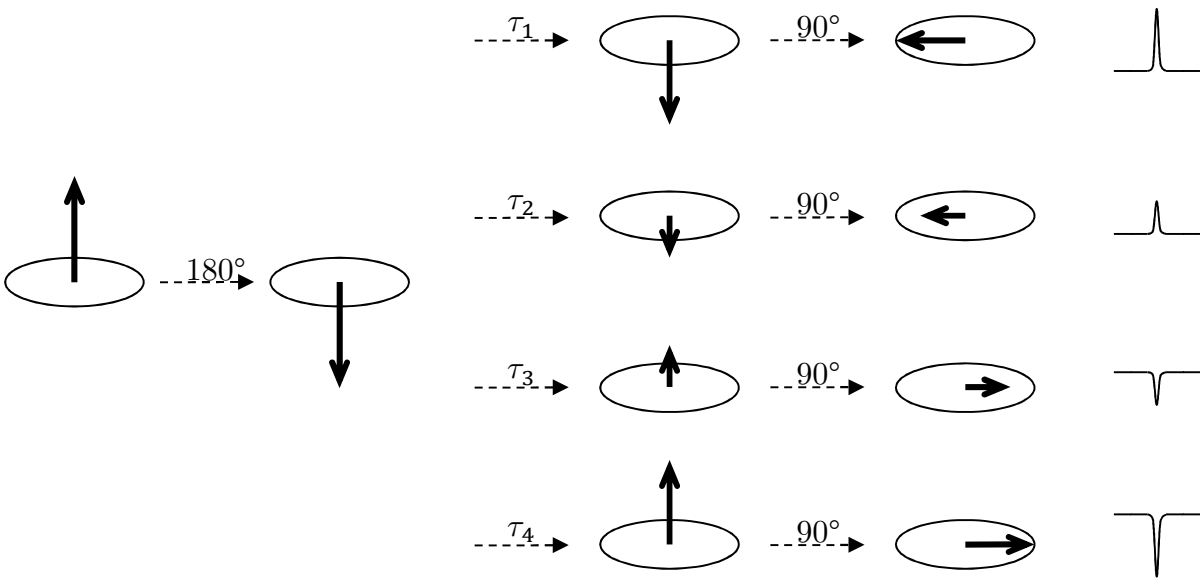


Figure 6.4 *Pulse sequence and magnetization vectors for an inversion-recovery experiment*

6.3. Results and Discussion

Calibration of the temperature using lead nitrate showed that the heating due to friction raised the sample temperature to 13-18 °C above the set temperature. All results shown in this section will use the calibrated sample temperature.

6.3.1. Room temperature spectra

The results in this section were acquired at an experimental temperature of 10 °C, which corresponds to a sample temperature of 24 °C.

Figure 6.5 shows the ^{19}F NMR spectra of the PFAC-n polymers along with peaks assignments (sidebands are marked with asterisks). In all cases, there is a single, narrow C$\underline{F}_3$ peak, a broad C$\underline{F}_2$—CH_2 peak, a narrower C$\underline{F}_2$—CF_3 peak, and a C$\underline{F}_2$—CF_2 resonance. In the latter case, there are a different number of C$\underline{F}_2$—CF_2 moieties in each of the PFAC-n polymers as the value of n increases. In the case of PFAC-4, there is a single peak corresponding to a single C$\underline{F}_2$—CF_2 moiety. In the case of PFAC-n with longer fluorinated side chains, the primary C$\underline{F}_2$—CF_2 has a shoulder, which indicates the presence of multiple moieties, but there is not complete splitting of these peaks at room temperature. As discussed in **Section 3.2.1**, the absence of C$\underline{F}$, CF(C$\underline{F}_3$)$_2$, and C(C$\underline{F}_3$)$_2$ peaks indicates good structural retention of the polymer; these peaks are present in spectra of fluoropolymers generated by continuous wave plasmas, but not those produced under pulsed conditions [88,100,101].

Figure 6.6 shows the chemical shifts, δ, of the C$\underline{F}_3$, C$\underline{F}_2$—CH_2, and C$\underline{F}_2$—CF_3 peaks for each of the PFAC-n polymers. The C$\underline{F}_3$ peak is shifted furthest

downfield for PFAC-4 such that δ follows the trend PFAC-10 $\approx$ PFAC-8 $<$ PFAC-6 $<$ PFAC-4. Moving to the adjacent C$\underline{F}_2$—CF_3 group trend is PFAC-10 $\approx$ PFAC-8 $\approx$ PFAC-6 $<$ PFAC-4. The C$\underline{F}_2$—CH_2 group, which is closest to the polymeric backbone, follows a different trend in that δ decreases in the order PFAC-6 $<$ PFAC-4 $<$ PFAC-8 $<$ PFAC-10. Despite the relatively high MAS frequency, sidebands are visible in all spectra. Both PFAC-10 and -8 have two sidebands for each peak within the spectral range, whilst the PFAC-4 and PFAC-6 spectra have a single, low-intensity sideband which corresponds to the CF_3 peak. The CSA for the CF_3 resonance is ~ 45 ppm for PFAC-10, ~40 ppm for PFAC-8, and ~20 ppm for both PFAC-6 and -4. For the C$\underline{F}_2$—CH_2 group, at the other end of the side chain, the CSA is ~ 85 ppm for both PFAC-8 and -10. The enhanced motion of the CF_3 group in comparison to the other functional groups will result in a lower CSA and less intense sidebands in comparison to the other functional groups. However, the greater intensity of the CF_3 primary peak in comparison to the other CF_2 peaks in the PFAC-4 and -6 spectra is why none of the sidebands from the CF_2 peaks are visible, and why their CSA's cannot be determined.

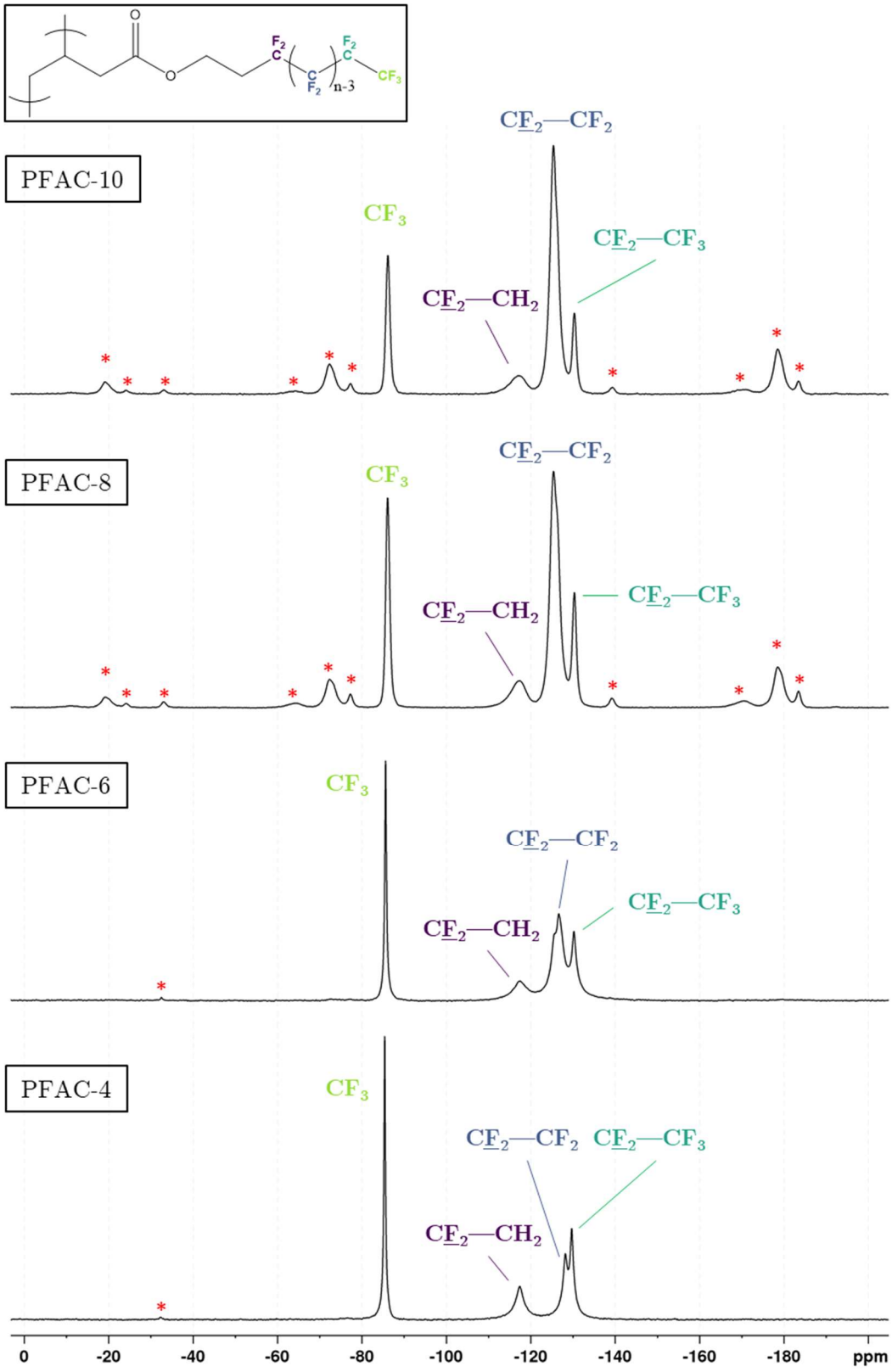


Figure 6.5 *^{19}F NMR spectra of PFAC-n polymers acquired at room temperature with a MAS frequency of 20 kHz. Asterisks denote side-bands, which occur at integer multiples of the MAS frequency away from the primary peak. Peak assignments are from Refs. [102,103]*

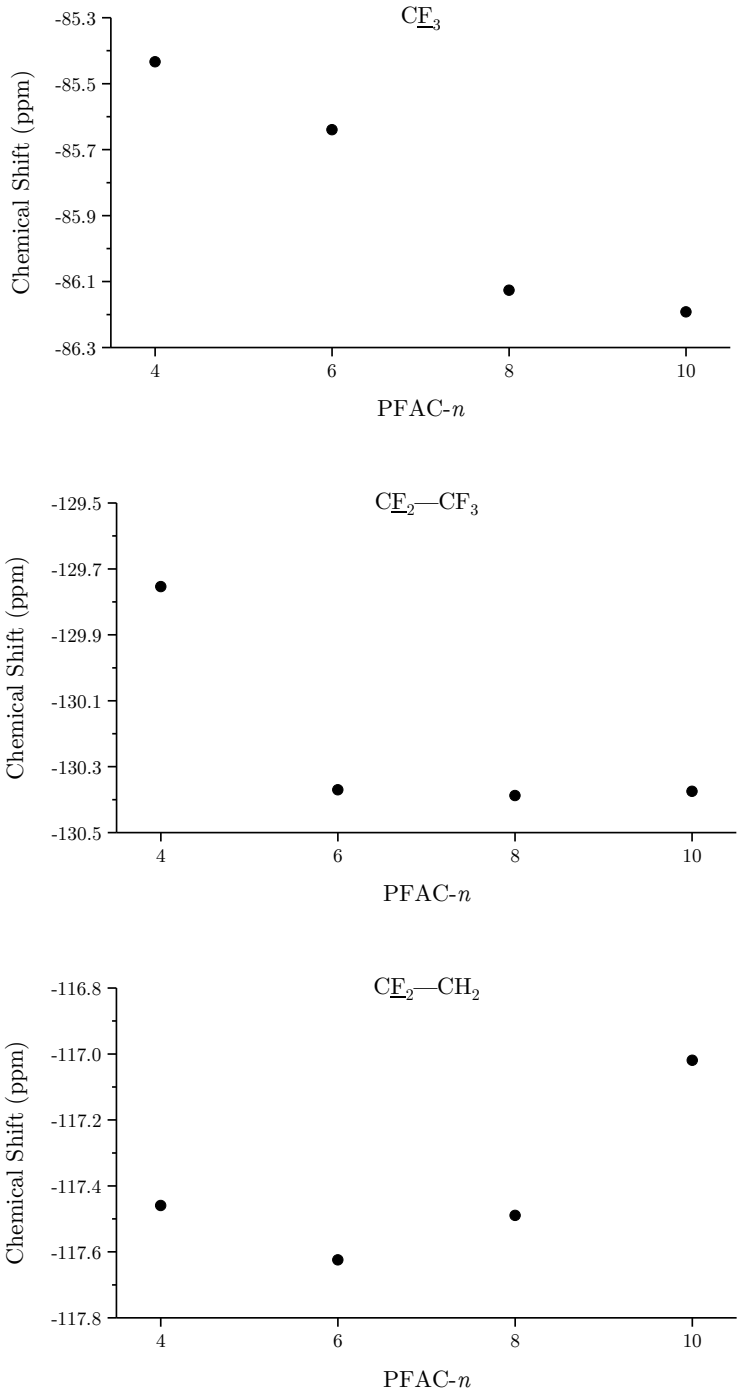


Figure 6.6 *Chemical shifts of the C<u>F</u>3, C<u>F</u>2—CF3, and C<u>F</u>2—CH2 groups in the ^{19}F NMR spectra of PFAC-n. Note that the y axes are at different positions, although span the same range*

6.3.2. Variable temperature spectra

Figure 6.7 to **Figure 6.10** show the variable temperature ^{19}F NMR spectra of the PFAC-n polymers, with change in δ between the lowest and highest temperatures also being marked. For the PFAC-10 spectra (**Figure 6.7**), the changes in the spectra are as a result of the motional narrowing of the peaks as the temperature increases. This motional narrowing is particularly apparent for the C$\underline{F}_2$—CH_2 peak, which is closest to the polymeric backbone and is therefore the least mobile fluorinated moiety. Along with the narrowing of the peaks, δ also sees a gradual increase with increasing temperature. At lower temperatures, the PFAC-8 spectra (**Figure 6.8**) follows similar behaviour to the PFAC-10 spectra. However, as the temperature traverses the melting point, the sidebands rapidly decrease in intensity, indicating a transition from solid-like to liquid-like behaviour. At the same time, the peaks narrow and the contributions from the individual C$\underline{F}_2$—CF_2 moieties start to separate out as the temperature increases further; by 118 °C, three contributions are discernible. The value of δ increases with temperature in a similar order of magnitude as for PFAC-10.

Both the PFAC-6 and PFAC-4 (**Figure 6.9** and **Figure 6.10** respectively) undergo motional narrowing as the temperature increases, although the peaks in the more mobile PFAC-4 are narrower to begin with. As with PFAC-8 above its melting point, the individual CF_2—CF_2 contribution in the PFAC-6 spectra start to separate out as the temperature increase and all three are visible by 118 °C. Again, the value of δ increases with temperature, although in both cases the increase is less than for either PFAC-8 or PFAC-10.

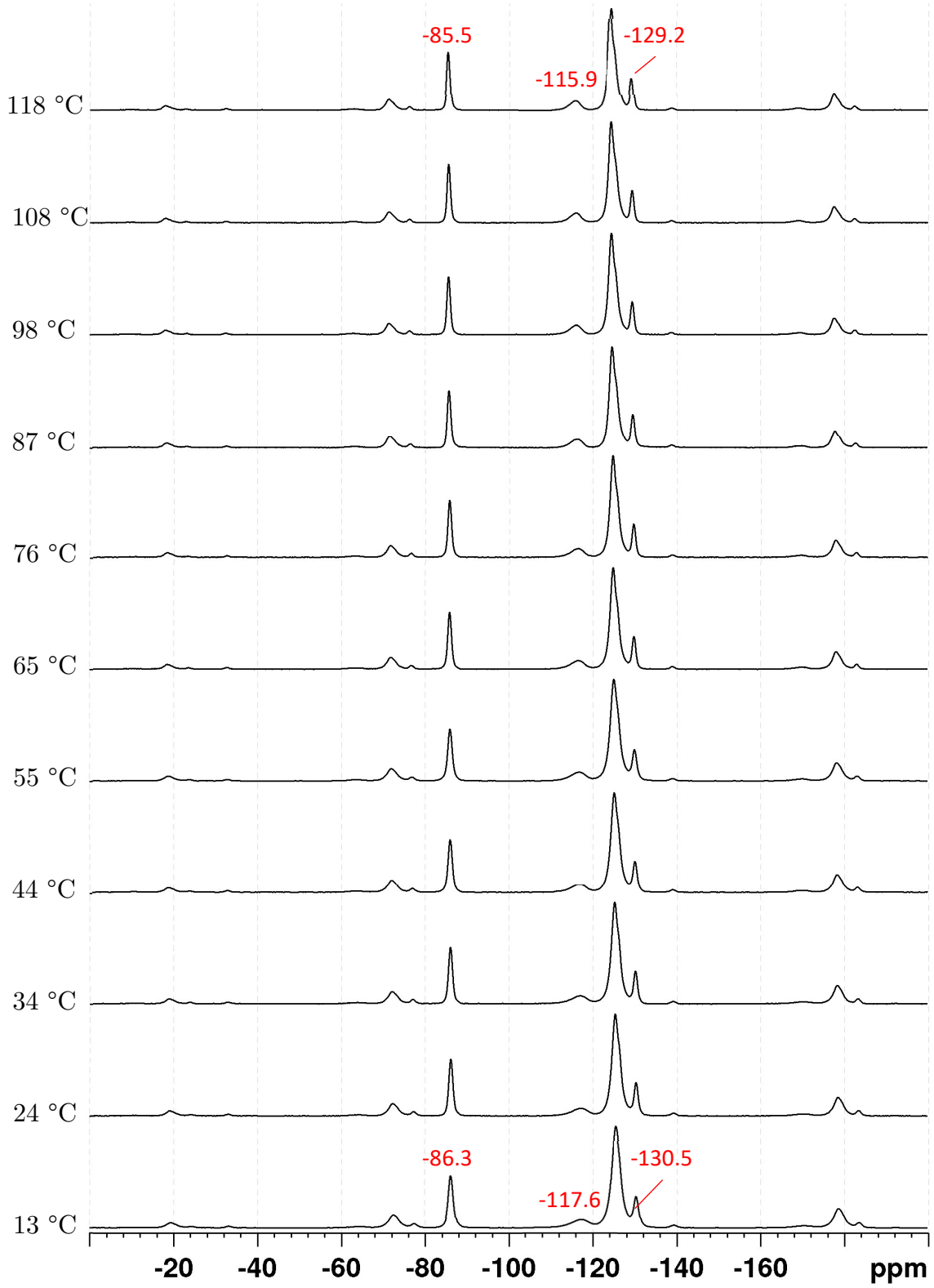


Figure 6.7 *Variable temperature ^{19}F NMR spectra of PFAC-10*

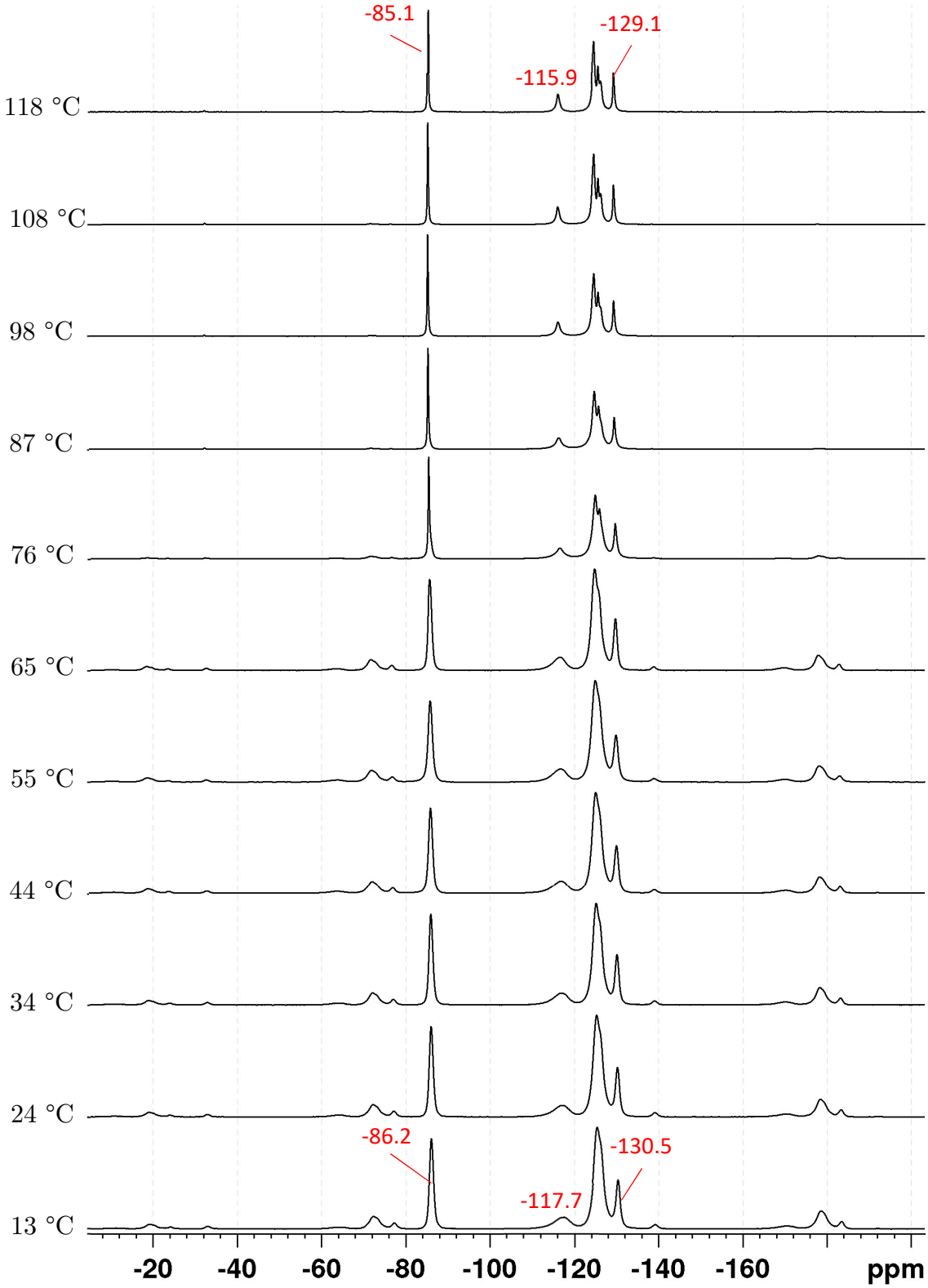


Figure 6.8 *Variable temperature ^{19}F NMR spectra of PFAC-8*

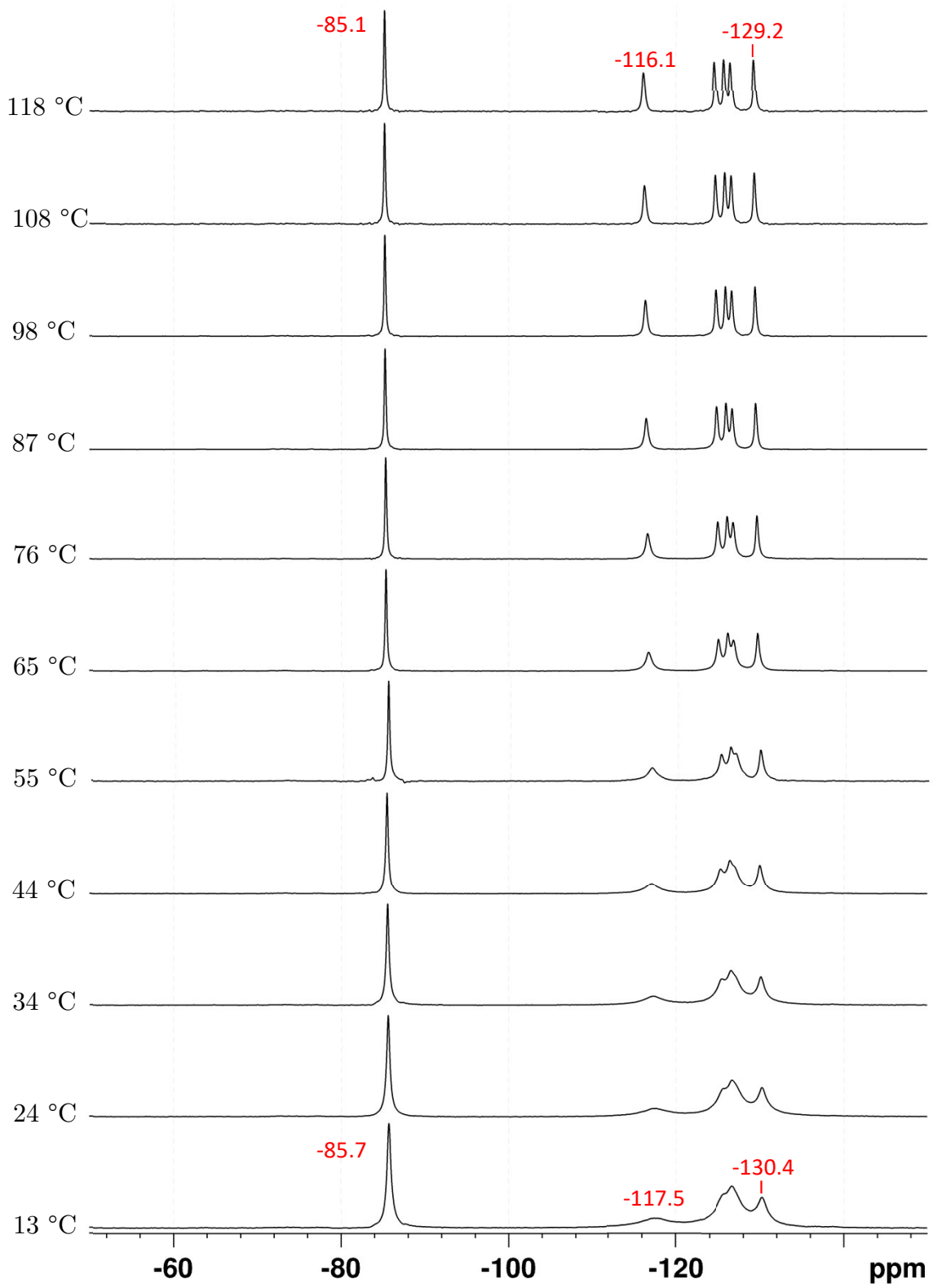


Figure 6.9 *Variable temperature ^{19}F NMR spectra of PFAC-6*

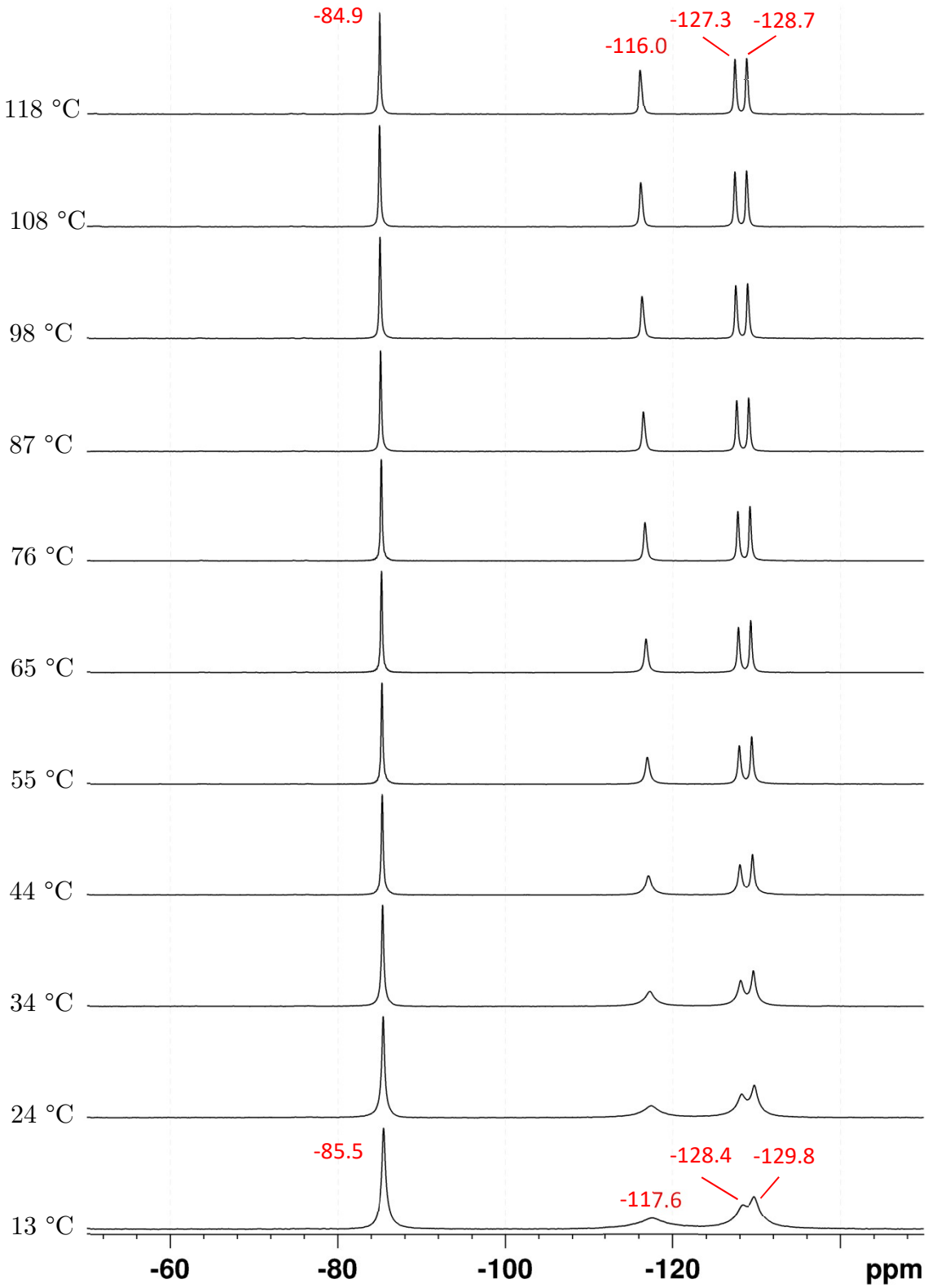


Figure 6.10 *Variable Temperature ^{19}F NMR spectra of PFAC-4*

6.3.3. ^{19}F spin-lattice relaxation time

Figure 6.11 to **Figure 6.14** show T_1 for the different fluorinated moieties in the PFAC-n polymers. The values were determined using the changes in peak intensity through the inversion recovery experiment, and so where separate peaks are insufficiently well-resolved, a single T_1 value is recorded. Note that the y axes for **Figure 6.11** (PFAC-10) is different to the others, although spans the same range.

Figure 6.11 shows the variation of T_1 with temperature for PFAC-10. For the CF_3 group and all of the CF_2 groups except the one closest to the backbone, there is a general increase in T_1 with increasing temperature. In contrast, T_1 for the $C\underline{F}_2$—CH_2 group stays approximately constant with temperature, before starting to decrease slowly at the upper end of the temperature range. PFAC-8 (**Figure 6.12**) also sees a general increase in T_1 with temperature at the lower end of the temperature range although, as with PFAC-10, T_1 for the $C\underline{F}_2$—CH_2 group stays approximately constant. Below the melting point, the different functional groups have very similar T_1 values which, after a sharp decrease at the melting point, then start to diverge. T_1 for the CF_3 group then increases with temperature, whilst T_1 for the CF_2—CH_2 group decreases with temperature; the intervening CF_2 groups fall on a spectrum between the two types of behaviour.

Both PFAC-6 (**Figure 6.13**) and PFAC-4 (**Figure 6.14**) have convergent T_1 values at the lower end of the temperature range which initially stay fairly constant. As the temperature increases, the T_1 values start to diverge in the same way as for PFAC-8 after the melting point. There is a sharp increase in all of the

T_1 values for PFAC-6 which occurs between 90-100 °C – this does not correspond to any apparent phase transition as measured by DSC.

Figure 6.15 to **Figure 6.17** show T_1 for the C$\underline{F}_3$, C$\underline{F}_2$—CF_3, and C$\underline{F}_2$—CH_2 groups for all of the PFAC-*n* polymers as a function of temperature. At the lower end of the temperature range, the T_1 relaxation times increase such that PFAC-6 < PFAC-4 < PFAC-8 < PFAC-10. Below its melting point, the T_1 values for PFAC-8 are closer in magnitude to those of PFAC-10, whilst the values for PFAC-4 and -6 are also similar to one another. Above its melting point, the T_1 values for PFAC-8 become closer to those of PFAC-4 and -6. Similarly, the T_1 values for PFAC-6 are lower than PFAC-4 up until the transition at 90 °C, where the values start to converge for all three moieties.

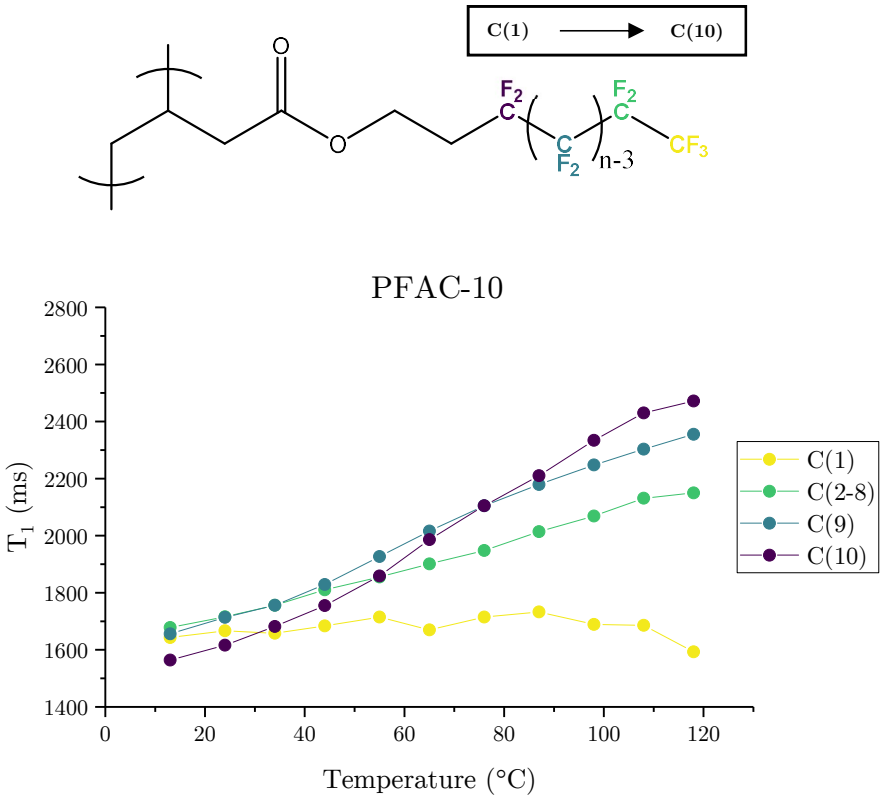


Figure 6.11 *^{19}F Spin-lattice relaxation times of the fluorinated side-chain of PFAC-10. C(1) represents the C$\underline{F}_2$—CH$_2$ group, whilst C(10) is the C$\underline{F}_3$ group at the other end of the side-chain. Not all individual fluorine environments can be fully resolved. Lines are included to guide the eye*

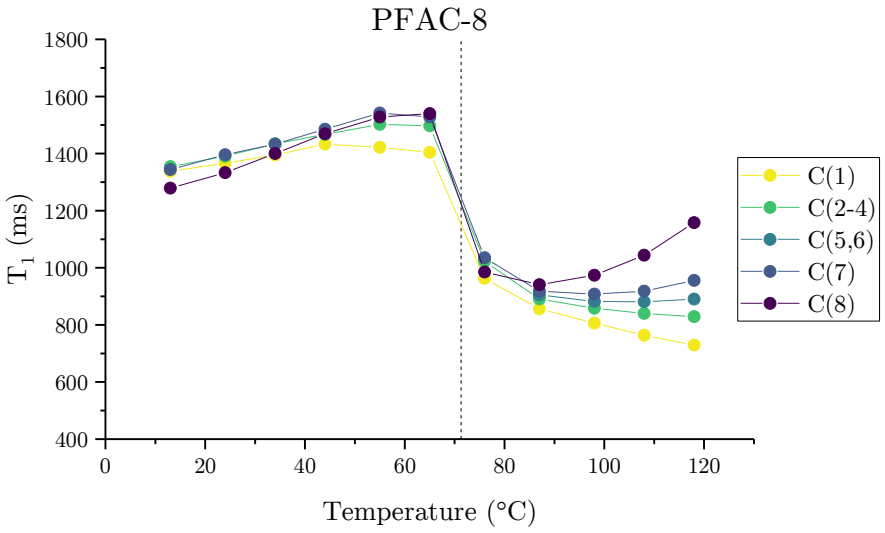


Figure 6.12 *^{19}F Spin-lattice relaxation times of the fluorinated side-chain of PFAC-8. C(1) represents the C$\underline{F}_2$—CH$_2$ group, whilst C(8) is the C$\underline{F}_3$ group at the other end of the side-chain. The dashed line indicates the melting temperature as measured by DSC*

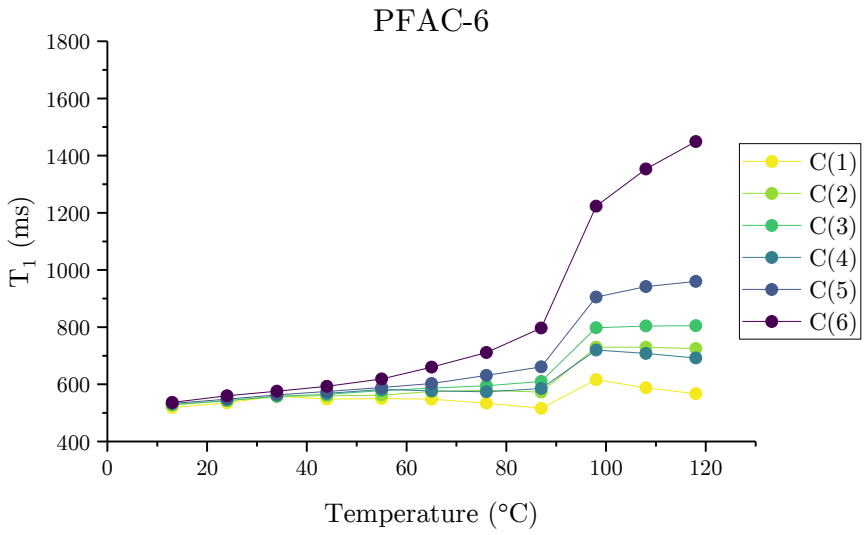


Figure 6.13 *^{19}F Spin-lattice relaxation times of the fluorinated side-chain of PFAC-6. C(1) represents the C$\underline{F}_2$—CH_2 group, whilst C(6) is the C$\underline{F}_3$ group at the other end of the side-chain. Lines are included to guide the eye*

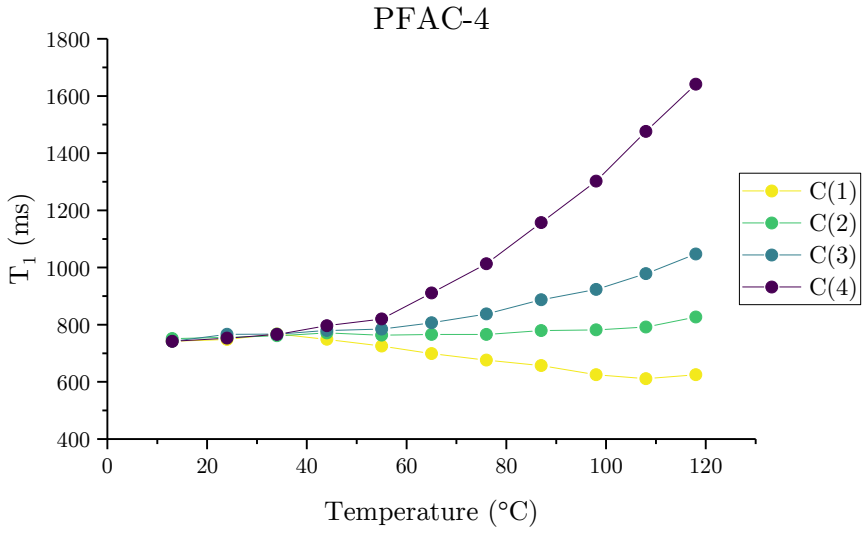


Figure 6.14 *^{19}F Spin-lattice relaxation times of the fluorinated side-chain of PFAC-4. C(1) represents the C$\underline{F}_2$—CH_2 group, whilst C(4) is the C$\underline{F}_3$ group at the other end of the side-chain. Lines are included to guide the eye*

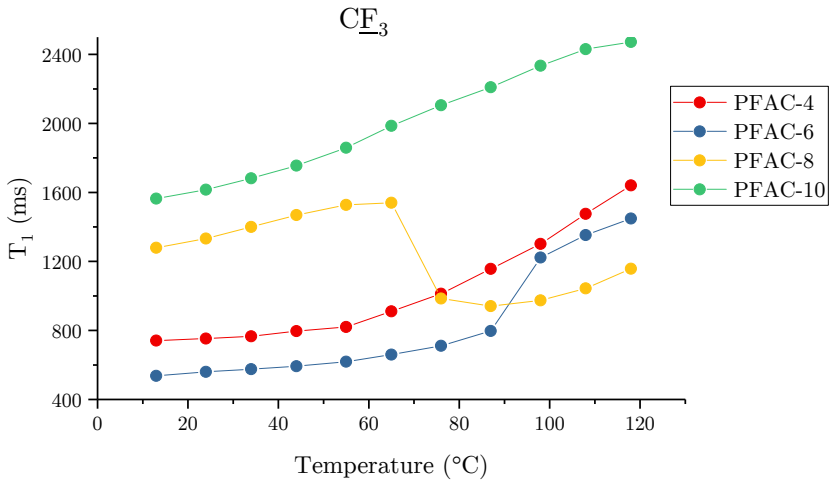


Figure 6.15 *T_1 for the CF_3 group in PFAC-n. Lines are included to guide the eye*

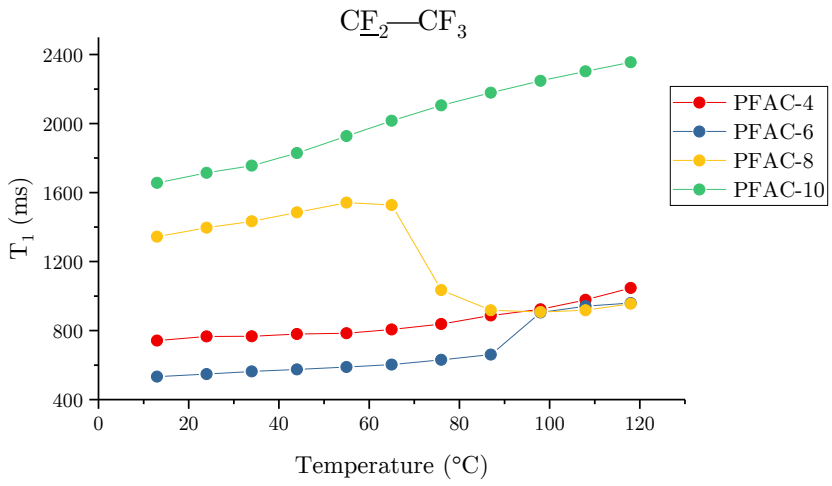


Figure 6.16 *T_1 for the CF_2—CF_3 group in PFAC-n. Lines are included to guide the eye*

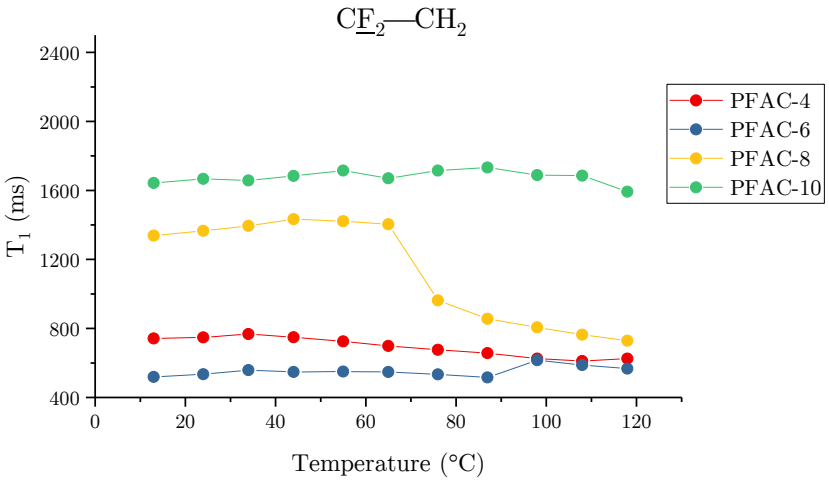
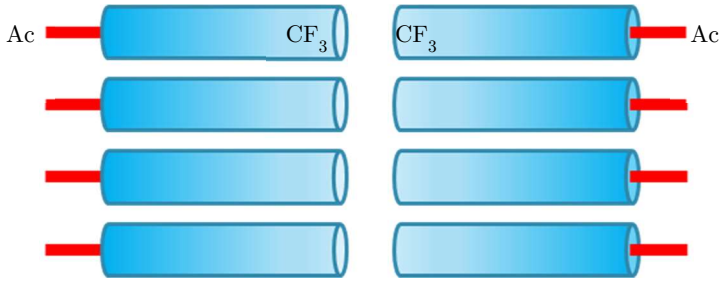


Figure 6.17 *T_1 for the C$\underline{F}_2$—CH_2 group in PFAC-n. Lines are included to guide the eye*

6.3.4. Discussion

As discussed in the introduction to this chapter, the ^{19}F chemical shift is very sensitive to the local environment of the fluorine nucleus and the differences in chemical shift between the same fluorinated group in different PFAC-n give an indication of the different environments and aggregation states of the side chains. The chemical shift of all of the CF_3 groups is low, with $\delta <$ -85 ppm in all cases. A more fluorous environment results in a lower chemical shift, and it seems that in all cases, the CF_3 is surrounded by other fluorinated moieties and is segregated away from the hydrocarbon moieties. The preferential segregation of hydrocarbon and fluorocarbon moieties is a well-known phenomenon and has been discussed elsewhere in this thesis [29,32]. PFAC-8 and -10 have the lowest δ and are therefore surrounded by more CF_3 moieties, which suggests end-to-end packing of the fluorocarbon chains in bilayers. This behaviour has been observed by Lee *et al.* in semifluorinated alkane systems [158] via solid-state ^{19}F NMR and is consistent with the smectic-B bilayer structures which PFAC-n with $n \geq 8$ adopt [119]; this structure is shown in **Figure 6.18**.



Bilayer Structure

Figure 6.18 *Bilayer structure of PFAC-8 and -10 with end-to-end packing of the CF_3 groups. The fluoroalkyl chain is shown in blue, whilst the acrylate group (Ac) is shown in red*

The $C\underline{F}_3$ δ for PFAC-6 and -4 are higher, which suggests that they surrounded by increased amounts of CF_2 moieties and that there is therefore increased interdigitation of the side chains. The $C\underline{F}_2$—CH_2 functionality is closest to the hydrocarbon acrylate group and polymeric backbone, and where the fluorinated chains are packed end-to-end, such as in PFAC-8 and -10, it is expected that this is the least fluorous environment. Conversely, where the sidechains have greater levels of flexibility and interdigitation, this functional group is exposed to enhanced amounts of fluorine. The trends in chemical shift support this conclusion, with the chemical shift being lower for lower values of n. It is interesting, however, that the minimum occurs at PFAC-6 rather than -4, and it is not entirely clear why this should be the case.

The decrease in the chemical shift with increasing temperature is a phenomenon seen in a variety of fluorinated systems, including solid-state semifluorinated alkanes [158] and perfluoroalkanoic SAM's [186]. The changes that occur to the $C\underline{F}_2$—CH_2 peak with temperature are primarily a result of the increase in mobility with temperature. Being closer to the polymeric backbone, it has the most hindered motion at room temperature and undergoes the most dramatic

decrease in peak width. In contrast, the CF_2—CF_3 group is close to the end of the side chain and therefore has much greater freedom of movement even at lower temperatures. The CF_3 group has greater rotational freedom than any of the CF_2 groups, as well as the greater translational freedom which comes from occupying the end of the chain. For this reason, the CF_3 peaks undergo the least motional narrowing with increasing temperature. The increase in δ for the CF_3 and CF_2—CF_3 peaks with increasing temperature is attributed to the greater interdigitation and less efficient packing of the chains at higher temperature. The change in chemical shift with temperature is larger for PFAC-8 and -10 because these systems have ordered end-to-end packing of the CF_3 groups at low temperatures, whilst the PFAC-4 and -6 chains are already disordered at low temperatures and undergo a smaller relative change to their environment.

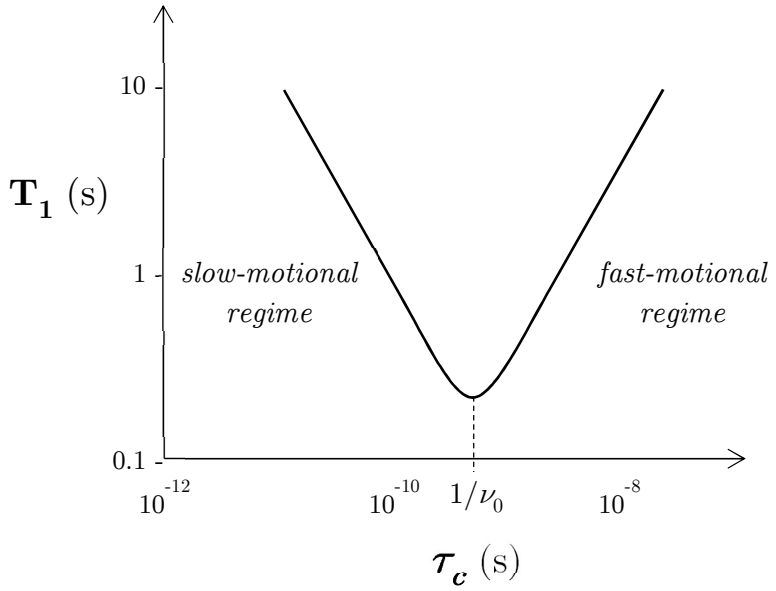


Figure 6.19 *Change in spin-lattice relaxation time, T_1, with rotational correlation time, τ_c. The minimum occurs when $\tau_c = 1/\nu_0$, where ν_0 is the Larmor frequency*

Spin-lattice relaxation time reaches a minimum at the temperature where the rotational correlation time, τ_c of the molecule equals the inverse of the Larmor frequency, ν_0. Below this temperature is the slow-motional regime, where T_1 time decreases with increasing temperature, and above this temperature is the fast-motional regime, where the T_1 time increases with increasing temperature; these relationships are shown in **Figure 6.19**. For PFAC-4 and -6, and for PFAC-8 above its melting temperature, the functional groups towards the end of the side chain see an increase in T_1 with temperature and are in the fast-motional regime. Meanwhile, the functional groups closer to the polymeric backbone have not yet achieved their minimum T_1 value. Because PFAC-4 has a shorter side chain and is more mobile than PFAC-6, it reaches its minimum T_1 value at a lower temperature and therefore has larger T_1 values across most of the temperature range. PFAC-6 undergoes a transition at approximately 90 °C, which allows increased freedom of motion for the side chains. This transition is not visible as a glass or melting transition via DSC, or as a significant change in the adaptive wetting behaviour of PFAC-6. It is possible that this transition corresponds with the onset of a co-operative motion with polymeric backbone [198,199].

At low temperatures, the T_1 values of PFAC-4 and -6 converge to a single value, and this can be interpreted in several ways. Firstly, a single T_1 value can indicate that the side chain moves as a single, cohesive unit. As the temperature increases, the side chain loses its cohesion as the groups towards the end gain more motional freedom. Another possible interpretation is that the relaxation times have been averaged out by spin diffusion. This is the process of equilibration of magnetization via direct interaction between individual spins and occurs on a

much quicker timescale than spin-lattice relaxation – thus resulting in a single T_1 value. Spin diffusion is reduced by rapid molecular motion, which causes the T_1 values to diverge at higher temperatures. It is also reduced by high MAS speeds, although spin diffusion has been observed as MAS frequencies of up to 35 kHz (in comparison to 20 kHz in this study) [200]. Given that the short PFAC-4 and -6 side chains do not crystallise [84,115], spin diffusion seems a more likely candidate for the homogeneous T_1 values.

PFAC-10 is in the solid state throughout the measurement range, as is PFAC-8 below 70 °C. In particular, the double peak in the DSC trace of the annealed PFAC-10 in **Figure 3.16** is indicative of a thermotropic side chain liquid crystal melting via a mesophase [118,119]. The rigidity of the longer fluoroalkyl chain means that it is expected to move as a single unit [201], without the flexion which can occur above the melting point. This should give a common T_1 value for the whole chain, albeit with increased mobility of the CF_3 group, which has free rotation, and a difference at the $C\underline{F}_2$—CH_2 functionality, where the fluoroalkyl chain meets the acrylate spacer group. Experiments with comb-like polymers having alkyl (Giotto *et al.* [202]) and fluoroalkyl (Ryu *et al.* [203]) brushes found single-component T_1 relaxation times for the side chain. The expectation for a solid is that the T_1 will be in the slow-motional regime and decrease with increasing temperature. The magnitude of the changes to T_1 will depend on how much the packing density of the chains and the flexibility of the spacer group restrict the motions of the side chain [114,198]. Examining the results for PFAC-10 and -8 in its solid state, the trends are quite different to the prediction. Most notably, although PFAC-10 exhibits longer relaxation times than PFAC-8,

the T_1 values for all functional groups except C$\underline{F}_2$—CH_2, which remains approximately constant, increase with temperature. This would suggest that the relaxation behaviour is in the fast-motional regime. Here, it is likely that spin diffusion once again plays a role. Coupling to the CF_3 group, which has free rotation and a more rapid correlation time, results in a common T_1 value which falls in the fast-motional regime [204]. This explanation seems robust when considering PFAC-8, where the T_1 times are convergent for all functional groups. The situation is more complex for PFAC-10, where the T_1 relaxation times for C$\underline{F}_3$, C$\underline{F}_2$—CF_2 and C$\underline{F}_2$—CF_3 are similar but not identical. The T_1 relaxation time for the eight C$\underline{F}_2$—CF_2 groups has been derived from the intensity of a single peak, without any deconvolution being attempted. It is possible that there is a heterogeneity in T_1 along the chain, or, since spin diffusion is related to internuclear distance, that there is a heterogeneity in in the coupling to the CF_3 group along the chain. In either case, it is clear that further investigation is required.

6.4. Conclusions

Solid state ^{19}F MAS NMR has been used successfully to examine the morphology and aggregation of PFAC-*n* polymers at a variety of temperatures. Information from chemical shifts demonstrates that even in the polymer melts, there is segregation between fluorinated and non-fluorinated moieties. For the longer chain PFAC-*n* polymers below their melting point, there is evidence that the side chains are arranged in bilayers with end-to-end packing of the CF_3 groups. At temperatures below the melt, the changes in chemical shift indicate that a small degree of side chain mixing occurs prior to the melting temperature.

Spin-lattice relaxation time is a useful measure of molecular mobility, particularly at higher temperatures where spin diffusion effects are lessened and for shorter side chain lengths where there is enhanced molecular mobility. T_1 measurements reflected the greater mobility of the PFAC-4 side chains in comparison to PFAC-6, which is also observed in the adaptive wetting behaviour, and the onset of side chain motion above the melting point of PFAC-8. There are some features of particular interest which warrant further investigation; the discontinuity in the PFAC-6 T_1 relaxation time at 90 °C is one such example. Similarly, the relaxation times for PFAC-10 are, upon initial inspection, at odds with the DSC data which indicates liquid crystalline behaviour – this is likely to be related to spin diffusion effects.

In order to overcome the challenges presented by spin diffusion, measurements could be made at higher MAS speeds. Alternatively, the lack of coupling in ^{13}C experiments result in a lack of spin diffusion effects. To explore the relaxation behaviour further, measurements of the spin-lattice relaxation times in the rotating frame, $T_{1\rho}$, would complement the measurements made in this investigation. Whilst T_1 is on the same timescale as segmental motions within polymers (MHz), $T_{1\rho}$ probes the local motion on the kHz timescale. Similarly, measurements of the spin-spin relaxation time, T_2, would provide further insight into the local environment of the side chains.

6.5. References

[29] M. P. Krafft and J. G. Riess, Chemical Reviews **109**, 1714 (2009).

[32] P. Long and J. Hao, Advances in Colloid and Interface Science **171**–**172**, 66 (2012).

[84] K. Honda, M. Morita, H. Otsuka, and A. Takahara, Macromolecules **38**, 5699 (2005).
[88] E. J. Kinmond, S. R. Coulson, J. P. S. Badyal, S. A. Brewer, and C. Willis, Polymer **46**, 6829 (2005).
[100] K. K. Lau and K. K. Gleason, Journal of The Electrochemical Society **146**, 2652 (1999).
[101] K. K. S. Lau and K. K. Gleason, Journal of Fluorine Chemistry **104**, 119 (2000).
[102] E. Katoh, H. Sugimoto, Y. Kita, and I. Ando, Journal of Molecular Structure **355**, 21 (1995).
[103] J. Emsley and L. Phillips, Progress in Nuclear Magnetic Resonance Spectroscopy **7**, 1 (1971).
[114] Q. Wang, Q. Zhang, X. Zhan, and F. Chen, Journal of Polymer Science Part A: Polymer Chemistry **48**, 2584 (2010).
[115] K. Honda, I. Yamamoto, M. Morita, H. Yamaguchi, H. Arita, R. Ishige, Y. Higaki, and A. Takahara, Polymer **55**, 6303 (2014).
[118] C. B. McArdle, *Side Chain Liquid Crystal Polymers* (Springer Science & Business Media, 1990).
[119] J. Wang, G. Mao, C. K. Ober, and E. J. Kramer, Macromolecules **30**, 1906 (1997).
[124] J. Genzer, E. Sivaniah, E. J. Kramer, J. Wang, H. Körner, K. Char, C. K. Ober, B. M. DeKoven, R. A. Bubeck, D. A. Fischer, and S. Sambasivan, Langmuir **16**, 1993 (2000).
[156] J. Lüning, J. Stöhr, K. Y. Song, C. J. Hawker, P. Iodice, C. V. Nguyen, and D. Y. Yoon, Macromolecules **34**, 1128 (2001).
[158] Y. J. Lee, C. G. Clark, R. Graf, M. Wagner, K. Müllen, and H. W. Spiess, The Journal of Physical Chemistry B **113**, 1360 (2009).
[179] H. W. Spiess, Macromolecules **50**, 1761 (2017).
[180] H. W. Spiess, Colloid and Polymer Science **261**, 193 (1983).
[181] M. R. Hansen, R. Graf, and H. W. Spiess, Accounts of Chemical Research **46**, 1996 (2013).
[182] L. Yang and L. M. Zhang, Carbohydrate Polymers **76**, 349 (2009).
[183] K. Schmidt-Rohr and H. W. Spiess, *Multidimensional Solid-State NMR and Polymers* (Elsevier, 2012).
[184] R. Kimmich and N. Fatkullin, Advances in Polymer Science **170**, 1 (2004).
[185] W. R. Dolbier, *Guide to Fluorine NMR for Organic Chemists* (John Wiley & Sons, 2016).
[186] S. Pawsey and L. Reven, Langmuir **22**, 1055 (2006).
[187] L. Nordstierna, I. Furó, and P. Stilbs, Journal of the American Chemical Society **128**, 6704 (2006).
[188] A. Kotzev, A. Laschewsky, P. Adriaensens, and J. Gelan, Macromolecules **35**, 1091 (2002).
[189] K. A. Page, W. Jarrett, and R. B. Moore, Journal of Polymer Science Part B: Polymer Physics **45**, 2177 (2007).

[190] J. Preuschen, S. Menchen, M. A. Winnik, A. Heuer, and H. W. Spiess, Macromolecules **32**, 2690 (1999).
[191] K. A. Page, K. M. Cable, and R. B. Moore, Macromolecules **38**, 6472 (2005).
[192] K. Aimi and S. Ando, Magnetic Resonance in Chemistry **42**, 577 (2004).
[193] P. J. Hore, *Nuclear Magnetic Resonance* (Oxford University Press, USA, 2015).
[194] P. Atkins and J. de Paula, *Atkins' Physical Chemistry* (Oxford University Press, New York, 2002).
[195] D. C. Apperley, R. K. Harris, and P. Hodgkinson, *Solid-State NMR: Basic Principles and Practice* (Momentum Press, 2012).
[196] P. Schanda and M. Ernst, Progress in Nuclear Magnetic Resonance Spectroscopy **96**, 1 (2016).
[197] L. Van Gorkom, J. Hook, M. Logan, J. Hanna, and R. Wasylishen, Magnetic Resonance in Chemistry **33**, 791 (1995).
[198] H. J. Kim, W. R. Jackson, and G. P. Simon, European Polymer Journal **30**, 1201 (1994).
[199] M. Gaborieau, R. Graf, S. Kahle, T. Pakula, and H. W. Spiess, Macromolecules **40**, 6249 (2007).
[200] T. W. Su and D. L. M. Tzou, Polymer **41**, 7289 (2000).
[201] N. Plate and V. Shibaev, Macromolecular Reviews Part D - Journal of Polymer Science **8**, 117 (1974).
[202] M. Giotto, D. Azar, J. Gosselin, P. T. Inglefield, and A. A. Jones, Journal of Polymer Science Part B: Polymer Physics **39**, 1548 (2001).
[203] S. Y. Ryu, J. W. Chung, and S. Y. Kwak, Langmuir **31**, 9473 (2015).
[204] A. Badia, W. Gao, S. Singh, L. Demers, L. Cuccia, and L. Reven, Langmuir **12**, 1262 (1996).

7. Plasma Polymerization for Oil/Water Separation

One of the underlying aims of this thesis has been to aid the development of a surface which is universally repellent to all liquids, regardless of surface tension and/or composition. However, there are many circumstances in which it might be desirable to have a surface which has different wetting behaviour towards different liquids. This might either be an intrinsic property of the surface, or it might be a result of the surface undergoing change when exposed to particular stimuli – so-called 'smart' surfaces. One such application is the separation of oil and water.

The prevalence of oil spills and the enormous damage that they cause to the environment is a particularly prominent driving force behind research on efficient oil and water separation [205-207], although is by no means the only one [208,209]. Industrial wastewater often contains large amounts of oily pollutants [210], whilst the presence of water as a contaminant in oils or fuels can also be problematic. There are a number of methods for removing oil from water including gravity separation, centrifugal separation, and skimming, but these methods are labour intensive and rarely result in complete separation [6,211,212]. As well as having

environmental benefits, efficient separation allows the oil to be recycled and/or reused which is also economically beneficial.

In recent years, significant attention has been focussed on harnessing the difference in wettability between water and oils to create effective filters. The materials used can have a variety of different wetting behaviours [136,209]; they can have orthogonal wettability to oils and water (superhydrophilic and superoleophobic or superhydrophobic and superoleophilic) [6,136,213-215], or have different properties when immersed in water (superhydrophilic and underwater superoleophobic) [216-218], or have adaptive wetting properties which change when in contact with oil or water [135,219,220]. In this investigation, efforts will be directed towards using plasma polymerization to synthesize a surface that is hydrophilic and oleophobic. The advantage of using an oleophobic surface in oil/water separation is that the filter does not adsorb oil, ensuring that a greater proportion of the oil can be recycled and that the filter does not become fouled, allowing it to be re-used. In the context of the work presented so far, it seems likely that the introduction of a polar monomer into the polymer would promote hydrophilicity, without compromising oleophobicity. Because the plasma polymerization methods used in this thesis are already used commercially, the investigation will also aim to change the apparatus and protocols as little as possible.

The work in this chapter presents preliminary results for the synthesis of a surface suitable for oil/water separation through the co-polymerization of PFAC-6 and 2-hydroxyethyl methacrylate (HEMA). The HEMA and HEMA-co-PFAC-6 surfaces are characterized in terms of their chemical composition via XPS, their

topographies via AFM, and their wetting properties via contact angle goniometry. The characterization data for PFAC-6, which has been discussed in detail in **Chapters 1** and **0** will be briefly presented again to aid comparison. The results for the co-polymer will then be discussed in terms of its suitability for a substrate for use in oil/water separation processes.

7.1. Experimental

7.1.1. Plasma polymerization

The two monomers used were PFAC-6, and 2-hydroxyethyl methacrylate (HEMA). The structure of HEMA is shown in **Figure 7.1**. Both monomers were purified via multiple freeze-thaw processes (see **Section 3.1.1**).

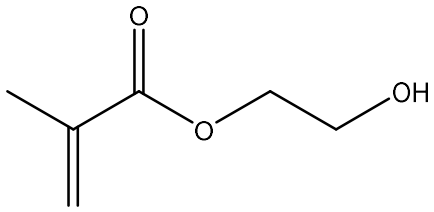


Figure 7.1 *Structure of 2-hydroxyethyl methacrylate*

The single monomer inlet of the plasma chamber was replaced with a double inlet to allow two monomer tubes to be attached to the apparatus. Each monomer tube was fitted with a Young tap so that the flow of the monomers could be controlled separately. The substrates were placed in the chamber within the copper coils. The whole system was then evacuated to base pressure (5×10^{-3} mbar) before HEMA monomer vapour was introduced at a pressure of

1 x 10^{-1} mbar. After 5 minutes, PFAC-6 monomer vapour was introduced to give a pressure of 2 x 10^{-1} mbar for the co-polymer synthesis; this step was omitted for the synthesis of pure HEMA. After 5 mins the pressure gauge was sealed off, and the radiofrequency generator was switched on to ignite a pulsed plasma (13.56 MHz, 40 W, t_{on}= 40 μs, t_{off}= 20 ms) for 10 minutes. When the deposition was complete, the RF generator was switched off and the pressure gauge opened up. When the pressure reached 2 x 10^{-1} mbar, the monomer vapour was allowed to flow for a further 5 minutes before being sealed off and the whole system being evacuated back to base pressure. After use, the chamber was cleaned prior to use by running an air plasma (2 x 10^{-1} mbar, 50 W) for two hours.

This process differs from the protocol used in previous chapters in that it includes the introduction of two monomers, one after the other. It also omits the 30s continuous wave plasma prior to the pulsed processing, which was causing 'flashback' of the plasma down the monomer tube when depositing at lower pressures and degrading the monomer.

7.1.2. Surface characterization

The following techniques were used to characterize the pure HEMA and HEMA-co-PFAC-6 surfaces; XPS to determine chemical composition (see **Section 2.1.3**, does not include angle-resolved), AFM to determine surface topography (see **Section 2.1.5**), and contact angle goniometry (see **Section 2.1.6)** to determine wetting behaviour.

As well as the contact angle measurements used earlier in the thesis, sliding contact angle measurements were also made using a Krüss DSA100 contact angle

goniometer fitted with a tilting stage. The measurements were made by placing a 15 μl drop of either water, ethylene glycol, or hexadecane on a level surface and slowly tilting it until the drop slid off – this angle was recorded as the sliding angle.

7.2. Results and Discussion

7.2.1. Chemical composition

Figure 7.2 shows the XPS survey spectra of HEMA, PFAC-6, and HEMA-co-PFAC-6 with the major peaks annotated. The absence of silicon peaks in any of the spectra indicates complete coverage of the glass substrate. The spectrum for HEMA shows a small amount of fluorine contamination, comprising 0.5 % of the total content. This is due to the high affinity of fluorine for the glass walls of the plasma chamber rendering it impossible to clean completely. The compositions of the polymers as determined from the peak area in the survey scans are shown in **Figure 7.3**. PFAC-6 has a slight excess of fluorine and carbon, and a slight deficit of oxygen, whilst HEMA has a slight excess of carbon and deficit of oxygen. The composition of the co-polymer is approximately 1:4 HEMA:PFAC-6. The calculated percentage of HEMA falls between 17-22 % depending on which element is used as the benchmark and whether the calculation is performed assuming structurally intact and randomly oriented PFAC-6 and HEMA, or using the composition as measured via XPS.

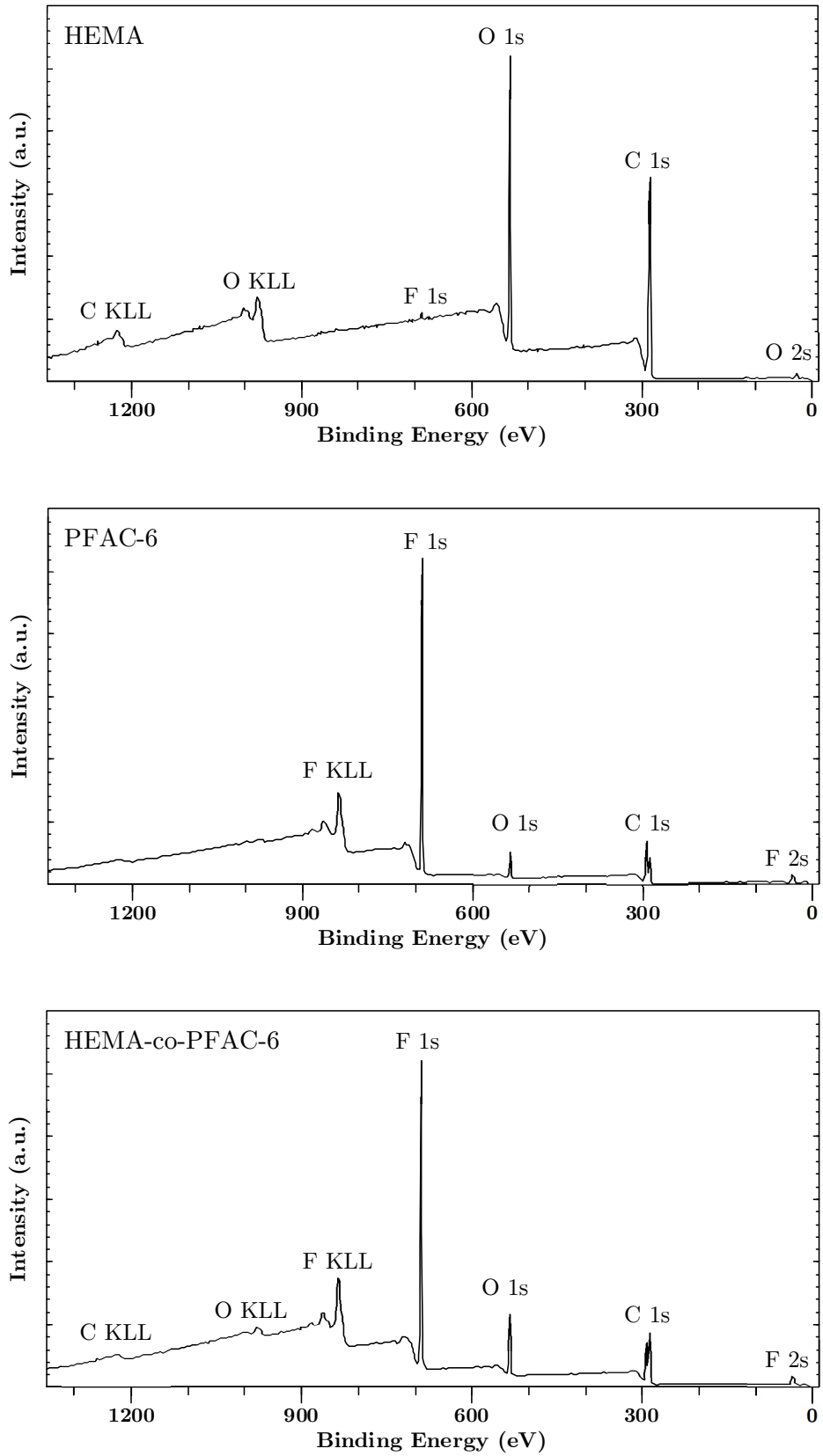


Figure 7.2 *XPS survey spectra of HEMA, PFAC-6 and HEMA-co-PFAC-6 polymers with the significant peaks annotated. Note that C KLL and O KLL peaks are present in the PFAC-6 spectra, but are obscured by the presence of fluorine, which has a large sensitivity factor*

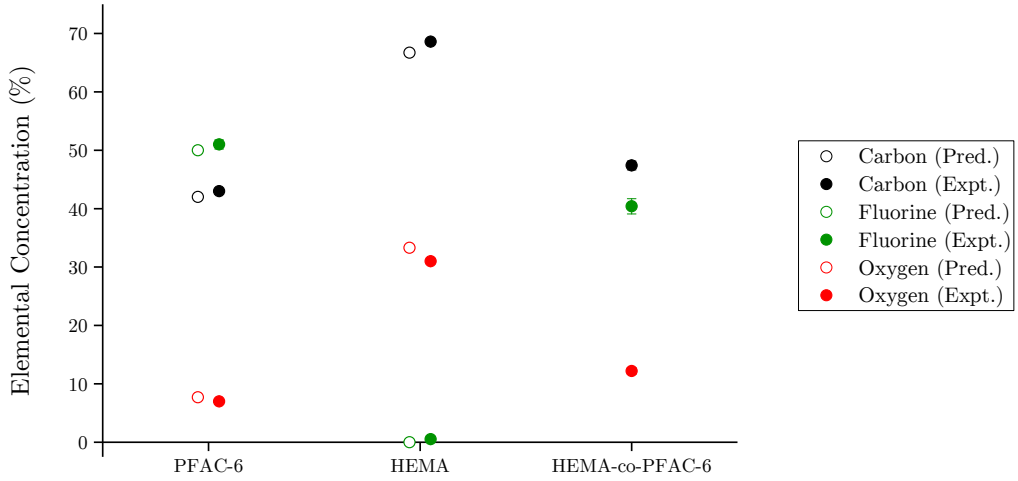


Figure 7.3 *The composition of PFAC-6, HEMA, and HEMA-co-PFAC-6 plasma polymers. The predicted values (open circles) are calculated assuming complete structural retention of the monomer species during polymerization, and random orientation of the polymer. The measured values (solid circles) are calculated from the areas of the 1s peaks in the XPS survey scans.*

Figure 7.4 shows the deconvolved carbon 1s XPS spectra of HEMA, PFAC-6 and HEMA-co-PFAC-6. The HEMA spectrum could be resolved into contributions from four different carbon environments; C—CH_n at 285.0 eV, C—C=O(O) at 285.8 eV, C—O at 286.8 eV, and C=O at 289.0 eV. The PFAC-6 spectrum could be resolved into contributions from six different carbon environments; C—CH_n/C—C=O(O) at 285.0 eV, C—CF_n at 285.8 eV, C—O at 286.7 eV, C=O at 288.8 eV, CF_2 at 291.1 eV, and CF_3 at 293.4 eV. The co-polymer spectrum could be resolved into contributions from six different environments C—CH_n/C—C=O(O) at 285.0 eV, C—CF_n at 286.0 eV, C—O at 286.7 eV, C=O at 288.8 eV, CF_2 at 291.4 eV, and CF_3 at 293.6 eV. **Figure 7.5** shows the different concentration of the carbon species in each of the polymers calculated from the peak areas in these spectra. The number and area of the peaks for both HEMA and PFAC-6 are consistent with the structurally intact

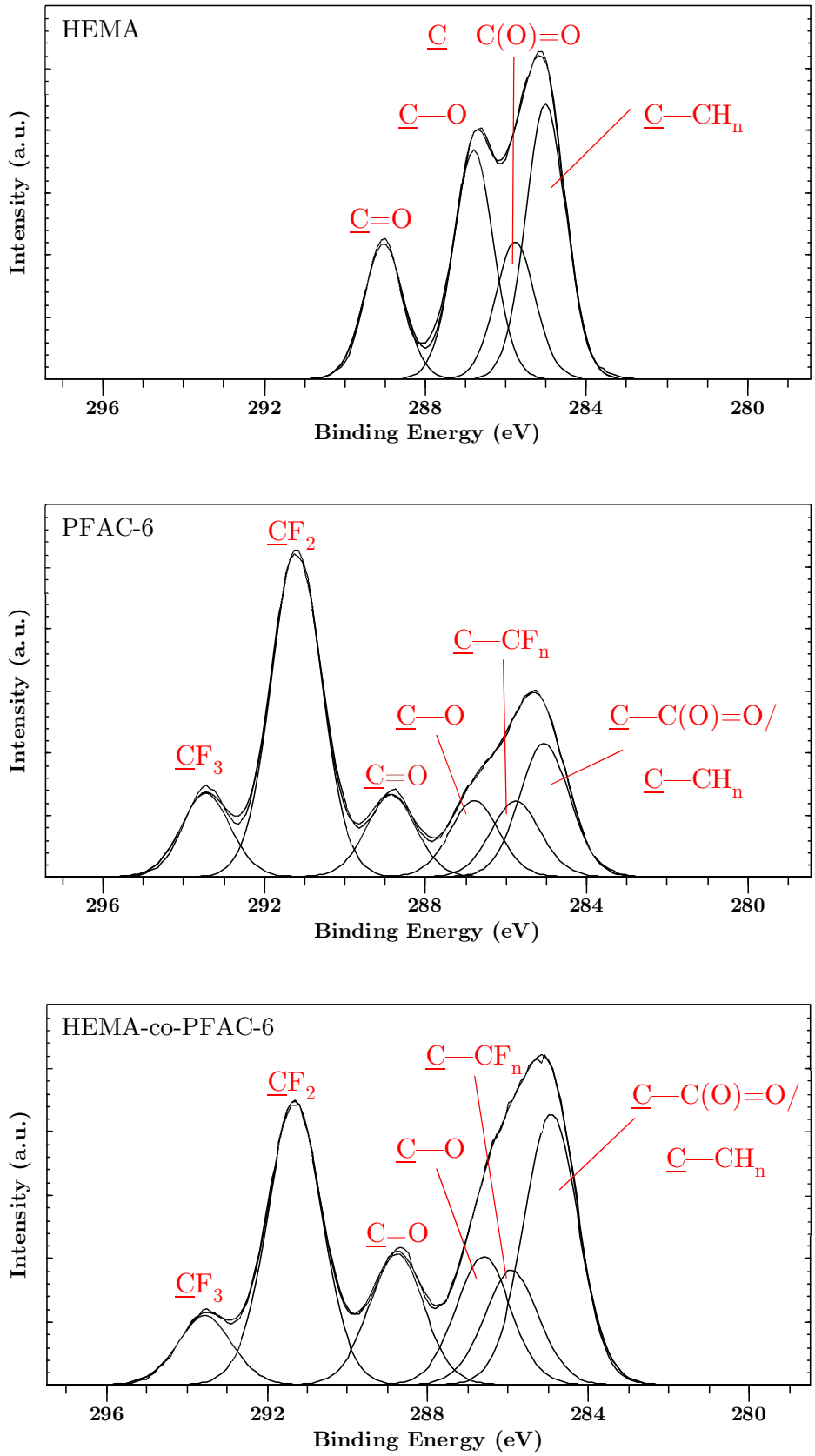


Figure 7.4 *Carbon 1s spectra of HEMA (FWHM = 1.15 eV), PFAC-6 (FWHM = 1.44 eV), and HEMA-co-PFAC-6 (FWHM = 1.58 eV)*

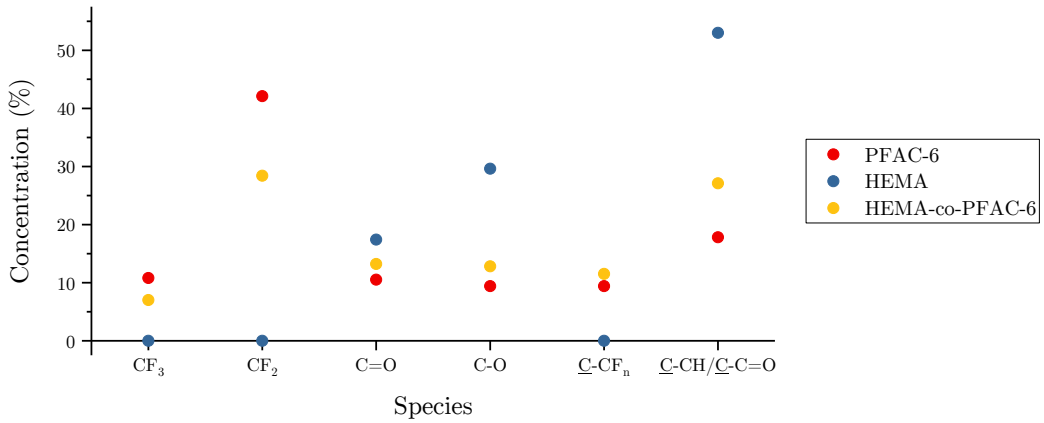


Figure 7.5 *Concentration of different carbon species in the PFAC-6 and HEMA homopolymers, and the HEMA-co-PFAC-6 copolymer*

polymers, and it seems reasonable to assume that they will retain their integrity when incorporated into the co-polymer.

7.2.2. Topography

Figure 7.6 and **Figure 7.7** show AFM micrographs of HEMA and HEMA-co-PFAC-6. Both are relatively smooth surfaces with HEMA having an rms roughness of 0.8 nm, which is close to the noise-level of the AFM, and HEMA-co-PFAC-6 having an rms roughness of 1.7 nm. Phase data indicates complete coverage of the substrate. As discussed in earlier chapters, the PFAC-6 polymer is too soft to acquire an image of this surface; it appears that the incorporation of HEMA results in a harder surface, allowing for AFM imaging of the co-polymer.

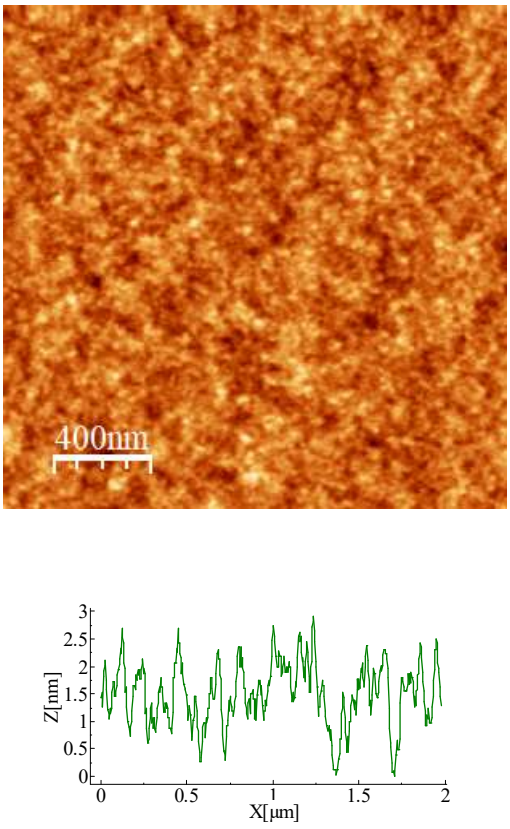


Figure 7.6 *A 2x2 µm² AFM micrograph and section profile of HEMA. The z scale of the micrograph is 7 nm*

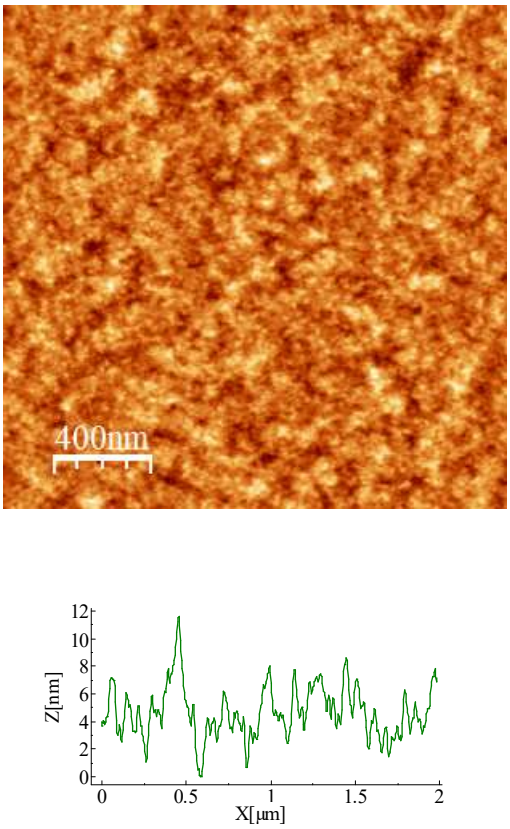


Figure 7.7 *A 2x2 µm² AFM micrograph and section profile of HEMA-co-PFAC-6. The z scale of the micrograph is 14 nm*

7.2.3. Surface energy and wetting properties

Figure 7.8 shows the static contact angles of water and DD on PFAC-6, HEMA, and HEMA-co-PFAC-6. The contact angles on the co-polymer are slightly lower than those on PFAC-6, whilst both liquids spread on HEMA. The spreading of the probe liquids HEMA meant that it was not possible to estimate the surface energy. The surface energy of the co-polymer was estimated as being 13 mJ m^{-2} (γ^d = 12 mJ m^{-2}, γ^p = 1 mJ m^{-2}).

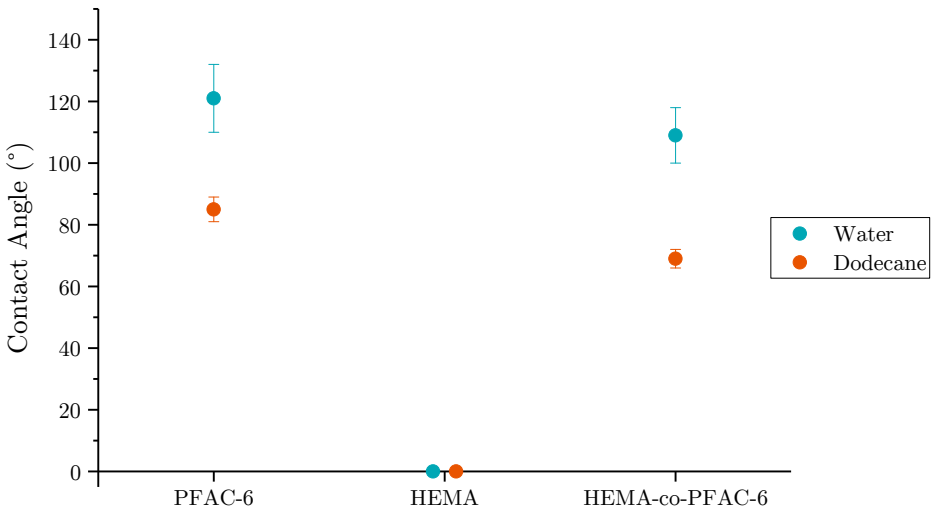


Figure 7.8 *Static contact angles of water and dodecane on PFAC-6, HEMA, and HEMA-co-PFAC-6*

Table 7.1 shows the sliding contact angles on the polymer surface. The spreading of the probe liquids on HEMA meant it was not possible to measure the sliding angles. On PFAC-6, all probe liquids (water, EG, *n*-HD) were pinned to the surface and did not slide, even at angles of 90°. For HEMA-co-PFAC-6, water and EG were pinned at all angles whilst *n*-HD had a sliding angle of $20° \pm 1$ despite having a lower static contact angle than either of the other two liquids.

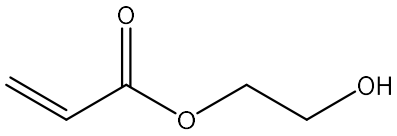
Material	$\boldsymbol{\theta^{W}_{slide}}$ (°)	$\boldsymbol{\theta^{EG}_{slide}}$ (°)	$\boldsymbol{\theta^{n-HD}_{slide}}$ (°)
HEMA	N/A	N/A	N/A
PFAC-6	Pinned	Pinned	Pinned
HEMA-co-PFAC-6	Pinned	Pinned	20

Table 7.1 *Sliding angles of water (W), ethylene glycol (EG), and dodecane (DD) on HEMA, PFAC-6, and HEMA-co-PFAC-6*

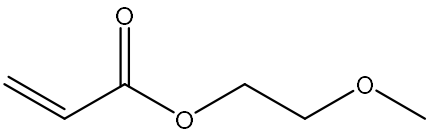
7.2.4. Discussion

PFAC-6 was chosen as the oleophobic monomer due to the fact that it exhibited the highest contact angles of DD and *n*-HD and can be polymerized at room temperature. As a monomer with a C6 perfluorinated chain, it is not the subject of bioaccumulation concerns in the same way that PFAC-8 or -10 are.

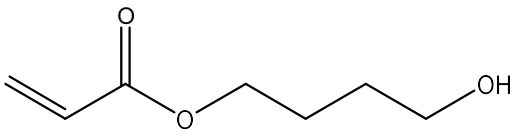
The selection of a suitable hydrophilic monomer was subject to trial and error. One of the requirements for the monomer were that it has a sufficiently high vapour pressure to achieve a pressure of $\gtrsim 1 \times 10^{-1}$ mbar under vacuum without a carrier gas. This pressure is the approximate minimum pressure at which a plasma can be sustained and would ensure that a significant amount of hydrophilic monomer would be incorporated into the final product. Attempting to run a plasma polymerization at low pressure can also result in 'flashback' of the plasma down the monomer tube, resulting in degradation of the monomer. The monomer was also required to be stable under vacuum. It was desirable that the required pressure could be achieved without needing to heat the plasma apparatus. Safety and environmental impact of the monomer and its polymerization by-products were also considered. As significant work has already been invested in optimizing the plasma parameters for acrylate monomers and as the hydrophobic monomer, PFAC-6, is acrylic, initial investigations focussed on acrylate monomers. **Figure 7.9** shows the structures of the acrylic monomers which were subject to initial tests: **a)** 2-hydroxyethyl acrylate, **b)** 2-methoxyethyl acrylate, **c)** 4-hydroxybutyl acrylate, and **d)** 2-(2-ethyoxyethyoxy)ethyl acrylate. Monomers **b)** and **c)** were eliminated as not being sufficiently volatile. Monomers **a)** and **d)** were able to produce pressures of up to approximately 1.5×10^{-1} mbar



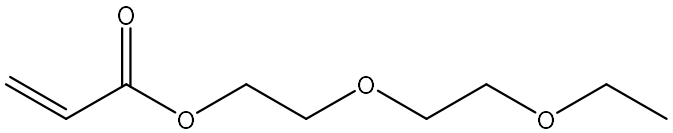
a) 2-Hydroxyethyl Acrylate



b) 2-Methoxyethyl Acrylate



c) 4-Hydroxybutyl Acrylate



d) 2-(2-Ethoxyethoxy)ethyl Acrylate

Figure 7.9 *Hydrophilic acrylic monomers subject to initial tests*

under vacuum but were not sufficiently stable under vacuum. Acrylic monomers are typically stored with an inhibitor to prevent them polymerizing *in situ* and the inhibitor requires oxygen to work. Some acrylic monomers, such as PFAC-*n* are stable under vacuum, but unfortunately both **a)** and **d)** degraded very quickly. At this point, the decision was made to replace **a)** with its less reactive methacrylate analogue, HEMA, which is stable under vacuum and has been successfully used in plasma polymerization [221]. The pressure conditions used for both HEMA and PFAC-6 were simply the conditions achieved by stirring the monomers under vacuum. This procedure therefore has the benefit of simplicity, and of ease of implementation on industrial scales.

The incorporation of HEMA:PFAC-6 into the co-polymer was in the ratio 1:4. The smaller quantity of HEMA reflects the lower pressure of the monomer vapour under vacuum ($1 \times 10^{-1} : 2 \times 10^{-1}$ mbar HEMA:PFAC-6) as well as the lower reactivity of methacrylate radicals in comparison to acrylates [222]. At this point, the distinction should be made between co-polymers, where covalent bonds exist between the different types of monomer unit, and mixed polymers. Although not included as part of this investigation, work by Foucquet *et al.* has shown that acrylate co-polymerization does occur in the plasma phase, even when using hydrocarbon and fluorocarbon monomers which would typically segregate in the solution phase [59,223]. It therefore seems reasonable to assume that a co-polymer, rather than a mixed polymer has been synthesized. One unusual aspect of the co-polymer is that it is harder than PFAC-6 (as observed via AFM). HEMA is not expected to interact strongly with the PFAC-6 side chain but may hydrogen bond to the acrylate group, resulting in a more rigid side chain structure.

The wetting properties of the co-polymer are interesting in that, whilst it is hydrophobic ($\theta_{\text{stat}} > 90°$) and oleophilic ($\theta_{\text{stat}} < 90°$), water is strongly pinned to the surface, whilst *n*-HD slides off at an incline of 20°. The strong pinning on PFAC-6, and example of which is shown in can be linked to the surface reconstruction. The area under the drop and at the triple phase line has high adhesion to the liquid, whilst the area ahead of the triple phase line has low adhesion to the liquid; this presents an energy barrier that the triple phase line has to overcome before it can move. In contrast, although it has stronger adhesion to the liquids than PFAC-6, the HEMA surface is uniform and there is therefore no strong barrier to motion along the surface. It is hypothesized that the hydroxyl

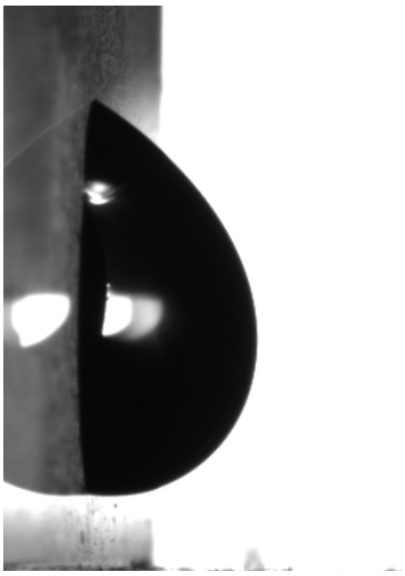


Figure 7.10 *Drop of water pinned to a vertical PFAC-6 surface*

group in HEMA forms an H-bond to the carbonyl group in PFAC-6, inhibiting surface reconstruction. This allows the non-polar liquids such as *n*-HD to slide easily across the surface. However, the presence of a polar liquid such as water or EG would be able to disrupt the H-bonding and allow PFAC-6 to undergo reorientation.

7.3. Conclusions

A co-polymer of HEMA and PFAC-6 has been successfully and reproducibly synthesised using plasma polymerization with only minor adjustments to existing protocols. The resulting surface is smooth and is harder than PFAC-6, with good coverage of the glass substrate. XPS analysis indicates good retention of the functional groups of both polymers. More work is needed to characterize this surface. For example, DSC would confirm whether this is a true co-polymer. The stability of this surface after immersion in water or oil has been not investigated and is an important part of establishing the viability of this coating for its intended use.

Although more work is required, the orthogonal sliding behaviours observed for oil and for polar liquids is extremely promising in the context of oil/water separation. **Figure 7.11** shows an example of an inclined super-oleophobic and -hydrophilic mesh developed by Brown *et al.* which has been used to separate oil and water successfully [12]; the water passes through the mesh, whilst the oil runs down the mesh into a different container and it is proposed that a similar process might be used with HEMA-co-PFAC-6.

Now that an effective protocol has been established, the composition of the surface could also be modified by reducing the flow of either the HEMA or PFAC-6 monomer. This would allow the wetting properties of the coating to be optimised further for improved sliding of oils and pinning of polar liquids.

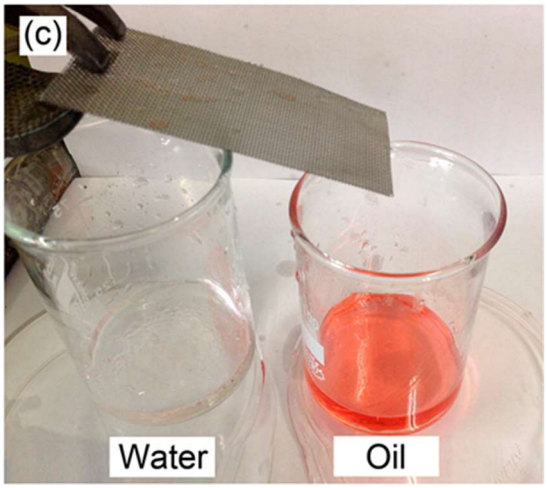


Figure 7.11 *Super-oleophobic and -hydrophilic mesh developed by Brown et al. for effective oil/water separation. Photograph from Ref. [12]*

7.4. References

[6] B. Wang, W. Liang, Z. Guo, and W. Liu, Chemical Society Reviews **44**, 336 (2015).
[12] P. S. Brown, O. D. L. A. Atkinson, and J. P. S. Badyal, ACS Applied Materials & Interfaces **6**, 7504 (2014).

[59] T. Fouquet, G. Mertz, M. Delmée, C. Becker, J. Bardon, and H. Sato, Plasma Processes and Polymers **13**, 862 (2016).
[135] L. Zhang, Z. Zhang, and P. Wang, NPG Asia Materials **4**, e8 (2012).
[136] Z. Chu, Y. Feng, and S. Seeger, Angewandte Chemie International Edition **54**, 2328 (2015).
[205] C. H. Peterson, S. D. Rice, J. W. Short, D. Esler, J. L. Bodkin, B. E. Ballachey, and D. B. Irons, Science **302**, 2082 (2003).
[206] A. B. Nordvik, J. L. Simmons, K. R. Bitting, A. Lewis, and T. Strøm-Kristiansen, Spill Science & Technology Bulletin **3**, 107 (1996).
[207] P. F. Kingston, Spill Science & Technology Bulletin **7**, 53 (2002).
[208] Z. Xue, Y. Cao, N. Liu, L. Feng, and L. Jiang, Journal of Materials Chemistry A **2**, 2445 (2014).
[209] Q. Ma, H. Cheng, A. G. Fane, R. Wang, and H. Zhang, Small **12**, 2186 (2016).
[210] M. Cheryan and N. Rajagopalan, Journal of Membrane Science **151**, 13 (1998).
[211] B. Tansel and J. Regula, Journal of Environmental Science and Health, Part A **35**, 1557 (2000).
[212] K. Gaaseidnes and J. Turbeville, Pure and Applied Chemistry **71**, 95 (1999).
[213] C. Wang, T. Yao, J. Wu, C. Ma, Z. Fan, Z. Wang, Y. Cheng, Q. Lin, and B. Yang, ACS Applied Materials & Interfaces **1**, 2613 (2009).
[214] J. Song, S. Li, C. Zhao, Y. Lu, D. Zhao, J. Sun, T. Roy, C. J. Carmalt, X. Deng, and I. P. Parkin, Nanoscale **10**, 1920 (2018).
[215] L. Feng, Z. Zhang, Z. Mai, Y. Ma, B. Liu, L. Jiang, and D. Zhu, Angewandte Chemie International Edition **43**, 2012 (2004).
[216] P. C. Chen and Z. K. Xu, Scientific Reports **3**, 2776 (2013).
[217] Z. Xue, S. Wang, L. Lin, L. Chen, M. Liu, L. Feng, and L. Jiang, Advanced Materials **23**, 4270 (2011).
[218] F. Zhang, W. B. Zhang, Z. Shi, D. Wang, J. Jin, and L. Jiang, Advanced Materials **25**, 4192 (2013).
[219] J. J. Li, L. T. Zhu, and Z. H. Luo, Chemical Engineering Journal **287**, 474 (2016).
[220] M. Tao, L. Xue, F. Liu, and L. Jiang, Advanced Materials **26**, 2943 (2014).
[221] C. Tarducci, W. C. E. Schofield, J. P. S. Badyal, S. A. Brewer, and C. Willis, Chemistry of Materials **14**, 2541 (2002).
[222] F. Hochart, J. Levalois-Mitjaville, and R. De Jaeger, Polymer **41**, 3159 (2000).
[223] G. Mertz, M. Delmée, J. Bardon, A. Martin, D. Ruch, T. Fouquet, S. Garreau, A. Airoudj, A. Marguier, and L. Ploux, Plasma Processes and Polymers **15**, 1800073 (2018).

8. Conclusions and Outlook

This thesis has primarily been a multi-faceted investigation of the properties of plasma polymerized perfluoroalkyl acrylates. A wide range of characterization techniques, including XPS, solid-state NMR, and extensive contact angle measurements, have been used to understand the behaviour of these surfaces both in air and in contact with a variety of different liquids. A number of other polymer surfaces have also been studied, although in somewhat less detail – these include the C6 perfluorinated monomers investigated in **Chapter 1**, and HEMA, a hydrophilic monomer used to create a copolymer investigated in **Chapter 7**. The pulsed plasma conditions developed by Coulson *et al.* [77] have been used to successfully synthesize acrylate (PFAC-*n*) and methacrylate (HEMA) polymers with a high degree of structural retention. However, the same conditions when used for monomers with an alkene or saturated polymerizable group resulted in highly cross-linked polymers.

The phase behaviour of PFAC-*n* has been explored via both DSC and NMR experiments, as well as more indirectly through wetting measurements. Based on these measurements, it is now possible to construct an (approximate) phase diagram for the bulk and surface phases of PFAC-*n*. **Figure 8.1** shows a phase diagram of the PFAC-*n* side chains (prior to annealing) at the in the bulk and at the surface at temperatures from 0-100 °C; the transition at 90 °C for PFAC-6

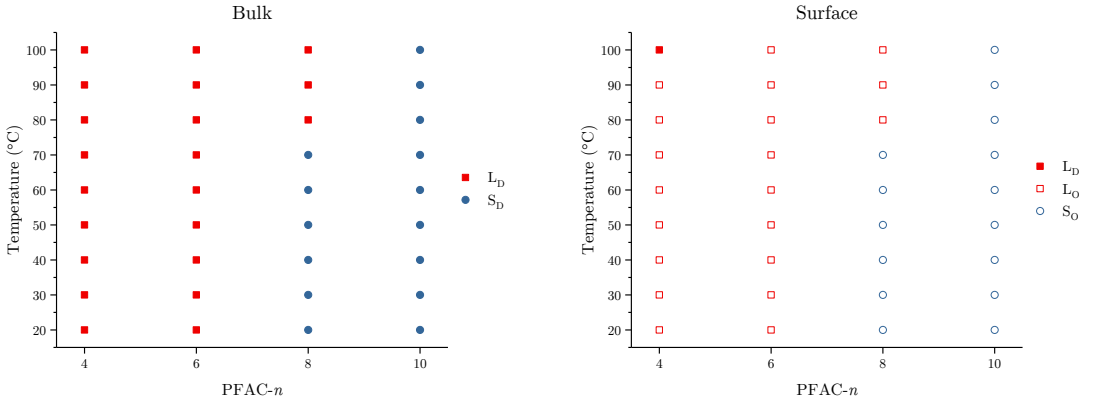


Figure 8.1 *Phase diagrams for PFAC-n polymers at the surface in the bulk and at the surface. S and L denote the solid or liquid phase, whilst the subscripts O and D denote ordered or disordered arrangements. The L_O-L_D transition temperature is somewhat arbitrarily defined as the temperature at which adaptive wetting no longer occurs.*

visible only in the NMR spectra has not been included. In the bulk, PFAC-10 and PFAC-8 (where $T < 70$ °C) exist in a solid disordered (S_D), polycrystalline state whilst PFAC-4, -6, and -8 (where $T > 70$ °C) exist in isotropic melts (liquid disordered, L_D). At the surface, there is increased ordering of the side-chains and angle-resolved XPS shows that there is preferential segregation of the CF_3 group at the surface; this is referred to as the liquid ordered (L_O) or solid ordered (S_O) phase. In the latter case, it is important to note that, in this context, this reflects *increased* ordering compared to the bulk rather than in an *absolute* sense. It is not until the PFAC-8 and -10 surfaces have been annealed that the side chains crystallize into a truly ordered state. Similarly, PFO shows increased ordering and preferential segregation of CF_3 at the surface, but the presence of cross-linked regions prevents any sort of crystallisation. In terms of surface energy, the trend is S_O (post-anneal) $< L_O < S_O$ (pre-anneal). This effect is seen in the low surface energy of PFAC-6 at room temperature, and the initial decrease in surface energy of PFAC-8 upon melting. As a brief aside on the subject of annealing – thermal

annealing is used to promote polymer crystallinity and often also used to generate a smooth surface. This study did not manage to successfully identify annealing conditions which made the PFAC-*n* polymers sufficiently smooth for use as an 'ideal' surface in wetting studies, although annealed PFAC-8 and -10 were used in NMR studies of the bulk polymer. Further work on annealed surfaces would provide an interesting point of comparison to the work presented here, particularly on the subject of adaptive wetting.

The liquid state is where the side chains are sufficiently mobile to undergo reorientation and adaptive wetting occurs. At lower temperatures, the surface is in the L_O state with the CF_3 outermost but when it is exposed to a liquid such as ethylene glycol or hexadecane, the side chains rearrange so that the liquid is in contact with the acrylate groups rather than the fluoroalkyl chain. The transition temperature from the L_O to L_D phase shown in the phase diagram for PFAC-4 corresponds to the temperature at which adaptive wetting ceases. This is a somewhat arbitrary definition as the contact angle aging experiments do not distinguish between the case where no surface reorganization occurs and the case where surface reorganization occurs on a timescale much shorter than the experiment. However, it is clear that the onset of the L_D state occurs at considerably higher temperatures at the surface than in the bulk, and that the contact angle of a probe liquid immediately after deposition depends on the ordering of the side chains at the PFAC-*n* surface.

One of the most interesting conclusions of this thesis is that surface reorganization can be driven by both by polar interactions, and also by the preferential segregation of hydrocarbon and fluorocarbon moieties. It has also been

demonstrated that the adaptive wetting process of the PFAC-*n* surfaces follows the first order kinetic model proposed by Butt *et al.* [139]. An interesting line of future enquiry would be a repeat of these experiments with fluorinated liquids, or on hydrocarbon analogues of the PFAC-*n* polymers. Honda *et al.* performed XPS experiments with water frozen into PFAC-*n* which showed significant changes in composition compared to the spectra in air [84]. Given that most of the dialogue surrounding surface reorganization has focussed on polar interactions, another stimulating line of enquiry would be to repeat these experiments with non-polar fluorocarbon and hydrocarbon liquids.

Having gained a better understanding of the physiochemical properties of PFAC-*n*, the wetting of chemical warfare agents on theses surfaces was examined. Several items of note have arisen from this investigation. Firstly, that neither the wetting of conventional probe liquids nor of common CWA simulants are able to predict the wetting behaviour of CWA's on PFAC-*n* surfaces. The disparity between predicted and observed behaviour is particularly large and for the CWA's Sarin and Soman. It is hypothesized that the presence of fluorine in these two CWA's is what drives the spreading of these liquids on PFAC-*n* surfaces. Secondly, that the CWA's and their simulants spread more readily on PFAC-*n* with shorter chain lengths, and that the contact angles increase with increasing chain length. This is contrary to the surface energy trends as determined earlier in the investigation. Clearly, more work on the subject of CWA wetting is required and proposed future work includes sorption experiments using a technique such as QCM. The presence of ^{31}P in both the G-series and V-series nerve agents and ^{19}F in both Sarin and Soman suggests that solid-state NMR might be a viable route

for examining the interactions between CWA's and PFAC-n. Indeed, a similar investigation using DMMP and Nafion has been undertaken by Giotto *et al.* [224].

Returning finally to the **Aim of Study** and the search for a suitable replacement for PFAC-8 in the manufacture of liquid-repellent clothing; PFAC-6 has the curious distinction of having a lower measured surface energy than PFAC-8, but being less repellent towards CWA's. Although this thesis has focussed on understanding the wetting behaviour of PFAC-n polymers, others have focussed their efforts on a more direct search for replacements for C8 perfluorinated compounds. Cross-linking has been used to good effect by several researchers to prevent surface reconstruction of C6 and C4 perfluorinated chains [66,225,226]. Similarly, Jiang *et al.* have co-polymerized C4 perfluorinated monomers with longer chain hydrocarbon analogues which form crystalline domains to inhibit surface reorganization [227]. These are promising solutions for low energy surfaces in general, but the work in this thesis has shown that this will not necessarily translate to good CWA repellency. There are still many challenges ahead both in terms of understanding the wetting of CWA's and in developing environmentally friendly and effective alternative materials.

8.1. References

[66] A. Liu, E. Goktekin, and K. K. Gleason, Langmuir (2014).

[77] S. R. Coulson, I. S. Woodward, J. P. S. Badyal, S. A. Brewer, and C. Willis, Chemistry of Materials **12**, 2031 (2000).

[84] K. Honda, M. Morita, H. Otsuka, and A. Takahara, Macromolecules **38**, 5699 (2005).

[139] H.-J. Butt, R. Berger, W. Steffen, D. Vollmer, and S. A. L. Weber, Langmuir **34**, 11292 (2018).

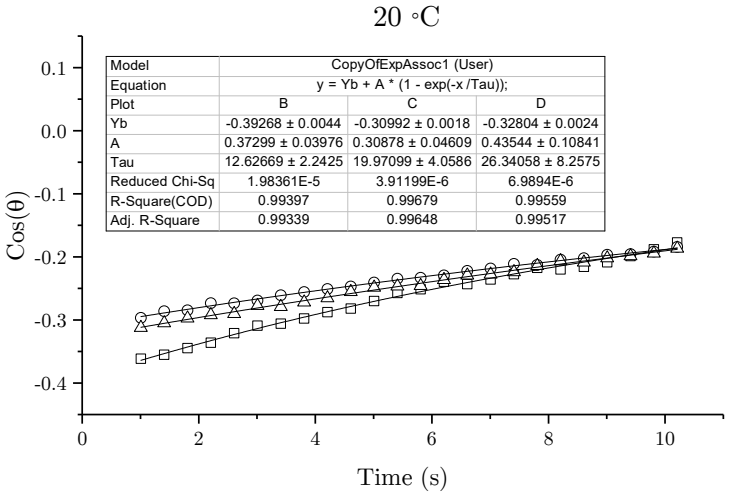
[224] M. V. Giotto, J. Zhang, P. T. Inglefield, Wen, and A. A. Jones, Macromolecules **36**, 4397 (2003).

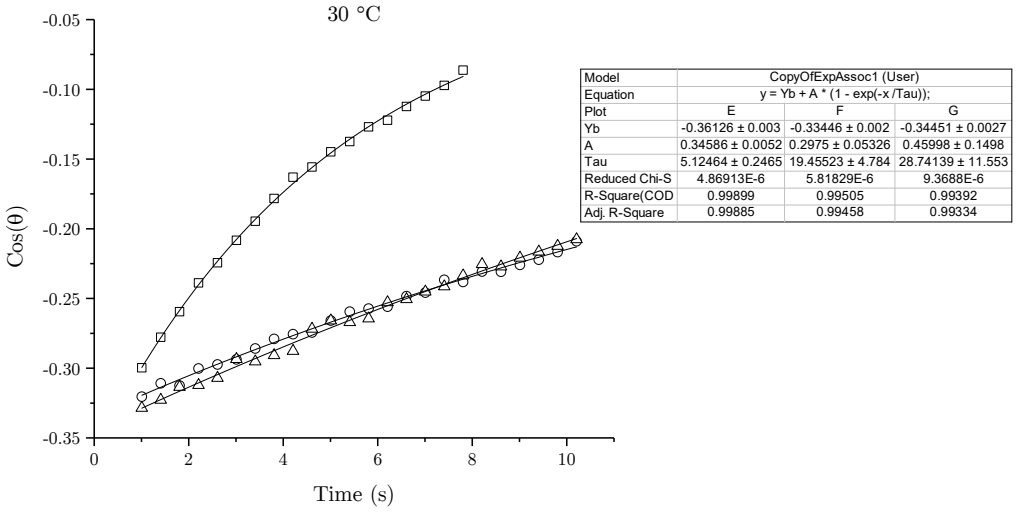
[225] J. L. Yagüe and K. K. Gleason, Macromolecules **46**, 6548 (2013).
[226] T. Darmanin and F. Guittard, Macromolecular Chemistry and Physics **214**, 2036 (2013).
[227] J. Jiang, G. Zhang, Q. Wang, Q. Zhang, X. Zhan, and F. Chen, ACS Applied Materials & Interfaces **8**, 10513 (2016).

Appendix A: Complete Results for Drop Aging Experiments

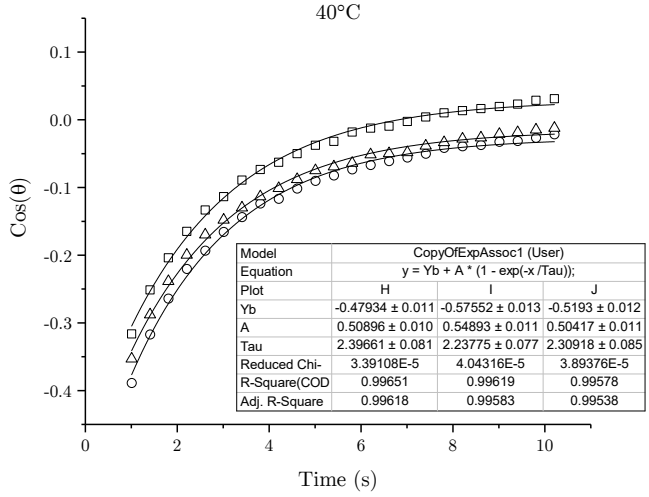
A. PFAC-4

A.1. Ethylene Glycol

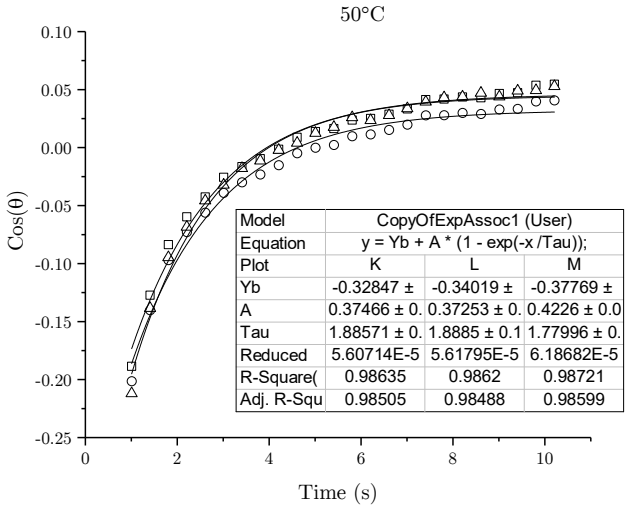




Model	CopyOfExpAssoc1 (User)		
Equation	y = Yb + A * (1 - exp(-x /Tau));		
Plot	E	F	G
Yb	-0.36126 ± 0.003	-0.33446 ± 0.002	-0.34451 ± 0.0027
A	0.34586 ± 0.0052	0.2975 ± 0.05326	0.45998 ± 0.1498
Tau	5.12464 ± 0.2465	19.45523 ± 4.784	28.74139 ± 11.553
Reduced Chi-S	4.86913E-6	5.81829E-6	9.3688E-6
R-Square(COD	0.99899	0.99505	0.99392
Adj. R-Square	0.99885	0.99458	0.99334

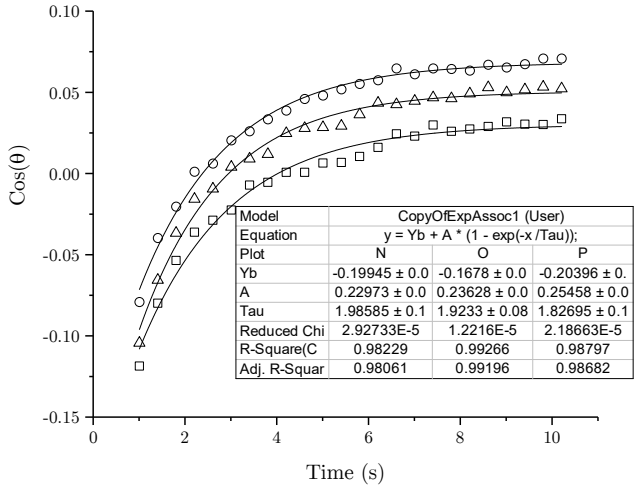


Model	CopyOfExpAssoc1 (User)		
Equation	y = Yb + A * (1 - exp(-x /Tau));		
Plot	H	I	J
Yb	-0.47934 ± 0.011	-0.57552 ± 0.013	-0.5193 ± 0.012
A	0.50896 ± 0.010	0.54893 ± 0.011	0.50417 ± 0.011
Tau	2.39661 ± 0.081	2.23775 ± 0.077	2.30918 ± 0.085
Reduced Chi-	3.39108E-5	4.04316E-5	3.89376E-5
R-Square(COD	0.99651	0.99619	0.99578
Adj. R-Square	0.99618	0.99583	0.99538



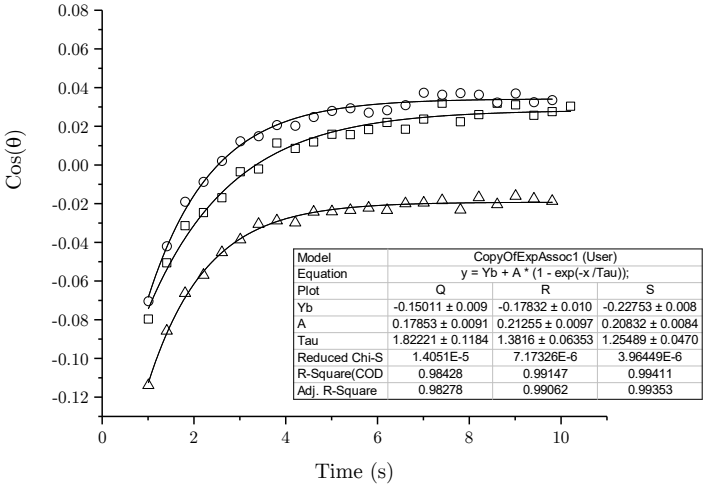
Model	CopyOfExpAssoc1 (User)		
Equation	y = Yb + A * (1 - exp(-x /Tau));		
Plot	K	L	M
Yb	-0.32847 ±	-0.34019 ±	-0.37769 ±
A	0.37466 ± 0.	0.37253 ± 0.	0.4226 ± 0.0
Tau	1.88571 ± 0.	1.8885 ± 0.1	1.77996 ± 0.
Reduced	5.60714E-5	5.61795E-5	6.18682E-5
R-Square(	0.98635	0.9862	0.98721
Adj. R-Squ	0.98505	0.98488	0.98599

60°C



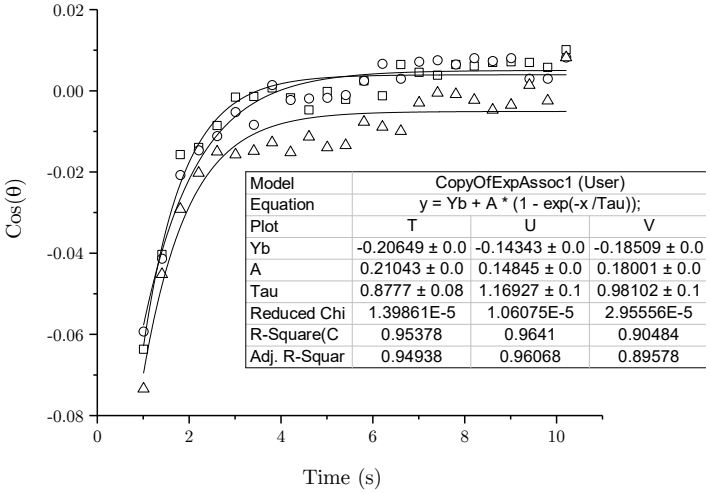
Model	CopyOfExpAssoc1 (User)		
Equation	y = Yb + A * (1 - exp(-x /Tau));		
Plot	N	O	P
Yb	-0.19945 ± 0.0	-0.1678 ± 0.0	-0.20396 ± 0.
A	0.22973 ± 0.0	0.23628 ± 0.0	0.25458 ± 0.0
Tau	1.98585 ± 0.1	1.9233 ± 0.08	1.82695 ± 0.1
Reduced Chi	2.92733E-5	1.2216E-5	2.18663E-5
R-Square(C	0.98229	0.99266	0.98797
Adj. R-Squar	0.98061	0.99196	0.98682

70°C



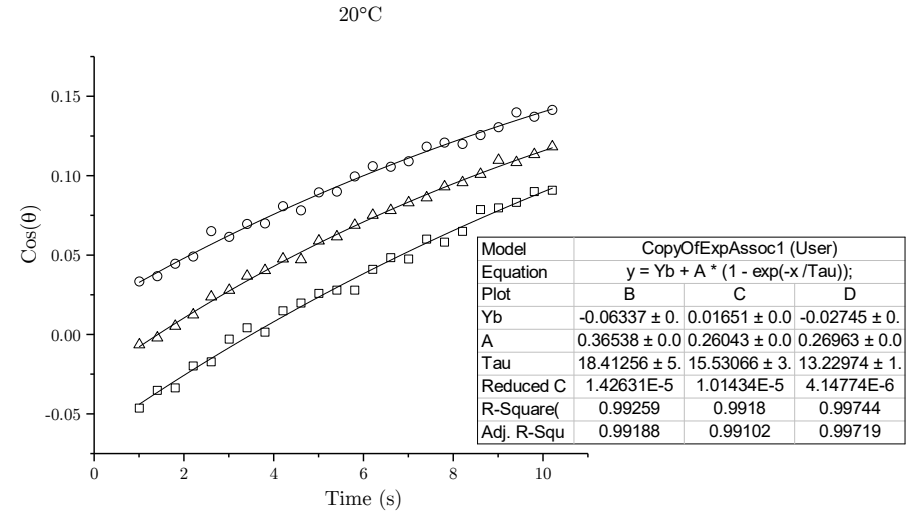
Model	CopyOfExpAssoc1 (User)		
Equation	y = Yb + A * (1 - exp(-x /Tau));		
Plot	Q	R	S
Yb	-0.15011 ± 0.009	-0.17832 ± 0.010	-0.22753 ± 0.008
A	0.17853 ± 0.0091	0.21255 ± 0.0097	0.20832 ± 0.0084
Tau	1.82221 ± 0.1184	1.3816 ± 0.06353	1.25489 ± 0.0470
Reduced Chi-S	1.4051E-5	7.17326E-6	3.96449E-6
R-Square(COD	0.98428	0.99147	0.99411
Adj. R-Square	0.98278	0.99062	0.99353

80°C

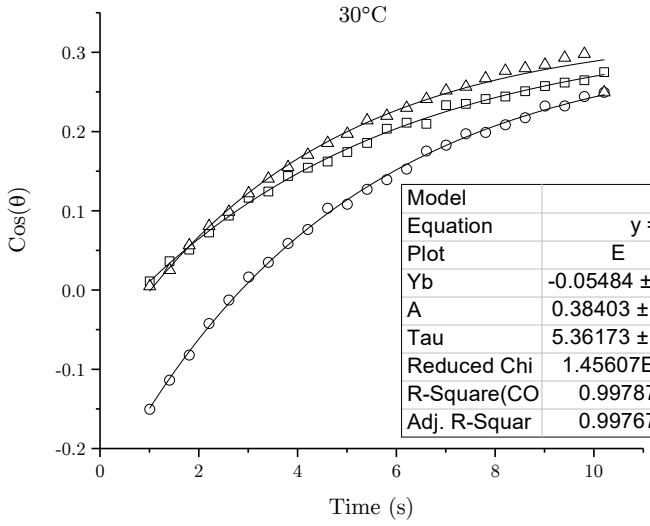


Model	CopyOfExpAssoc1 (User)		
Equation	y = Yb + A * (1 - exp(-x /Tau));		
Plot	T	U	V
Yb	-0.20649 ± 0.0	-0.14343 ± 0.0	-0.18509 ± 0.0
A	0.21043 ± 0.0	0.14845 ± 0.0	0.18001 ± 0.0
Tau	0.8777 ± 0.08	1.16927 ± 0.1	0.98102 ± 0.1
Reduced Chi	1.39861E-5	1.06075E-5	2.95556E-5
R-Square(C	0.95378	0.9641	0.90484
Adj. R-Squar	0.94938	0.96068	0.89578

A.2. *n*-Hexadecane

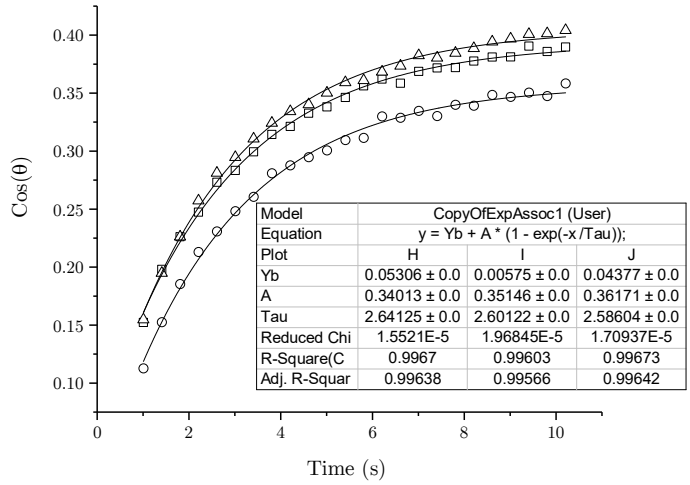


Model	CopyOfExpAssoc1 (User)		
Equation	y = Yb + A * (1 - exp(-x /Tau));		
Plot	B	C	D
Yb	-0.06337 ± 0.	0.01651 ± 0.0	-0.02745 ± 0.
A	0.36538 ± 0.0	0.26043 ± 0.0	0.26963 ± 0.0
Tau	18.41256 ± 5.	15.53066 ± 3.	13.22974 ± 1.
Reduced C	1.42631E-5	1.01434E-5	4.14774E-6
R-Square(	0.99259	0.9918	0.99744
Adj. R-Squ	0.99188	0.99102	0.99719



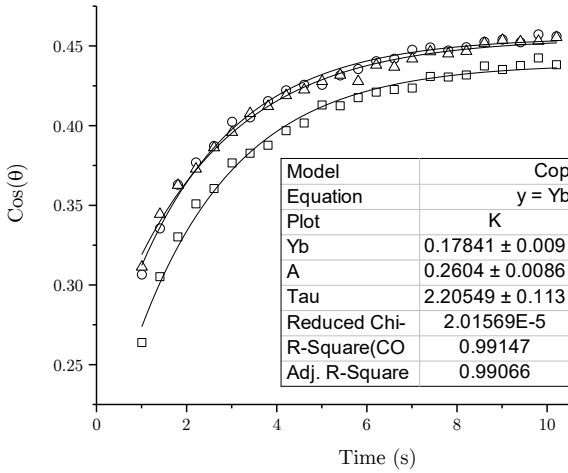
Model	CopyOfExpAssoc1 (User)		
Equation	y = Yb + A * (1 - exp(-x /Tau));		
Plot	E	F	G
Yb	-0.05484 ± 0.0	-0.25842 ± 0.0	-0.08969 ± 0.0
A	0.38403 ± 0.0	0.57146 ± 0.00	0.41777 ± 0.01
Tau	5.36173 ± 0.2	4.74494 ± 0.14	4.23497 ± 0.40
Reduced Chi	1.45607E-5	1.79804E-5	1.06285E-4
R-Square(CO	0.99787	0.99885	0.9875
Adj. R-Squar	0.99767	0.99874	0.9863

40°C



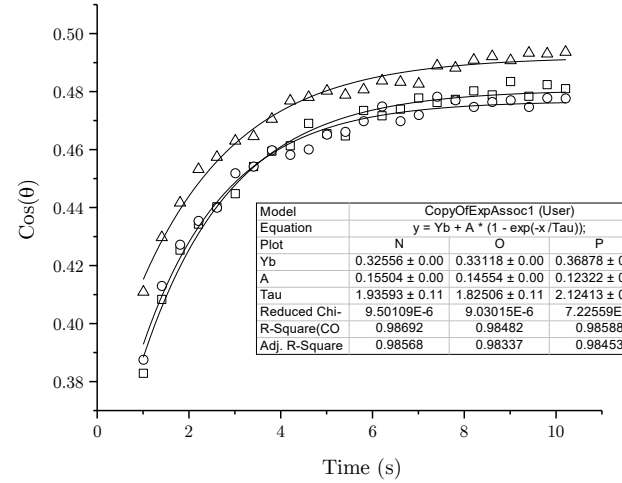
Model	CopyOfExpAssoc1 (User)		
Equation	y = Yb + A * (1 - exp(-x /Tau));		
Plot	H	I	J
Yb	0.05306 ± 0.0	0.00575 ± 0.0	0.04377 ± 0.0
A	0.34013 ± 0.0	0.35146 ± 0.0	0.36171 ± 0.0
Tau	2.64125 ± 0.0	2.60122 ± 0.0	2.58604 ± 0.0
Reduced Chi	1.5521E-5	1.96845E-5	1.70937E-5
R-Square(C	0.9967	0.99603	0.99673
Adj. R-Squar	0.99638	0.99566	0.99642

50°C

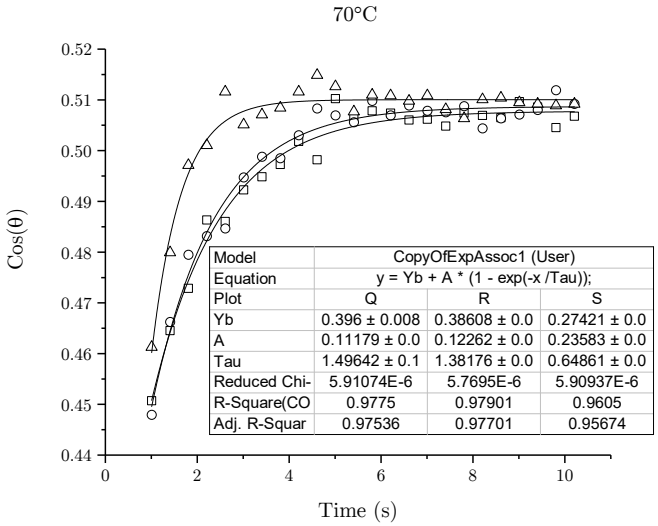


Model	CopyOfExpAssoc1 (User)		
Equation	y = Yb + A * (1 - exp(-x /Tau));		
Plot	K	L	M
Yb	0.17841 ± 0.009	0.22948 ± 0.007	0.2494 ± 0.0070
A	0.2604 ± 0.0086	0.2259 ± 0.0067	0.20562 ± 0.006
Tau	2.20549 ± 0.113	2.20229 ± 0.102	2.42806 ± 0.126
Reduced Chi-	2.01569E-5	1.25016E-5	1.2897E-5
R-Square(CO	0.99147	0.99295	0.99201
Adj. R-Square	0.99066	0.99228	0.99124

60°C



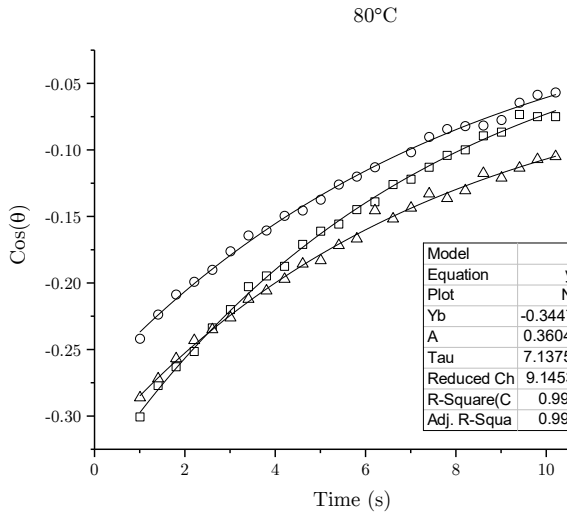
Model	CopyOfExpAssoc1 (User)		
Equation	y = Yb + A * (1 - exp(-x /Tau));		
Plot	N	O	P
Yb	0.32556 ± 0.00	0.33118 ± 0.00	0.36878 ± 0.00
A	0.15504 ± 0.00	0.14554 ± 0.00	0.12322 ± 0.00
Tau	1.93593 ± 0.11	1.82506 ± 0.11	2.12413 ± 0.13
Reduced Chi-	9.50109E-6	9.03015E-6	7.22559E-6
R-Square(CO	0.98692	0.98482	0.98588
Adj. R-Square	0.98568	0.98337	0.98453



Model	CopyOfExpAssoc1 (User)		
Equation	y = Yb + A * (1 - exp(-x /Tau));		
Plot	Q	R	S
Yb	0.396 ± 0.008	0.38608 ± 0.0	0.27421 ± 0.0
A	0.11179 ± 0.0	0.12262 ± 0.0	0.23583 ± 0.0
Tau	1.49642 ± 0.1	1.38176 ± 0.0	0.64861 ± 0.0
Reduced Chi-	5.91074E-6	5.7695E-6	5.90937E-6
R-Square(CO	0.9775	0.97901	0.9605
Adj. R-Squar	0.97536	0.97701	0.95674

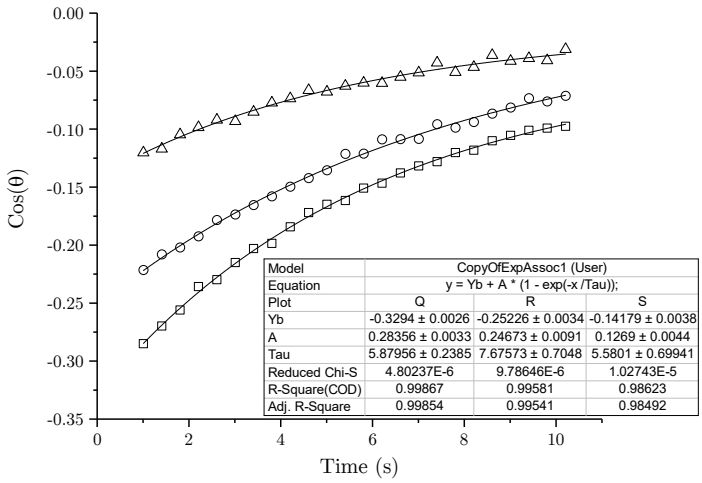
B. PFAC-6

B.1. Ethylene Glycol



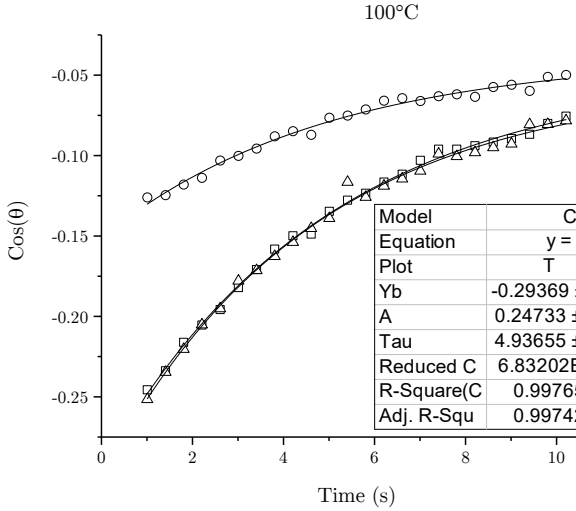
Model	CopyOfExpAssoc1 (User)		
Equation	y = Yb + A * (1 - exp(-x /Tau));		
Plot	N	O	P
Yb	-0.3447 ± 0.0	-0.27169 ± 0.	-0.3221 ± 0.0
A	0.36049 ± 0.	0.2966 ± 0.01	0.28731 ± 0.0
Tau	7.1375 ± 0.3	8.04198 ± 0.6	7.22686 ± 0.6
Reduced Ch	9.14536E-6	1.0218E-5	1.3167E-5
R-Square(C	0.99825	0.99698	0.99602
Adj. R-Squa	0.99809	0.99668	0.99564

90°C



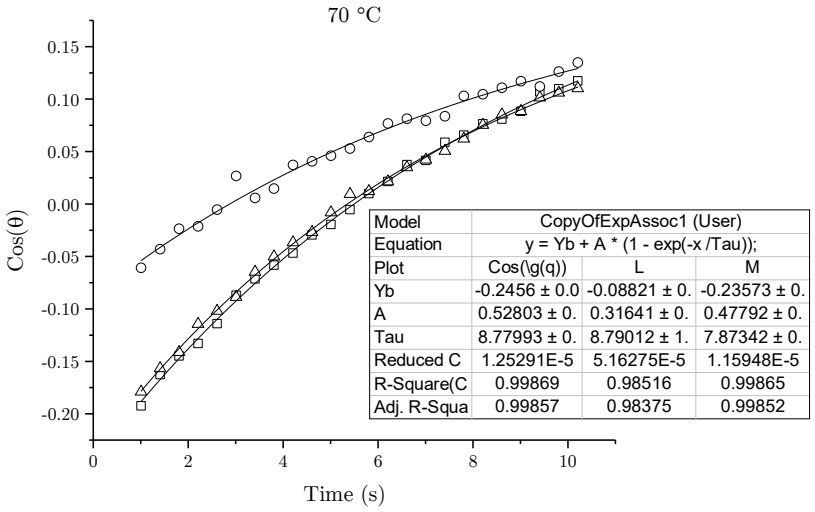
Model	CopyOfExpAssoc1 (User)		
Equation	y = Yb + A * (1 - exp(-x /Tau));		
Plot	Q	R	S
Yb	-0.3294 ± 0.0026	-0.25226 ± 0.0034	-0.14179 ± 0.0038
A	0.28356 ± 0.0033	0.24673 ± 0.0091	0.1269 ± 0.0044
Tau	5.87956 ± 0.2385	7.67573 ± 0.7048	5.5801 ± 0.69941
Reduced Chi-S	4.80237E-6	9.78646E-6	1.02743E-5
R-Square(COD)	0.99867	0.99581	0.98623
Adj. R-Square	0.99854	0.99541	0.98492

100°C

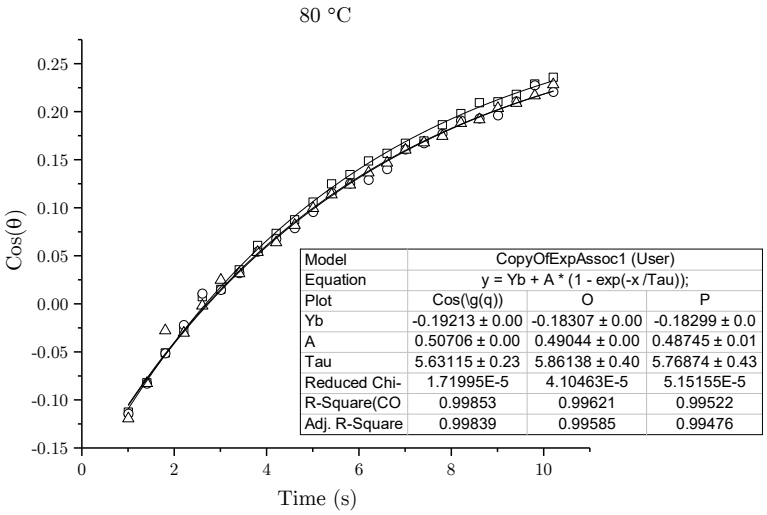


Model	CopyOfExpAssoc1 (User)		
Equation	y = Yb + A * (1 - exp(-x /Tau));		
Plot	T	U	V
Yb	-0.29369 ± 0.	-0.15118 ± 0.	-0.29937 ± 0.
A	0.24733 ± 0.	0.11313 ± 0.	0.24612 ± 0.
Tau	4.93655 ± 0.	4.90821 ± 0.	4.62494 ± 0.
Reduced C	6.83202E-6	7.60602E-6	1.48608E-5
R-Square(C	0.99765	0.98762	0.9949
Adj. R-Squ	0.99742	0.98644	0.99441

B.2. *n*-Hexadecane

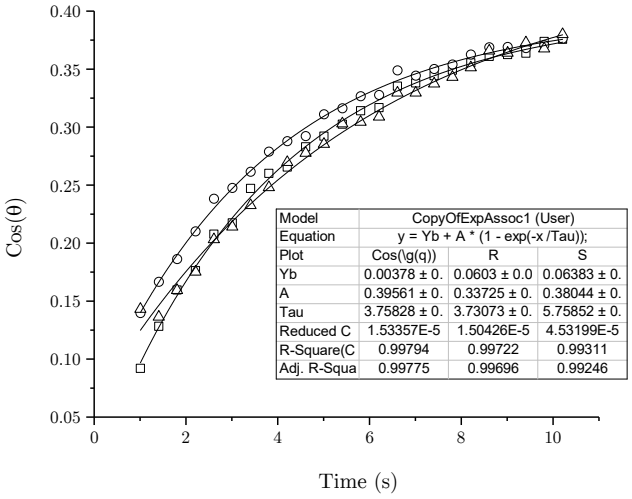


Model	CopyOfExpAssoc1 (User)		
Equation	y = Yb + A * (1 - exp(-x /Tau));		
Plot	Cos(\g(q))	L	M
Yb	-0.2456 ± 0.0	-0.08821 ± 0.	-0.23573 ± 0.
A	0.52803 ± 0.	0.31641 ± 0.	0.47792 ± 0.
Tau	8.77993 ± 0.	8.79012 ± 1.	7.87342 ± 0.
Reduced C	1.25291E-5	5.16275E-5	1.15948E-5
R-Square(C	0.99869	0.98516	0.99865
Adj. R-Squa	0.99857	0.98375	0.99852



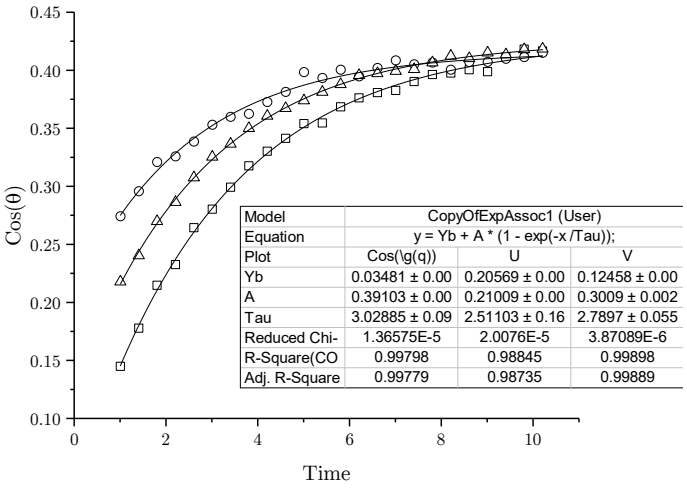
Model	CopyOfExpAssoc1 (User)		
Equation	y = Yb + A * (1 - exp(-x /Tau));		
Plot	Cos(\g(q))	O	P
Yb	-0.19213 ± 0.00	-0.18307 ± 0.00	-0.18299 ± 0.0
A	0.50706 ± 0.00	0.49044 ± 0.00	0.48745 ± 0.01
Tau	5.63115 ± 0.23	5.86138 ± 0.40	5.76874 ± 0.43
Reduced Chi-	1.71995E-5	4.10463E-5	5.15155E-5
R-Square(CO	0.99853	0.99621	0.99522
Adj. R-Square	0.99839	0.99585	0.99476

90 °C



Model	CopyOfExpAssoc1 (User)		
Equation	y = Yb + A * (1 - exp(-x /Tau));		
Plot	Cos(\g(q))	R	S
Yb	0.00378 ± 0.	0.0603 ± 0.0	0.06383 ± 0.
A	0.39561 ± 0.	0.33725 ± 0.	0.38044 ± 0.
Tau	3.75828 ± 0.	3.73073 ± 0.	5.75852 ± 0.
Reduced C	1.53357E-5	1.50426E-5	4.53199E-5
R-Square(C	0.99794	0.99722	0.99311
Adj. R-Squa	0.99775	0.99696	0.99246

100 °C



Model	CopyOfExpAssoc1 (User)		
Equation	y = Yb + A * (1 - exp(-x /Tau));		
Plot	Cos(\g(q))	U	V
Yb	0.03481 ± 0.00	0.20569 ± 0.00	0.12458 ± 0.00
A	0.39103 ± 0.00	0.21009 ± 0.00	0.3009 ± 0.002
Tau	3.02885 ± 0.09	2.51103 ± 0.16	2.7897 ± 0.055
Reduced Chi-	1.36575E-5	2.0076E-5	3.87089E-6
R-Square(CO	0.99798	0.98845	0.99898
Adj. R-Square	0.99779	0.98735	0.99889